

**STUDY OF GROUP-IVB METAL OXIDES IN BULK AND LOWER DIMENSION  
USING PERTURBED  $\gamma$ - $\gamma$  ANGULAR CORRELATION TECHNIQUE**

by

**Debashis Banerjee**

**Enrolment No: CHEM01201004008**

**Bhabha Atomic Research Centre (VECC)**

**Kolkata-700064, India.**

*A thesis submitted to the  
Board of studies in Chemical Sciences  
in partial fulfillment of the requirements  
for the degree of*

**Doctor of Philosophy**

of

**Homi Bhabha National Institute**

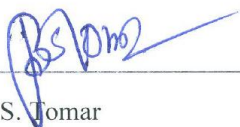


**October, 2014**

## Home Bhabha National Institute

### Recommendations of the Viva Voce Board

As members of the Viva Voce Board, we certify that we have read the dissertation prepared by Shri Debashis Banerjee entitled "Study of Group-IVB Metal Oxides in Bulk and Lower Dimension using Perturbed  $\gamma$ - $\gamma$  Angular Correlation Technique" and recommend that it may be accepted as fulfilling the dissertation requirement for the Degree of Doctor of Philosophy.



Date: 29/10/2014

Chairman - Prof. B. S. Tomar



Date: 10.10.2014

Guide/ Convener - Prof. S. K. Das



Date: 10/10/14

Member 1 - Prof. S. Bhattacharya



Date: 10.10.2014

Member 2 - Dr. D. P. Chowdhury

Final approval and acceptance of this dissertation is contingent upon the candidate's submission of the final copies of the dissertation to HBNI.

I hereby certify that I have read this dissertation prepared under my direction and recommend that it may be accepted as fulfilling the dissertation requirement.

Date: 10.10.2014

Place: Kolkata



Guide

## STATEMENT BY AUTHOR

This dissertation has been submitted in partial fulfillments of requirements for an advanced degree at Home Bhabha National Institute (HBNI) and is deposited in the library to be made available to borrowers under rules of the HBNI.

Brief quotations from this dissertation are allowable without special permission, provided that accurate knowledge of source is made. Requests for permission for extended quotation from or reproduction of this manuscript in whole or in part may be granted by the competent authority of HBNI when in his or her judgement the proposed use of the material is in the interests of scholarship. In all other instances, however, permission must be obtained from the author.



**(Debashis Banerjee)**

## DECLARATION

I, hereby declare that the investigation presented in the thesis has been carried out by me. The work is original and has not been submitted earlier as a whole or in part for a degree/diploma at this or any other Institute/University.

A handwritten signature in black ink, appearing to read 'Debashis Banerjee', with a stylized flourish at the end.

(Debashis Banerjee)

## List of Publications arising from the thesis

### A. Journal:

#### a. Published:

1. “Study of surface-bulk mass transport and phase transformation in nano-TiO<sub>2</sub> using hyperfine interaction technique”, **D. Banerjee**, S.K. Das, S.V. Thakare, P.Y. Nabhiraj, R. Menon, R.K. Bhandari, K. Krishnan, *J. Phys. Chem. Solids*, **2010**, *71*, 983–987.
2. “Zr-doped rutile TiO<sub>2</sub>: a nuclear quadrupole interaction study”, **D. Banerjee**, S. K. Das, P. Das, S. V. Thakare, T. Butz; *Hyperfine Interaction*, **2011**, *197*, 193–198.
3. “Effect of  $\gamma$ -dose on the crystal structure and leaching behaviour of TiO<sub>2</sub> matrix labeled with <sup>181</sup>Hf/<sup>181</sup>Ta tracer”, **D. Banerjee**, R. Guin, S. K. Das, S. V. Thakare, *J. Radioanal. Nucl. Chem.*, **2011**, *290*, 119–121.
4. “Nuclear quadrupole interaction at <sup>181</sup>Ta in hafnium dioxide fiber: Time differential perturbed angular correlation measurements and ab initio calculations”, **D. Banerjee**, P. Das, R. Guin, S. K. Das, *J. Phys. Chem. Solids*, **2012**, *73*, 1090-1094.
5. “Study of the Role of Metal Core on the Thermal Behavior of Ag@TiO<sub>2</sub> Core-Shell Nanoparticles”, **D. Banerjee** and S. K. Das, *J. Radioanal. Nucl. Chem.*, **2014**, *300*, 99-105.

#### b. Communicated:

1. **D. Banerjee**, S.K. Das, S. V. Thakare, P.Y. Nabhiraj, R. Menon; Nano-phase Evolution of HfO<sub>2</sub> Thin Film on Si (111) Surface: A Nuclear Quadrupole Interaction Study, *Thin Solid Films*.

### B. Conferences:

1. **D. Banerjee**, R. Guin & S.K. Das; Study of Leaching Property of TiO<sub>2</sub> matrix labeled with <sup>181</sup>Hf, *Nuclear and Radiochemistry Symposium (NUCAR)-2009*.

2. **D. Banerjee** and S. K. Das; Annealing Behavior of Hafnium Oxide Fiber Used as a Target for Radioactive Ion Beam Preparation, *Synthesis and Characterization of Smart Materials-2009*.
3. **D. Banerjee**, P. Ghosh, R.K. Chatterjee and S. K. Das; Hyperfine interaction study of 5% Mn<sup>+2</sup> doped TiO<sub>2</sub>, *Condensed Matter Days-2009*.
4. P. Das, **D. Banerjee** and S. K. Das; Electronic and structural properties of anatase and rutile TiO<sub>2</sub> doped with Ta: Experimental study and *ab initio* calculations, *Joint International Conference on HFI and NQI-2010*.
5. **D. Banerjee** and S. K. Das; Nano-phase Hindered Evolution of HfO<sub>2</sub> Thin Film on Si (111) Surface: A Nuclear Quadrupole Interaction Study, *Joint International Conference on HFI and NQI-2012*.
6. **D. Banerjee**, P. Das, S.V. Thakare and S.K. Das; Study of Annealing Behavior of Probe Lattice Interaction in Gr-IVB oxides by Nuclear Quadrupole Interaction, *NUCAR-2013*.
7. **D. Banerjee**, S. Bhattacharya, T. Bhattacharjee and S.K. Das; Fast-slow coincidence measurements with LaBr<sub>3</sub> (Ce) detectors, *NUCAR-2013*.



**(Debashis Banerjee)**

## **Acknowledgements**

I would like to express my special appreciation and thanks to my guide Professor Dr. S. K. Das, you have been a tremendous mentor for me. I would like to thank you for encouraging my research and for allowing me to grow as a research scientist. Your advice on both research as well as on my career have been priceless. I would also like to thank my committee members, Professor B. S. Tomar, Professor S. Bhattacharya and Dr. D. P. Chowdhury for serving as my committee members even at hardship. I am also very grateful to Dr. Tumpa Bhattacharjee for her scientific advice and knowledge and many insightful discussions and suggestions. I am also thankful to Dr. S. V. Thakare for his continuous cooperation for carrying out experiments.

I extend my heartiest thanks to Dr. R. Guin, Mr. R. K. Chatterjee and Mr. A. Gangopadhyaya for their cooperation inside the laboratory. I thank Mr. Y. N. Rao for his sincere help in some of the sample preparations. I am grateful to Head, Radiochemistry Division (BARC) for his support and encouragement in carrying this research work. I am also grateful to all my senior colleagues and friends at VECC, Kolkata for their sincere cooperation and help at any point of time.

I convey my deepest gratitude to my parents. Their filial love and affection has made me reach this stage of my life. I will be ever grateful to them for their sacrifice. I express my sincere thanks to my wife for her sacrifice and encouragement to complete my thesis.

I am also grateful Mrs. L. Barua and Mrs. S. SahaDas for their continuous support and encouragement in carrying out my research program. Finally, I cannot escape one name Mr. P. Tribedy, my friend and colleague, who has been a real inspiration in my life for carrying out good research program and also for enriching me with versatile knowledge.

Debashis Banerjee

## Table of Contents

SYNOPSIS.....	1
List of Figures .....	15
List of Tables: .....	18
Chapter 1. Introduction .....	19
1.1. Group-IVB Metal Oxides: .....	19
1.1.1 Crystal Structure: .....	20
1.1.2. Phase Transformation: .....	22
1.1.3. Applications in Bulk and Lower Dimensions: .....	28
1.1.4. Doped Oxides: .....	35
1.2 Perturbed Angular Correlation Spectroscopy: .....	42
1.2.1. Historical Background on PAC: .....	45
1.2.2. Electric Quadrupole Moment and EFG: .....	46
1.2.3. Directional Correlation Function: .....	52
1.2.4. Perturbed Angular Correlation Function:.....	61
1.2.5. Static Magnetic and Electric Fields: .....	70
1.2.6. Time-Dependent Perturbations: .....	78
1.2.7. Influence of Preceding Decays on Angular Correlations:.....	83
1.2.8. Methodology and PAC Isotopes: .....	85
1.2.9. Application of TDPAC Technique: .....	91
1.3. Other Techniques: .....	100
1.3.1. XRD Measurement: .....	100
1.3.2. Transmission Electron Microscopy (TEM): .....	102
1.3.3. Scanning Electron Microscope (SEM): .....	102
1.3.4. Atomic Force Microscope (AFM): .....	103
1.3.5. UV-Vis Spectrophotometry: .....	105
1.3.6. RBS Spectroscopy: .....	106
1.4. Motivation and Scope of the Thesis:.....	106
Chapter 2. Development of Fast-Slow Coincidence Setup with LaBr <sub>3</sub> (Ce) Detectors .....	109
2.1. Detectors: .....	112
2.2. Photo Multiplier Tube:.....	113

2.3. Resolving Time: .....	116
2.4. Electronic Modules: .....	118
2.5. Energy of Photons: .....	122
2.6. Data Reduction: .....	122
2.7. Conclusion: .....	124
Chapter 3. TDPAC Study of Group-IVB Oxides in Bulk Dimension .....	125
3.1. Bulk Oxides: .....	125
3.1.1. Introduction: .....	125
3.1.2. Sample Preparation: .....	126
3.1.3. Results and Discussion: .....	127
3.2. Doped Oxides: .....	132
3.2.1. Introduction: .....	132
3.2.2. Sample Preparation: .....	134
3.2.3. Results and Discussion: .....	134
3.3. Radiation Damage Study: .....	138
3.3.1. Introduction: .....	138
3.3.2. Sample Preparation: .....	139
3.3.3. Leaching Study: .....	139
3.3.4. Results and Discussion: .....	140
3.4. Study of HfO <sub>2</sub> Fibre: .....	142
3.4.1. Introduction: .....	142
3.4.2. Experiments and Measurements: .....	144
3.4.3. Results and Discussion: .....	145
3.4.4. Wien2K Calculation: .....	146
3.5. Conclusion: .....	153
Chapter 4. TDPAC Study of Group-IVB Oxides in Low Dimension.....	154
4.1. Phase Transition in Nano TiO <sub>2</sub> : .....	154
4.1.1. Introduction: .....	154
4.1.2. Sample Preparation: .....	155
4.1.3. Results and Discussion: .....	156
4.2. Study of Core-shell Nanoparticles: .....	163
4.2.1. Introduction: .....	163

4.2.2. Experimental Procedure and Measurements: .....	165
4.2.3. Results and Discussion: .....	166
4.3. Study of Thin Film:.....	174
4.3.1. Introduction:.....	174
4.3.2. Experimental Study:.....	176
4.3.3. Results and Discussion: .....	178
4.4. Conclusion: .....	185
Chapter 5. Summary and Outlook.....	186
References:.....	190
Index .....	202

## SYNOPSIS

The topic of the present thesis is mainly divided into two parts:

- a. The development of a fast-slow coincidence setup for the Time Differential Perturbed Angular Correlation (TDPAC) measurements based on  $\text{LaBr}_3(\text{Ce})$  detectors.
- b. The hyperfine study of different physico-chemical phenomena related to group-IVB metal oxides using the above TDPAC spectrometer and to envisage the sensitivity of the present nuclear hyperfine technique TDPAC in order to study chemical matrices in atomic level.

The objective of the present work is to perceive the sensitivity and versatility of TDPAC technique in different types of chemical phenomena with an atomic scale resolution. The study is not confined in a particular field of chemical phenomena; rather the wide applicability of the hyperfine technique has been emphasized. For the study with this hyperfine tool, a fast-slow coincidence circuit with a CAMAC-based data-acquisition system has been developed. The latest available  $\text{LaBr}_3(\text{Ce})$  scintillation detectors coupled to a fast PM Tube have been used in the above circuit. After coupling the detector-assembly to the coincidence circuit, the characteristics of the detector system has also been studied in order to optimize the best operational condition for the present measurements. This setup was used for the subsequent TDPAC measurements in order to study the different chemical phenomena. For this, group-IVB metal oxides, viz.,  $\text{TiO}_2$ ,  $\text{ZrO}_2$  and  $\text{HfO}_2$ , have been chosen based on their versatile application of these three oxides. The areas of the study in the present thesis have been chosen on the basis of the applications of these oxides. Further the nuclear probe used in the present study, i.e.,  $^{181}\text{Hf}$ , falls in the same group and hence, has got the maximum probability to replace the lattice site in any of these three oxides prepared by a soft chemical method along with the probe. The minute changes in the different

chemical phenomena, which otherwise are hardly perceived by any other tool, have been discussed with the help of TDPAC in the present thesis. In some cases, the present work has delivered several new data in the field of TDPAC. Along with the different types of chemical phenomena, the technique has also been used to study the different dimensions (viz., bulk, thin film and nano) of materials. Another aspect of TDPAC, viz., the effect of radioactive decay process feeding the  $\gamma$ - $\gamma$  cascade has also been studied with  $^{111}\text{In}/^{111}\text{Cd}$  probe in case of pure oxides. In some cases, the experimental results have been corroborated by the theoretical calculations of EFG at  $^{181}\text{Ta}$  site using Wien2k code.

TDPAC is a nuclear probe technique based on hyperfine interaction. In case of TDPAC, it requires a  $\gamma$ - $\gamma$  cascade fed by the decay of a parent isotope. The parent isotope is produced by a nuclear reaction and then decays by particle or  $\gamma$ -ray emission to produce the daughter isotope. Then the daughter atom, inside the matrix under study, acts as “wound-up spy” to transfer information of its host matrix while returning to its ground state. The interaction of the nuclear electric quadrupole moment of the intermediate level with an electric field gradient (EFG) leads to a perturbation or attenuation in the angular correlation pattern. The essence of a TDPAC experiment is to extract the TDPAC parameters, viz., the quadrupole frequency, asymmetry of EFG and frequency distribution. Over the other hyperfine techniques, PAC has got some advantages. In PAC, there is no temperature and solid state restriction and so, high-temperature phase transition, solution chemistry of metal complexes and rotational diffusion of macromolecules can be studied by this technique. There is no constraint about the amount of material. In PAC, the probe is added to the matrix in high dilution so that the crystal structure of the matrix under study does not get affected and hence, the same probe can be utilized to study different matrices. PAC has been utilized in the borderline of Physics, Chemistry and Biology. It

has been applied in defect study, surface study, study of phase-transition, solid state reactions, rotational diffusion etc.

In the present thesis, the TDPAC parameters for pure bulk oxides have been measured and then used for all the subsequent measurements. The values for the TDPAC parameters were explained in terms of the crystal structure of the three oxides. The parameters for anatase  $\text{TiO}_2$  were measured for the first time by us. In literature, there exists a wide variation in the measured value for quadrupole frequency in case of  $\text{HfO}_2$ . Hence the TDPAC parameters for  $\text{HfO}_2$  have been remeasured and compared with that for  $\text{ZrO}_2$ . The TDPAC parameters also reflect the identical crystal structure for both  $\text{HfO}_2$  and  $\text{ZrO}_2$ . The optical properties of  $\text{TiO}_2$  can be modified by doping with suitable dopant. The role of dopant in the modification of different properties can not be described by any single theory. The study in the atomic scale is required to probe the role of the dopant in modifying the properties of the host matrices. In this motivation, the TDPAC method has been utilized to study the role of Mn and Zr atoms in rutile matrix. One is transition element with different possible valence states and the other is the same group element as Ti. The minute difference in metal-metal interaction in these doped systems could be resolved by TDPAC technique. The other oxide  $\text{HfO}_2$ , in its fiber form, is used as the target material for Radioactive Ion Beam (RIB) preparation. For this application, the thermal behavior of the fiber is of major importance. In the present thesis, it has been shown that the high temperature behavior of the fiber material could well be studied by the TDPAC method and the meager loss in crystallinity at 1673K, which could otherwise not be possible to realize, could be distinctly perceived from the measurement of TDPAC parameters. Those parameters are so sensitive to the local environment around the probe atom that any minute change could easily be identified. The effect of  $\gamma$ -irradiation in bulk anatase and rutile structures has also been studied by the TDPAC

technique. Although, these crystal structures are so compact that it is not apparently expected to have any effect of  $\gamma$ -irradiation on these structures, it is a good opportunity to reinvestigate and confirm the present scenario by this hyperfine tool TDPAC.

In case of  $\text{TiO}_2$ , anatase and rutile have got their own applications. The mechanism of phase transition from anatase to rutile is of much importance in order to stabilize a particular phase for a specific application. In nano dimension, anatase is used as photocatalyst and photocatalytic efficiency can be enhanced by inserting a nano metal core in nano  $\text{TiO}_2$  shell. The mechanism of phase transition in 70nm  $\text{TiO}_2$  along with the role of surface to bulk mass transfer has been investigated with this hyperfine tool TDPAC. Again the effect of nano Ag metal core in the above phase transition has been studied by TDPAC method in case of  $\text{Ag@TiO}_2$  core-shell nanoparticles. The  $\text{HfO}_2$  thin film is presently a leading candidate to replace  $\text{SiO}_2$  in gate dielectrics. The thin film of  $\text{HfO}_2$  on Si surface is reported to undergo Hf-silicide formation which is of major concern for its application as gate-dielectric. In the present thesis, TDPAC technique has been utilized to study the evolution of  $\sim 50$  nm Hf thin film on Si(111) surface to the monoclinic  $\text{HfO}_2$  phase under 10 mbar  $\text{O}_2$  partial pressure. The possibility of Hf-silicide formation has also been revisited by this hyperfine technique.

The work embodied in this thesis has been divided into five chapters:

- Introduction: Group-IVB metal oxides, TDPAC and other complimentary methods.
- Development of Fast-Slow Coincidence Setup with  $\text{LaBr}_3(\text{Ce})$  Detectors for TDPAC Measurements.
- TDPAC Study of Group-IVB Metal Oxides in Bulk and Wien2K Calculation.
- TDPAC Study of Group-IVB Metal Oxides in Low Dimension.
- Summary and Outlook.

## **Chapter 1: Introduction**

A general introduction has been furnished in three parts. First part contains the possible details of Group-IVB metal oxides. A little history about the Group-IVB elements, viz., Ti, Zr and Hf, along with some of their relevant properties has been given in a concise form. Then the crystal structures of these three oxides have been described in moderate details as the knowledge of their crystal structure is required to carry out their structural variation including phase transitions.

The second part contains the details about the PAC technique. The historical background of PAC has been given followed by a little theory on the electric quadrupole moment and electric field gradient. Then the theory of directional correlation function has been described. After discussing the unperturbed directional correlation function, the influence of extranuclear fields on the angular correlation function has been introduced. Semiclassically, the interaction produces a precessional motion of the intermediate spin about the symmetry axis defined by the direction of emission of the first  $\gamma$ -ray. Thus the orientation of the intermediate spin gets altered in the time interval between the emission of  $\gamma_1$  and  $\gamma_2$  and the angular correlation function is perturbed. Quantum mechanically, the interaction produces the transition among the non-degenerate m-states leading to the emission of  $\gamma_2$  from an m-state with an attenuated population density. The influence of static electric and magnetic field has been discussed. Then the time-dependent EFG has been introduced. Due to jump diffusion of vacancies in the solids, the tumbling motion of a molecule in a liquid and atomic collision in the gas phase, the magnetic field or electric field gradient arising due to the movement of electric charges, electric or magnetic moments of ions change in a random fashion. The two limiting models, viz., Diffusion Model and Strong Collision Model, explaining the random reorientation of the magnetic field or the EFG at the nucleus have been discussed. The influence of the mode of radioactive decay by the parent atom

to produce the daughter element, viz., electron capture (EC), internal conversion (IC),  $\alpha$ - and  $\beta$ -decay, on the directional correlation of  $\gamma$ - $\gamma$  cascade has been discussed. The methodology of the technique and the different types of PAC techniques has also been presented. The suitability of TDPAC probe and the properties of typical TDPAC probes have been furnished. Lastly, the application of TDPAC technique in the field of solid state physics and chemistry, solid state physics and biology, solution chemistry, super-viscous medium, hot atom chemistry and radiation damage study has been discussed in moderate details.

The last part contains the preliminary aspects of other characterization techniques, viz., X-ray Diffraction (XRD), Transmission Electron Microscopy (TEM), Scanning Electron Microscopy (SEM), Atomic Force Microscopy (AFM) etc. The last chapter ends with a concise motivation of the present thesis.

## **Chapter 2: Development of Fast-Slow Coincidence Setup with LaBr<sub>3</sub>(Ce) Detectors for TDPAC Measurements.**

This is devoted to the development of a Fast-Slow Coincidence setup for TDPAC measurements used in the present work. The coincidence circuit consists of three planar LaBr<sub>3</sub>(Ce) detectors coupled with XP2020URQ Photo Multiplier Tubes (PMTs) having both anode and dynode outputs. The dynode output is used for energy coincidence while the anode output is used for time coincidence. The LaBr<sub>3</sub>(Ce) detectors have a better energy resolution than any other scintillation detectors till date and desirable time resolution. The coincidence circuit has a time resolution of  $340 \pm 10$  ps for the 511-511 cascade. The characteristics of the LaBr<sub>3</sub>(Ce) detectors with respect to energy linearity and time resolution have also been discussed. The coincidence setup is based on CAMAC data acquisition system where the data are collected in LIST mode so

that the gates in the relevant cascade  $\gamma$ -energies can be applied in the post-acquisition period to extract the coincidence information.

The confidence of the TDPAC data analysis and the scope of application of this technique significantly depend on the time resolution of the coincidence setup. Theoretically the best time resolution means the time response with a delta function. In practice, there exists a finite width in the time response function. This arises due to the detector, photomultiplier tube and the associated electronics. The response function has a Gaussian distribution over the theoretical function. The effect of these electronic modules along with the detectors on the time resolution of the coincidence circuit has been discussed.

### **Chapter 3: TDPAC Study of Group-IVB Metal Oxides in Bulk and Wien2k Calculation.**

The chapter encompasses the experimental details along with the results and discussion of all the studies carried out by TDPAC technique have been presented for Group-IVB oxides in bulk dimension. The anatase and rutile  $\text{TiO}_2$ ,  $\text{HfO}_2$  and  $\text{ZrO}_2$  were doped with the TDPAC probe  $^{181}\text{Hf}/^{181}\text{Ta}$  by soft chemical co-precipitation method. Then they were counted on the TDPAC spectrometer. Another probe  $^{111}\text{In}/^{111}\text{Cd}$  has also been used to look into the occupation of  $^{111}\text{In}$  probe-atom at the metal lattice site in the Ti, Zr and Hf oxides and also look into the difference in behavior, if any, for the present PAC probe  $^{111}\text{In}/^{111}\text{Cd}$  from our previous probe  $^{181}\text{Hf}/^{181}\text{Ta}$ . The effect of EC decay in case of  $^{111}\text{In}/^{111}\text{Cd}$  probe on the directional correlation pattern has also been studied.

The effect of Mn and Zr-doping on the rutile structure has been performed with TDPAC technique in order to study the metal-metal interaction in doped rutile structure. TDPAC study of 5% Mn-doped  $\text{TiO}_2$  indicates that there is no structural change in the  $\text{TiO}_2$  matrix due to doping. In another study, the rutile matrix was doped with three different percentage of Zr, viz., 1%, 5%

and 10%. Upto 10% Zr-doping, there is no such significant change in the crystal structure of rutile. The TDPAC parameters remain almost unchanged except an increase in the width of the frequency distribution.

In other experiment, the study of radiation damage on the anatase and rutile crystal structure has also been carried out by following the leaching behaviour of the  $^{181}\text{Hf}$  activity from those matrices as well as by the hyperfine study using TDPAC. After incorporating  $^{181}\text{Hf}$  tracer into  $\text{TiO}_2$  matrix, the leaching property of the resulting matrix was studied in water, sodium chloride and humic acid solutions. The leaching was measured in each of the case by following the radioactivity of  $^{181}\text{Hf}$ .  $\text{TiO}_2$  matrices were exposed to  $\gamma$ -radiation using  $^{60}\text{Co}$   $\gamma$ -irradiator at a dose of  $\sim 5.3\text{kGy/h}$  for 7 days. Then the leaching behaviour was again followed under similar condition and was found to get unaffected by the irradiation. The structural aspects before and after  $\gamma$ -irradiation have been investigated with TDPAC technique which showed that the lattice structure of titania remains undisturbed even under a strong radiation field.

Lastly, the thermal behavior of hafnium oxide fiber has been investigated with the aid of TDPAC technique along with XRD and SEM measurements. This study has yielded a good thermal stability of the fibrous material up to 1173K and the fiber loses its crystallinity to a meager extent at 1673K. No phase transition has been observed up to 1673K in fiber. TDPAC parameters for the  $\text{HfO}_2$  fiber annealed at 1173K have been found to be  $\omega_Q=124.6(3)$  Mrad/s and  $\eta=0.36(1)$ . These values remain unaltered for the  $\text{HfO}_2$  fiber annealed even at 1673K. Electronic structure calculations based on density functional theory for  $\text{HfO}_2$  doped with tantalum has been performed using Wien2K code and calculated EFG parameters are in reasonable agreement with the experimental values.

#### **Chapter 4: TDPAC Study of Group-IVB Metal Oxides in Low Dimension**

The chapter focuses the study of Group-IVB oxides in lower dimensions, viz., in thin film of nano dimensions and nanoparticles. The phase transition from anatase to rutile for the 70nm TiO<sub>2</sub> crystallite has been investigated. The study involved the annealing of the TiO<sub>2</sub> nano crystals, adsorbed with the nuclear probe (<sup>181</sup>Hf/<sup>181</sup>Ta) at trace level, at different temperatures for different durations. The TDPAC measurement was supported with XRD measurement where the width of the peak increases with the increase in annealing temperature indicating a crystal growth. The samples annealed up to 823K for 4h showed no phase transition, except the growth of the crystallites. However, it showed phase transition at the same temperature (823K), when annealed for longer duration indicating the slower kinetics of the phase transition process. Further the sample, when annealed at 1123K for 4h, showed the phase transition. It has also been observed that the <sup>181</sup>Hf tracer, adsorbed on 70nm anatase TiO<sub>2</sub>, diffuses from surface to bulk during the phase transition process and the extent of diffusion in anatase differs from that in rutile phase. However, surface to bulk mass-transfer is found to play a significant role in the phase transition process.

The thermal behavior of the TiO<sub>2</sub> shell in the core-shell Ag@TiO<sub>2</sub> system has been investigated by the TDPAC technique in the temperature range from 473K-1073K. These results are supplemented with the TEM and XRD measurements. Although the thickness of the TiO<sub>2</sub> shell increases on annealing as evident from the XRD measurement, the TDPAC results show that the anatase phase persists till 1073K. This is in contrast with the results for the pure TiO<sub>2</sub> nanoparticles of the similar dimensions. These observations suggest that the phase transformation from anatase to rutile is hindered in case of core-shell nanoparticles possibly

because the growth of the shell thickness in case of Ag@TiO<sub>2</sub> nanoparticles is not effective for rutile formation due to the presence of Ag-core.

The structural evolution of Hf metal thin film on Si (111) surface with temperature has been investigated under 10 mbar oxygen pressure. The evolution was characterized by TDPAC technique along with Atomic Force Microscopy (AFM). The Hf-thin film of ~50 nm thickness, deposited on Si (111) substrate by ion-beam sputtering method, was annealed at 673K, 873K and 1073K for 4h. Up to 1073K, there was no signature of monoclinic phase. After annealing at 1273K for 4h, monoclinic phase started to appear along with another component and after 12h at the same temperature, there exists only the monoclinic phase. The thin film was also directly annealed at 1273K for 4h, 8h and 12h. Although after 12h, only the monoclinic phase exists, there was a slight difference in the evolution process. The Hf-silicide formation could not be found by this hyperfine technique under the present experimental condition.

### **Chapter 5: Summary and Outlook**

The present thesis describes the details of a fast-slow coincidence setup with the latest LaBr<sub>3</sub>(Ce) detectors, the study of these detectors with respect to energy linearity and time resolution and the versatile application of TDPAC technique in different types of physico-chemical problems. The energy linearity of the detectors could be decided over a range of PM tube bias voltages. The time resolution of the setup was also monitored for different bias voltages. An optimum operational condition could be found from the present work where the energy linearity is maintained without hampering the time resolution of the setup. The coincidence setup was then used for the subsequent TDPAC measurements. At first, the setup was used for the measurement of known TDPAC parameters in case of rutile TiO<sub>2</sub> and it was found that the values exactly match with that mentioned in the literature. After that, the parameters for anatase TiO<sub>2</sub> was found

for the first time with the same PAC setup. The study also confirmed the TDPAC parameters for bulk  $\text{HfO}_2$  and  $\text{ZrO}_2$  for which the literature data have wide variations. The present thesis also describes for the first time how the PAC technique can be applied to detect the minute difference in metal-metal interactions for doped oxides. It can be perceived from the study that such a small difference in interaction is hard to detect by any other technique. Similarly, the study reveals a small loss of crystallinity and no phase transition at high temperature in case of  $\text{HfO}_2$  fiber. The stability of the  $\text{TiO}_2$  matrix under strong gamma-field was reviewed by the present hyperfine tool. The technique was also applied in nano dimension of the materials. The theoretical calculation by the Wien2k code based on DFT provides a valuable support to the experimental results. The calculation revealed the information about the electrons of the probe atom Ta contributing to the EFG as well as the charge state of the Ta atom in the fiber matrix. The transfer of the PAC probe from surface to bulk during anatase to rutile phase transition could be identified by TDPAC and such a mass transfer is hardly perceived by any other technique. The present study also describes a comparative study on the stability of anatase phase in case of pure  $\text{TiO}_2$  and  $\text{Ag@TiO}_2$  core-shell nanoparticles as investigated by TDPAC technique. The surface study in case of evolution of  $\text{HfO}_2$  on  $\text{Si}(111)$  surface has also been described in the present thesis. The present thesis can be summarized in the following way:

- The new  $\text{LaBr}_3(\text{Ce})$ -based TDPAC spectrometer coupled to CAMAC data-acquisition system has got unique advantage in its LIST-mode data collection facility.
- The versatile application of TDPAC technique has been presented in the field of different chemical phenomena as well as different dimensions of material ranging from bulk materials in doped form to core-shell nanomaterials.

- The theoretical calculation in combination with experimental results can provide complete information about the electronic environment surrounding the probe atom in atomic scale resolution.

The following studies can be carried out in future:

The present coincidence setup can be modified by coupling the  $\text{LaBr}_3(\text{Ce})$  detectors to other fast PM Tubes in order to get a better energy linearity and time resolution. The study of the doped system to identify the metal-metal interaction can be pursued for a number of other doped oxides. Specially, the oxides doped with transition metal are also of practical importance. The study on the radiation stability of the  $\text{TiO}_2$  matrix can be further extended by simulating the radiation environment of a high-level nuclear waste and monitoring the similar radiation stability. The similar study can be extended to different nuclear materials and the behavior of those materials under simulated nuclear environment can be studied in minute details. The study with the thin films and nano materials including core-shell type are of real challenge in the field of TDPAC. The similar study with nano-alloys can also be performed with this hyperfine tool.

## **Publications:**

### **A. Journal:**

#### **a. Published:**

1. **D. Banerjee**, S.K. Das, S.V. Thakare, P.Y. Nabhiraj, R. Menon, R.K. Bhandari, K. Krishnan; Study of surface-bulk mass transport and phase transformation in nano- $\text{TiO}_2$  using hyperfine interaction technique, *J. Phys. Chem. Solids* 71 (2010) 983–987.
2. **D. Banerjee**, S. K. Das, P. Das, S. V. Thakare, T. Butz; Zr-doped rutile  $\text{TiO}_2$ : a nuclear quadrupole interaction study, *Hyperfine Interaction* 197 (2011) 193–198.

3. **D. Banerjee**, R. Guin, S. K. Das, S. V. Thakare; Effect of  $\gamma$ -dose on the crystal structure and leaching behaviour of TiO<sub>2</sub> matrix labeled with <sup>181</sup>Hf/<sup>181</sup>Ta tracer, *J. Radioanal. Nucl. Chem.* 290 (2011) 119–121.
4. **D. Banerjee**, P. Das, R. Guin, S. K. Das; Nuclear quadrupole interaction at <sup>181</sup>Ta in hafnium dioxide fiber: Time differential perturbed angular correlation measurements and ab initio calculations, *J. Phys. Chem. Solids* 73 (2012) 1090-1094.

b. **Accepted:**

**D. Banerjee** and S. K. Das; Study of the Role of Metal Core on the Thermal Behavior of Ag@TiO<sub>2</sub> Core-Shell Nanoparticles, *J. Radioanal. Nucl. Chem.* (In Press).

c. **Communicated:**

1. **D. Banerjee**, S.K. Das, S. V. Thakare, P.Y. Nabhiraj, R. Menon; Nano-phase Evolution of HfO<sub>2</sub> Thin Film on Si (111) Surface: A Nuclear Quadrupole Interaction Study, *Thin Solid Films*.

**B. Other Publications:**

1. **D. Banerjee**, R. Guin & S.K. Das; Study Of Leaching Property of TiO<sub>2</sub> matrix labeled with <sup>181</sup>Hf, *Nuclear and Radiochemistry Symposium (NUCAR)-2009*.
2. **D. Banerjee** and S. K. Das; Annealing Behavior of Hafnium Oxide Fiber Used as a Target for Radioactive Ion Beam Preparation, *Synthesis and Characterization of Smart Materials-2009*.
3. **D. Banerjee**, P. Ghosh, R.K. Chatterjee and S. K. Das; Hyperfine interaction study of 5% Mn<sup>+2</sup> doped TiO<sub>2</sub>, *Condensed Matter Days-2009*.
4. P. Das, **D. Banerjee** and S. K. Das; Electronic and structural properties of anatase and rutile TiO<sub>2</sub> doped with Ta: Experimental study and *ab initio* calculations, *Joint International Conference on HFI and NQI-2010*.

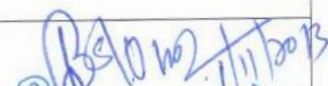
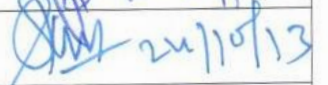
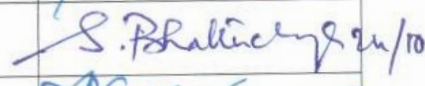
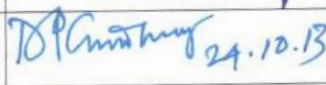
5. **D. Banerjee** and S. K. Das; Nano-phase Hindered Evolution of  $\text{HfO}_2$  Thin Film on Si (111) Surface: A Nuclear Quadrupole Interaction Study, *Joint International Conference on HFI and NQI-2012*.
6. **D. Banerjee**, P. Das, S.V. Thakare and S.K. Das; Study of Annealing Behavior of Probe Lattice Interaction in Gr-IVB oxides by Nuclear Quadrupole Interaction, *NUCAR-2013*.
7. **D. Banerjee**, S. Bhattacharya, T. Bhattacharjee and S.K. Das; Fast-slow coincidence measurements with  $\text{LaBr}_3(\text{Ce})$  detectors, *NUCAR-2013*.



Date: 22.10.2013

(Signature of Student)

**Doctoral Committee:**

S. No.	Name	Designation	Signature with Date
1	Prof. B. S. Tomar	Chairman	 24/10/13
2.	Prof. S. K. Das	Convener	 24/10/13
3.	Prof. S. Bhattacharya	Member	 24/10
4.	Dr. D. P. Chowdhury	Member	 24.10.13

### List of Figures

<b>Figure1.1</b>	Crystal structure of rutile (left) and anatase (right); Ti: grey and O: red	21
<b>Figure1.2</b>	Crystal Structure of ZrO <sub>2</sub> (baddeleyite); Zr: grey and O: red	21
<b>Figure1.3</b>	Phase transformation of ZrO <sub>2</sub> at different temperatures	24
<b>Figure1.4</b>	Three phases of hafnia and zirconia; a: cubic, b: tetragonal, c: monoclinic	25
<b>Figure1.5</b>	Types of displacive transformation	26
<b>Figure1.6</b>	Pictorial representation of the two phases in zirconia	27
<b>Figure1.7</b>	Hysteresis in martensitic transformation	28
<b>Figure1.8</b>	Mechanism of Photo-oxidation by charge-carriers for TiO <sub>2</sub>	30
<b>Figure1.9</b>	Formation of YSZ in a step-wise manner	35
<b>Figure1.10</b>	System of charges arranged in a particular manner	47
<b>Figure1.11</b>	Electric Quadrupole Interaction and splitting of energy levels	51
<b>Figure1.12</b>	Decay of parent (P) to daughter (D) nuclei and subsequent emission of cascade $\gamma$ -rays from the daughter atom	54
<b>Figure1.13</b>	Splitting of Intermediate level with $I = 5/2$ in presence of external field	62
<b>Figure1.14</b>	Effect of $\eta$ on perturbation function for $I=5/2$ state	75
<b>Figure1.15</b>	Decay schemes of <sup>181</sup> Hf/ <sup>181</sup> Ta (left) and <sup>111</sup> In/ <sup>111</sup> Cd probes	90
<b>Figure2.1</b>	Fast-Slow coincidence circuit diagram for TDPAC measurement	110
<b>Figure2.2</b>	The energy spectra obtained with LaBr <sub>3</sub> (Ce) detector <sup>133</sup> Ba, <sup>152</sup> Eu and <sup>106</sup> Ru	115
<b>Figure2.3</b>	The energy response curve for LaBr <sub>3</sub> (Ce) detector up to 1.4 MeV	116
<b>Figure2.4</b>	Prompt for 511-511 cascade of <sup>22</sup> Na source	117
<b>Figure2.5</b>	The variation of time resolution of the detector at different bias voltages	118
<b>Figure3.1</b>	TDPAC spectra with cosine transform for anatase and rutile with <sup>181</sup> Ta probe	128
<b>Figure3.2</b>	Representative TDPAC spectra with cosine transform for HfO <sub>2</sub> and ZrO <sub>2</sub>	129

<b>Figure3.3</b>	TDPAC spectra with cosine transform for rutile TiO <sub>2</sub> with <sup>111</sup> In probe	130
<b>Figure3.4</b>	Representative TDPAC spectrum for HfO <sub>2</sub> and ZrO <sub>2</sub> with <sup>111</sup> In probe	131
<b>Figure3.5</b>	TDPAC spectrum for 5% Mn-doped anatase TiO <sub>2</sub>	134
<b>Figure3.6</b>	TDPAC spectrum for 5% Mn-doped rutile TiO <sub>2</sub>	135
<b>Figure3.7</b>	TDPAC spectrum for 1% Zr-doped rutile TiO <sub>2</sub>	135
<b>Figure3.8</b>	TDPAC spectra for 5% (left) and 10% (right) Zr -doped rutile TiO <sub>2</sub>	136
<b>Figure3.9</b>	TDPAC spectrum with cosine transform for $\gamma$ -irradiated rutile TiO <sub>2</sub>	141
<b>Figure3.10</b>	XRD spectra of the HfO <sub>2</sub> fiber annealed at different temperatures	145
<b>Figure3.11</b>	SEM picture of HfO <sub>2</sub> fiber annealed at (a) 1173K and (b) 1673K	145
<b>Figure3.12</b>	TDPAC spectra for the HfO <sub>2</sub> fiber annealed at different temperatures	146
<b>Figure3.13</b>	HfO <sub>2</sub> crystal doped with Ta	148
<b>Figure3.14</b>	Lowest panel: Plot of Total Density of states (DOS) vs energy for Ta doped HfO <sub>2</sub> . Middle panel: Plot of Atom (Ta) projected DOS vs energy, Upper panel: Plot of projected DOS vs energy of probe Ta in HfO <sub>2</sub> .	150
<b>Figure3.15</b>	Lowest panel: Plot of Density of states vs energy for pure HfO <sub>2</sub> . Upper panel: Plot of atom projected density of states vs energy of nearest neighbour of probe Ta.	151
<b>Figure4.1</b>	Size distribution of the TiO <sub>2</sub> nanoparticles	156
<b>Figure4.2</b>	XRD spectra of TiO <sub>2</sub> annealed at different temperatures	157
<b>Figure4.3</b>	TDPAC spectra of nano TiO <sub>2</sub> samples annealed at different temperatures	159
<b>Figure4.4</b>	UV-Vis absorption spectra for Ag and Ag@TiO <sub>2</sub> nanoparticles.	166
<b>Figure4.5</b>	TEM picture of Ag@TiO <sub>2</sub> core-shell nanoparticles.	166
<b>Figure4.6</b>	XRD patterns at different annealing temperature for Ag@TiO <sub>2</sub> nanoparticles	167

<b>Figure4.7</b>	XRD patterns at different annealing temperature for pure TiO <sub>2</sub> nanoparticles	167
<b>Figure4.8</b>	Nature of grain growth with annealing temperature	169
<b>Figure4.9</b>	TDPAC spectra of Ag@TiO <sub>2</sub> at different annealing temperatures	169
<b>Figure4.10</b>	TDPAC spectra of pure TiO <sub>2</sub> and Ag@TiO <sub>2</sub> nanoparticles at 1073K	170
<b>Figure4.11</b>	Schematic of particle growth in pure TiO <sub>2</sub> and Ag@TiO <sub>2</sub> nanoparticles	171
<b>Figure4.12</b>	Schematic of Thin film preparation by ion beam sputter deposition	177
<b>Figure4.13</b>	RBS spectrum for unannealed Hf thin film on Si (111) substrate	178
<b>Figure4.14</b>	TDPAC spectra of thin film annealed under 10mbar O <sub>2</sub> pressure	179
<b>Figure4.15</b>	TDPAC spectra of the thin film annealed at 1273K under 10mbar O <sub>2</sub> pressure for different durations	180
<b>Figure4.16</b>	TDPAC spectrum of the thin film annealed directly at 1273K under 10mbar O <sub>2</sub> pressure for different durations	180
<b>Figure4.17</b>	Evolution of monoclinic phase under different annealing conditions	181
<b>Figure4.18</b>	AFM pictures of thin film as prepared (left) and annealed at 1273K (right)	181

**List of Tables:**

<b>Table1.1</b>	Some properties of Ti, Zr and Hf (Taken from “Chemistry of the Elements” by N. N.Greenwood and A. Earnshaw)	19
<b>Table1.2</b>	Properties of Typical TDPAC Probes	91
<b>Table3.1</b>	TDPAC parameters for $^{181}\text{Hf}/^{181}\text{Ta}$ probe	129
<b>Table3.2</b>	TDPAC parameters for $^{111}\text{In}/^{111}\text{Cd}$ probe	131
<b>Table3.3</b>	TDPAC parameters for Zr-doped rutile different samples	136
<b>Table3.4</b>	Result of leaching of $^{181}\text{Hf}$ from different $\text{TiO}_2$ samples	140
<b>Table3.5</b>	Hyperfine parameters for rutile $\text{TiO}_2$ before and after $\gamma$ -irradiation	141
<b>Table3.6</b>	Results for the TDPAC measurements of $\text{HfO}_2$ fiber	146
<b>Table3.7</b>	Comparison between neutral and charged state calculations for $^{181}\text{Ta}$ doped $\text{HfO}_2$ bulk samples	149
<b>Table3.8</b>	Change in EFG parameters after relaxation of atomic position	152
<b>Table4.1</b>	Width of XRD peak for $\text{TiO}_2$ samples annealed at different temperatures	157
<b>Table4.2</b>	Description of the $\text{TiO}_2$ samples with annealing condition	158
<b>Table4.3</b>	TDPAC parameters for different samples	158
<b>Table4.4</b>	Grain sizes and phases present at different annealing temperatures	168
<b>Table4.5</b>	TDPAC parameters for different annealing conditions under 10 mbar $\text{O}_2$ pressure	182

## Chapter 1. Introduction

### 1.1. Group-IVB Metal Oxides:

In the Periodic Table, Group-IVB contains Titanium (Ti), Zirconium (Zr) and Hafnium (Hf) as naturally-occurring elements. William Gregor, Franz Joseph Muller and Martin Heinrich Klaproth independently discovered titanium between 1791 and 1795. Klaproth named it for the Titans of Greek mythology [1]. Klaproth also discovered zirconium in the mineral zircon in 1789 and named it after the already known Zirkonerde (zirconia). Hafnium was discovered by Dirk Coster and Georg von Hevesy in 1923 in Copenhagen, Denmark, validating the original 1869 prediction of Mendeleev [2]. The properties of these elements are summarized in Table 1.1.

**Table 1.1:** Some properties of Ti, Zr and Hf (Taken from “Chemistry of the Elements” by N. Greenwood and A. Earnshaw)

Properties	Ti	Zr	Hf
Atomic number	22	40	72
Number of naturally occurring isotopes	5	5	6
Atomic weight	47.867(1)	91.224(2)	178.49(2)
Electronic configuration	[Ar]3d <sup>2</sup> 4s <sup>2</sup>	[Kr]4d <sup>2</sup> 5s <sup>2</sup>	[Xe]4f <sup>14</sup> 5d <sup>2</sup> 6s <sup>2</sup>
Electronegativity	1.5	1.4	1.3
Metal radius (pm)	147	160	159
Melting point (°C)	1667	1857	2222
Boiling point (°C)	3285	4200	4450
Density at 25°C (g/cc)	4.50	6.51	13.28

All these elements have typically hcp structure which gets transformed to bcc structure at high temperatures (882°, 870° and 1760°C for Ti, Zr and Hf respectively). These metals are highly

resistant to corrosion due to the formation of a dense, adherent, self-healing oxide film. The most common oxidation state for these elements is +4. The oxides of these three elements have recently attracted the attention to a great extent because of their different applications.

**Titanium dioxide**, also known as **titanium(IV) oxide** or **titania**, is the naturally occurring oxide of titanium with chemical formula  $\text{TiO}_2$ . Generally it is sourced from ilmenite, rutile and anatase. **Hafnium(IV) oxide** is the inorganic compound with the formula  $\text{HfO}_2$ . Also known as **hafnia**, this colourless solid is one of the most common and stable compounds of hafnium. **Zirconium dioxide** ( $\text{ZrO}_2$ ), sometimes known as **zirconia** (not to be confused with zircon), is a white crystalline oxide of zirconium.

### 1.1.1 Crystal Structure:

$\text{TiO}_2$ , among several natural polymorphs, exists in three main crystalline modifications- rutile, anatase and brookite, each of which occurs naturally. Of these, rutile is the most stable form. Other forms are converted into rutile on heating. Each contains 6 coordinate Ti but rutile is the most common form, both in nature and as produced commercially. The rutile structure is based on slightly distorted hcp of oxygen atoms with half the octahedral interstices being occupied by Ti atoms. Anatase and brookite are both based on cubic rather than hexagonal close packing of oxygen atoms, but again the Ti atoms occupy half the octahedral interstices. Anatase and Rutile, both have tetragonal lattice structure with different lattice parameters ( $a = b = 4.5845 \text{ \AA}$ ;  $c = 2.9533 \text{ \AA}$  for Rutile and  $a = b = 3.7842 \text{ \AA}$ ;  $c = 9.5146 \text{ \AA}$  for Anatase). The structures of rutile and anatase crystalline forms are shown in Fig.1.1. The titanium cations have a coordination number of 6 meaning they are surrounded by an octahedron of 6 oxygen atoms. The oxygen anions have a co-ordination number of 3 resulting in a trigonal planar co-ordination.

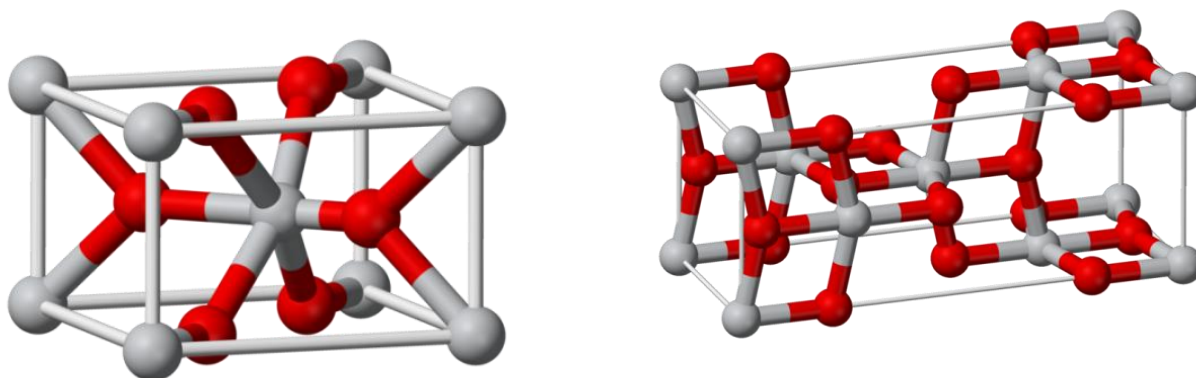


**Figure 1.1:** Crystal structure of rutile (left) and anatase (right); Ti: grey and O: red (Wikipedia)

In 1959 Adam and Rogers [3] first suggested the similarity between the crystal structures of monoclinic  $\text{HfO}_2$  and  $\text{ZrO}_2$  [4]. It is explained on the basis of similarity between the  $\text{Hf}^{4+}$  and  $\text{Zr}^{4+}$  ions. Both the elements belong to the same Group-IVB in the periodic table with similar valence electrons ( $4f^{14}5d^26s^2$  for Hf and  $4d^25s^2$  for Zr). Due to lanthanide contraction, the ionic size of  $\text{Hf}^{4+}$  and  $\text{Zr}^{4+}$  are very similar ( $\sim 0.8 \text{ \AA}$ ). At room temperature,  $\text{ZrO}_2$  (baddeleyite) and isomorphous  $\text{HfO}_2$  have a structure in which the metal is 7-coordinate as shown in Fig. 1.2. The unit cell dimensions for  $\text{HfO}_2$  and  $\text{ZrO}_2$  are  $a = 5.1156 \text{ \AA}$ ,  $b = 5.1722 \text{ \AA}$ ,  $c = 5.2948 \text{ \AA}$  and  $a = 5.1454 \text{ \AA}$ ,  $b = 5.2075 \text{ \AA}$ ,  $c = 5.3107 \text{ \AA}$  respectively.

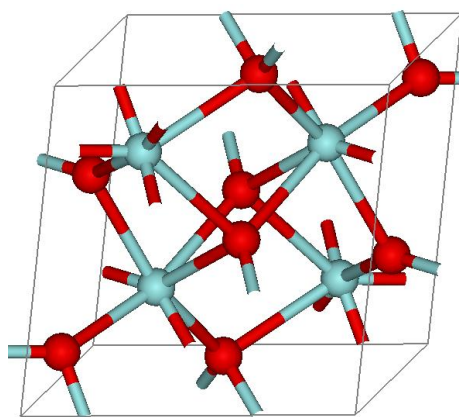


**Figure 1.2:** Crystal Structure of  $\text{ZrO}_2$  (baddeleyite); Zr: grey and O: red (Wikipedia)

The monoclinic phase of  $\text{ZrO}_2$  is a distortion of fluorite ( $\text{CaF}_2$ ) structure with Zr atom in seven-coordination. The baddeleyite structure was determined by McCullough and Trueblood in 1959

[5]. It has space group symmetry of  $P2_1/c$  with four  $ZrO_2$  in the unit cell. The coordination polyhedron around Zr-atom might be ideally visualized as being derived from a cube. In this view, four oxide ions are at the four corners of the base of the cube (designated as  $O_{II}$ ). Among the other three (designated as  $O_I$ ), one at one of the upper corners of the cube and the remaining two are at the midpoints of the cube-edges connecting the unoccupied corners. Another interesting feature of this structure is the alternation of fluorite-like layers containing  $O_{II}$  ions in tetrahedral coordination with layers which contain  $O_I$  ions in triangular coordination. In the  $O_{II}$  coordination tetrahedron, the Zr- $O_{II}$  distances range from 2.16Å to 2.26Å and in  $O_I$  coordination triangle, Zr- $O_I$  distances are 2.04Å, 2.10Å and 2.15Å. At higher temperatures the oxides get transformed into tetragonal and cubic phases. In tetragonal and cubic phases, the metal ions have 8-fold oxygen atom coordination as in fluorite structure.

### **1.1.2. Phase Transformation:**

Anatase is kinetically while rutile is thermodynamically stable [6]. However, thermodynamic stability depends on its particle-size, and at particle diameters below ~14 nm, anatase is more stable than rutile [6]. The transformation sequence among the three titania polymorphs anatase, brookite, and rutile is size dependent, because the energies of the three polymorphs are sufficiently close that they can be reversed by small differences in surface energy [7]. The temperature range at which the phase transition from anatase to rutile takes place is 673K - 1473K [8] for bulk  $TiO_2$ . The transformation from rutile to anatase for the bulk is forbidden. But at nano dimension (<16nm) phase transformation reverses from rutile to anatase [6]. This is attributed to a higher surface energy of rutile than that of anatase ( $1.32 \text{ J.m}^{-2}$  for anatase and  $1.91 \text{ J.m}^{-2}$  for rutile). Therefore, the stability of either polymorph has an important dependence on the size of the crystallite. This aspect of the average size dependence on the anatase to rutile phase

transformation has been studied by several authors [9-12]. If particle sizes of the three nanocrystalline phases are equal, anatase is the most thermodynamically stable at sizes less than 11 nm, brookite is most stable for crystal sizes between 11 and 35 nm, and rutile is most stable at sizes greater than 35 nm [7]. The activation energy of the anatase to brookite transformation is small ( $11.9 \text{ kJ mol}^{-1}$ ), thus the transformation can proceed at lower temperatures. The activation energy of the brookite to rutile transformation is higher ( $163.8 \text{ kJ mol}^{-1}$ ), thus the transformation proceeds rapidly only at higher temperatures. Recently, in the review article by Dorian et al. [13], the anatase to rutile phase transformation has been examined followed by a discussion on the thermodynamics of the phase transformation and the factors affecting its observation. The conditions affecting the kinetics to control the anatase to rutile phase transformation is of considerable importance. This is particularly important in case of high-temperature applications, such as gas sensors and porous gas separation membranes [14-16], where the phase transformation may occur. Therefore, the kinetics of their phase transformation along with the parameters affecting them has to be understood properly in order to obtain different polymorphs for different applications. Both anatase, space group  $I4_1/amd$ , and rutile, space group  $P4_2/mnm$ , are tetragonal in structure. Both crystal structures consist of  $\text{TiO}_6$  octahedra, sharing four edges in anatase and two in rutile [17-18]. The anatase to rutile transformation is reconstructive involving the breaking and reforming of bonds [19]. This is in contrast to a displacive transformation, in which the original bonds are distorted but retained. The reconstructive anatase to rutile transformation involves a contraction of the c-axis and an overall volume contraction of  $\sim 8\%$  [20]. This volume contraction explains the higher density of rutile relative to anatase. Shannon and Pask (1964) proposed a mechanism in which the (112) nearly close-packed oxygen planes of anatase are retained as the (100) nearly close-packed oxygen planes of rutile. Within

these planes a cooperative rearrangement of  $\text{Ti}^{4+}$  and  $\text{O}^{2-}$  ions is thought to occur in which the  $\text{Ti}^{4+}$  ions need break only two of their six Ti-O bonds in order to reach their new sites [21-22]. The c-axis of anatase appears to be significantly longer than that of rutile only because anatase has more atoms per unit cell than rutile. There have been a number of kinetic studies on this phase transition. Using spectroscopically pure anatase, Czanderna, Rao and Honig (1957) found the transition fits "second order kinetics" in which a plot of  $1/(1-\alpha)$  is linear, where,  $\alpha$  is the extent of reaction [23]. Rao (1961) later re-investigated their results in a more accurate way and concluded that the reaction was "first order" in which a plot of  $\log(1-\alpha)$  vs. time is linear [24]. However, this phase transformation is affected by several factors, namely defects in oxygen sublattice, dopants etc. The impurities or conditions which increase the number of oxygen vacancies accelerate the reaction and those which form interstitial oxygen ions would slow it down [20].

$\text{HfO}_2$  and  $\text{ZrO}_2$  have three polymorphs: Monoclinic, Tetragonal and Cubic. The room temperature polymorph, known as the baddeleyite structure, has monoclinic space group  $P2_1/c$ . The monoclinic phase is converted to tetragonal at  $1720^\circ\text{C}$  for  $\text{HfO}_2$  and at  $1170^\circ\text{C}$  for  $\text{ZrO}_2$  [25]. The cubic phase is attained at  $2600^\circ\text{C}$  for  $\text{HfO}_2$  and at  $2370^\circ\text{C}$  for  $\text{ZrO}_2$  shown in Fig. 1.3.

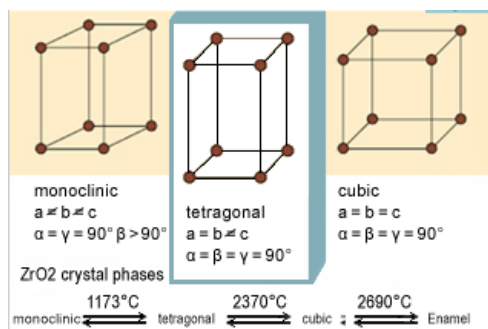


**Figure 1.3:** Phase transformation of  $\text{ZrO}_2$  at different temperatures (Wikipedia).

The oxides in the tetragonal fluorite structure have the  $P4_2/nmc$  space group symmetry. This crystal structure was first accurately described by Teufer in 1962 using high temperature x-ray

diffraction [26]. The highest temperature polymorph of  $\text{HfO}_2$  and  $\text{ZrO}_2$  has the cubic fluorite structure with the  $Fm\bar{3}m$  space group symmetry. In the tetragonal and cubic phases the metal ions have 8-fold oxygen atom coordination and oxygen is 4-fold coordinated with metal ions. The lattice parameters of the monoclinic cell in  $\text{HfO}_2$  at  $1700^\circ\text{C}$  would be similar to the lattice parameters of  $\text{ZrO}_2$  at  $1100^\circ\text{C}$ . This provided evidence for a critical metal oxygen bond length, above which the monoclinic structure is no longer stable. It has been proposed that the difference in transformation temperature is hence due to a critical bond length, between metal ion and oxygen that must be reached in the monoclinic phase before the tetragonal phase becomes stable [27]. The high temperature phases cannot be quenched at room temperature. However, these high temperature modifications, when stabilized by proper dopant, have different technical applications. By incorporating suitable cation dopants and hence, introducing oxygen-vacancies, tetragonal or cubic phase can be stabilized. Again, metastable phases can be stabilized by controlling the particle-sizes due to the difference in surface-energies for different polymorphs. Bulk crystalline hafnia and zirconia both undergo a similar sequence of phase transitions from monoclinic to tetragonal to high symmetry cubic phase. The structures of each phase have been depicted in Fig. 1.4. Hf/Zr-atoms are shown by smaller 'red' spheres while O-atoms are shown by bigger spheres.

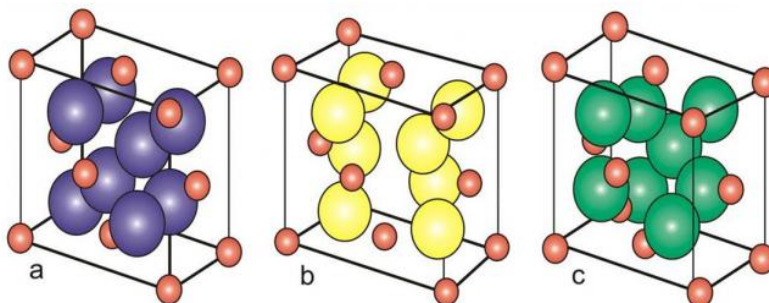


**Figure 1.4:** Three phases of hafnia and zirconia; a: cubic, b: tetragonal, c: monoclinic

(Wikipedia).

Martensitic transformations are well-observed in case of bulk solid materials [28]. Martensite was the name originally given to the hard material obtained during the quenching of steels. Martensite is formed in carbon steels by the quenching of austenite at such a high rate that carbon atoms do not have time to diffuse out of the crystal structure in large enough quantities to form cementite ( $\text{Fe}_3\text{C}$ ). As a result, the face centered cubic austenite transforms to a highly strained body centered cubic form of ferrite that is supersaturated with carbon. The shear deformations that result produce large numbers of dislocations, which is a primary strengthening mechanism of steels. This type of transformation occurs by a *diffusionless shearing* mechanism. A diffusionless transformation is a phase change that occurs without the long-range diffusion of atoms but rather by some form of cooperative, homogeneous movement of many atoms that results in a change in crystal structure. These movements are small, usually less than the inter-atomic distances, and the atoms maintain their relative relationships. When a structural change occurs by the coordinated movement of atoms (or groups of atoms) relative to their neighbors then the change is termed *displacive* transformation. This covers a broad range of transformations and so further classifications have been developed [Cohen 1979]. The first distinction can be drawn between transformations dominated by *lattice-distortive strains* and those where *shuffles* are of greater importance as shown in Fig. 1.5.

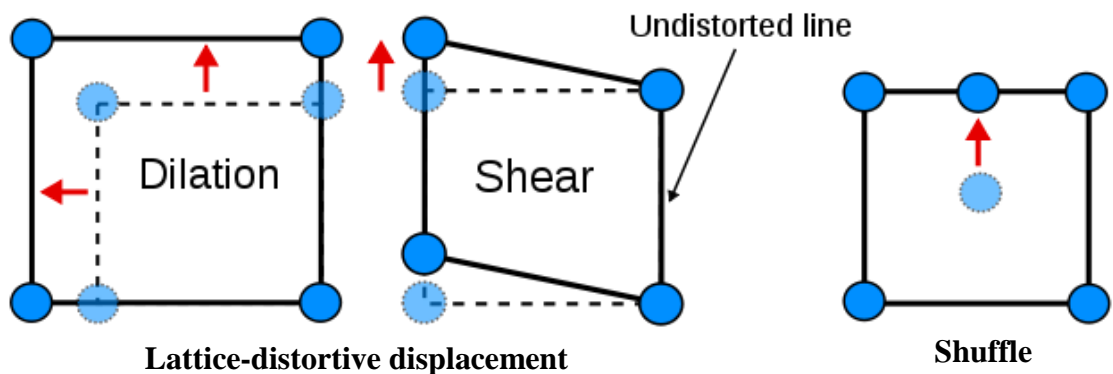


**Figure 1.5:** Types of displacive transformation (Wikipedia).

In martensitic transformation, the parent and the product phases have the same composition and their crystal structures are closely related. This transformation does not involve diffusion and because there is no activation energy of diffusion is involved; the rate of this transformation is very high. Unlike other phase transitions, the martensitic transformations do not take place at a particular temperature, but over a wide range of temperatures. The monoclinic-tetragonal phase transformation is a kind of martensitic transformation. Both these polymorphs have distorted fluorite structure and transformation takes place by a diffusionless shear mechanism over a range of temperatures [29] as shown in Fig 1.6.

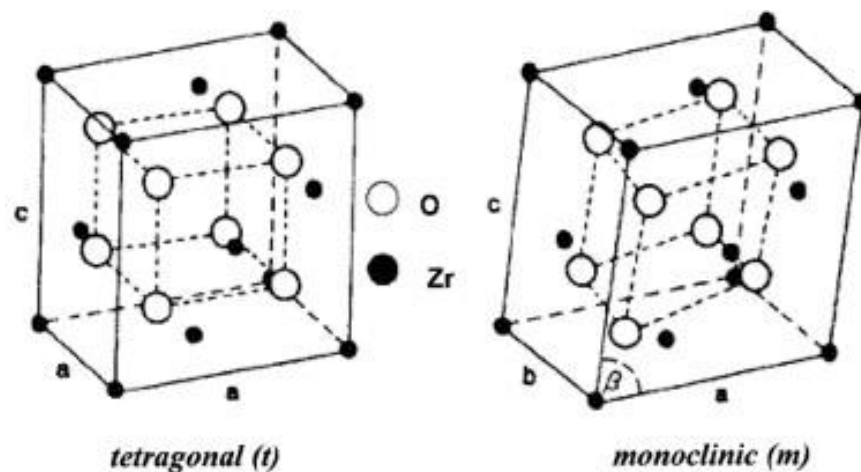


**Figure 1.6:** Pictorial representation of the two phases in zirconia (Wikipedia).

On heating, the transformation to the tetragonal phase starts above  $\sim 1000^{\circ}\text{C}$  but is not complete until  $\geq 1120^{\circ}\text{C}$ . The transformation exhibits a hysteresis (shown in Fig. 1.7) of about  $200^{\circ}\text{C}$  and the reverse transformation on cooling begins at only  $\leq 930^{\circ}\text{C}$ . Hence, the high temperature tetragonal phase is formed from the low temperature monoclinic phase at a higher temperature than that at which tetragonal phase is formed from monoclinic phase.

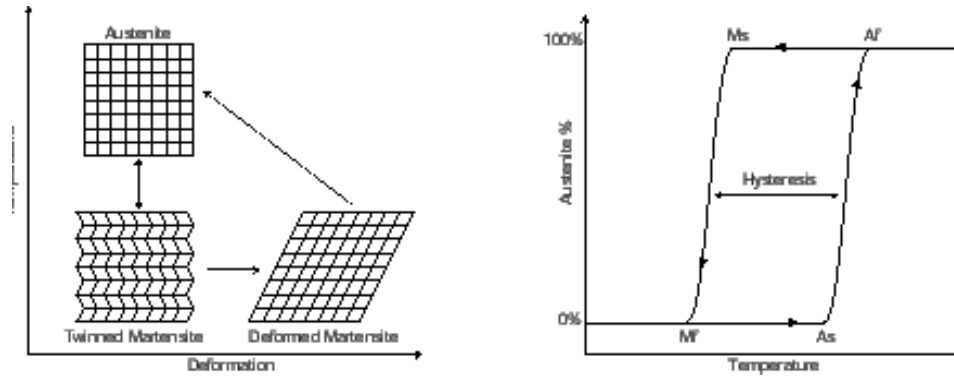


**Figure 1.7:** Hysteresis in martensitic transformation (Wikipedia).

The transformation is classified as athermal because it takes place over a range of temperatures and the percentage transformation within that range does not change with time as long as temperature remains constant. The details of the monoclinic-tetragonal-cubic phase transition series and its relation to the stabilization of the cubic phase of  $\text{ZrO}_2$  has increasingly gained interest due to the rapidly growing applications of the  $\text{ZrO}_2$  ceramics in different fields.

### 1.1.3. Applications in Bulk and Lower Dimensions:

$\text{TiO}_2$  has high refractive index which gives it the quality of an opacifier and its whiteness makes it very useful as white paint. It is transparent in the visible light but absorbs in the UV range. The primary application of titanium dioxide is as a white pigment in paints, food coloring, cosmetics, toothpastes, polymers, and other fields where white coloration is required [30]. This is attributed to the high refractive indices of rutile (2.79) and anatase (2.54) resulting in high reflectivity from the surfaces. Hence,  $\text{TiO}_2$  of smaller particle size with higher surface areas is used for this purpose due to its enhanced opacifying power and brightness. However, paints utilize polymeric binders to fix the pigment and while in contact with titania, the polymer may oxidize when exposed to sunlight. This effect is known as *chalking* and, in addition to the direct degrading effect of ultraviolet (UV) radiation, is accelerated by the photocatalytic activity of  $\text{TiO}_2$ , which

also is enhanced by the high surface area of this material [31]. The potential for the application of the photocatalytic effect in  $\text{TiO}_2$  has attracted considerable interest over the last few decades. Titania as photocatalyst is known to be applicable in a range of important technological areas, viz., electrolysis of water to generate hydrogen [32-33], dye-sensitized solar cells [34-35], air purification [36-37], water treatments [38-40] etc.

$\text{TiO}_2$  is a large band gap [41] semiconductor with 3.2 eV for anatase and 3.06 eV for rutile and these have absorption in the UV region ( $\lambda \leq 380$  nm).  $\text{TiO}_2$  is a compound semiconductor whose valence band and the conduction comprise of the 2p electrons of oxygen and the 3d & 4s electrons of Ti respectively. Excitation of electrons from the valence band causes equivalent number of holes in the valence band. This is equivalent to the movement of electrons from bonding orbitals to the antibonding orbitals. Therefore photo-excitation leaves the material in an unstable state and the semiconductor breaks down in many cases. However  $\text{TiO}_2$  is very stable in this respect making  $\text{TiO}_2$  an excellent photocatalyst. The photo-catalyzed reactions for the above applications are facilitated by the presence of adsorbed radicals (from air or water) on the  $\text{TiO}_2$  surface [42-43]. These radicals, which are atomic species with a free unpaired electron, are formed upon reaction of an adsorbed molecule (such as  $\text{O}_2$  or  $\text{H}_2\text{O}$ ) with a photo-generated charge carrier (electron-hole pair or exciton) when  $\text{TiO}_2$  is exposed to radiation exceeding its band gap; this radiation normally is in the UV wavelength region (290–380 nm). These electron-hole pairs are formed when an electron is elevated from the valence to the conducting band, leaving behind an electron hole, as shown in Fig. 1.8. The holes produced in the valence band cleaves the water molecule to produce  $\text{OH}\cdot$  radical which is a strong oxidizing agent (oxidation potential is 2.8 V) to cause damage to other molecules in the surrounding. In some cases the holes directly oxidize the molecules surrounding it. The electrons in the conduction band

facilitate reduction of electron acceptors and the holes facilitate oxidation of electron donors [44].

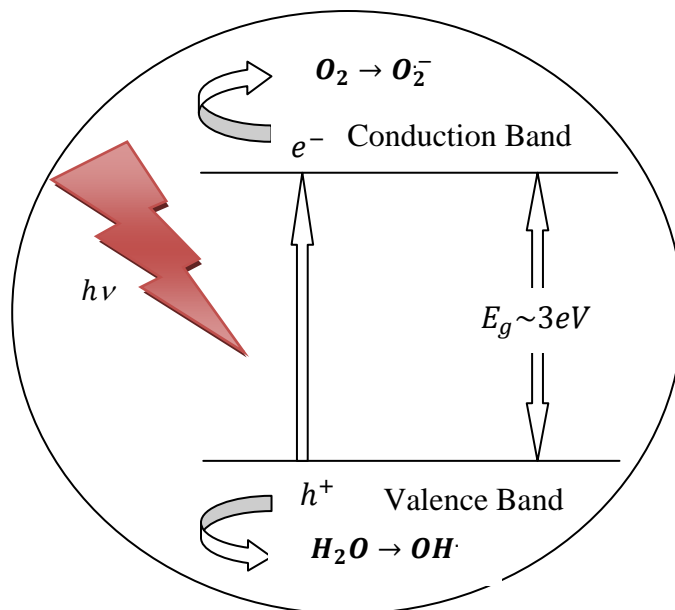
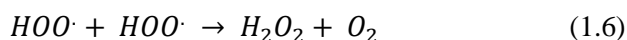
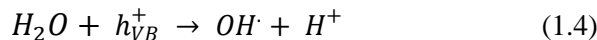
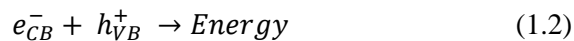
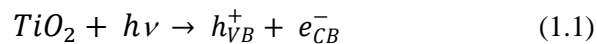


**Figure 1.8:** Mechanism of Photo-oxidation by charge-carriers for TiO<sub>2</sub>.

It must be noted that during the photocatalytic reaction, at least two events must occur simultaneously in order for the successful production of reactive oxidizing species to occur. Typically, the first involves the oxidation of dissociatively adsorbed H<sub>2</sub>O by photo-generated holes, the second involves reduction of an electron acceptor by photoexcited electrons; these reactions lead to the production of a hydroxyl ( $\text{OH}^{\bullet}$ ) and superoxide ( $\text{O}_2^{\bullet -}$ ) radical anion, respectively [45]. Charge carriers can be trapped as  $\text{Ti}^{3+}$  and  $\text{O}^-$  defect sites in the TiO<sub>2</sub> lattice, or they can recombine, dissipating energy [46]. Alternatively, the charge carriers can migrate to the catalyst surface and initiate redox reactions with adsorbates [47]. Positive holes can oxidize OH<sup>-</sup> or water at the surface to produce OH radicals as mentioned above. Electrons in the conduction band can be rapidly trapped by molecular oxygen adsorbed on the titania particle, which is reduced to form superoxide radical anion ( $\text{O}_2^{\bullet -}$ ) that may further react with H<sup>+</sup> to generate hydro-

peroxyl radical ( $\cdot\text{OOH}$ ) and further electrochemical reduction yields  $\text{H}_2\text{O}_2$  [48-49]. The reactions involved in the photocatalytic mechanism of  $\text{TiO}_2$  are furnished below:



Recombination of photogenerated charge carriers is the major limitation in semiconductor photocatalysis as it reduces the overall quantum efficiency [49]. When recombination occurs, the excited electron reverts to the valence band without reacting with adsorbed species (Eq. 1.2) [50] non-radiatively or radiatively, dissipating the energy as light or heat. A key factor of the photocatalytic ability of titania is its high surface area, the same property that contributes to its optical properties. A high surface area leads to a higher density of localised states, which involve electrons with energies between the conduction band and valence band [51]. Titania has a relatively slow rate of charge carrier recombination in comparison with that for other semiconductors [52]. In spite of the larger band gap of anatase ( $\sim 3.2$  eV), compared with that of rutile ( $\sim 3.0$  eV), the photocatalytic performance of anatase generally is considered superior to that of rutile. This is attributed to a higher density of localized states and consequent surface-adsorbed hydroxyl radicals and slower charge carrier recombination in anatase relative to rutile [53-54], parameters that contribute to an improved performance. The higher rate of electron-hole recombination in rutile is explained in terms of its larger grain-size leading to a lower capacity to absorb species. In some cases, rutile may be advantageous for certain applications, viz., rutile containing residual anatase [55], Iron-doped rutile [56] etc. It is possible that electron transfer

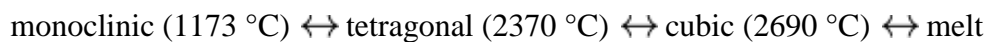
between rutile and a residual quantity of anatase [55] may deliver improved photo-oxidative reactions. For example, the TiO<sub>2</sub> crystallites of Evonik (Degussa) P25 contain a combination of anatase (~80%) and rutile (~20%). The conduction band potential of rutile is more positive than that of anatase and hence, the rutile phase may act as an electron sink for photogenerated electrons from the conduction band of the anatase phase. Many researchers attribute the high photocatalytic activity of this preparation to the intimate contact between two phases, enhancing separation of photogenerated electrons and holes and resulting in reduced recombination [57]. Therefore, in the field of surface area, morphology, and doping, an insight of the titania polymorphs, their transformation, and the methods by which they can be controlled is to be achieved in order to optimize its photocatalytic efficacy.

Two ceramics, zirconia (ZrO<sub>2</sub>) and hafnia (HfO<sub>2</sub>), are known for their similar behaviour, and are important for several advanced applications. ZrO<sub>2</sub> is mostly used for its structural properties. The strengthening afforded by its martensitic phase transformation has made it the material of choice for high-temperature applications. Other common applications include fuel cell electrodes [58], thermal barrier coatings [59], cutlery and jewelry etc. HfO<sub>2</sub> is often thought to be a higher temperature substitute for ZrO<sub>2</sub>. This is mostly due to the similarities in their chemical properties. HfO<sub>2</sub> has uses in nuclear applications also due to its high neutron absorption efficiency. More recently it has found application as high-k dielectric materials and has proved to be a promising candidate to replace SiO<sub>2</sub> as the gate oxide in transistors, to obtain electronics with smaller feature sizes. It is well known that the cubic phase of ZrO<sub>2</sub> can be stabilized by incorporating another oxide such as MgO, CeO<sub>2</sub>, or Y<sub>2</sub>O<sub>3</sub>. At high temperatures, phase transformation has been reported with a significant concomitant change in the electrical conductivity [60-61]. ZrO<sub>2</sub> has a high dielectric constant (22-24), a high breakdown field (3.3-

5.7 MV/cm) and a large band gap (5-7 eV) [62]. Regarding electrical property,  $\text{ZrO}_2$  is oxygen deficient when non-stoichiometric therefore the predominant defects have been proposed to be oxygen ion vacancies. A recent review article [63] furnishes the development of hafnium-based high- $\kappa$  materials. For the complementary metaloxide- semiconductor field effect transistor (CMOSFET) application, an amorphous  $\text{ZrO}_2$  film is preferred to prevent leakage current through crystalline grain boundaries.  $\text{TiO}_2$  has the highest dielectric constants (80–110) among these three IV-B oxides due to its high polarizability resulting in the smallest band-gap ( $\sim 3\text{eV}$ ). Although, the high dielectric constant of  $\text{TiO}_2$  makes it a potential gate oxide candidate in MOSFET, small band-gap and other limitations such as multiple oxidation states,  $\text{Ti}^{3+}$  and  $\text{Ti}^{4+}$ , leading to various Ti–O bonds that provide leakage paths [64-66] restricts its application in this field. Among all IV-B oxides and other transition metal oxides,  $\text{HfO}_2$  is the most promising candidate due to its large band-gap (5.5–6.0), relatively high dielectric constant (22–25), high breakdown field (3.9-6.7 MV/cm), high thermal stability and large heat of formation (271 kcal/mol). Thin  $\text{HfO}_2$  films deposited on silicon substrate exhibit favorable parameters, such as high thermal stability and low leakage current [67-69]. The performance of these thin films as gate-dielectrics is affected by the presence of lattice defects, particularly oxygen defects. The presence of interstitial oxygen may trap the electrons and holes while the oxygen-defects may affect the leakage current. Hafnia is used in optical coatings. Because of its very high melting point, hafnia is also used as a refractory material in the insulation of such devices as thermocouples, where it can operate at temperatures up to 2500 °C.

Zirconia is often more useful in its phase 'stabilized' state. Upon heating, zirconia undergoes disruptive phase changes. By adding small percentages of yttria, these phase changes are

eliminated and the resulting material has superior thermal, mechanical, and electrical properties. A special case of zirconia is that of tetragonal zirconia polycrystal, or TZP, which is indicative of polycrystalline zirconia composed of only the metastable tetragonal phase. **Yttria-stabilized zirconia** (YSZ) is a zirconium-oxide based ceramic, in which the particular crystal structure of zirconium oxide is made stable at room temperature by an addition of yttrium oxide. As discussed above, pure zirconium dioxide undergoes a phase transformations from monoclinic (stable at the room temperature) to tetragonal and then to cubic, according to the scheme:



The ionic radius of  $\text{Zr}^{4+}$  ( $0.82 \text{ \AA}$ ) is too small for ideal lattice of fluorite nature for the tetragonal zirconia. The stabilization of the tetragonal zirconia over wider range of temperatures is accomplished by substitution of some of the  $\text{Zr}^{4+}$  ions in the zirconia crystal lattice with slightly larger ions, e.g., those of  $\text{Y}^{3+}$  (ionic radius of  $0.96 \text{ \AA}$ ) as depicted in Fig. 1.9. The resulting doped zirconia materials are termed as *stabilized zirconia* [70]. The addition of yttria to pure zirconia replaces some of the  $\text{Zr}^{4+}$  ions in the zirconia lattice with  $\text{Y}^{3+}$  ions. This produces oxygen vacancies, as three  $\text{O}^{2-}$  ions replace four  $\text{O}^{2-}$  ions. It also permits yttrium stabilized zirconia to conduct  $\text{O}^{2-}$  ions (and thus conduct an electrical current), provided there is sufficient vacancy site mobility, a property that increases with temperature. This ability to conduct  $\text{O}^{2-}$  ions makes yttria-stabilized zirconia well suited to use in solid oxide fuel cells, although it requires that they operate at high enough temperatures. The ionic conductivity of the stabilized zirconias increases with increasing dopant concentration (linearly for low dopant concentrations), then saturates, and then starts to decrease.

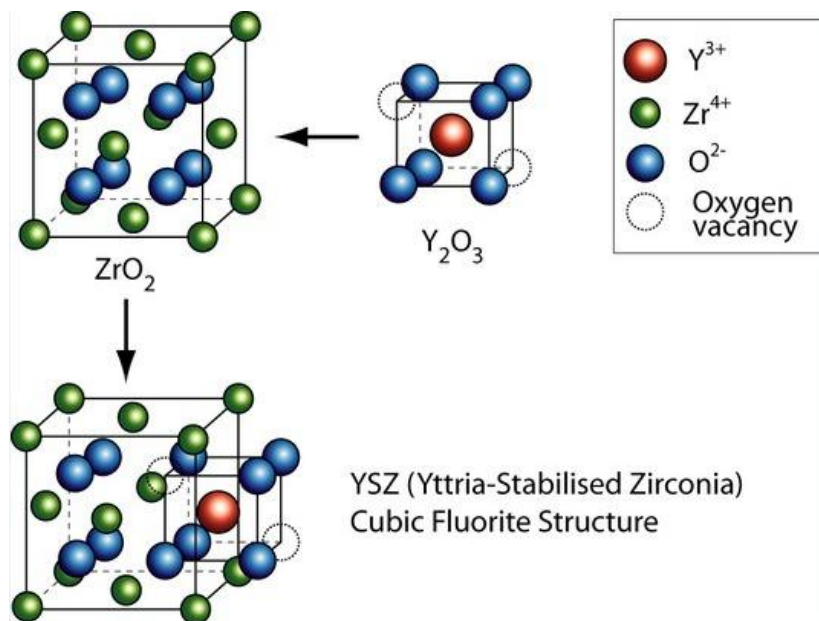


**Figure 1.9:** Formation of YSZ in a step-wise manner (Wikipedia).

The very low thermal conductivity of cubic phase of zirconia also has led to its use as a thermal barrier coating, or TBC, in jet and diesel engines to allow operation at higher temperatures. This material is also used in dentistry. Single crystals of the cubic phase of zirconia are commonly used as diamond simulant in jewellery. Like diamond, cubic zirconia has a cubic crystal structure and a high index of refraction. Visually discerning a good quality cubic zirconia gem from a diamond is difficult, and most jewellers will have a thermal conductivity tester to identify cubic zirconia by its low thermal conductivity (diamond is a very good thermal conductor). This state of zirconia is commonly called "cubic zirconia," (CZ).

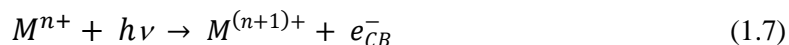
#### 1.1.4. Doped Oxides:

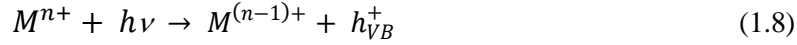
The versatile applications of anatase and rutile  $TiO_2$  polymorphs utilize its optical properties.  $TiO_2$  has a band gap of  $\sim 3eV$  and absorbs UV photons. But the solar radiation that reaches the earth's surface lies in the range of 1.0-1.9 eV. Again, it would be desirable to decrease the

photocatalytic efficiency of  $\text{TiO}_2$  to be used as a paint opacifier since it causes the radical-formation resulting in the degradation of the organic binders in paint. Hence, the optical properties of  $\text{TiO}_2$  are to be tuned properly for its use in different applications. Again, for another important application of the photocatalytic property of  $\text{TiO}_2$  towards the hydrogen production, it is required to adjust band-gap of  $\text{TiO}_2$ . For hydrogen production, the energy of the CB of  $\text{TiO}_2$  should be such that it becomes more negative than hydrogen production level ( $E_{\text{H}_2/\text{H}_2\text{O}}$ ) while that of VB of  $\text{TiO}_2$  should be more positive than water oxidation level ( $E_{\text{O}_2/\text{H}_2\text{O}}$ ) to ensure the efficient photocatalytic oxygen production from water. A recent review article [71] provides information about the methods of preparation of doped- $\text{TiO}_2$  with metallic and nonmetallic species, including various types of dopants and doping methods. Again the effect of doping on the optical and photocatalytic properties of  $\text{TiO}_2$  has also been furnished [72] with possible explanation of those effects. For this purpose,  $\text{TiO}_2$  is doped with transition metal ions (Fe, Mn, Ni, Cr etc.) and non-metals (N, S, C, B etc.). First non-metal doped  $\text{TiO}_2$  was described in 1986 by Sato, *et al.* [73]. After the success of Asahi *et al.* [74], nitrogen-doped  $\text{TiO}_2$  has been studied quite extensively in order to tune the band-gap and photocatalytic activity of titania so that it absorbs photons in the visible region. It was suggested that the 2p state of N atom hybrids with the 2p states O atom in anatase  $\text{TiO}_2$  doped with nitrogen because their energies are very close, and thus the band gap of N- $\text{TiO}_2$  is narrowed and able to absorb visible light. It was also suggested [75] that in  $\text{TiO}_2$  the oxygen sites substituted by nitrogen atom form isolated impurity energy levels above the valence band. Irradiation with UV light excites electrons in both the VB and the impurity energy levels, but illumination with visible light only excites electrons in the impurity energy level. Although S can decrease the band-gap of  $\text{TiO}_2$ , its use is restricted due to the incompatible ionic size of S for its incorporation into the titania matrix. The energy states

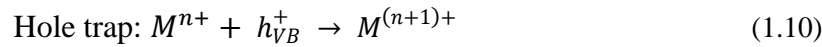
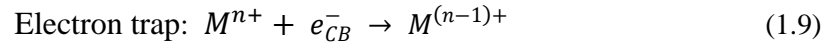
introduced by the C and P dopants are so deep that the photo-generated charge carriers are difficult to get transferred to the surface of the catalyst. Hence, these are inefficient anion-dopants for the present purpose. In addition to the above observations, Umebayashi et al. [76] also reported the preparation of S doped TiO<sub>2</sub> by the oxidation annealing of TiS<sub>2</sub> followed by its annealing at 600°C. On annealing, TiS<sub>2</sub> gets partly converted to anatase TiO<sub>2</sub> and the residual S atoms in the anatase TiO<sub>2</sub> form S-doped TiO<sub>2</sub> by Ti-S bond-formation. The calculation for band structures of S-doped TiO<sub>2</sub> based on the super cell approach revealed the mixing of S 3p states with the VB of TiO<sub>2</sub> increased the width of VB resulting in narrowing of band gap. Ohno et al. developed a new method to prepare S-doped TiO<sub>2</sub> powder [77]. Titanium isopropoxide was mixed with thiourea and the mixture was stirred in ethanol. After subsequent evaporation, aging and calcination, S-doped TiO<sub>2</sub> powder was obtained. The S-ions were incorporated to replace some of the Ti atoms in the form of S<sup>4+</sup>. The photocatalytic activity of S-doped TiO<sub>2</sub> was then evaluated by photodecomposition of 2-propanol and methylene blue. It was found that S-doped TiO<sub>2</sub> has better photocatalytic efficiency than the pure TiO<sub>2</sub> under visible light irradiation. The oxidation ability of S-doped TiO<sub>2</sub> was found to be still high even after the VB was shifted upwards. There have been reports on C and F ion doped TiO<sub>2</sub> also and it was found that they can also expand the photo-response in visible spectrum [78-80].

There has been an extensive study on the effect of transitional metal ion doping and rare earth metal ion doping for enhancing the photocatalytic efficiency of titania. Choi et al. [81] extensively studied the effect of doping by 21 metal ions on the photocatalytic activity of TiO<sub>2</sub>. The study revealed that the impurity energy levels are generated within the band-gap of TiO<sub>2</sub> after the incorporation of metal ion ( $M^{n+}$ ) within the TiO<sub>2</sub> matrix as indicated below:





The metal-ion can then act as electron trap as well as hole trap. Thus the electron-hole recombination is thus modified by the electron (hole) transfer between metal-ion and TiO<sub>2</sub> as below:



The energy level of M<sup>n+</sup>/M<sup>(n-1)+</sup> should be less negative than that of the CB edge of TiO<sub>2</sub>, while the energy level of M<sup>n+</sup>/M<sup>(n+1)+</sup> should be less positive than that of the VB edge of TiO<sub>2</sub>. Again the photocatalytic reaction will take place only if the trapped charge-carriers are transferred to the surface of the photocatalyst. Therefore, metal ions should be doped near the surface of TiO<sub>2</sub> particles for a better transfer of charge-carriers to the surface. In case of deep doping, such transfer of charge-carriers becomes difficult and hence, metal ions behave as recombination centers. Furthermore, there exists an optimum concentration for the doped metal ion above which the photocatalytic activity decreases due to the increase in recombination of charge-carriers. Among the 21 metal ions studied by Choi et al., V, Fe, Mo, Ru, Os, Re and Rh ions can increase photocatalytic activity, while dopants Co and Al ions cause detrimental effects. The metal-ions which can trap both the electrons and holes, are generally recommended for enhancing the photocatalytic efficiency. Wu et al. [82] qualitatively investigated the effect of doping with transitional metal ions (Cr, Mn, Fe, Co, Ni & Cu) on photocatalytic activity of TiO<sub>2</sub>. The Mn, Fe and Cu metal-ions can trap both electrons and holes while Cr, Co and Ni metal-ions can only trap one type of charge carrier. Hence, the doping with the first three metal-ions (Mn, Fe & Cu) is expected to work better than the later three metal-ions (Cr, Co & Ni) for the present

purpose. The similar study on different rare earth metal ions (La, Ce, Er, Pr, Gd, Nd and Sm) by Xu et al. [83] revealed the fact that the Gd metal-ion most is the most effective one in enhancing the photocatalytic activity due to its highest ability to transfer charge carriers to the surface of TiO<sub>2</sub>. Noble metals, including Pt, Au, Pd, Rh, Ni, Cu and Ag, have also been found to be very effective for enhancing the photocatalytic efficiency of TiO<sub>2</sub>. Due to the fact that the Fermi levels of these noble metals are lower than that of TiO<sub>2</sub>, the photo-excited electrons can be transferred from CB of TiO<sub>2</sub> to metal particles deposited on the surface of TiO<sub>2</sub>. However, the photo-generated holes still remain in the VB of TiO<sub>2</sub> and hence, the probability of electron-hole recombination is greatly reduced resulting in a better photocatalytic effect. A comprehensive review by M. Ni et al. [84] provides information about the recent developments in the different methods to improve the photocatalytic ability of TiO<sub>2</sub>.

The other two oxides, namely HfO<sub>2</sub> and ZrO<sub>2</sub> have found their applications in different phase including high-temperature phases. At room temperature, they both exist in the monoclinic phase. The monoclinic phase is converted to tetragonal at 1720°C for HfO<sub>2</sub> and at 1170°C for ZrO<sub>2</sub>. The cubic phase is attained at 2600°C for HfO<sub>2</sub> and at 2370°C for ZrO<sub>2</sub>. These high temperature phases have found different applications in different fields. Zhao et al. [85] employed density functional theory to model the undoped HfO<sub>2</sub> and predicted a higher permittivity in the cubic ( $\kappa \sim 29$ ) or in the tetragonal ( $\kappa \sim 70$ ) structures than that in the monoclinic phase. There have been a number of studies on the stabilization of high-temperature phases by doping with suitable elements. The doping with a tetravalent cation (same valence as of Hf<sup>4+</sup> and Zr<sup>4+</sup>) with a larger ionic radius than Hf<sup>4+</sup> or Zr<sup>4+</sup> ions leads to an enlargement of the crystal system in order to accommodate the larger resulting in the stabilization of the high temperature phases. Again, the doping with a cation having a lower valence than the Hf<sup>4+</sup> or Zr<sup>4+</sup> ions

introduces oxygen vacancies which play a key role in the stabilization of the high temperature phases. For Y-stabilized hafnia [86], a phase boundary between the monoclinic and cubic structures exists between 6 and 8 atom % of  $Y_2O_3$ , while a single cubic phase exists above 8 atom %  $Y_2O_3$  at  $1500^\circ C$ . The study on the cubic  $HfO_2-R_2O_3$  ( $R=Lu, Ho, Gd, Sm, Yb, Y$  and  $Sc$ ) with  $R^{+3}$  ions has revealed that the deep vacancy trapping leads to the decrease in the ionic conductivity at high dopant concentrations [87]. A recent study on the Mn-doped  $HfO_2$  [88] reveals the fact that the Mn-dopant stabilizes the cubic phase of hafnia. The variable valences of Mn leading to the different ionic-sizes of Mn and the oxygen vacancies play an important role to stabilize the cubic phase. Tetragonal Zirconia Polycrystal (TZP) is a new type of zirconia-based engineering ceramics. A comprehensive review article [89] provides the information about the microstructural development and mechanical properties of TZP. The metastable TZP materials are usually fabricated in  $ZrO_2-Y_2O_3$  system due to the wide-range of yttria solubility in tetragonal zirconia. This  $ZrO_2-Y_2O_3$  system is also believed to have a comparatively large critical particle-size below which the tetragonal phase can be stabilized at room temperature. Recently interest has also been shown in the potentially more economic  $ZrO_2-CeO_2$  system. The high strength and toughness of TZP is considered to be largely due to the stress-induced martensitic transformation of the metastable tetragonal phase to the stable monoclinic phase. The common notation used in TZP literature involves placing the cation symbol of the stabilising oxide before the TZP abbreviation. In some cases the molarity of the stabilising oxide will be indicated by a number before the cation symbol, e.g.  $ZrO_2-3 \text{ mol\% } Y_2O_3 = 3Y-TZP$ . When heated to about  $1170^\circ C$ , zirconia undergoes a phase transformation from monoclinic to tetragonal and volume shrinkage of more than 3-5%. Further heating produces another change to cubic at  $2370^\circ C$ . The cubic phase is maintained until the melting point of zirconia is reached ( $\sim 2680^\circ C$ ). On cooling

from sintering temperatures and/or high temperature exposure, zirconia undergoes the tetragonal to monoclinic transformation at 950°C and an expansion similar in magnitude of the shrinkage during heat up. The large volumetric change associated with this phase transformation is large enough to affect the structural integrity of the material. Repeated heating and cooling cycles would result in further erosion of mechanical integrity and properties. In partially stabilized zirconias, similar additions are made but not enough to stabilize all of the material and hence the name “partially stabilized zirconia” or “PSZ”. These materials typically consist of two or more of the phases cubic, tetragonal and monoclinic. If produced properly, the resultant microstructure consists of lens or elliptical-shaped precipitates of tetragonal zirconia within the cubic grains. Normally the tetragonal phase would transform into the monoclinic phase at low enough temperatures, but the high strength of the cubic phase prevents the required expansion from happening, freezing in the tetragonal precipitates. Monoclinic zirconia may also be present in the cubic grains and at the grain boundaries. Normally the tetragonal phase would transform into the monoclinic phase at low enough temperatures, but the high strength of the cubic phase prevents the required expansion from happening, freezing in the tetragonal precipitates. Monoclinic zirconia may also be present in the cubic grains and at the grain boundaries. This is called “Transformation Toughening” and is a stress induced martensitic transformation to the monoclinic phase [90]. The PSZ materials have got excellent fracture toughness, wear resistance, impact resistance, resistance to thermal shock, chemical resistance and corrosion resistance. The PSZ materials have found several applications as dies and tooling, knives, scissors and blades, wear resistant components including bearings and linings, pump parts etc. Hence, zirconia based ceramic materials have received extensive interest as important structural ceramic and biomedical materials [91] due to its excellent mechanical properties. Zirconia in tetragonal phase

has got a long-term biocompatibility which makes it possible to be used in prosthetic hip, knee-bearings, dental material for crown etc. So the tetragonal phase has to be stabilized for these kinds of applications. Now, as discussed earlier, the transformation from tetragonal to monoclinic phase is diffusionless and requires only shear of the parent structure to obtain the daughter phase, and the transformation at any temperature is almost instantaneous. There have been a number of attempts to get an explanation of these low-temperature degradation phenomena [92]. The postulated degradation mechanism states that a tetragonal surface grain transforms to the monoclinic structure when the water vapor draws sufficient yttria from a small volume element on the surface of the tetragonal grain. As the monoclinic nucleus grows by further depletion of yttria, it will eventually attain a critical size. At this critical size, growth-process becomes so spontaneous it does not require any further diffusion of yttria to complete transformation of the tetragonal grain on which the nucleus was growing. If the grain is sufficiently large, the transformation will be accompanied by microcracking of the matrix. The microcracks will open up new surfaces on the subgrains which initiate further diffusion of yttria and subsequent transformation. The kinetics of this degradation process has also been studied [93] for 3Y-TZP. The study reveals that the kinetics of transformation of 3Y-TZP is of first order, with time exponent approaching unity, which indicates that a nucleation and growth mechanism dominated on the specimen surface.

## **1.2 Perturbed Angular Correlation Spectroscopy:**

The origin of the different nuclear probe techniques relies on those nuclear properties which are sensitive to the chemical state of the radioactive probe atoms and to the chemical properties of the environment surrounding the probe atom. Radioactive decay processes are, in general, independent of the chemical state of the atom undergoing radioactive disintegration. However,

there are certain decay processes where the extra-nuclear electrons are involved (e.g., in case of internal conversion and electron capture decay) and the decay rate in those processes has been found to depend on the chemical state of the atom. Nuclear probe techniques, such as, Perturbed Angular Correlation (PAC), Positron Annihilation Spectroscopy (PAS), Nuclear Magnetic Resonance (NMR), Mossbauer Spectroscopy (MS), Nuclear Quadrupole Resonance (NQR) etc. are also based on the effect of chemical environment on the nuclear phenomenon. In the case of PAS, the extent of Doppler broadening in the gamma ray peak of 511 keV annihilation gamma ray is dependent upon the momentum of the electron with which the positron annihilates, and hence on the chemical state of the atom in the medium. Similarly the formation probability of the ortho-positronium (Ps), depends upon the electron density in the medium in which the positron is stopped. In the case of Mossbauer spectroscopy the hyperfine interaction between the electric field gradient and the quadrupole moment of the absorbing nucleus leads to splitting in the gamma-absorption spectrum. A relatively slow development of PAC technique in chemistry in comparison with NMR or MS techniques originates from the lack of complete rigorous theory and availability of commercial "Push Button" instrument. The PAC instrument has to be fabricated by the experimenter and a chemist may not be so familiar with the complicated electronic circuit-diagrams required for nuclear experiments. Although the number of suitable isotopes for PAC seems to exceed that of MS, most of the chemical applications are limited to compounds of a few elements. Again data-acquisition in PAC is more time-consuming and data-analysis is also more intricate than that in MS. However, the same probe can be used for the study of various matrices and the number of probe-atoms present in the matrix under study is so diluted ( $\sim 10^{-3}$ - $10^{-4}$  atom %) that it does not affect the crystal structure of the matrix. Again, PAC permits the removal of temperature and solid-state restrictions. Hence, high-temperature phase

transition, solution chemistry of metal complexes, rotational diffusion of macromolecules etc. are some of the special topics of investigation in the field of PAC. Besides, PAC has certain subtle edges over the other complementary methods NMR or MS, viz., it requires no external RF field or magnetic field, sensitivity is independent of vibration (hence, stirred bath can be used) and temperature etc. Again PAC can be applied to a trace quantity of sample while the other resonance techniques require at least ~mg quantity of material. In solid state chemistry, PAC cannot be a competitive but a complimentary technique with MS for those elements lacking isotopes with suitable transitions for  $\gamma$ -resonance.

The method relies on the fact that when a nucleus emits two or more radiations in cascade, they have a spatial distribution with respect to each other depending on the spins of the nuclear levels and multi-polarities of the radiations involved in the cascade. This angular correlation is the manifestation of the population of the m-states in the intermediate level. However, if the intermediate state, after the emission of first radiation, interacts with the extranuclear field, then the population of the m-states in the intermediate level gets altered and thereby changing the angular correlation pattern. This is called the perturbation of the angular correlation which depends on the chemical environment surrounding the probe atom. This interaction can be either static or time-dependant depending on whether the interaction Hamiltonian is independent of time or fluctuates with time respectively. The unperturbed angular correlation is represented by the sum of the even order Legendre polynomials multiplied by the radiation parameters. However, when the perturbation takes place, the above product contains another term called perturbation or attenuation factor. This factor provides all the information about the electronic structure and hence the chemical environment at the site of the probe.

In actual experiment, one measures the coincidence between cascade radiations at least at two different angles (viz.  $90^\circ$  and  $180^\circ$ ) and after fitting the experimental values with the theoretical expression, one gets the perturbation factor. Depending on the resolving time ( $\tau_R$ ) of the instrument, two different methodologies are followed. If the resolving time ( $\tau_R$ ) of the instrument is more than the life time of the intermediate level, integral PAC (IPAC) method is followed and if it is less, Time Differential PAC (TDPAC) method is followed. IPAC is an average process and one loses the detailed information about the mechanism of interaction. Although the information obtained from TDPAC method is more useful than that obtained from IPAC, later method becomes the only choice in certain cases. With the advent of accelerators, other PAC methods, viz., Time Differential Perturbed Angular Distribution (TDPAD), In Beam PAC study have also been possible. However, present thesis deals with TDPAC with the  $\gamma$ - $\gamma$  angular correlation being perturbed by the electric field gradient (EFG).

### **1.2.1. Historical Background on PAC:**

The pioneer work on the theory of directional correlation was done in 1940 by Hamilton [94]. After that, some attempts were made to experimentally verify the predictions of Hamilton's theory but without any remarkable success. The theoretical investigation of the influence of extranuclear fields on the directional correlation was performed by Goertzel [95] in 1946. The first successful experiment was carried out by Brady and Deutsch [96] in 1947 with Geiger counters. Subsequently, the angular correlation works were improved by scintillation counters. A typical run that takes a day with scintillation counters would require more than a thousand years of continuous work with Geiger counters. A scintillation counter has a high counting efficiency, speed and energy sensitivity and hence, with the development of fast electronics, angular correlation technique gradually became a well-established tool in nuclear spectroscopy. At first,

the angular correlation measurements were utilized for the measurement of spin and parities of nuclear levels and radiations. As soon as the sensitivity of the correlation pattern to the extranuclear fields with a specified life time of the intermediate state was realized, the technique was used in the determination of g-factor [97] and quadrupole moment [98] of the excited nuclear states. After the discovery of parity non-conservation, the angular correlation experiments were also used in the field of  $\beta$ -decay. In 1960's and 1970's, the angular correlation experiments were mainly motivated towards the hyperfine interaction of the magnetic and electric fields between the host-matrix and the probe nucleus. After the discovery of ion-implantation, the angular correlation experiments were also used in the study of point defects including geometric arrangement of vacancies and interstitials inside the host matrix [99]. From 1980's, PAC technique started to get applied in the field of materials science. After that, PAC Spectroscopy was extensively used in Chemistry, Materials Science and Biology [100] for the last few decades. However, this is still being used in the study of defects and diffusion. The defect formation energy, association energy and migration barriers can also be extracted from the analysis of the PAC spectra [101]. With this formal background of PAC, general theory of angular correlation and the effect of the external magnetic or electric field on this correlation pattern will be discussed. However, a brief overview of electric quadrupole moment and the electric field gradient (EFG) will be provided before discussing the detailed theory of angular correlation technique. The basic background theory required for the development of the above theory will not be discussed separately but be referred in a proper manner.

### **1.2.2. Electric Quadrupole Moment and EFG:**

When the time average of the spatial distribution of electric charge within a nucleus deviates from perfect spherical symmetry, the nucleus will possess finite electric multipole moments. The

electrostatic field produced at the position of the nucleus by the atomic and molecular configurations generates a non-uniform field.

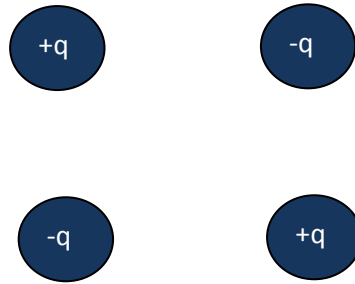


**Figure 1.10:** System of charges arranged in a particular manner

Considering the system of charges shown in Fig.1.10, there is no resultant charge and dipole moment. Unlike a dipole, it will experience neither a net force nor a net torque in any external uniform field. It may or may not experience a net force in an external non-uniform field. In case of quadrupole being thought of as two dipoles, each dipole will experience a force proportional to the local field gradient in which it resides. If the field gradients at the location of each dipole are equal, the forces on each dipole will be equal but opposite and there will be no net force on the quadrupole. If, however, the field gradients at the positions of the two dipoles are unequal, the forces on the two dipoles will not be equal and there will be resultant force acting on the quadrupole. Thus there will be a net force if there is a non-zero field gradient. Furthermore, when the system resides in a non-uniform field, it may feel resultant torque acting in a particular direction although there might not be net force unless the field gradient on each pair is unequal. Thus the system possesses a Quadrupole Moment. In comparison with a point charge being a scalar quantity and a dipole moment being a vector quantity, the quadrupole moment is a second order tensor. The quadrupole moment  $Q$  has nine components defined by  $Q_{xx} = \sum q_i x_i^2$ ,  $Q_{xy} = \sum q_i x_i y_i$  and so on. The matrix representation of this second order tensor is given as follows:

$$Q = \begin{bmatrix} Q_{xx} & Q_{xy} & Q_{xz} \\ Q_{xy} & Q_{yy} & Q_{yz} \\ Q_{xz} & Q_{yz} & Q_{zz} \end{bmatrix} \quad (1.11)$$

By suitable rotation of axes in the usual way, the matrix can be diagonalized and the diagonal elements are then the Eigen values of the quadrupole moment, and the trace of the matrix is unaltered by the rotation.

In general, quadrupole produces a potential which varies inversely with the cube of distance and its quadrupole moment has the dimensions of (charge) X (area).

Multipole moments are also exhibited in the potential due to a single point charge, if that charge is not located at the origin of the coordinate system. In the rectangular coordinates  $x, y, z$  the scalar electrostatic potential  $\varphi$  at the external point  $P (0, 0, d)$  on the  $z$ -axis due to a charge  $+e$  at the point  $(x, y, z)$  is:

$$\varphi = \frac{e}{d_1} = \frac{e}{d} \left( 1 - 2 \frac{r}{d} \cos \vartheta + \frac{r^2}{d^2} \right)^{-\frac{1}{2}} \quad (1.12)$$

Where  $d_1 = (d^2 - 2rd \cos \varphi + r^2)^{1/2}$  is the distance from the point  $P$  to the charge,  $r = (x^2 + y^2 + z^2)^{1/2}$  is the distance from the origin to the charge and  $\cos \vartheta = z/r$  describes the angle between  $r$  and  $d$ . Expanding the eqn. (1.12) and collecting terms in  $1/d^n$ , we obtain the general expression:

$$\varphi = \frac{e}{d} + \frac{er}{d^2} \cos \vartheta + \frac{er^2}{d^3} \left( \frac{3}{2} \cos^2 \vartheta - \frac{1}{2} \right) + \frac{er^3}{d^4} \left( \frac{5}{2} \cos^3 \vartheta - \frac{3}{2} \cos \vartheta \right) + \dots \quad (1.13)$$

Or, more generally,

$$\varphi = \sum_{n=0}^{\infty} \frac{er^n}{d^{n+1}} P_n(\cos \vartheta) \quad (1.14)$$

Where  $P_n(\cos \vartheta)$  are Legendre polynomials and  $n$  (or more exactly,  $2^n$ ) is the multipole order.

So, in eqn. (1.13), the coefficient of  $1/d$  is the monopole strength, of  $1/d^2$  is the  $z$ -component of

the dipole moment, of  $1/d^3$  is the z-component of the quadrupole moment. Now putting  $\cos\vartheta = z/r$ , we obtain the coefficient of  $1/d^3$  which is the effective classical quadrupole moment  $Q^{(2)}$  in the direction  $z$  as exhibited at  $P(0, 0, d)$  as:

$$Q^{(2)} = \frac{e}{2}(3z^2 - r^2) \quad (1.15)$$

For a continuous charge distribution with a mean charge density  $\rho$  of nuclear charge in the volume element  $d\tau$  at the point  $(z, r)$ , the nuclear electric quadrupole moment  $Q$  is defined as:

$$Q \equiv \frac{1}{e} \int \rho(3z^2 - r^2)d\tau = \frac{1}{e} \int \rho r^2(3\cos^2\varphi - 1)d\tau \quad (1.16)$$

Where  $z = r\cos\varphi$

The effective value  $Q(m_I)$  in the state  $m_I$  is related to its value  $Q$  in the state  $m_I = I$  by the following two equations:

$$Q(m_I) = \frac{3m_I^2 - I(I+1)}{I(2I-1)} Q \quad (1.17)$$

And 
$$\cos\varphi = \frac{m_I}{\sqrt{I(I+1)}} \quad (1.18)$$

Nuclei with  $I = 0$  or  $I = 1/2$  can show no quadrupole moment. In case of  $I = 1/2$ ,  $\cos\varphi = 1/\sqrt{3}$  according to eqn. (1.18) and an average value of  $(3\cos^2\varphi - 1)$  in eqn. (1.16) becomes zero. This does not signify that those nuclei possess a perfect spherical charge distribution, but only the maximum observable component  $Q$  is zero. Finite electric quadrupole moments are therefore observed only for those nuclei which have angular momentum  $I \geq 1$ .

The nuclear quadrupole moment operator  $Q_{ij}$  for a discrete system of point charges each with charge  $q_l$  and position  $\vec{r}_l = (r_{xl}, r_{yl}, r_{zl})$  relative to the coordinate system origin is defined as:

$$Q_{ij} = \sum_l q_l(3r_{il} \cdot r_{jl} - r_l^2 \delta_{ij}) \quad (1.19)$$

The indices  $i, j$  run over the Cartesian coordinates  $x, y, z$  and  $\delta_{ij}$  is the Kronecker delta.

For a continuous system with nuclear charge density  $\rho_N(r)$ , the components of  $Q_{ij}$  are defined by integral over the charge density [102]:

$$Q_{ij} = \int \rho_N(r)(3x_i x_j - r^2 \delta_{ij}) dr \quad (1.20a)$$

Or can be expressed in terms of nuclear spin operators:

$$Q_{ij} = \frac{eQ}{I(2I-1)} \left\{ \frac{3}{2} (I_i I_j + I_j I_i) - \delta_{ij} I(I+1) \right\} \quad (1.20b)$$

Nuclear quadrupole moments are generally expressed in the unit of barn (1 barn =  $10^{-24}$  cm<sup>2</sup>) and show a wide range of values for spherical to highly deformed nuclei.

The **quadrupole moment tensor** is a rank-two tensor (3x3 matrix) and is traceless (i.e.,  $Q_{xx} + Q_{yy} + Q_{zz} = 0$ ). The quadrupole moment tensor has thus 9 components, but because of the rotational symmetry and zero-trace property, only 5 of these are independent.

The **electric field gradient (EFG)** measures the rate of change of the electric field at an atomic nucleus generated by the electronic charge distribution and the other nuclei. The EFG couples with the nuclear electric quadrupole moment of quadrupolar nuclei (those with spin quantum number greater than one-half) to generate an effect which can be measured using several spectroscopic methods, such as nuclear magnetic resonance (NMR), electron paramagnetic resonance (EPR, ESR), nuclear quadrupole resonance (NQR), Mössbauer spectroscopy or perturbed angular correlation (PAC). The EFG is non-zero only if the charges surrounding the nucleus violate cubic symmetry and therefore generate an inhomogeneous electric field at the position of the nucleus. EFGs are highly sensitive to the electronic density in the immediate vicinity of a nucleus.

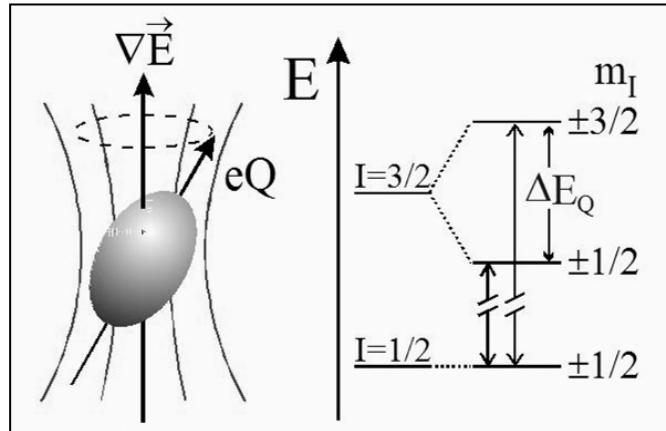


**Figure 1.11:** Electric Quadrupole Interaction and splitting of energy levels.

This is because the EFG operator scales as  $r^{-3}$ , where  $r$  is the distance from a nucleus. A given charge distribution of electrons and nuclei,  $\rho(\mathbf{r})$ , generates an electrostatic potential  $V(\mathbf{r})$ . The derivative of this potential is the negative of the electric field generated. The first derivatives of the field, or the second derivatives of the potential, are the electric field gradient. The nine components of the EFG are thus defined as the second partial spatial derivatives of a classical electrostatic potential, evaluated at the nuclear site:

$$V_{ij} = \frac{\partial^2 V}{\partial x_i \partial x_j} \quad (1.21)$$

Where  $V_{ij}$  is clearly symmetric. At this point we assume that all the charges producing the electrostatic potential are external to the nucleus. This assumption, which excludes the contribution from s-electrons, is justified by the fact that the s-electrons are spherically symmetrical and thus do not contribute to the field gradient. It is from this assumption that the Laplace's equation  $\nabla^2 V = 0$  is invoked to show that the trace of  $V_{ij}$  vanishes. The Hamiltonian

operator describing the nuclear quadrupole interaction with an external electrostatic field is given by the product of the two rank-two tensors:

$$H = \frac{1}{6} \sum_{ij} Q_{ij} V_{ij} \quad (1.22)$$

The above eqn. is only valid when the charge producing the external electrostatic field does not overlap the nuclear charge distribution. Relaxing this assumption, a more general form of the EFG tensor [103] which retains the symmetry and traceless character is:

$$\varphi_{ij} = V_{ij} - \frac{1}{3} \delta_{ij} \nabla^2 V \quad (1.23)$$

where  $\nabla^2 V(\mathbf{r})$  is evaluated at a given nucleus.

As  $V$  (and  $\varphi$ ) is symmetric it can be diagonalized. The principal tensor components are usually denoted  $V_{zz}$ ,  $V_{yy}$  and  $V_{xx}$ . Given the traceless character, only two of the principal components are independent. Typically these are described by  $V_{zz}$  and the **asymmetry parameter**,  $\eta$ , defined as:

$$\eta = \left| \frac{V_{xx} - V_{yy}}{V_{zz}} \right| \quad (1.24)$$

Where the principle axes are choosen in such a way that  $|V_{zz}| \geq |V_{yy}| \geq |V_{xx}|$ . This ensures the fact that  $0 \leq \eta \leq 1$  since  $\nabla^2 V = 0$ .

### 1.2.3. Directional Correlation Function:

Any two radiations, emitted in cascade, have definite spatial correlation with respect to their directions of emission due to the conservation of angular momentum of nuclear levels involved in the cascade and the multipolarities of the radiations. In other words, there exists a definite angular distribution of the two radiations emitted in cascade. Under ordinary condition, the nuclei are randomly oriented in space and emission of the individual radiation is isotropic. An anisotropic radiation pattern is observed only when the ensemble of nuclei is not randomly oriented. One way to achieve such an oriented radiation pattern is to place the radioactive source

at a very low temperature in a strong magnetic field or electric field gradient when the nuclei get aligned and the angular distribution of the emitted radiation is measured with respect to the direction of the applied field. Other way is to select only those nuclei whose spins are oriented in a particular direction. In case of nuclei emitting two radiations  $R_1$  and  $R_2$  successively, the observation of  $R_1$  in a particular direction  $k_1$  selects an ensemble of nuclei having a nonisotropic distribution of spin orientations. Thus, a definite angular correlation with respect to  $k_1$  is observed in case of the succeeding radiation  $R_2$ . The term angular correlation consists of directional correlation and polarization correlation. In directional correlation, only the directions of the two radiations are observed while in polarization correlation, the linear or circular polarization of one or both of the radiations is observed. In deriving the expression for angular correlation function for successive emission of two  $\gamma$ -radiations, we will first consider that there is no extranuclear field acting on the nucleus. Such measurements of unperturbed directional correlation function yield the information about the properties of the nuclear levels involved in the cascade emission of the two  $\gamma$ -radiations and about the angular momenta carried away by the  $\gamma$ -photons. In this present context, it is to be remembered that the  $\alpha$ - $\gamma$  or  $\gamma$ - $\gamma$  directional correlation yields the spins of the nuclear levels but not the parities. However the relative parities can be determined by observing, in addition to the direction, also the polarization of the two  $\gamma$ -radiations or by measuring the directional correlation between conversion electrons. After discussing the unperturbed directional correlation function, we will introduce the influence of extranuclear fields on the angular correlation function.

Let us consider the following decay scheme:

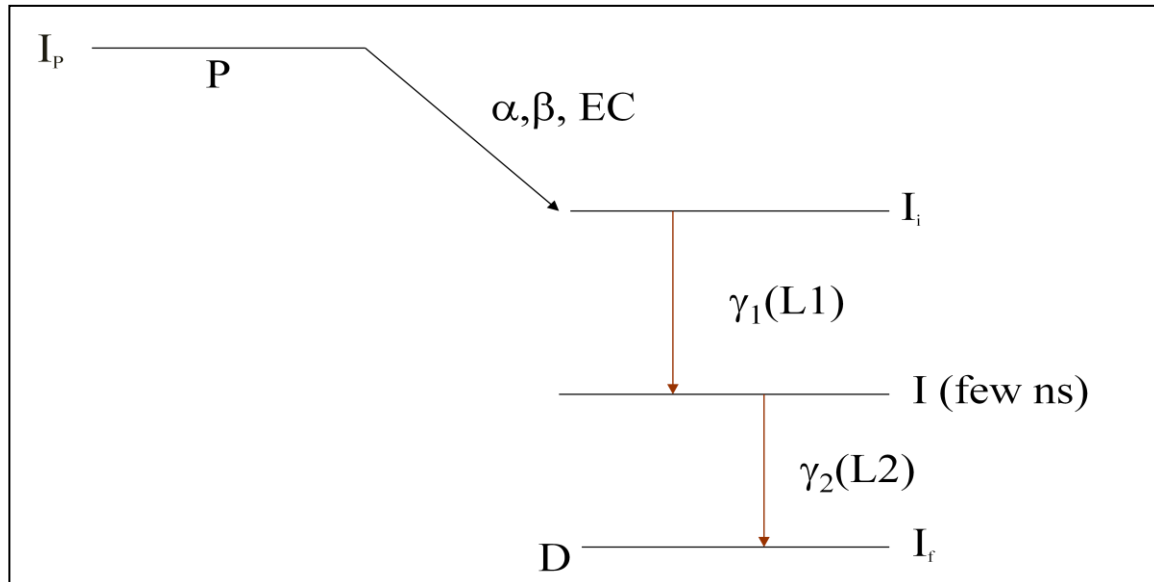


**Figure 1.12:** Decay of parent (P) to daughter (D) nuclei and subsequent emission of cascade  $\gamma$ -rays from the daughter atom.

In case of TDPAC, it requires a  $\gamma$ - $\gamma$  cascade fed by the decay of a parent isotope. The parent isotope is produced by a nuclear reaction and then decays by particle or  $\gamma$ -ray emission to produce the daughter isotope. Then the daughter atom, inside the matrix under study, acts as an “wound-up spy” [104] to transfer information of its host matrix while returning to its ground state. The intermediate state of the cascade should have a lifetime in the range of 10-1000 ns. This is a crucial parameter as the intermediate state must have a sufficiently long lifetime to feel the perturbation. Again the extranuclear field must be significant enough to interact with the quadrupole moment of the intermediate state. The interaction of the nuclear electric quadrupole moment with an electric field gradient (EFG) leads to a perturbation or attenuation in the angular correlation pattern. Semiclassically, the interaction produces a precessional motion of the intermediate spin about the symmetry axis defined by the direction of emission of the first  $\gamma$ -ray. Thus the orientation of the intermediate spin gets altered in the time interval between the emission of  $\gamma_1$  and  $\gamma_2$  and the angular correlation function is perturbed. Quantum mechanically,

the interaction produces the transition among the non-degenerate m-states leading to the emission of  $\gamma_2$  from an m-state with an attenuated population density [105]. The precession of the intermediate spin is characterized by an angular rotation frequency  $\omega$ . The time change in the correlation function is observed if the rotation is significant in the time scale of the lifetime of intermediate state, i.e.,  $\omega\tau \geq 0.01$  which assigns the lower limit of the workable lifetime to 10 ps for a typical angular velocity of  $1000 \text{ Mrad s}^{-1}$ . A nucleus that emits  $\gamma_2$  immediately after the emission of  $\gamma_1$  (prompt coincidence) contributes to an unperturbed correlation because it got no time to precess. In actual experiment, a coincidence histogram is recorded as a function of time elapsed between the emission of  $\gamma_1$  and  $\gamma_2$  at two different angles, viz.,  $90^\circ$  and  $180^\circ$ . The excess (or deficit) of the coincidence count rate at opposite detectors ( $\theta=180^\circ$ ) compared to the isotropic average is called “anisotropy” (positive for excess and negative for deficit). Again when  $\gamma_1$  is detected in a particular direction, an aligned ensemble of nuclear spins is selected by virtue of the conservation of angular momentum. However, all the nuclei in that selected ensemble do not emit  $\gamma_1$  into the detector with equal probability. Therefore, the emission of a subsequent  $\gamma_2$  from the same nucleus which has already emitted  $\gamma_1$  will in general depend on the angle between  $\gamma_1$  and  $\gamma_2$ , i.e., the coincidence count rate is *anisotropic*. For unperturbed system (zero EFG), we would get different count rates for two detectors at  $180^\circ$  and  $90^\circ$ , both decaying exponentially with a lifetime of the intermediate state (in case of lifetime measurement). In presence of the extranuclear field, the coincidence histogram gets modulated over the exponential decay and the modulated exponential decay contains all relevant information on the hyperfine-split intermediate level. It is a common practice to Fourier transform this perturbation function in order to retrieve the energy (or frequency) splitting of the hyperfine split state.

There have been a number of papers [106-114] which describe the general theory of angular correlation and the effect of extranuclear field on this correlation pattern. In this section, the discussion will be restricted to only the theory of PAC pertaining to  $\gamma$ - $\gamma$  cascade only.

Let us consider a radionuclide from its first excited state  $(I_i, m_i)$  decaying to a final  $(I_f, m_f)$  state by emission of two successive photons  $\gamma_1 (L_1, M_1 = m_i - m)$  and  $\gamma_2 (L_2, M_2 = m - m_f)$  with propagation vectors  $\vec{k}_1$  and  $\vec{k}_2$  respectively. The excited state is populated from a radionuclide by  $\alpha$  or  $\beta$  emission, electron capture or an isomeric transition. The intermediate level has a mean lifetime  $\tau$  and an electric quadrupole moment  $Q$ . Let us also choose the z-axis as the axis of quantization and  $m_i, m$  and  $m_f$  as quantum numbers for the projection of  $(I_{zi}, I_z, I_{zf})$  of the spin angular momentum onto this axis. The parities of the three states are denoted by  $\pi_i, \pi$  and  $\pi_f$  respectively. For the conservation of angular momentum, we have  $I_i = I + L_1$ . From Quantum mechanics, we have the conditional relationship:  $|I_i - I| \leq L_1 \leq |I_i + I|$  and the corresponding projections of the spin angular momentum as  $m_i = m + M_1$ . Similarly,  $|I - I_f| \leq L_2 \leq |I + I_f|$  and  $m = m_f + M_2$ . The emitted  $\gamma$ - ray is then characterised by the multipolarity  $L$ , and magnetic quantum number  $M$ , with  $L^2 = L(L+1)\hbar^2$ ,  $L_z = M\hbar$ . The multipole character of the electromagnetic radiation field is determined by  $2^L$ . For  $L=1$  we have dipole radiation, for  $L=2$ , quadrupole radiation and so on.

The emission probability of a photon in the direction  $\vec{k}$  relative to the spin axis  $\vec{I}$  of the nucleus depends on the angle  $(\vec{I}, \vec{k})$ . Let us consider  $\vec{k}_1$  be the direction in which the first radiation  $\gamma_1$  is observed and  $\vec{k}_2$  be that in which the second radiation  $\gamma_2$  is observed. Since the spins of the nucleus are randomly oriented in space, the emission of radiations  $\gamma_1$  and  $\gamma_2$  is isotropic in nature when measured independently. To observe the correlation between the directions of the two

successive  $\gamma$ -rays, it is necessary to select the ensemble of nuclei emitting  $\gamma_1$  in a fixed direction  $\vec{k}_1$  and to measure the intensity of  $\gamma_2$  as a function of the angle  $\theta$  with respect to  $\vec{k}_1$ . Therefore if the detector  $D_1$  registers  $\gamma_1$ , the response of detector  $D_2$  at an angle  $\theta \equiv (\vec{k}_1, \vec{k}_2)$  is a representation of the directional correlation of the two successive photons. The angular correlation between the two gamma-radiations  $\gamma_1$  and  $\gamma_2$  holds only if the two gamma quanta originate from the same decaying nucleus. This is possible only if the second  $\gamma_2$  quantum is detected in *fast coincidence* with initial gamma. In order to avoid the accidental coincidence, i.e., the second  $\gamma_2$  quantum detected from another nucleus, the activity of the source should be sufficiently low. It is assumed that all  $m_i$  substates in the initial level are equally populated at the time of emission of  $\gamma_1$ . The direction of the emission of first  $\gamma$  is chosen along the z axis. The relative population  $P(m)$  of each  $m$  sublevel in the intermediate state is determined by the initial transitions. It is obtained by summing over all  $m_i \rightarrow m$  transitions leading to the intermediate  $m$  substate

$$P(m) \propto \sum_{m_i} [CG(m_i m)]^2 F_{L_1}^{M_1}(\bar{\theta}) \quad (1.25)$$

The term in the square bracket is the Clebsch-Gordan coefficient [115] for the  $m_i \rightarrow m$  transition. It denotes the transition probability for  $m_i \rightarrow m$  transition.  $F_{L_1}^{M_1}(\bar{\theta})$  is the characteristic directional distribution for each  $(m_i \rightarrow m)$  transition and  $\bar{\theta}$  is the angle between the emitted  $\gamma$  and the z-axis. Let  $|I_i, m_i\rangle$  be one of an orthonormal set  $|I'_i, m'_i\rangle$  of eigenfunctions of the operators  $I_i^2$  and  $(I_i)_z$  with eigenvalues  $I_i(I_i + 1)\hbar^2$  and  $m_i\hbar$  respectively. Let  $|I, m\rangle$  and  $|L_1, M_1\rangle$  be similar eigenfunctions for the vector operator  $I$  and  $L_1$ , and  $\mathbf{I}_i = \mathbf{I} + \mathbf{L}_1$ ,  $m_i = m + M$ . The Clebsch-Gordan coefficients are the coefficients in the expansion of  $|I_i, m_i\rangle$  in terms of products  $|I, m\rangle |L_1, M_1\rangle$

$$|I_i, m_i\rangle = \sum_{m, M_1} |I, m\rangle |L_1, M_1\rangle \langle ImL_1M_1|I_i m_i\rangle \quad (1.26)$$

The Clebsch-Gordan coefficients  $\langle ImL_1M_1|I_i m_i\rangle$  are the elements of a unitary matrix.

$$CG(m_i, m) = \langle ImL_1M_1|I_i m_i\rangle \quad (1.27)$$

The phases of the eigen functions are so chosen that the coefficients are real numbers and hence the matrix is orthogonal. We define the relative transition probability to be equal to the square of the Clebsch-Gordan coefficient for the vector addition  $\mathbf{I}_i = \mathbf{I} + \mathbf{L}_1$  and  $m_i = m + M_1$

$$G(m_i, m) = [CG(m_i, m)]^2 = \langle ImL_1M_1|I_i m_i\rangle^2 \quad (1.28)$$

The most general derivation of the above equation (1.28) is based on the group theoretical methods [116]. The relative populations  $P(m_i)$  depend on the energies of the different  $m_i$  states and on the way in which level  $i$  was created. If the nuclei are randomly oriented so that all  $m_i$  states are equally populated for any choice of the z-axis, then  $F_L(\theta)$  is independent of  $\theta$  and the distribution becomes isotropic.

The choice of  $\vec{k}_1$  as the z-axis makes  $\bar{\theta} = 0$  and limits the summation to  $M_1 = \pm 1$ . Hence from eqn. (1.25) and eqn. (1.27), we get:

$$P(m) \propto \sum_{m_i} \langle ImL_1 \pm 1|I_i m_i\rangle^2 F_{L_1}^{\pm 1}(0) \quad (1.29)$$

The angular correlation function  $W(\theta)$  is the probability of the emission of  $\gamma_2$  at angle  $\theta$  versus the z-axis. It depends on the relative population of the  $m$ -states, the transition probability  $G(m, m_f)$  and the directional distribution  $F_{L_2}^{M_2}(\theta)$  for each component. The angular correlation function  $W(\theta)$  is then given as:

$$W(\theta) \propto \sum_{mm_f} P(m) [G(m, m_f)]^2 F_{L_2}^{M_2}(\theta) \quad (1.30)$$

Substituting  $P(m)$  with  $M_1 = m_i - m$  &  $M_2 = m - m_f$ :

$$W(\theta) \propto \sum_{m_f m m_i} \langle ImL_1 \pm 1|I_i m_i\rangle^2 F_{L_1}^{\pm 1}(0) \langle I_f m_f L_2 M_2|Im\rangle^2 F_{L_2}^{M_2}(\theta) \quad (1.31)$$

The above eqn. (1.31) for directional correlation function involves tedious sums over unobserved magnetic quantum numbers and applies to the directional correlation of two pure  $\gamma$ -rays emitted by free and unpolarized nuclei. A general expression for the angular correlation function of two successive radiations utilizes the Racah algebra [117-118] and density matrix formalism [119-120]. In the derivation of eqn. (1.31), the quantization axis coincides with the direction of emission of first radiation. This special choice eliminates interference terms and facilitates the description of this radiation. However, the description of the second radiation is not simplified. In the general derivation of the theory [109, 121-123], a separate coordinate system is introduced for each of the two radiations  $R_1$  and  $R_2$ . The z-axis of each system coincides with the direction of emission  $k_i$  of  $R_i$ . The two radiations are connected through an arbitrary quantization axis  $z$  by using the transformation properties of the eigen functions of  $R_1$  and  $R_2$ . The eigen function of  $R$  describes a system with total angular momentum  $L$  and thus transforms according to the  $(2L+1)$ -dimensional irreducible representation  $D^L$  of the three dimensional rotation group. Using this fact, the eigen functions of  $R_1$  and  $R_2$ , quantized along the arbitrary z-axis, are expressed in terms of the functions quantized along the directions of emission  $k_1$  and  $k_2$ . This approach leads to an expansion of the correlation function  $W(k_1, k_2)$  in terms of representations  $D^L$  (which reduce to Legendre Polynomials  $P_L(\cos\theta)$  for directional correlation). The derivation of  $W(k_1, k_2)$  is based on first order perturbation theory. A nucleus with spin  $I_i$  in its initial level  $i$  described by the density matrix  $\rho(k_1)$ , decays to the intermediate level with spin  $I$  when the radiation  $R_1$  is emitted in the direction  $k_1$ . The second step of the cascade  $I \rightarrow I_f$  leads to the density matrix  $\rho_f(k_1, k_2)$ . In presence of the extranuclear field, the density matrix  $\rho_a(k_1)$  describing the end product of the first transition is no longer identical with the density matrix  $\rho_b(k_1)$  describing the initial state of the second transition. The extranuclear

field induces transitions among different m-states and thus causes a change in the density matrix.

The change of  $\rho(k_1)$  can be described by a unitary transformation.

The expression for  $W(k_1, k_2)$  is given as follows:

$$W(k_1, k_2) \propto \sum_{m_f m m' m_i} \langle m_f | H_2 | m \rangle \langle m | H_1 | m_i \rangle \langle m' | H_1 | m_i \rangle^* \langle m_f | H_2 | m' \rangle^* \quad (1.32)$$

Here, the matrix element of the operator  $H_1$ , describing the interaction between the nucleus and the radiation field of  $\gamma_1$ , is taken between the initial states  $m_i$  and the intermediate state  $m$ . Similarly, the matrix element of  $H_2$ , describing the interaction between the nucleus and the radiation field of  $\gamma_2$ , is taken between  $m$  and the final states  $m_f$ . The complex conjugate matrix elements are also entered in order to obtain an observable probability. Since none of the sublevels  $m_i$ ,  $m$  or  $m_f$  is observed separately, we have to sum over all. The angular part of these matrix elements can be factored out using Wigner-Eckart Theorem [115]. From eqn. (1.32), we can arrive at the expression for the correlation function as follows:

$$W(k_1, k_2) \propto \sum_{k_1 k_2 N_1 N_2} A_{k_1}(1) A_{k_2}(2) \frac{1}{\sqrt{(2k_1+1)(2k_2+1)}} Y_{k_1}^{N_1*}(\theta_1, \phi_1) Y_{k_2}^{N_2}(\theta_2, \phi_2) \quad (1.33)$$

With

$$A_k(1) = F_k(L_1 L_1 I_i I) = (-1)^{I_i+I-1} (2L_1+1) \sqrt{(2I+1)(2k+1)} \begin{pmatrix} L_1 & L_1 & k \\ 1 & -1 & 0 \end{pmatrix} \begin{Bmatrix} L_1 & L_1 & k \\ I & I & I_i \end{Bmatrix},$$

$$A_k(2) = F_k(L_2 L_2 I_f I) = (-1)^{I_f+I-1} (2L_2+1) \sqrt{(2I+1)(2k+1)} \begin{pmatrix} L_2 & L_2 & k \\ 1 & -1 & 0 \end{pmatrix} \begin{Bmatrix} L_2 & L_2 & k \\ I & I & I_f \end{Bmatrix}.$$

Here,  $Y_k^N(\theta_i, \phi_i)$  is a spherical harmonic with  $\theta_i$  and  $\phi_i$  representing the polar and azimuthal angles of the vector  $k_i$ . The symbols in the definition of  $A_k$  are vector coupling coefficients, namely Wigner 3j- and 6j-symbols [124]. The  $k_1$  and  $k_2$  on the right hand side of eqn. (1.33) are summation indices which range from 0 to  $k_{max}$  with even  $k$ -values as parity is conserved in  $\gamma$ - $\gamma$  correlation measurement. Here  $k_{max} = \min(2L_1, 2L_2, 2I)$  with  $L_1, L_2$  being the lowest multipolarity of  $\gamma_1$  and  $\gamma_2$  and  $I$  denoting the intermediate state spin. The indices  $N_1$  and  $N_2$  run

from  $-k_1$  to  $+k_1$  and  $-k_2$  to  $+k_2$  respectively in steps of 1. The sum over  $N_1$  and  $N_2$  in eqn. (1.33) can be carried out using the addition theorem for spherical harmonics:

$$\sum_N Y_{k_1}^{N_1*}(\theta_1, \phi_1) Y_{k_2}^{N_2}(\theta_2, \phi_2) = (2k+1) P_k \cos\theta \quad (1.34)$$

$P_k \cos\theta$  denotes the Legendre polynomial with  $\theta$  being the angle between  $k_1$  and  $k_2$ :

$$\cos\theta = \cos\theta_1 \cos\theta_2 + \sin\theta_1 \sin\theta_2 \cos(\phi_1 - \phi_2) \quad (1.35)$$

From eqn. (1.35), we finally arrive at the expression for unperturbed angular correlation function:

$$W(k_1, k_2) = W(\theta) = \sum_k A_k(1) A_k(2) P_k \cos\theta \quad (1.36)$$

Considering the lowest order term, we have:

$$W(\theta) \propto 1 + A_2(1) A_2(2) P_2(\cos\theta) = 1 + A_{22} \left( \frac{3}{2} \cos^2\theta - \frac{1}{2} \right) \quad (1.37)$$

Here,  $A_{22}$  (the anisotropy) is abbreviation for  $A_2(\gamma_1) A_2(\gamma_2)$ .

Considering a finite lifetime of the intermediate level but explicitly excluding any interaction, we would have then a time dependant coincidence count rate:

$$W(\theta) \propto \exp\left(\frac{-t}{\tau_N}\right) \sum_k A_{kk} P_k(\cos\theta) \quad (1.38)$$

Which decays exponentially with lifetime  $\tau_N$  but the angular correlation is not perturbed. This situation is used to extract information on nuclear spin and multiplicities of transitions.

#### 1.2.4. Perturbed Angular Correlation Function:

If the nucleus in its intermediate excited level interacts with extranuclear perturbing fields, then the intermediate level undergoes splitting as shown in Fig. 1.13:

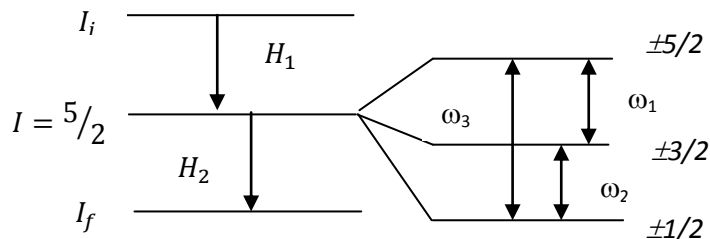


**Figure 1.13:** Splitting of Intermediate level with  $I = 5/2$  in presence of external field.

The possibility of extranuclear perturbations was already mentioned by Hamilton in his pioneer paper [94]. The first detailed study was performed by Goertzel [95] who investigated the hyperfine structure interaction and externally applied magnetic field. The theory was extended by Alder [109] who presented expressions that could be applied to the actual experimental situation. A thorough investigation of magnetic dipole and magnetic quadrupole interaction including time dependant effects has been performed by Abraham and Pound [110]. The non-axial EFG has been demonstrated by Matthias et al. [125]. The angular correlation of a cascade  $I_i \rightarrow I \rightarrow I_f$  will, in general, be altered as soon as the nuclei in their intermediate level  $I$  are subject to torque, due to the interaction of either the magnetic dipole moment  $\mu$  with an extranuclear magnetic field  $B$ , or of the electric quadrupole moment  $Q$  with electric field gradient  $\partial^2 V / \partial x^2$ . In semiclassical picture, these interactions produce a precession of the nuclei around the symmetry axis. The changing nuclear orientation results in an altered angular correlation. According to quantum mechanics, if the quantization axis was chosen to coincide with the direction of the first radiation, the interactions cause transitions among the  $m$ -states. The second radiation is emitted from a level with an altered population distribution and this change is responsible for attenuation of the correlation. The semiclassical picture of precessing nucleus satisfactorily describes the effect of perturbation if the extranuclear field is static. However, the extra nuclear fields might be time-dependent in nature. In time dependent fields e.g viscous liquids, the fluctuating electric

field gradient at the site of the nucleus induce transitions among the  $m$ -states. One major difference between the static and dynamic can be perceived by the following description. Considering a static interaction in an axially symmetric *single crystal*, the populations of the  $m$ -states quantized along the symmetry axis remain constant and hence, the correlation is unperturbed if the symmetry axis points towards the direction of one counter (i.e., coincides with the direction of emission of one radiation). If it points towards any other direction, then populations of the  $m$ -states quantized along the direction of emission change with time and this change causes an attenuation of the angular correlation. In a *polycrystalline* source, this description applies to each microcrystal and eventually for each nucleus. The angular correlation in a polycrystalline sample is never completely attenuated because a certain fraction of nuclei experience the static field in such a direction that their correlation is unperturbed or only slightly attenuated. Static interactions in polycrystalline samples thus never reduce the correlation below the ‘*hard-core*’ value. Time-dependant interactions, can however wipe out the correlation completely as the direction of the field at each nucleus changes continuously in a random fashion. The magnitude of the static perturbations is described by the precessional frequency ( $\omega$ ). In case of magnetic interaction,  $\omega$  is equal to the Larmor frequency  $\omega_B$  which is again proportional to  $\mu$  and  $H$ . In case of electric quadrupole interaction, Quadrupole frequency  $\omega_Q$  is proportional to  $Q$  and  $\delta^2 V / \delta z^2$ . Time-dependant perturbations can be described by an inverse time constant  $\lambda$ : the  $m$ -states approach a uniform population exponentially and  $\lambda$  represents the corresponding *relaxation constant*. According to the theory of directional correlation, the angular correlation equation is given by:

$$W(k_1, k_2) =$$

$$\sum_{m_i m_a m_b m'_a m'_b m_f} \langle m_f | H_2 | m_b \rangle \langle m_a | H_1 | m_i \rangle \delta_{m_a m_b} \langle m_f | H_2 | m'_b \rangle^* \langle m'_a | H_1 | m_i \rangle^* \delta_{m'_a m'_b} \quad (1.39)$$

Where  $H_1$  and  $H_2$  represent the interaction between nucleus and radiation field only. In absence of any external perturbation, the final states  $\langle m_a |$  and  $\langle m'_a |$ , after emission of first radiation, are identical with the initial states  $\langle m_b |$  and  $\langle m'_b |$  of the second radiation. Now, we consider an interaction of the nucleus in its intermediate state  $I$  with some extranuclear fields. This interaction, which we describe by the Hamiltonian  $\mathbf{K}$ , is assumed to act from the time the first radiation is emitted ( $t=0$ ) until the time  $t$  at which the second radiation is emitted. During this time interval the states  $\langle m_a |$  changes to different states  $\langle m_b |$  under the influence of the extranuclear perturbation. This change can be represented by unitary operator  $\Lambda(t)$  that describes the evolution of the state vectors  $\langle m_b |$  and the perturbed angular correlation can be expressed as,

$$W(k_1, k_2, t) = \sum_{m_i m_a m'_a m_f} \langle m_f | H_2 \Lambda(t) | m_a \rangle \langle m_a | H_1 | m_i \rangle \langle m_f | H_2 \Lambda(t) | m'_a \rangle^* \langle m'_a | H_1 | m_i \rangle^* \quad (1.40)$$

The states  $|m\rangle$  form a complete set and the state vector  $\Lambda(t)|m_a\rangle$  can be expressed as:

$$\Lambda(t)|m_a\rangle = \sum_{m_b} |m_b\rangle \langle m_b | \Lambda(t) | m_a \rangle \quad (1.41)$$

And similar for  $\Lambda(t)|m'_a\rangle$ . The expansion coefficients are the matrix elements of the time evolution operator  $\Lambda(t)$  in the  $m$ -representation.  $\Lambda(t)$  Operator satisfies the Schrodinger equation,

$$\frac{\partial}{\partial t} \Lambda(t) = -\frac{i}{\hbar} \hat{K} \Lambda(t) \quad (1.42)$$

If  $K$  does not depend on the time  $t$  (static interaction), the solution of this equation is:

$$\Lambda(t) = \exp(-i\hat{K}t/\hbar) \quad (1.43)$$

For time-dependant interaction, the solution of eqn. (1.42) can be given symbolically as:

$$\Lambda(t) = \exp\left(-\frac{i}{\hbar} \int_0^t \hat{K}(t') dt'\right) \quad (1.44)$$

where the integral must be evaluated according to Feynman's rules for ordered operators [126].

The perturbed angular correlation can now be written as:

$$\begin{aligned}
& W(k_1, k_2, t) \\
&= \sum_{m_i m_a m_b m'_a m'_b m_f} \langle m_f | H_2 | m_b \rangle \langle m_b | \Lambda(t) | m_a \rangle \langle m_a | H_1 | m_i \rangle \langle m_f | H_2 | m'_b \rangle^* \langle m'_b | \Lambda(t) | m'_a \rangle^* \langle m'_a | H_1 | m_i \rangle^*
\end{aligned} \tag{1.45}$$

In terms of density matrix operator  $\varrho(\mathbf{k})$ , we have the following relationships:

$$\langle m | \varrho(k_1) | m' \rangle = \sum_{m_i} \langle m | H_1 | m_i \rangle \langle m' | H_1 | m_i \rangle^* \tag{1.46}$$

$$\langle m' | \varrho(k_2) | m \rangle = \sum_{m_f} \langle m_f | H_2 | m \rangle \langle m_f | H_2 | m' \rangle^* \tag{1.47}$$

The matrix element  $\langle m_a m'_a | G(t) | m_b m'_b \rangle$  describing the influence of an extranuclear perturbation on angular correlation is given by:

$$\langle m_a m'_a | G(t) | m_b m'_b \rangle = \langle m_b | \Lambda(t) | m_a \rangle \langle m'_b | \Lambda(t) | m'_a \rangle^* \tag{1.48}$$

Now the correlation function can be written as:

$$W(k_1, k_2, t) = \sum_{m_a m_b m'_a m'_b} \langle m_a | \varrho(k_1) | m'_a \rangle \langle m'_b | \varrho(k_2) | m_b \rangle \langle m_a m'_a | G(t) | m_b m'_b \rangle \tag{1.49}$$

The above expression for the correlation function can be simplified as:

$$\begin{aligned}
W(k_1, k_2, t) = \sum_{k_1 k_2 N_1 N_2} A_{k_1}(1) A_{k_2}(2) G_{k_1 k_2}^{N_1 N_2}(t) \frac{1}{\sqrt{(2k_1+1)(2k_2+1)}} Y_{k_1}^{N_1^*}(\theta_1, \phi_1) Y_{k_2}^{N_2}(\theta_2, \phi_2)
\end{aligned} \tag{1.50}$$

With the perturbation function:

$$\begin{aligned}
G_{k_1 k_2}^{N_1 N_2}(t) = \sum_{m_a m_b} (-1)^{2I+m_a+m_b} \sqrt{(2k_1+1)(2k_2+1)} \langle m_b | \Lambda(t) | m_a \rangle \langle m'_b | \Lambda(t) | m'_a \rangle^* \\
\cdot \begin{pmatrix} I & I & k_1 \\ m'_a & -m_a & N_1 \end{pmatrix} \begin{pmatrix} I & I & k_2 \\ m'_b & -m_b & N_2 \end{pmatrix} \tag{1.51}
\end{aligned}$$

The above expression for angular correlation represents the *time-differential* perturbed angular correlation, i.e., the correlation is measured if the second radiation is observed within the time  $t$  and  $t+dt$  after the emission of the first radiation.

In actual experiment, the probability with which second radiation is registered at a time  $t$  after the emission of the first radiation is given by  $f(t - T)$  where  $T$  is the delay given in that channel of the coincidence analyzer that accepts the first radiation. The measured delayed correlation function is given by the weighted average:

$$\overline{W(k_1, k_2, T)} = \frac{\int_0^\infty f(t-T)e^{-t/\tau}W(k_1, k_2, t)dt}{\int_0^\infty f(t-T)e^{-t/\tau}dt} \quad (1.52)$$

In most of the cases, the time response function of the coincidence system is approximated by a step function:

$$f(t - T) = \begin{cases} 1 & \text{for } T - \tau_0 \leq t \leq T + \tau_0 \\ 0 & \text{for } T + \tau_0 < t < T - \tau_0 \end{cases}$$

Where  $\tau_0$  is the resolving time of the coincidence system. With this approximation, the observed angular correlation function is given by

$$\overline{W(k_1, k_2, T, \tau_0)} = \frac{\int_{T-\tau_0}^{T+\tau_0} e^{-t/\tau}W(k_1, k_2, t)dt}{\int_{T-\tau_0}^{T+\tau_0} e^{-t/\tau}dt} \quad (1.53)$$

The total time-integrated correlation

$$W(k_1, k_2, \infty) = \frac{1}{\tau} \int_0^\infty e^{-t/\tau}W(k_1, k_2, t)dt \quad (1.54)$$

is observed if the resolving time  $\tau_0$  of the coincidence system is much larger than the lifetime of the intermediate level ( $\tau$ ):  $\tau_0 \gg \tau$ .

Since only the perturbation factors  $G_{k_1 k_2}^{N_1 N_2}(t)$  depend on the time  $t$ , the time-integrated perturbation coefficients can be defined in a similar way:

$$\overline{G_{k_1 k_2}^{N_1 N_2}(T)} = \frac{\int_0^\infty f(t-T) e^{-t/\tau} G_{k_1 k_2}^{N_1 N_2}(t) dt}{\int_0^\infty f(t-T) e^{-t/\tau} dt} \quad (1.55)$$

$$\overline{G_{k_1 k_2}^{N_1 N_2}(\infty)} = \frac{1}{\tau} \int_0^\infty e^{-t/\tau} G_{k_1 k_2}^{N_1 N_2}(t) dt \quad (1.56)$$

Now, suppose the evolution operator  $\Lambda(t)$  is diagonal and expressed in terms of the eigen values  $E_m$  of the perturbing Hamiltonian:

$$\langle m_b | \Lambda(t) | m_a \rangle = \exp\left(\frac{-i}{\hbar} E_m t\right) \delta_{m m_a} \delta_{m m_b} \quad (1.57)$$

Then the perturbation function gets simplified to:

$$G_{k_1 k_2}^{NN}(t) = \sum_m (-1)^{2I+m_a+m_b} \sqrt{(2k_1+1)(2k_2+1)} \begin{pmatrix} I & I & k_1 \\ m' & -m & N \end{pmatrix} \begin{pmatrix} I & I & k_2 \\ m' & -m & N \end{pmatrix} \exp\left[-\left(\frac{i}{\hbar}\right)(E_m - E_{m'})t\right] \quad (1.58)$$

This is to be noted that here  $N_1 = N_2 = N$ . This diagonal situation is attained in case of magnetic dipole interaction and axially symmetric electric quadrupole interaction. If the axially symmetric field is parallel to the propagation direction of one of the two radiations, then the angular correlation is not influenced by such a field. It can be understood semiclassically. If we choose  $\mathbf{k}_I$  as quantization axis and the axially symmetric field is parallel to  $\mathbf{k}_I$ , then the influence of this field can be interpreted as a precession of spin  $I$  of the intermediate nuclear level about  $\mathbf{k}_I$ . The projections of  $I$  on  $\mathbf{k}_I$  do not change and the population of  $m$ -states with respect to  $\mathbf{k}_I$  remains the same. Thus the angular distribution for the second radiation with respect to  $\mathbf{k}_I$  is not disturbed. For non-axially symmetric quadrupole interactions, we need a unitary matrix  $U$  which diagonalizes the interaction Hamiltonian  $K$ :

$$U^{-1}KU = E \quad (1.59)$$

Where  $E$  is the diagonal energy matrix with the diagonal elements  $E_n$  (energy eigen values). With the expansion of the exponential function, it can be shown that the following relation holds:

$$Ue^{-(i/\hbar)Kt}U^{-1} = e^{-(i/\hbar)Et} \quad (1.60)$$

Equation (1.43) can now be rewritten as:

$$\Lambda(t) = Ue^{-(i/\hbar)Et}U^{-1} \quad (1.61)$$

The matrix elements of  $\Lambda(t)$  in the  $m$ -representation are therefore

$$\langle m_b | \Lambda(t) | m_a \rangle = \sum_n \langle n | m_b \rangle^* e^{-(i/\hbar)E_n t} \langle n | m_a \rangle \quad (1.62)$$

Where the  $\langle m | n \rangle$  are the matrix elements of the unitary matrix  $U$  that is obtained from the solution of the eigen value equation (1.59). The perturbation factor is then

$$G_{k_1 k_2}^{N_1 N_2}(t) = \sum_{m_a m_b n n'} (-1)^{2I+m_a+m_b} \sqrt{(2k_1+1)(2k_2+1)} \begin{pmatrix} I & I & k_1 \\ m'_a & -m_a & N_1 \end{pmatrix} \begin{pmatrix} I & I & k_2 \\ m'_b & -m_b & N_2 \end{pmatrix} \cdot \langle n | m_b \rangle^* \langle n | m_a \rangle \langle n' | m'_b \rangle \langle n' | m'_a \rangle^* \exp \left[ -\left( \frac{i}{\hbar} \right) (E_n - E_{n'}) t \right] \quad (1.63)$$

The sum over  $n, n'$  describes the mixing of the sublevels due to the broken axial symmetry. Now, the perturbation function can be further simplified by confining our discussion into the randomly oriented samples (molecules, microcrystals, powders), i.e., we average over the Euler angles describing the quantization axis in each microcrystal with respect to the laboratory coordinate system in which  $\mathbf{k}_1$  and  $\mathbf{k}_2$  (directions of emission of the two successive radiations) are defined. This leads to the condition  $k_1 = k_2 = k$  and  $N_1 = N_2 = N$  (even for non-axial symmetry). The

“powder” perturbation function is defined as a sum over certain “single crystal” perturbation functions:

$$G_{kk}(t) = \frac{1}{2k+1} \sum_{N=-k}^k G_{kk}^{NN}(t) \quad (1.64)$$

Since,  $G_{kk}(t)$  is independent of  $N_1$  and  $N_2$ , the addition theorem of spherical harmonics can be applied to eqn. (1.50) and the “powder” angular correlation is obtained in the form:

$$W(\theta, t) = \sum_k A_k(1)A_k(2)G_{kk}(t)P_k(\cos \theta) \quad (1.65)$$

The effect of the randomly oriented perturbation does not change the form of the angular correlation function. It only leads to an attenuation of the  $P_k(\cos \theta)$ . The perturbation factors  $G_{kk}(t)$  for those sources which as a whole do not show any preferential direction are therefore called the *attenuation factors*.

For axial symmetry, the perturbation function in (1.64) can be rewritten as:

$$G_{kk}(t) = \frac{1}{2k+1} + \sum_{n \neq n'} \begin{pmatrix} I & I & k \\ n' & -n & N \end{pmatrix}^2 \cos \left[ \frac{(E_n - E_{n'})t}{\hbar} \right] \quad (1.66)$$

The total time integrated attenuation factor is:

$$\overline{G_k(\infty)} = \frac{1}{2k+1} + \sum_{n \neq n'} \begin{pmatrix} I & I & k \\ n' & -n & N \end{pmatrix}^2 \frac{1}{1 + \left[ \frac{(E_n - E_{n'})\tau}{\hbar} \right]^2} \quad (1.67)$$

It is indeed an interesting and important feature of the time integrated attenuation factors for a randomly oriented static interaction is that they have a finite lower limit or “hardcore” value that is independent of interaction. Thus the time-integrated angular correlation is never wiped out completely as long as the interaction is static and random irrespective of the strength of the interacting fields in the microcrystals. For axially symmetric fields, the “hardcore” values are easily obtained from eqn. (1.67):

$$\overline{G_k(\infty)}_{lim} = \frac{1}{2k+1} \quad (1.68)$$

### 1.2.5. Static Magnetic and Electric Fields:

The lowest order magnetic interaction is the magnetic dipole interaction. The interaction takes place between the magnetic dipole moment of the probe nuclei and an extranuclear magnetic field. The dipole moment depends proportionally to the total angular momentum of the nucleus and is conventionally expressed as a dimensionless g-factor. The magnetic field may be either external or internal in the case of ferromagnetic- and anti-ferromagnetic materials. Semiclassically, a magnetic field exerts a torque on any nucleus with a nonzero magnetic dipole moment, resulting in a precession of the moment about the field. The frequency of precession is termed as the Larmor frequency  $\omega_L$ .

For a magnetic field  $\mathbf{B}$  in the direction of the positive z-axis, the Hamiltonian describing the interaction of a nuclear magnetic dipole moment  $\mu$  with the fixed magnetic field  $\mathbf{B}$  is given by:

$$K_B = -\bar{\mu} \cdot \bar{B} = -\mu_z B \quad (1.69)$$

where  $\mu = \gamma \mathbf{I}$  is the magnetic dipole moment operator. Since  $\mu_z = \gamma I_z$ , the interaction matrix is diagonal and the matrix elements are given as

$$E_m = \langle \text{Im} | K_B | \text{Im} \rangle = -B \mu_N m / I \quad (1.70)$$

The Larmor frequency  $\omega_L$  is defined as

$$\omega_L = \frac{E_{m+1} - E_m}{\hbar} = \frac{B \mu_N}{\hbar I} = -g \mu_N B / \hbar \quad (1.71)$$

where  $g$  is the g-factor of the intermediate state and  $\mu_N$  is the nuclear magneton. By substituting the value of  $\omega_L$  in the energy eigen value expression we get

$$E_m = \hbar \omega_L m \quad (1.72)$$

Quantum mechanically, the magnetic interaction results in a complete lifting of the degeneracy

in the intermediate nuclear spin state of the probe nucleus. The energy difference between successive m-states is  $\hbar\omega_L$  and transitions with frequencies that are integer multiple of  $\omega_L$  take place among different m-states. The perturbation can now be written in the form:

$$G_{k_1 k_2}^{NN}(t) = \sqrt{(2k_1 + 1)(2k_2 + 1)} \exp(-iN\omega_L t) \sum_m \begin{pmatrix} I & I & k_1 \\ m' & -m & N \end{pmatrix} \begin{pmatrix} I & I & k_2 \\ m' & -m & N \end{pmatrix}$$

Or, after using the orthogonality rule for 3j-symbols,

$$G_{k_1 k_2}^{NN}(t) = \exp(-iN\omega_L t) \delta_{k_1, k_2} \quad (1.73)$$

The powder perturbation functions are obtained from eqn. (1.64):

$$G_{22}(t) = \frac{1}{5} (1 + 2 \cos \omega_L t + 2 \cos 2\omega_L t) \quad (1.74)$$

The higher order perturbation functions are all constructed in the same way.

The interaction Hamiltonian of a fixed electric field gradient (EFG) with the electric quadrupole moment of a nuclear state is given by [127]:

$$K_Q = \frac{4}{5} \pi \sum_q (-1)^q T_q^{(2)} V_{-q}^{(2)} \quad (1.75)$$

Where  $T^{(2)}$  is the second rank tensor operator of the nuclear quadrupole moment with the components

$$T_q^{(2)} = \sum_p e_p r_p^2 Y_2^q(\theta_p, \varphi_p) \quad (1.76)$$

And where  $e_p$  are the (point) charges in the nucleus at the points  $(r_p, \theta_p, \varphi_p)$ .  $V^{(2)}$  is the tensor operator of the classical external field gradient. If the electrostatic field is produced by point charges  $e_c$  (ions in a crystal lattice) at positions  $(r_c, \theta_c, \varphi_c)$  with respect to the nuclear center, the spherical components of the field tensor  $V^{(2)}$  are given by:

$$V_q^{(2)} = \sum_c \frac{e_c}{r_c^3} Y_2^q(\theta_c, \varphi_c) \quad (1.77)$$

Now choosing a coordinate system  $xyz$  (principal axes system) in such a way that the mixed derivatives of the potential  $V$  disappear, we get:

$$V_0^{(2)} = \frac{1}{4} \sqrt{\frac{5}{\pi}} V_{zz},$$

$$V_{\pm 1}^{(2)} = 0, \quad (1.78)$$

$$V_{\pm 2}^{(2)} = \frac{1}{4} \sqrt{\frac{5}{6\pi}} (V_{xx} - V_{yy}) = \frac{1}{4} \sqrt{\frac{5}{6\pi}} \eta V_{zz}$$

Where  $\eta$  is the asymmetry parameter as defined by the eqn. (1.24). The EFG tensor is then determined by two parameters  $V_{zz}$  and  $\eta$ .

In case of axially symmetric field with respect to  $z$ -axis where  $\eta=0$ , the EFG tensor is given by  $V_{zz}$ . The interaction Hamiltonian then becomes:

$$K_Q = \sqrt{\frac{1}{5}} \pi T_0^{(2)} V_{zz} \quad (1.79)$$

The quadrupole interaction matrix elements are obtained by the application of Wigner-Eckart theorem as:

$$\langle Im | K_Q | Im \rangle = E_m = \frac{3m^2 - I(I+1)}{4I(2I-1)} eQV_{zz} \quad (1.80)$$

Here we introduce another parameter Quadrupole Frequency ( $\omega_Q$ ) defined by the following:

$$\omega_Q = \frac{eQV_{zz}}{4I(2I-1)\hbar} \quad (1.81)$$

The matrix elements for the interaction Hamiltonian in eqn. (1.80) then become:

$$\langle Im | K_Q | Im \rangle = E_m = \{3m^2 - I(I+1)\} \hbar \omega_Q \quad (1.82)$$

The angular frequency  $\omega_0$  equivalent to the smallest non-vanishing energy difference is:

$$\omega_0 = \begin{cases} 3\omega_Q & \text{for even } I \\ 6\omega_Q & \text{for odd } I \end{cases} \quad (1.83)$$

The energy splitting due to the static quadrupole interaction is not uniform and the states are twofold degenerate (+m and -m give the same energy). The influence of a quadrupole interaction on an angular correlation can no longer be described semiclassically by a simple precession of the correlation pattern.

The perturbation factor for the static quadrupole interaction is given as:

$$G_{k_1 k_2}^{NN}(t) = \sqrt{(2k_1 + 1)(2k_2 + 1)} \sum_{mm'} \begin{pmatrix} I & I & k_1 \\ m' & -m & N \end{pmatrix} \begin{pmatrix} I & I & k_2 \\ m' & -m & N \end{pmatrix} \exp[-3i(m^2 - m'^2)\omega_Q t] \quad (1.84)$$

The above perturbation factor can also be written as 128:

$$G_{k_1 k_2}^{NN}(t) = \sum_n S_{nN}^{k_1 k_2} \cos(n\omega_0 t) \quad (1.85)$$

Where the summation index  $n$  can assume all positive integers values (including zero)  $|m^2 - m'^2|$  for integer  $I$  and  $2|m^2 - m'^2|$  for half-integer  $I$ . The coefficients  $S_{nN}^{k_1 k_2}$  are given by:

$$S_{nN}^{k_1 k_2} = \sum'_{mm'} \begin{pmatrix} I & I & k_1 \\ m' & -m & N \end{pmatrix} \begin{pmatrix} I & I & k_2 \\ m' & -m & N \end{pmatrix} \sqrt{(2k_1 + 1)(2k_2 + 1)} \quad (1.86)$$

Where prime on the summation sign signifies that the summation over  $m$  and  $m'$  should only include those terms where  $m$  and  $m'$  satisfy the condition  $|m^2 - m'^2| = n$  for integer  $I$  and  $2|m^2 - m'^2| = n$  for half-integer  $I$ . Numerical values of the  $S_{nN}^{k_1 k_2}$  coefficients are tabulated in ref. [128]. With these, the directional correlation perturbed by an axially symmetric electrostatic gradient in an arbitrary direction can be calculated from eqn. (1.85) and (1.86).

The influence of an axially symmetric quadrupole interaction in a polycrystalline powder source is represented by the attenuation coefficient:

$$G_{kk}(t) = \sum_{mm'} \begin{pmatrix} I & I & k \\ m' & -m & p \end{pmatrix}^2 \exp[-3i(m^2 - m'^2)\omega_Q t] \quad (1.87)$$

This expression can also be written in the following form:

$$G_{kk}(t) = \sum_n S_{kn} \cos(n\omega_0 t) \quad (1.88)$$

With

$$S_{kn} = \sum_{m,m'} \left( \begin{matrix} I & I & k \\ m' & -m & -m' + m \end{matrix} \right)^2 \quad (1.89)$$

$S_{kn}$  are the geometric coefficients (square of Clebsch-Gordon coefficients) where again  $|m^2 - m'^2| = n$  for integer  $I$  and  $2|m^2 - m'^2| = n$  for half-integer  $I$  respectively.

Now the theoretical shape of the perturbation function defined by the eqn. (1.88) is greatly affected due to instrumentation, asymmetry of EFG and quality of the sample along with the population mode of the  $\gamma$ - $\gamma$  cascade. First, because of the intrinsic time resolution of the coincidence circuit, an event which is recorded at time  $t$  might actually have occurred at some time prior to or after  $t$ . The perturbation measured at time  $t$  is given by:

$$G_k(t) = \frac{\int G_k(t') P(t' - t) dt}{\int P(t' - t) dt}$$

Where  $P(t')$  is the prompt resolution curve. With the approximation that the resolution function is a Gaussian distribution function of width  $\tau_r$ , a correction factor  $\exp\left(-\frac{1}{2}\omega_n^2\tau_r^2\right)$  [129] is introduced into the expression of  $G_k(t)$ . The multiplication with this correction factor attenuates the amplitude of oscillations and shifts the zero time from its true value. The second effect arises from a situation where the EFG has no axial symmetry or the asymmetry ( $\eta$ ) of EFG. The eigen values of the  $m$  states are approximated by power series of  $\eta$  [130] and the transition frequencies become  $\eta$ -dependant with the loss of harmonic nature of quadrupole frequency (with exception for  $\eta=1$ ). However, the necessary condition  $\omega_1 + \omega_2 = \omega_3$  is still valid.

The effect of asymmetry in EFG is the progressive loss of periodicity and distortion of the perturbation function as shown in Fig. 1.14.

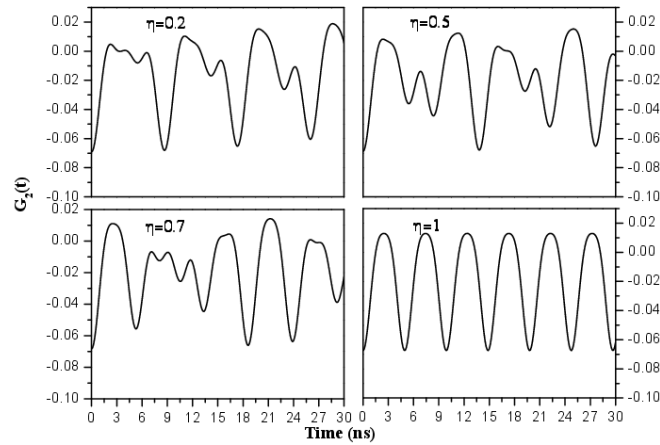


**Figure 1.14:** Effect of  $\eta$  on perturbation function for  $I=5/2$  state.

The sensitivity of the perturbation function with asymmetry of EFG is clearly visible from Fig. 1.14. The third effect originates from the inhomogeneity of a polycrystalline solid, defects present in that sample and after-effects of the radioactive decay feeding the  $\gamma$ - $\gamma$  cascade.

So far we assumed that the electric field gradients acting on the nuclear quadrupole moments are same at every nuclear site. But in reality there is slight variation of crystalline fields due to lattice imperfections and impurity centres. The defects are introduced during the preparation and labelling of the sample. The radiation damage due to neutron-irradiation of the sample also introduces defects in the matrix. In many cases the radioactive decay process transforms the atom in a lattice into an impurity centre. In addition, the recoil momentum imparted to an atom by a nuclear decay process may displace the atom from its regular lattice position to some less well defined point. This effect may result in situations where the crystalline fields experienced by the nucleus in its intermediate state vary considerably from nucleus to nucleus. This influence of such field variation on angular correlation has been calculated by Matthias et al.[125]. The experimental curve cannot be fitted with a single set of three frequencies but rather with a distribution of frequencies. A narrow Lorentzian frequency distribution is generally assumed for a unique type of defect at close distance from the nucleus. More often many defects contribute to the EFG and the distribution is better described by a broad Gaussian distribution:

$$P(\omega - \bar{\omega}_n)d\omega = \frac{1}{\sigma\sqrt{2\pi}} \exp\left\{-\frac{(\omega - \bar{\omega}_n)^2}{2\sigma^2}\right\} d\omega$$

Where  $\bar{\omega}_n$  is the centroid of the distribution for each of the n-values. The relative width of the distribution is described by the parameter  $\delta = \frac{\sigma}{\bar{\omega}_n}$ . The averaged perturbation factor is obtained from the integration over all frequencies:

$$\begin{aligned} \overline{G_k(t)} &= \frac{\int G_k(t)P(\omega - \bar{\omega}_n)d\omega}{\int P(\omega - \bar{\omega}_n)d\omega} = \\ &= S_{k0} + \sum_{n=1}^3 S_{kn} \exp\left\{-\frac{1}{2}(\delta_n \bar{\omega}_n t)^2\right\} \cos \bar{\omega}_n t \end{aligned} \quad (1.90)$$

In practice, it is assumed that  $\delta_1 = \delta_2 = \delta_3$  and  $\delta_n$  is replaced by a single  $\delta$ -value. After incorporating all the effects into the expression of perturbation function, we get the final form of perturbation function as follows:

$$G_k(t) = S_{k0} + \sum_{n=1}^3 S_{kn} \exp\left\{-\frac{1}{2}(\delta \omega_n t)^2\right\} \times \exp\left(-\frac{1}{2} \omega_n^2 \tau_r^2\right) \cos(\omega_n t) \quad (1.91)$$

Considering the Lorentzian distribution of quadrupole frequency, the above expression is modified and expressed as follows:

$$G_k(t) = S_{k0} + \sum_{n=1}^3 S_{kn} \exp(-\delta \omega_n t) \times \exp\left(-\frac{1}{2} \omega_n^2 \tau_r^2\right) \cos(\omega_n t) \quad (1.92)$$

The shape of the perturbation function gets modified with the resolution time  $\tau_r$ , the frequency distribution  $\delta$  and quadrupole frequency  $\omega_Q$ . The effect of the frequency distribution is significant on the shape of the perturbation function and it becomes even more prominent at higher values of quadrupole frequency.

For a static quadrupole perturbation and a polycrystalline sample, the total time-integrated attenuation coefficients are expressed as follows:

$$\overline{G_k(\infty)} = \frac{1}{\tau} \int_0^{\infty} e^{-t/\tau} \sum_n S_{kn} \cos \omega_n t dt = S_{k0} + \sum_{n=1}^3 \frac{S_{kn}}{1+(\omega_n \tau)^2} \quad (1.93)$$

In the above expression, the first term  $S_{k0}$  is called the “hard core” which is independent of the frequency distribution and varies only with the asymmetry of EFG to a little extent. It implies that the angular correlation can never be attenuated below a limiting value for a polycrystalline sample. Physically it can be perceived in the way that for an ensemble of nuclei, a fraction of nuclei are so oriented that they feel no or negligible perturbation at any time.

Till now either a magnetic dipole or an electric quadrupole interaction on an angular correlation was considered. In this section the combined influence of magnetic and electric interaction will be considered. The Hamiltonian for combined magnetic and electric interaction is represented by the following relation:

$$K_{tot} = K_B + K_Q \quad (1.94)$$

In the above equation, it has been assumed that the external magnetic field  $B$  does not influence the electric crystalline field. The matrix elements (in the z-axis system) of the total interaction Hamiltonian describing the combined magnetic and electric interaction can be written in the form:

$$\langle m|K_{tot}|m'\rangle = \langle m|K_B|m'\rangle + \langle m|K_Q|m'\rangle \quad (1.95)$$

Here the axially symmetric electric field gradient is at an angle  $\beta$  with respect to the z-axis and  $\mathbf{B}$  coincides with the z-axis. Here the attenuation coefficient is a function of  $\tau$ ,  $y$  and  $\beta$ , where  $y = \omega_B/\omega_Q$  is the ratio of the magnetic to the electric interaction frequency. The general theory of combined magnetic and electric interactions and numerical results for the perturbation coefficients have been presented by Adler et al. [128]. The influence of a combined magnetic and nonaxial quadrupole interaction in powder sources on angular correlations has been considered by Matthias et al. [131].

### 1.2.6. Time-Dependent Perturbations:

Due to jump diffusion of vacancies in the solids, the tumbling motion of a molecule in a liquid and atomic collision in the gas phase, the magnetic field or electric field gradient arising due to the movement of electric charges, electric or magnetic moments of ions change in a random fashion. Instantaneously, however, a certain local configuration which is similar to the stationary local configuration in solid [132], can be described by an average value of the local field acting in certain direction  $Z'$ . Due to random collision there is a continual reorientation of  $Z'$  with respect to external co-ordinates. If many such uncorrected directions of  $Z'$  occur within the lifetime ' $\tau$ ' of the intermediate level of the nucleus in the radiation cascade, there will not be any preferred direction for the nucleus as far as the angular correlation is concerned. However, if the direction of the first radiation is taken as the quantization axis, there will be smearing or damping of the angular correlation of static case. This will depend on the correlation time  $\tau$  the time for which the system retains its identity. There are two limiting models for the random reorientation of the magnetic field or the EFG at the nucleus. These are:

1. Diffusion Model
2. Strong Collision Model

The diffusion model assumes that the reorientation of the molecular axis follows a diffusion equation. In this case, the reorientation takes place through many small angular steps and there exists a strong correlation between the orientation of molecular axis before and after the collision. In the case of strong collision model it is assumed that there is no correlation between the initial and final orientation and all orientation are equally probable. This is also called random phase approximation (RPA).

In case of liquid the reorientation depends on the molecular size and the mass of the probe system compared to that of the solvent. In gas phase this depends on the collision frequency which depends on pressure and temperature. In solids there is jump diffusion of vacancies that lead to reorientation of the field axis through large angles. The perturbation of the angular correlation depends on the relative magnitude of three characteristic times i) correlation time  $\tau_c$ , ii) inverse of interaction frequency  $\langle\omega^2\rangle^{-1/2}$  and iii) time of observation 't' in the differential and  $\tau$ (lifetime of the intermediate level) in the time integral PAC experiment.

### **STOCHASTIC THEORY:**

Stochastic theory is used for the calculation of attenuation factor. Blume's theory [133], in which the perturbing field is assumed to jump between two possible stochastic states, is used to calculate the attenuation factor in solids. On the other hand, in the limit of RPA, Scherrer-Blume model [134-135] is used to calculate the attenuation factor for any  $\tau_c$  and it applies to the isotropic hyperfine interaction (magnetic) for free atom in a gas. The atomic angular momentum (J) is assumed to be randomly oriented after each collision with the neighbouring gas atoms. For liquids and gases, a large number of stochastic states are assumed. If one assumes the diffusion model to be valid for reorientation, the perturbation factor can be calculated for fast ( $\langle\omega^2\rangle^{-1/2}\tau_c \ll 1$ ) and slow ( $\langle\omega^2\rangle^{-1/2}\tau_c \gg 1$ ) relaxation processes using perturbation theory.

### **ABRAGAM AND POUND MODEL (FAST RELAXATION):**

For many years, this model [110] remains as the most widely used first order treatment of the perturbation of the angular correlation by random time-dependent interaction for  $\tau_c \ll \tau$  and  $\tau_c \ll \tau_N$  for time-differential and time-integral measurements respectively. Solving the eqn.

(1.51) for the evolution operator with time-dependent Hamiltonian and using Gaussian correlation function, time-differential perturbation factor is obtained as:

$$G_k(t) = \exp(-\lambda_k t) \quad (1.96)$$

Thus the time-dependent process is described as the relaxation process with a constant:

$$\lambda_k = \frac{3}{5} \langle \omega_Q^2 \rangle \tau_c k(k+1) [4I(I+1) - k(k+1)] \quad (1.97)$$

Above expression for the relaxation constant is for randomly fluctuating classical axially symmetric EFG. For magnetic interaction, the expression becomes:

$$\lambda_k = \frac{1}{3} k(k+1) \langle \omega_L^2 \rangle \tau_c \quad (1.98)$$

The time-integrated perturbation coefficient is expressed as:

$$\overline{G_k(\infty)} = \frac{1}{\tau} \int_0^{\infty} e^{t/\tau} dt = \frac{1}{1+\lambda_k \tau} \quad (1.99)$$

For large values of  $\lambda_k \tau$  the attenuation coefficient for a time-dependent perturbation vanishes and observed angular correlation becomes isotropic.

Fast relaxation of EFG takes place in dilute aqueous solutions of radioactive ions. The relaxation constant  $\lambda_k$  is proportional to the correlation time  $\tau_c$  and is small in dilute aqueous solution,  $\tau_c \approx 10^{-11}$  sec. When  $\lambda_k \tau \ll 1$ , the attenuation of the angular correlation is small even for large quadrupole couplings. The undisturbed anisotropies are often observed for free ions in solution. The correlation time increases with the size of the species in solution and with the viscosity of the medium. When  $\tau_c$  is of the order of  $\tau$  or even longer, the relaxation process is better described as the result of the slow rotational diffusion of the ion or molecule to which the probe atom is bound. The tumbling of large molecule produces a more slowly relaxing field than that of small ions solution. The correlation time is approximated by the Debye expression and is given by:

$$\tau_c = \frac{4}{3} \pi a^3 \frac{\bar{\eta}}{kT} \chi \quad (1.100)$$

Where  $a$  is the radius of the molecule,  $\eta$  the viscosity of the solvent at temperature  $T$  and  $\chi$  is a coefficient between 0 and 1.

### **ADIABATIC APPROXIMATION:**

For a slow molecular motion in case of large tumbling molecules in a liquid or small molecule in a viscous medium, Marshall and Meares [136] developed a model in which the quadrupole Hamiltonian acting on the intermediate state has an adiabatic variation with time. So the interaction remains constant with respect to the local frame of reference represented by the molecular axis, however the orientation of this frame within the laboratory co-ordinates changes with the rotational motion of the molecule. The final expression for the perturbation factor is then given by:

$$G_k(t) = G_k(t)_{static} e^{-\lambda_k t} \quad (1.101)$$

where the first term of the product is the usual perturbation factor for a static random interaction.

For a spherically symmetric molecule, with a rotational diffusion coefficient  $D$ :

$$\tau_k = \frac{1}{\lambda_k} = \frac{1}{k(k+1)D} \quad (1.102)$$

The adiabatic approximation be valid for  $\tau_k \gg 10^{-7}$  sec. The Marshall-Meares model is only one of the theoretical approaches to the sensitivity of PAC to the molecular dynamics. Slow molecular reorientations by random jumps caused by strong collisions have been considered by Lynden-Bell [137]. The effect of molecular shape and flexibility on  $\gamma$ - $\gamma$  angular correlation has been studied by Marshall et al. [138] while Shirley [139] developed extensively the theory of PAC patterns static and rotating labelled macromolecules with different geometrical configurations. These developments have an important impact on the study of biomolecules. The

applications of PAC method to the study of metal-protein have been reviewed by Graf et al. [140].

### **DILLENBURG-MARIS THEORY:**

In the treatment of random statistical perturbation by Abragam and Pound theory, it was assumed that a significant change in the spin state of the intermediate level is brought about by many random interactions each of which has a very small effect and hence, the first order perturbation could be used to calculate each independent (small) interaction. However, a time-dependant perturbation can also be caused by a few violent interactions of short durations. This situation can still be described by statistical methods but the effect of a single violent interaction can no longer be estimated by using the square of a first order perturbation matrix element. Dillenburg and Maris constructed a theory [141] of time-dependant perturbation that makes only the assumption of a statistical interaction, random in space, and invariant under the time-reversal and parity-transformation. For small independent magnetic dipole or electric quadrupole perturbation, the results of Dillenburg-Maris theory are reduced to that of Abragam and Pound. This treatment is valid in physical situation where surrounding atoms collide randomly with the atoms containing the probe nuclei in such way that any one collision occurs during a time interval which is short if compared with a typical relaxation time and the lifetime of the intermediate level. For an intermediate state spin  $I=5/2$  or  $I=2$  in a parity-conserving cascade, the expressions for second and fourth order perturbation factors are given as:

$$\left. \begin{aligned} G_2(t) &= (1 - \alpha)e^{-\lambda_2 t} + \alpha e^{-\lambda_4 t} \\ G_4(t) &= \beta e^{-\lambda_2 t} + (1 - \beta)e^{-\lambda_4 t} \end{aligned} \right\} \quad (1.103)$$

$\alpha, \beta, \lambda_2, \lambda_4$  are the parameters that are to be determined experimentally. Experimental evidence that  $\alpha$  and  $\beta$  are different from zero would indicate the presence of a statistical perturbation that

that cannot be treated as a first-order coupling to random magnetic dipole or electric quadrupole fields.

### **1.2.7. Influence of Preceding Decays on Angular Correlations:**

The mode of radioactive decay by the parent atom to produce the daughter element is one of the important topics to be discussed in case of PAC study. Apart from Isomeric transition (IT) process, all other decay processes, viz., electron capture (EC), internal conversion (IC),  $\alpha$ - and  $\beta$ -decay; convert the parent atom into a different element. So, the effect of this preceding decay on the directional correlation of  $\gamma$ - $\gamma$  cascade is discussed in this section.

#### **EC AND IC:**

EC decay leads to K-capture or K-conversion by creating a hole in the K-shell. After the formation of the K-hole, the excited nucleus tends to reach their ground state by decaying through  $\gamma$ - $\gamma$  cascade while the excited atomic shell through the emission of Auger electron and X-rays. In case of free atom, the atom remains neutral immediately after the EC-decay. The emission of Auger electrons then makes the atom to become charged [142]. The average charge of an atom after K-capture is quite large. In practice, the probe atom is embedded in a solid or a liquid matrix. So the fate of the atomic shell after the K-capture depends strongly on the surrounding atomic environment. Here, three environments are considered, viz., a metal, an insulator and a liquid. In case of a metal, the atomic shell comes to its ground state after K-capture in a very short time ( $<10^{-12}$  sec). Hence the nucleus is not influenced by the field within its atomic shell and the directional correlation remains unperturbed if the atom is embedded in a lattice with zero EFG (cubic symmetry). The radioactive atom embedded in an insulator can act as an impurity center. In general, the impurity centers have long decay times in the outermost shell. The matrix element for the transition of the excited atomic shell to its ground state is small

and the lifetime is large. Thus the directional correlation with the probe embedded in an insulator should be attenuated. In a liquid, the effect should not differ to any significant extent from that in the corresponding solid. In a molten metal, the excited atomic shell relaxes very fast to its ground state and hence K-capture has no effect on the directional correlation. In a liquid insulator, the influence of the K-capture depends on the correlation time and the molecular interaction in the liquid. If the molecule containing the decaying nucleus rotates very fast in the liquid, the correlation will be unperturbed even if the atomic shell is not in the ground state due to the very small correlation time. However, if the correlation time can be increased so that  $\tau_c \gg \tau$ , the attenuation effect of K-capture in liquid can be perceived. Otherwise, it is hard to decide whether the K-capture exerts any influence or not.

### **$\beta^-$ - EMISSION:**

The escape of a  $\beta^-$ -particle from an atom takes place in a time scale that is short compared to the orbital period of the shell electrons. The abrupt change in the nuclear charge from  $Z$  to  $Z\pm 1$  introduces a perturbation into the electrostatic potential in which the shell electrons move. This sudden perturbation may result in the excitation and ionization of the electron shell. In case of  $\beta^-$  - emission it has been observed [143] that ~80% of the daughter atoms have a single positive charge after the loss of a  $\beta^-$  -particle. The remaining 20% of the atoms have a positive charge of two or more units indicating an additional shake-off of electrons from the shell. Thus the probability of the daughter atom to be in a highly ionized and excited state is much smaller for  $\beta^-$ -emission than for EC or IC. The recovery of the excited ionized or excited atoms follows the similar mechanism as that in case of EC.

## ALPHA DECAY:

In a typical  $\alpha$ -decay with decay energy of 5MeV and a mass number of 200, the emitted  $\alpha$ -particle imparts recoil energy of 100 keV to the daughter nucleus. This recoil effect has to be taken care of in case of  $\alpha$ - $\gamma$  correlation experiments.

### 1.2.8. Methodology and PAC Isotopes:

The methodology in PAC experiments implies the whether the method is time differential or time integral. This is decided by three characteristic times, viz., the resolving time of the coincidence setup, interaction time and the lifetime of the intermediate state of the probe nucleus. Since the interaction time is not known beforehand, the methodology is decided by the other two characteristic times. When the resolving time is shorter than the lifetime, one goes for time differential measurements. This reveals the details of the mechanism of interaction between the nucleus and the extranuclear surrounding. On the other hand, if the resolving time is large compared to the other characteristic times one has to go for time integral measurements in which only the gross or an average picture is obtained. The ultimate goal of a Time Differential PAC experiment is to extract the perturbation factor which contains all the information regarding the interaction of the probe atom with its surrounding. Experimentally the attenuation or perturbation factor is obtained by measuring the coincidence counts at least at two different angles, viz.,  $90^\circ$  and  $180^\circ$ . The perturbed angular correlation function, following the eqn. (1.65), can be rewritten as:

$$W(\theta, t) = \sum_{k=even} A_k G_k(t) P_k(\cos\theta)$$

In general, the term with  $k = 2$  is the most significant in the above summation series. Neglecting the higher order terms, the second order perturbation factor is expressed as:

$$A_2 G_2(t) = 2 \frac{W(180,t) - W(90,t)}{W(180,t) + 2W(90,t)} \quad (1.104)$$

As discussed earlier, theoretical shape of the perturbation function gets affected by three different factors, viz., resolving time of the coincidence setup, asymmetry of EFG and statistical distribution of frequency. The final theoretical function of  $G_2(t)$ , as expressed in eqn. (1.91) or (1.92), is least-square fitted with the experimental  $G_2(t)$  values as obtained from the coincidence measurements to extract the perturbation factor.

### **PERTURBED ANGULAR DISTRIBUTION (PAD):**

In PAC the nuclear orientation is achieved by taking the direction of the first gamma radiation as the reference and then the angular distribution of the second gamma is observed in a cascade. In PAD this reference direction is obtained by particle beam which is used to produce the intermediate level of the probe nucleus. Although the basic principle is same for PAC and PAD, they differ by some essential features. In PAC the gamma-gamma cascade is populated by the preceding decay, usually the beta-decay from the parent isotope. The number of atoms required in this case is determined by its half-life activity. Considering the half-life ranging from few hours to days, the number of atoms required for PAC experiment is of the order of  $10^{12}$  atoms.

In PAD, the probe atoms are produced in a nuclear reaction. The beam serves as start input to TAC. Various pulsed heavy ion beams are used to produce the isomeric states. In this case, only one gamma is counted in the direction with respect to the beam direction. So counting statistics does not pose any problem in PAD experiment. PAD is an online experiment and the probe nucleus is either produced in the matrix to be studied or it can be implanted to other matrices. This implantation is possible due to its large recoil energy. So only problem arises about the uncertainty in the position of the probe nucleus in the lattice during implantation.

The kind of information PAD can generate is similar to those obtained by PAC. Both these techniques can give hyperfine parameters like other nuclear techniques such as NMR, ESR and MB spectroscopy. The lacking information on the isomer shift in comparison with the MB is balanced by details in the magnetic contributions resolved in PAD and not easily detectable with the present Mossbauer cases. Also the experiments dealing with the temperature variation study or the study of lattice dynamics etc are amenable to PAD. Some important studies [144] such as local moments determination, magnetic characterisation of defects, Knight shift in nonmagnetic metals, study of high T<sub>c</sub> superconductors are worth mentioning.

#### **IN-BEAM PAC:**

It is another PAC technique used in case of those probe nuclei with the initial level of half-lives below several minutes. The half-life of the probe atom is of prime consideration in order to apply the PAC technique for any application. Nuclei having half-lives below minute order cannot be used in TDPAC or IPAC studies. Again the number of PAC probes with suitable half-life is not large. In the In-Beam technique [145], probe nuclei can be periodically produced in a nuclear reaction. In the beam-on condition, the gamma-gamma cascade is populated and then in the beam off condition, the coincidence is measured. This procedure is repeated as long as the desirable statistics is achieved. This In-Beam PAC technique can be used in the field of nuclear physics to obtain nuclear moments, spins and multipolarities. It can also be used in solid state physics as well. By the use of the probes with life times in  $\mu\text{s}$  to ms range, the In-Beam PAC method can offer valuable additional information about the fast annealing processes.

#### **CHOICE OF TDPAC ISOTOPE:**

The suitability of TDPAC probe is based on the following criteria: Long lifetime of the parent isotope (or the isomeric state), large anisotropy of the cascade, suitably long lifetime and large

quadrupole moment of the intermediate level, not too low  $\gamma$ -energy to avoid any absorption, suitable difference between two cascade  $\gamma$ -lines so that they can be separated. All the PAC probe-isotopes are either commercially available or produced by nuclear reactions such as thermal neutron capture, cyclotron irradiations or fission followed by radiochemical separation. The probe is then incorporated by a variety of methods: during synthesis of the matrix under study via coprecipitation, by implantation including recoil-implantation technique, irradiation of the sample etc. The following situations in choosing a PAC probe may arise:

- a. In the ideal case, the probe atom has a long-lived isomeric state and is a natural constituent of the sample. Here the interpretation of the PAC results is quite straightforward.
- b. The parent isotope is a constituent of the sample but its daughter is not. In this case, the sample preparation has no difficulty, but the daughter atom, on which the NQI is determined, becomes foreign atom to the matrix under study. Here, electronic (if the electronic rearrangement is too slow compared to the lifetime of the start level) or chemical after-effects (including breaking of weak bonds) may arise and the data-interpretation is not straightforward.
- c. The daughter atom is a constituent of the sample but parent is not. There can be impurity-specific problem during sample-preparation. However, usually the electronic and lattice rearrangement is fast enough to neglect the after-effects. There is no such problem in data-interpretation.
- d. Neither the parent nor the daughter isotope is a constituent of the sample. In this case, all possible above-mentioned complications are expected.

In most of the applications, the atom on which the NQI is studied is preferred to be the constituent of the sample. However, there are a large number of applications where a foreign atom at “infinite dilution” is used for the NQI study. In these cases, the study of impurity-defect or impurity- impurity interactions is also performed purposefully.

The list of isotopes for TDPAC study is given in Table 1.2. The relevant properties of the probe atoms have been mentioned in the table. In case of doping the probe atom inside the matrix under study, the doping condition has to be optimized in such a way that the probe atom occupies the definite lattice site inside the matrix. In practice, the probe atom is added in such a high dilution into the matrix (<0.01 atom %) that it hardly affects the crystal structure of the matrix even if the probe atom is foreign to that matrix and the same probe can be used for the study of different matrices. Now, the effect of preceding decay on the angular correlation pattern has already been discussed. Apart from the decay via isomeric transition (IT), the nuclear probe becomes chemically different from the parent atom. A prerequisite for the probe atom in case of PAC applications is the minimization of all the after-effects at the time of emission of first photon of the cascade and attainment of chemically stable configuration by the daughter atom in the host matrix.

In the present thesis, two probes, viz.,  $^{181}\text{Hf}/^{181}\text{Ta}$  and  $^{111}\text{In}/^{111}\text{Cd}$  have been used to study different matrices. In case of the first probe,  $^{181}\text{Hf}$  undergoes  $\beta^-$  decay to produce  $^{181}\text{Ta}$  which has 133-482 keV cascade being utilized for the PAC measurements. The emission of 0.4 MeV  $\beta^-$  particle by the parent nuclei imparts a maximum recoil energy of 1.6 eV to a free daughter atom. This exerts hardly any mechanical effect on the daughter atom. However, most of the Ta-atoms have one unit of positive charge more than the parent Hf-atom as a result of the  $\beta^-$  decay and the neutralization of the excess charge of Ta depends on the availability of electrons in the

surroundings. The outermost electronic configurations of Hf and Ta atoms are  $5d^26s^2$  and  $5d^36s^2$ . So Hf exists in +4 oxidation state with the  $5d^0$  configuration while Ta exists in +5 state. Had Ta been existed in +4 state with  $5d^1$  configuration, it would have exhibited a strong magnetic perturbation of the angular correlation which has never been observed. Again, the mean lifetime of the initial level of the  $\gamma$ - $\gamma$  cascade is sufficiently long ( $24\mu\text{s}$ ) to allow the complete relaxation of the atomic and molecular rearrangement processes. Hence it is assumed that  $^{181}\text{Ta}$  can attain its chemically stable form in the Hf-compounds and remains at the place of the parent Hf-atoms at the time of first  $\gamma$ -emission. In case of  $^{111}\text{Cd}$   $\gamma$ - $\gamma$  cascade, the nature of decay feeding the cascade has a consequence on the directional correlation. There is no after-effect associated with the IT decay of  $^{111\text{m}}\text{Cd}$  or  $\beta^-$  decay of  $^{111}\text{Ag}$ . However, the situation is quite different in case of  $^{111}\text{In}$  EC decay. The EC decay, as discussed earlier, is followed by intense Auger emission resulting in atomic and molecular disruptions. The daughter atom is left with a variety of charge states and the local defects introduced by the Auger electrons affect the correlation pattern. The decay schemes of the two probes used in the present thesis have been presented in Fig. 1.15.

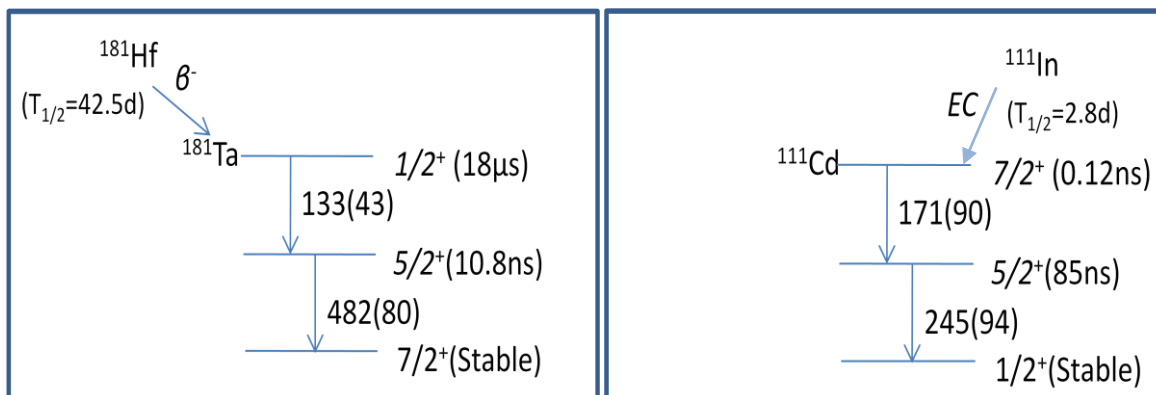


**Figure 1.15:** Decay schemes of  $^{181}\text{Hf}/^{181}\text{Ta}$  (left) and  $^{111}\text{In}/^{111}\text{Cd}$  probes

**Table 1.2:** Properties of Typical TDPAC Probes.

Parent Nuclide	Half-life	Intermediate Level lifetime(ns)	E <sub>1</sub> (keV)	I <sub>1</sub> (%)	E <sub>2</sub> (keV)	I <sub>2</sub> (%)	Intermediate Level Spin
<sup>44</sup> Ti	48y	153	78	100	68	100	2
<sup>99</sup> Rh	16d	21	354	20	90	80	3/2
<sup>100</sup> Pd	3.7d	214	84	70	75	70	2
<sup>111</sup> Ag	7.5d	84	95	0.5	247	1	5/2
<sup>111m</sup> Cd	49m	84	150	100	247	100	5/2
<b><sup>111</sup>In</b>	<b>2.7d</b>	<b>84</b>	<b>173</b>	<b>100</b>	<b>247</b>	<b>100</b>	<b>5/2</b>
<sup>117</sup> Cd	2.4h	60	89	7	345	16	3/2
<sup>131m</sup> Te	30h	5.9	102	5	200	10	9/2
<b><sup>181</sup>Hf</b>	<b>42d</b>	<b>10.8</b>	<b>133</b>	<b>93</b>	<b>482</b>	<b>85</b>	<b>5/2</b>
<sup>187</sup> W	24h	560	480	30	72	15	9/2
<sup>199m</sup> Hg	43m	2.3	375	100	158	100	5/2
<sup>204m</sup> Pb	67m	260	912	98	375	99	4
<sup>204</sup> Bi	11h	260	984	20	375	90	4
<sup>172</sup> Lu	6.7d	7.8	91	4.54	1094	62.5	3
<sup>140</sup> La	40.3h	3.5	329	20.3	487	45.5	4

**1.2.9. Application of TDPAC Technique:**

This hyperfine technique has a variety of applications in the interface of Physics, Chemistry and Biology. A brief overview of these applications will be presented in this section.

**SOLID STATE PHYSICS AND CHEMISTRY:**

The determination of NQI in solids yields valuable information and a distribution of  $V_{zz}-\eta$  characterizes the short-range order [146]. The great advantage of TDPAC technique is that the formation of molecule or compound along with the recrystallization process can be observed at an extremely early stage. The TDPAC spectroscopic technique is highly sensitive to the variations in charge-distribution around the neighborhood of the probe atoms. In case of surface study, the NQI parameters identify the atomic configuration around the probe nucleus in case of perfect surfaces. The surface reactions can also be monitored via the identification of different species formed by their previously known respective hyperfine parameters. Such studies are of great importance in case of technical surfaces used for different practical applications [147-149]. The probe-defect interaction is also studied by this hyperfine technique. Defects are created by irradiating the matrix at a low temperature (e.g. 4.2K) with high-energy particles, viz., proton, alpha, neutrons etc., via radiation damage. The defects are annealed by isochronous annealing where the sample is first kept for a fixed duration at consecutively increasing temperatures and then cooled down to the same measuring temperature. The defects, mainly interstitial atoms and vacancies, get trapped by the probe atoms forming probe atom-defect complexes during annealing. Otherwise, they cannot be detected due to their very low concentration. The potential of PAC is realized in the case of two or more coexisting complexes. The distinctively different PAC parameters for the different complexes along with the information regarding the variation of individual fraction with annealing temperature provide the insight about the formation and dissociation enthalpies of the coexisting complexes along with their fate with annealing [150-155]. The metal-metal interaction can be studied by the TDPAC technique where noble metals are used as the reaction media for investigating attractive interactions between probe atoms and impurity atoms added in a high dilution [156-157]. There occurs a formation of probe atom-

impurity atom pair which gradually vanishes with increasing temperature due to the pair-dissociation. From the temperature dependence of this pair-component, the formation enthalpy can also be derived. The structural phase transitions, involving the change in lattice position and electron density distribution, are studied via the variation in NQI parameters. In spite of the superiority of diffraction techniques to hyperfine techniques for the study of structural phase transition, there are cases where the structural changes are minute. Then PAC spectroscopy can determine the number and population of inequivalent sites in contrast to diffraction techniques. The information about the other dynamic processes, viz., fluctuations, rotations and diffusion processes, can also be extracted from the hyperfine technique. In magnetically ordered materials EFG measured by PAC has been used to study the phase transition in ferroelectric and antiferroelectric perovskites. Temperature dependence of EFG at  $^{181}\text{Hf}$  in  $\text{BaTiO}_3$  [158] obtained from PAC measurements in the temperature range from  $-200^\circ\text{C}$  to  $100^\circ\text{C}$  shows a phase transition of lattice from rhombohedral to tetragonal through monoclinic structure. Phase transitions in metal-hydrogen systems as well as hydrogen diffusion processes have been investigated in the metals Pd, Hf, Ta and Nb with different probes, viz.,  $^{99}\text{Rh}/^{99}\text{Ru}$ ,  $^{100}\text{Pd}/^{100}\text{Rh}$ ,  $^{181}\text{Hf}/^{181}\text{Ta}$  and are described in a review article by Weidinger [159]. The creation and destruction of recoil phonon influences angular correlation [160]. This method of PAC technique has been used to detect sound generated by electromagnetic field in liquid metals [161]. Attempts have been made to reveal the mechanism of superconductivity in high  $T_c$  superconductors by employing the PAC technique. Transient magnetic field (TMF) and transient EFG are expected to act at the nucleus of highly charged ions penetrating a ferromagnetic or a nonmagnetic material respectively. These are very intense in nature and so there is unique possibility to measure, by using these fields, the magnetic dipole and the electric quadrupole

moments of the nuclear states in the lifetime range of picoseconds. Magnetic field is considered to be experienced at low ion velocities. Research in this field [162] has created interests experimentally as well as theoretically. PAC technique has proved to be very important in this connection. The TDPAC technique is also utilized in the investigation of solid state reactions where the different phases are quantitatively characterized by their known hyperfine parameters. An essential advantage of TDPAC technique over other spectroscopic techniques is that the sensitivity of detection is largely sample-independent, i.e., the relative fractions of the observed spectral components are identical with the mole fractions of the individual phases. The temporal evolution of the different components can also be monitored provided that the data-acquisition is minimized by the multi-detector system with high efficiency. In the field of solid state reaction, the dehydration/rehydration reaction of  $\text{HfF}_4 \cdot 3\text{H}_2\text{O}$  [163], the thermal decomposition of  $(\text{NH}_4)_2\text{ZrF}_6$  [164], the formation of  $\text{CuIn}_2$  at the interfaces [165], the oxidation of Hf metal and internal oxidation processes of gas-phase transport reactions in situ [166] have been investigated by TDPAC technique. There are several studies on Hf(IV) complexes [167] with different ligands. TDPAC of Hf(IV) complexes with the ligands. PAC studies on tropolone, cupferon and N-benzoyl n-phenyl hydroxylamine (NBPHA) show that the quadrupole coupling parameters are sensitive to the nature of covalent ligands. The quadrupole interaction frequency increases from NBPHA to cupferon to tropolone, which indicates the increase in the electronic delocalisation on the chelate ring in the above order. From PAC pattern the tropolonate complex shows considerable relaxation behaviour at room temperature and 77K. For the other complexes, however, this is not observed because of rapid inter-conversion of cis-trans isomers. Apart from what has been mentioned above, a large number of studies by PAC technique in solid state chemistry can be obtained elsewhere [105, 113-114].

**SOLID STATE PHYSICS AND BIOLOGY:**

Due to the limited number of TPPAC isotopes having physiological function in biomolecules, the application of this hyperfine method in biology is also restricted. Still there are enough scope for mentioning the versatile application of TDPAC in the interface of solid state physics and biology. In general, two methods are adopted for labelling the biomolecule with the PAC probe. First method involves the unspecific labelling of biomolecules where the dissolved probe is added to the biomolecule in solution and the binding is recorded quantitatively by comparing the spectra of the dissolved probe with that of the bound probe. The second method involves the specific labelling of the biomolecule and the metal substitution in metalloenzymes. The “label” can be offered as free ions or “packed”, as, e.g., in EDTA or serum albumin. The area of application of TDPAC in biology can be classified in two categories: a. Coordination studies where non-uniform sites are identified and characterized according to their NQI parameters and b. Molecular dynamics where the tumbling motion of the biomolecules in solution is studied. The systematic investigation on Coordination studies was carried out by Bauer et al. [168] with  $^{111\text{m}}\text{Cd}$  probe ( $\tau_{1/2}=48\text{min}$ ) for Zn-containing enzymes in highly viscous medium. Bauer tried to correlate absolute values of NQI parameters with different coordination and different ligands. For the investigation of the tumbling motion of biomolecules in solution [169-170],  $^{111}\text{In}/^{111}\text{Cd}$  probe was bound unspecifically to the biomolecule. Due to this unspecific binding, the spectra of immobilized molecules are also very featureless and the information about the reorientational correlation is difficult to extract. However, the specifically bound  $^{111}\text{In}/^{111}\text{Cd}$  in serum albumin 169 also yields featureless spectra for immobilized states indicating a more fundamental problem, e.g., chemical aftereffects. It is important, in labelling cellular component of blood, to know the relative stability of a chelate of a metal ion with respect to other possible complexes

with macromolecules e.g. transferrin, albumin, haemoglobin etc with which the chelate comes into contact. PAC application in this connection has been made [171] in the case of the dissociation of In-chelate with ligands e.g. tropolone, acetylacetonone, oxine and oxine sulphate in presence of transferrin and haemoglobin. In presence of a potransferrin at certain mole ratio, it has been found that all these four chelates dissociate completely, releasing  $^{111}\text{In}$  for incorporation into the specific binding sites of transferrin. However for the iron free haemoglobin, the tropolonate chelate did not dissociate completely. Instead, In was bound to protein together with a single ligand molecule. TDPAC technique studies can give the dynamic aspects of binding of In-DNA as well [172].  $^{181}\text{Hf}$  has been also been used for biological study. TDPAC technique has been employed [173] for finding the binding parameters of Hf after in vivo uptake of  $^{181}\text{Hf}$  in rat plasma. Same authors [174] also investigated this at different temperatures to see the dynamical aspects of the binding. They also studied [175] the difference of binding configuration for Hf with human and rat serum.

### **SOLUTION CHEMISTRY:**

In solution, the Hamiltonian between the intermediate state and the surrounding field becomes time dependent. In addition to this, there may be relaxation due to rotational diffusion of the species to which the probe atom is attached. So determination of the attenuation factor which is related to the correlation time, can be used to study the complexation in term of its nature and stability constant, polymerisation, binding sites of the probe nucleus etc. The changes in the correlation time with the size of the species containing the PAC probe (e.g., in polymerisation reaction) can also modify the PAC parameters significantly. The application of TDPAC to the macromolecules in solution, biomolecules and their rotational correlation times, determination of conformational changes of the macromolecules, binding constants, metal-protein interaction etc.

is still left almost unturned. The potentiality of the PAC technique in the field of complexation has been demonstrated [176]. It has been found that as the fluoride to hafnium ratio is increased the attenuation factor increases and reaches the unperturbed value as the ratio reaches 6:1. The symmetric arrangement of six fluoride ions around hafnium nucleus reduces the EFG and thus resulting in the unperturbed value of the attenuation factor.

Influence of the complexation on the relaxation in aqueous solution has been demonstrated [177] for hydration of  $\text{In}^{3+}$  ion. Very weak perturbation at very high acidic or alkaline medium has been explained by formation of the symmetric complexes,  $[\text{In}(\text{H}_2\text{O})_6]^{3+}$  and  $[\text{In}(\text{OH})_6]^{3-}$  respectively. Stronger perturbation in the range of intermediate acidity is due to the formation of a less symmetric complex such as  $[\text{In}(\text{H}_2\text{O})_{6-x}(\text{OH})_x]^{3-x}$ . An interesting study has been carried out [178] in case of  $\text{Cd}(\text{CH}_3)_2$  in polycrystalline form as well as in frozen solution. Quadrupole coupling constants in both the cases were found to be same. So it was concluded that the origin of the EFG was molecular in nature and the correlation time obtained in this case was unambiguous.

### **SUPER-VISCOUS MEDIUM:**

Super-viscous system is a class of liquids which have properties different than the normal liquids in view of their transport properties e.g. viscosity and diffusion constant and their variation with temperature. Examples of such systems are molten glass, lubricating oil, glycerol, metallurgical slags etc. The study of such systems has practical as well as theoretical implications. The measurement of this kind is very rare. One such investigation [179] has been carried out in case of  $\text{H}_3\text{PO}_4 + \text{H}_2\text{O}$  system at different temperatures. Stochastic models have been used to obtain the relaxation constants. These when plotted in log scale against temperature show an Arrhenius

type of relation below 217K which is indication of super-viscous phase and above this temperature the transition takes place to normal liquid.

Further experiment in the other systems will be worthwhile to understand the basic nature of molecular motion in the super-viscous phase.

### **HOT ATOM CHEMISTRY:**

The effect of the preceding decay feeding the  $\gamma$ - $\gamma$  cascade on the directional correlation pattern has already been discussed. In all the preceding decays except isomeric transition, apart from the obvious changes in the nuclear charge, the after effects involve kinetic recoil, shake off excitation, secondary ionisation, Auger charging processes etc. So if the “hot” daughter atom does not attain the stable configuration, then PAC cannot be used for the insitu study of the above mentioned after effects. On the other hand, if the nucleus attains a stable configuration, then there exists a unique relationship between the chemical states of the daughter and so the PAC study pertaining to the daughter atom will help in understanding the insitu properties of the recoil atom which is the main feature of the hot atom chemistry.

Different probes such as  $^{181}\text{Ta}$  and  $^{111}\text{Cd}$  have been used to study several aspects of the hot atom chemistry. This includes the charge neutralisation process of the daughter nucleus after beta decay of the parent and its relation to the host matrix [113] depending on whether it is a metal or an insulator. In another study [176] it has been found that the after effects which are produced by the beta decay of the parent  $^{181}\text{Hf}$  do not exist during the first gamma emission of the cascade due to the long span of 24  $\mu\text{s}$  which is the lifetime of the initial level of the cascade. This has been carried out by observing the anisotropy in IPAC of  $^{181}\text{Hf}$  fluoride in aqueous solution as a function of time delay after the beta emission by  $^{181}\text{Hf}$ . It was found that the anisotropy remains constant as a function of delay time. This investigation of hafnium recoil chemistry has been

applied in case of Hf-EDTA and Hf-CDTA chelates. A recent study [180] has demonstrated the after effects of the beta decay of  $^{181}\text{Hf}$  which has been doped in monoclinic  $\text{ZrO}_2$  and TDPAC of  $^{181}\text{Ta}$  has been observed over a temperature range of 10K to 1300K. For high purity samples, the effective anisotropy has been found to be equal to the expected value above  $200^\circ\text{C}$  but decreased abruptly approximately by a factor of two at lower temperature. This unusual behavior has been explained in terms of the after effects of the beta decay that populates with approximately 50% probability an electron trap located about 1 eV below the conduction band. At low temperature this trapped electron causes Ta nucleus to relax rapidly and contributes to  $G_2(t)$  only near  $t=0$ . At high temperature or in doped samples the electron escapes quickly enough to have negligible effects on  $G_2(t)$ . The  $\gamma$ - $\gamma$  cascade of  $^{111}\text{Cd}$  has also been used to study the after effects.  $^{111}\text{Cd}$  obtained from IT of  $^{111\text{m}}\text{Cd}$  have little after effects. However the EC decay of  $^{111}\text{In}$  will have large after effects on atomic and molecular disruption following the Auger processes. This effect has been shown up in the smearing of the oscillation pattern in  $A_2G_2(t)$  for  $\text{InPO}_4$  [113]. So  $^{111}\text{In}$  can be used, as probe to study the after effects but not as a probe to study the matrix where well defined EFG is required to interpret the host matrix properties.

#### **RADIATION DAMAGE STUDY:**

In the context of hot atom chemistry, the use of PAC as a microscopic tool for the study of radiation damage in solids must be mentioned. The probe can be implanted into the matrix by ion-beam or by nuclear reactions. The local radiation damage surrounding the probe atom can be revealed by this technique. If the interstitials and vacancies can be frozen by performing the implantation at low temperatures, the probe-defect interaction can also be studied. In fact,  $^{111}\text{In}/^{111}\text{Cd}$  has been used as a probe in this connection. Several studies in this regard can be found in few articles [181-182]. A similar study on the different nuclear materials, viz., cladding

materials, fuel matrices etc., can be performed with this hyperfine tool TDPAC under simulated reactor condition.

### **1.3. Other Techniques:**

Apart from TDPAC, few other techniques were also used in order to either compliment the TDPAC data or to characterize the samples. The techniques include X-ray Diffraction (XRD), Transmission Electron Microscope (TEM), Scanning Electron Microscope (SEM), Atomic Force Microscope (AFM), UV-Vis Spectrophotometry and Rutherford Back-Scattering (RBS). Here, a brief account of all these techniques will be furnished.

#### **1.3.1. XRD Measurement:**

X-rays are short wavelength electromagnetic radiation produced by the deceleration of high energy electrons in the inner orbitals of atoms. The wavelength range of X-rays is from  $\sim 10^{-5}$  Å to 100 Å. X-rays have three major applications: X-ray radiography, X-ray Crystallography and X-ray fluorescence. Here, only the use of X-rays in X-ray Crystallography will be discussed.

XRD is used to characterize the long-range ordering in a crystal lattice and it can supplement the PAC spectroscopy very well as the PAC describes the short range ordering. X-ray crystallography is a method used for determining the atomic and molecular structure of a crystal, in which the crystalline atoms cause a beam of X-rays to diffract into many specific directions. By measuring the angles and intensities of these diffracted beams, a crystallographer can produce a three-dimensional picture of the density of electrons within the crystal. From this electron density, the mean positions of the atoms in the crystal can be determined, as well as their chemical bonds, their disorder and various other information. Crystals are regular arrays of atoms, and X-rays can be considered waves of electromagnetic radiation. Atoms scatter X-ray waves, primarily through the atoms' electrons. In common with the other types of

electromagnetic radiation, the interaction between the electric vector of X-radiation and the electron of the atoms in the crystal through which it passes results in scattering. When X-rays are scattered by the ordered environment in a crystal, interference (both constructive and destructive) takes place among the scattered rays because the distance the scattered centers are of the same order of magnitude as the wavelength of radiation. Diffraction is the result. The requirements for X-ray diffraction are: (i) the spacing between the layers of atoms must be roughly the same as the wavelength of the radiation and (ii) the scattering centers must be spatially distributed in a highly regular way. The requirement for constructive interference is that the optical path difference between the two waves be equal to an integral multiple of wavelengths. The Bragg's law is as follows:

$$n\lambda = 2d\sin\theta \quad (1.106)$$

The spectrum contains the diffraction intensity versus the diffraction angle. Then the computer software compares the results to the analytical standards to determine the composition of the sample. The intensity of the diffracted peaks is related to the long range ordering of the sample. The sharper and more intense the peaks are, more will be the uniformity of the crystal lattice. Again the FWHM of the peak at a particular diffraction angle can be related to the particle size of the sample by Debye-Scherrer formula. The Scherrer equation [183-184] in X-ray diffraction and crystallography, is a formula that relates the size of sub-micrometre particles, or crystallites, in a solid to the broadening of a peak in a diffraction pattern.

The Scherrer equation can be written as:

$$\tau = \frac{K\lambda}{\beta \cos\theta} \quad (1.107)$$

$\tau$  is the mean size of the crystallite,  $K$  is a dimensionless shape factor, with a value close to unity. The shape factor has a typical value of about 0.9, but varies with the actual shape of the

crystallite,  $\lambda$  is the X-ray wavelength,  $\beta$  is the line broadening at half the maximum intensity (FWHM), after subtracting the instrumental line broadening, in radians and  $\theta$  is the Bragg angle.

In the present thesis, XRD measurements have been performed in bulk as well as nano samples in order to study the long-range ordering. In some cases, the particle size has also been determined using the Debye-Scherrer formula.

### **1.3.2. Transmission Electron Microscopy (TEM):**

Transmission electron microscopy (TEM) is a microscopy technique where a beam of electrons is transmitted through an ultra-thin specimen, gets scattered as they pass through it, is focussed by an objective lens, gets amplified by a magnifying lens and finally produces the desired image. Electrons interact much more strongly with matter than do X-rays or neutrons with comparable energies or wavelengths. For ordinary elastic scattering of 100 keV electrons, the average distance traversed by the electrons between scattering events (mean free path) varies from ten to hundreds of nanometers for heavy elements. The best results are obtained in electron microscopy by using film thicknesses that are comparable with the mean free path. In the present thesis, TEM has been used to characterize the core-shell nanoparticles which were prepared along with the PAC probe and studied with TDPAC method.

### **1.3.3. Scanning Electron Microscope (SEM):**

A scanning electron microscope (SEM) is a type of electron microscope that produces images of a sample by scanning it with a focused beam of electrons. The electrons interact with atoms in the sample, producing various signals that can be detected and that contain information about the sample's surface topography and composition. The electron beam is generally scanned in a raster scan pattern (rectangular pattern of image capture), and the beam's position is combined with the

detected signal to produce an image. SEM can achieve resolution better than 1 nanometer. It is one type of scanning microscopy to obtain surface information of a specimen. Here, the electrons are deflected magnetically through magnetic fields generated by electric currents flowing through coils. The strength of the magnetic field produced by a coil is proportional to the voltage applied to the coil. The magnetic field produced by the coils exerts a force that deflects the electron beam from left to right along the direction of the line drawn at the bottom of the sample. Thus the electron beam scans repeatedly from left to right across the sample in a raster pattern that eventually covers the entire frame area on the sample.

The spatial resolution of the SEM depends on the size of the electron spot, which in turn depends on both the wavelength of the electrons and the electron-optical system that produces the scanning beam. The resolution is also limited by the size of the interaction volume, or the extent to which the material interacts with the electron beam. The spot size and the interaction volume are both large compared to the distances between atoms, so the resolution of the SEM is not high enough to image individual atoms, as is possible in the shorter wavelength (i.e. higher energy) transmission electron microscope (TEM). The SEM has compensating advantages, though, including the ability to image a comparatively large area of the specimen; the ability to image bulk materials (not just thin films or foils); and the variety of analytical modes available for measuring the composition and properties of the specimen. Depending on the instrument, the resolution can fall somewhere between less than 1 nm and 20 nm.

#### **1.3.4. Atomic Force Microscope (AFM):**

The technique in wide use for nanostructured surface studies is AFM which is also a scanning microscopy technique. AFM monitors the force exerted between the surface and the probe tip. It has resolution on the order of fractions of a nanometer. The AFM has two modes of operation. In

close-contact mode, the core-to-core repulsive forces with the surface dominate and in a greater separation non-contact mode, the relevant force is the gradient of the Van der Waals potential.

The AFM is one of the foremost tools for imaging, measuring, and manipulating matter at the nanoscale. The information is gathered by "feeling" the surface with a mechanical probe. Piezoelectric elements (*piezoelectricity* means electricity resulting from pressure) that facilitate tiny but accurate and precise movements on (electronic) command enable the very precise scanning. The AFM consists of a cantilever with a sharp tip (probe) at its end that is used to scan the specimen surface. The cantilever is typically silicon or silicon nitride with a tip radius of curvature on the order of nanometers. When the tip is brought into proximity of a sample surface, forces between the tip and the sample lead to a deflection of the cantilever according to Hooke's law. Typically, the deflection is measured using a laser spot reflected from the top surface of the cantilever into an array of photodiodes. If the tip was scanned at a constant height, a risk would exist that the tip collides with the surface, causing damage. Hence, in most cases a feedback mechanism is employed to adjust the tip-to-sample distance to maintain a constant force between the tip and the sample. Traditionally, the sample is mounted on a piezoelectric tube that can move the sample in the  $z$  direction for maintaining a constant force, and the  $x$  and  $y$  directions for scanning the sample.

AFM has several advantages over the scanning electron microscope (SEM). Unlike the electron microscope which provides a two-dimensional projection or a two-dimensional image of a sample, the AFM provides a three-dimensional surface profile. Additionally, samples viewed by AFM do not require any special treatments (such as metal/carbon coatings) that would irreversibly change or damage the sample. While an electron microscope needs an expensive vacuum environment for proper operation, most AFM modes can work perfectly well

in ambient air or even a liquid environment. This makes it possible to study biological macromolecules and even living organisms. In principle, AFM can provide higher resolution than SEM. A disadvantage of AFM compared with the scanning electron microscope (SEM) is the single scan image size. In one pass, the SEM can image an area on the order of square millimeters with a depth of field on the order of millimeters, whereas the AFM can only image a maximum height on the order of 10-20 micrometers and a maximum scanning area of about 150×150 micrometers. One method of improving the scanned area size for AFM is by using parallel probes. The scanning speed of an AFM is also a limitation. Traditionally, an AFM cannot scan images as fast as a SEM, requiring several minutes for a typical scan, while a SEM is capable of scanning at near real-time, although at relatively low quality. The relatively slow rate of scanning during AFM imaging often leads to thermal drift in the image making the AFM less suited for measuring accurate distances between topographical features on the image. AFM images can also be affected by nonlinearity, hysteresis and creep of the piezoelectric material and cross-talk between the  $x$ ,  $y$ ,  $z$  axes that may require software enhancement and filtering. In the present thesis, AFM has been utilized in order to study the surface morphology of thin film.

### **1.3.5. UV-Vis Spectrophotometry:**

Molecular absorption spectroscopy is based on the measurement of the transmittance  $T$  or the absorbance  $A$  of solutions contained in transparent cell having a pathlength of  $b$  cm. Ordinarily, the concentration  $c$  of an absorbing analyte is linearly related to absorbance as represented by the equation

$$A = -\log T = \log \frac{P_0}{P} = \epsilon bc \quad (1.108)$$

The power of the beam transmitted by the analyte solution ( $P_0$ ) is usually compared with the power of the beam transmitted by an identical cell containing only solvent ( $P$ ). The present spectroscopic technique has been used to characterize the pure and core-shell nanoparticles.

### **1.3.6. RBS Spectroscopy:**

Rutherford Backscattering Spectrometry (RBS) is a widely used nuclear technique for the surface layer analysis of solids. A target is bombarded with ions at energy typically in the range of 0.5–4 MeV and the energy of the backscattered projectiles is recorded with an energy sensitive detector, typically a solid state detector kept at an angle of 150-170°. RBS allows the quantitative determination of the composition of a material and measurement of depth profiling of individual elements. RBS is quantitative without the need for reference samples and non-destructive. It has a good depth resolution of the order of several nm and a very good sensitivity for heavy elements of the order of parts-per-million (ppm). The drawback of RBS is the low sensitivity for light elements. This technique has been used to measure the thickness of a thin film sample in the present thesis.

### **1.4. Motivation and Scope of the Thesis:**

The physico-chemical study in the atomic level has importance in order to investigate the microstructural aspects of the system under study. The information on the short-range interaction is also important in order to explain the different modifications of the macroscopic properties of the chemical systems required for different applications. To study such microscopic properties, the technique is expected to have a resolution in the range of atomic scale. TDPAC is a nuclear probe technique based on hyperfine interaction with atomic scale resolution. The short-range information is obtained with high sensitivity. In case of multiple species containing the probe atom inside the matrix under study, all the species can be identified along with their individual

populations. The analysis of the PAC spectrum provides the information about the strength of EFG, its asymmetry and the crystalline purity of the sample under study.

The technique TDPAC is a nuclear technique where a suitable radionuclide is doped inside the chemical matrix under study as a probe atom and its nuclear property under the chemical environment is exploited to acquire the microstructural information about the host matrix. To carry out TDPAC spectroscopy, it is required to develop the electronics coupled with a suitable data-acquisition system. For a fast-timing measurement, it is a prerequisite to have a fast detector. In addition, the best-possible energy resolution for the detectors is also desirable in order to separate the close-lying energy peaks. So the latest available  $\text{LaBr}_3(\text{Ce})$  detectors have been chosen for the present TDPAC spectrometer. A fast-slow coincidence circuit has been developed coupled to a CAMAC-based data-acquisition system. The advantage of this coincidence circuit lies in the fact that the data are collected in LIST mode and gates are given in the post-acquisition period. The energy resolution of the  $\text{LaBr}_3(\text{Ce})$  detectors is so good ( $\leq 3\%$  at 662 keV  $\gamma$ -energy) that it could separate the closely spaced  $\gamma$ -cascades. In order to optimize the operational condition for the spectrometer without hampering the time resolution of the coincidence circuit, a characteristics study on the  $\text{LaBr}_3(\text{Ce})$  detectors has also been carried out. The study has been carried out with the group-IVB metal oxides, viz.,  $\text{TiO}_2$ ,  $\text{ZrO}_2$  and  $\text{HfO}_2$ , based on their versatile applications both in pure and in doped forms. Again the method of sample preparation has also been a mild process following the coprecipitation technique. At first, the known TDPAC parameters for rutile system have been established with the above spectrometer and then the parameters for anatase system have been measured. The other two oxides in pure form have also been studied with this technique and their structural similarity has been established. The method has been uniquely applied in case of doped rutile systems, thin

films and nanoparticles including core-shell type. The minute changes under different chemical conditions have been perceived by this hyperfine tool and furnished in the thesis. The new observations in case of doped and core-shell nanosystems have been explained in the present work. The sensitivity and versatility of TDPAC technique in different types of chemical phenomena have also been presented in the present thesis.

## Chapter 2. Development of Fast-Slow Coincidence Setup with $\text{LaBr}_3(\text{Ce})$ Detectors

PAC measurements, as already discussed, are of two types depending on the resolving time of the coincidence circuitry, interaction time and the lifetime of the intermediate state of the probe nucleus. If the resolving time of the set-up is less than the lifetime of intermediate level, one goes for time differential measurements. On the other hand, if the resolving time is larger compared to the intermediate level then one has to go for time integral measurements.

In TDPAC measurements a time spectrum is obtained by the coincidence counting of two photons in a cascade as a function of the time difference between the two photons. The PAC experiments are carried out using a fast-slow coincidence setup. The role of fast coincidence part is to establish the time relationship between two photons and the slow part is to discriminate the  $\gamma$ -energies. The TDPAC spectrometer should fulfil some criteria, viz., the detectors should be able to detect all the  $\gamma$ -quanta with maximum efficiency in order to enhance statistics of the coincidence measurements, solid angle per detector should be as small as possible in order to prevent the loss of the angular part of the perturbation function, the energy resolution of the detectors should be sufficient to distinguish between two cascading  $\gamma$ -rays of interest and separate them from other irrelevant  $\gamma$ -rays, if any and time resolution of the setup should be as good as possible, preferably better than 1ns.

The coincidence setup used in the present thesis is based on CAMAC. Computer Automated Measurement And Control (CAMAC) is a standard bus for Data acquisition and control. The bus allows data exchange between plug-in modules (up to 24 in a single crate) and a crate controller, which then interfaces to PC. Within the dataway, modules are addressed by slot (Geographical addressing). The left-most 22 slots are available for application modules while the right-most two slots are dedicated to a crate controller. The CAMAC based setup acquires all the coincidence

data in LIST mode and the gates are given between the relevant  $\gamma$ -energies in the post-acquisition period. So, data for more than one probe can be extracted in a single experiment and the gates can be given in the post-acquisition period among the different  $\gamma$ -cascades relevant to the respective probes in order to extract the informations for different probes separately in a single measurement. For this, the detectors should be able to distinguish all the  $\gamma$ -cascades involved in the probes used and the lifetime of the intermediate states for the different probes should be comparable so that the gated coincidence spectra for all the different probes can be adjusted in the same time-scale.

The circuit diagram of the Fast-Slow coincidence setup is shown in Fig. 2.1:

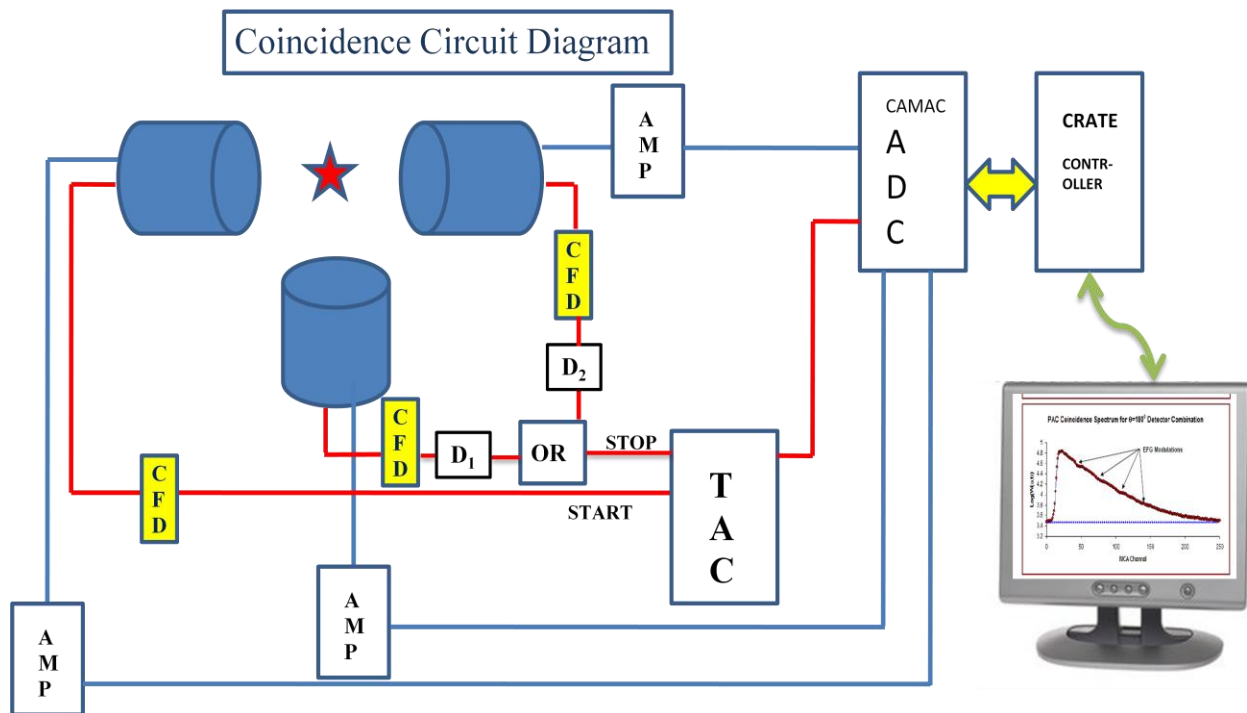


**Figure 2.1:** Fast-Slow coincidence circuit diagram for TDPAC measurement.

The circuit has several components and each of these components will be discussed one by one in the context of their role in the coincidence measurement. The basic components of TDPAC

system are three detectors each coupled to PM tube. There are two outputs from each PM tube, viz., Dynode output and Anode output. Dynode output is used for energy discrimination while the anode output is used for timing measurements. Three dynode outputs are fed into three amplifier (AMP) model no: Ortec 572 and the amplified outputs are fed into the CAMAC Quad Analogue to Digital Converter (ADC) model no: AD413A. Negative anode output from the photomultiplier tube is taken through a constant fraction discriminator (CFD) model no: Ortec 584 which produces a fast logic pulse by taking the rise part of the input pulse. The time spectrum is obtained by using a time-to-amplitude converter (TAC) model no: Ortec 467. One CFD output which detects first  $\gamma$ -photon of the cascade acts as a START signal to TAC and either of the two CFD outputs detecting second  $\gamma$ -photon of the cascade at  $90^\circ$  and  $180^\circ$  acts as a STOP signal to TAC. The two STOP signals from CFDs are delayed ( $D_1$  for  $90^\circ$  detector and  $D_2$  for  $180^\circ$  detector generally with  $D_2 > D_1$ ) and passed through logic OR gate when the logic output acts as the STOP signal to TAC. This is the timing or the fast part of coincidence circuit. This gives the coincidence with respect to time only. TAC will generate a pulse, the height of which is proportional to the time difference between the two events. The data acquisition was performed with LAMPS software [185]. The Single Channel Analyzer (SCA) output of TAC is used as the master gate to ADC.

The spectrometer consists of three planar  $\text{LaBr}_3(\text{Ce})$  detectors and source is kept at a distance of 1-2 cm. from the detector. The activity of the source is generally kept to be  $\sim 30\text{-}40$  KHz to get a coincidence count rate of  $\sim 1\text{-}2$  kbps. The unipolar output from each of the amplifiers with a shaping time of  $1\ \mu\text{s}$  is used for the energy measurement. The gain of the amplifiers is so adjusted that the  $\gamma$ -ray of interest lies in the middle of the 8K channel. The added advantage of the present coincidence setup is that if there is any sudden drift in the amplifier during acquisition, the

energy-gates can be accordingly adjusted in the post-acquisition period. The time walk for each of the three CFDs is adjusted from the monitor output triggered by the CFD output. The threshold adjustment for each CFD is performed depending on the energy of the  $\gamma$ -ray and the bias voltage applied to the corresponding PM tube. However, in the present work all the measurement has been performed at a negative bias of 2500V. The threshold is so adjusted that the chance coincidences are minimized without hampering the true coincidence. The delay in each of the CFD has been adjusted in such a way that the two coincidence spectra at  $90^\circ$  and  $180^\circ$  are well separated with respect to the life time of the intermediate level of the probe atom. The TAC output is checked for it to fall within the mastergate provided by its SCA output. The time calibration for the TAC is performed by Ortec time calibrator model 462 in order to adjust the time per channel (TPC) depending on the lifetime of the intermediate level. The CAMAC ADC output is connected to PC by a CAMAC Crate Controller CMC100. Before each acquisition, the time resolution of the system is checked with a prompt source.

### **2.1. Detectors:**

The nature and the size of the detector are important to decide the time resolution of the circuit. The detector should have fast timing characteristics for the scintillation, i.e., the rise time of the output light should be as small as possible. In this regard, plastic scintillators [186] are well known. But the plastic scintillators have very low efficiency and poor energy resolution.

In the present measurement,  $\text{LaBr}_3$  (Ce) scintillator detectors with an improved energy resolution were used in the present work. BrillanCe<sup>TM</sup>380 [ $\text{LaBr}_3$  (Ce)] [187] is a transparent scintillator material that offers the best energy resolution, fast emission and excellent linearity. It has a higher light output than  $\text{NaI(Tl)}$  and also better energy resolution. In the present thesis, 30mmX30mm  $\text{LaBr}_3$  (Ce) detectors have been used with energy resolution of  $\sim 3\%$  at 662keV

energy. An improved energy resolution has been achieved with this detector due to its high scintillation output of  $\sim 63$  photons/keV [188], compared to other available scintillators. A low decay time of  $\sim 20$  ns makes it ideal for timing measurements from few ns to few picoseconds.

For a particular detector, its size is of significant importance in deciding its time response. Larger the size of the crystal, greater is the variation in the path length of the photons, generated at different points of the crystal, in reaching the photocathode. Consequently, the distribution in the time of arrival of the photons at the photocathode increases resulting in the increase in the width of the time response function. Therefore, a smaller crystal will give a better time response, but the efficiency decreases with smaller volume. So a compromise is made between the size of the crystal and its efficiency to optimize the time response function. A large volume detector with a very high efficiency cannot be used in a timing measurement.

## **2.2. Photo Multiplier Tube:**

The detector is coupled to PM Tube and the PM Tube has a very important role in deciding the time response function. The spread in the transit time of the photoelectrons through the dynodes of the PM tube contributes to the spread in the distribution of the time response. The transit time in a PM tube is defined as the average time difference between the arrival of the photon at photocathode and collection of the subsequent electron burst at the anode. The spread in the transit time arises due to the difference in the path lengths of the electrons generated at different parts of photocathode and also between the dynodes. Further, the distribution in the initial velocities of the photoelectrons leaving the photocathode also results in the spread in the transit time. If the initial velocity is less, there will be large variation of transit time for the electrons having different path lengths. However if the velocity is large, this spread in transient time is reduced for the same path length distribution. So it is desirable to have higher initial velocity for

the photoelectrons to get a sharper time response. This is done by using larger voltage difference between the photocathode and the first dynode. Other factors related to PM tubes that affect the time resolution are;

- (i) Number of dynodes in the PM tube has significant role in the response function. Fewer stages of multiplication give better timing since this reduces the spread in the transit time of electrons.
- (ii) Smaller is the diameter of the photocathode, better is the time resolution. If the diameter of the photocathode is smaller the distribution of path length between the photocathode and dynode reduces. So the transit time reduces. Best timing will be achieved when the central area of the photocathode is illuminated.
- (iii) The design of both K-d1 (cathode to first dynode) region and the electron multiplier are critical in obtaining optimum time performance. The equalisation of the path length to d1 independent of the point of origin should be maintained. The focussing of electron trajectories onto small area of each dynode and short inter-electrode distance reduces this dispersion. This can be achieved by using planoconcave window linear focussed electron multipliers.

Another important property that a PM tube should have is the high gain so that the preamplifier or the amplifier can be avoided and the anode output can be used directly for timing purpose. This would reduce the unnecessary jitter due to extra electronic components. Further, in the use of negative high voltage in the cathode and anode in the ground potential, dc coupled output can be derived from the anode. This procedure reduces the noise level in the output.

In the present thesis, XP2020/URQ fast PM Tube has been used. The XP2020/URQ is a widely used UV sensitive ultra-fast photomultiplier tube with a high gain and short transit time. This

photomultiplier is a focused tube with twelve dynode stages having the highest gain of  $\sim 10^8$ . The tube has a transit time spread down to 0.2 ns and a rise time of 1.4 ns making it suitable to couple to a fast scintillator. Two outputs are furnished: the negative signal from the anode is intended for timing applications and the linear signal from tenth dynode is for energy measurements. The negative high voltage is applied to the cathode and the anode is operated essentially at ground potential. This facilitates the incorporation of several features that augment the fast timing performance. The anode output is dc-coupled with the anode being connected to ground through a 50- $\Omega$  load resistor. This eliminates the base-line shift caused by varying counting rates in ac-coupled systems. It also suppresses reflections by providing back-termination for the anode output connection. The LaBr<sub>3</sub> (Ce) crystals of size 30 mm X 30 mm, sealed inside Al-housing, has been coupled to XP2020/URQ PMT via UV sensitive coupling glue. The energy and timing properties of the detector have been studied at different bias voltages of the tube. The measurements have been performed at different bias voltages of the PMT from 2000 – 2500 V at an interval of 100 V. The energy spectra obtained with the LaBr<sub>3</sub> (Ce) detector, for different sources, are shown in Fig. 2.2.

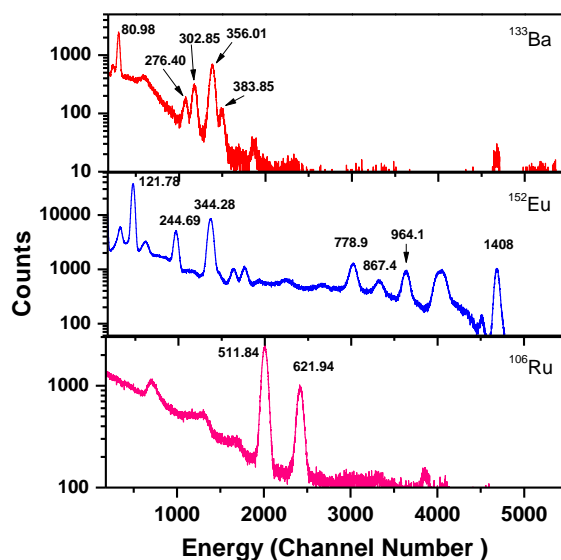


**Figure 2.2:** The energy spectra obtained with LaBr<sub>3</sub> (Ce) detector <sup>133</sup>Ba, <sup>152</sup>Eu and <sup>106</sup>Ru.

The excellent energy resolution of LaBr<sub>3</sub> (Ce) detector can easily be realized from the above figure. The energy response of the detector has been found to be linear up to 622 keV for all the bias voltages. The energy response becomes nonlinear at energies higher than 622 keV for all the bias voltages above 2000 Volt as shown in Fig. 2.3. The energy resolutions have been determined from the Full Width at Half Maxima (FWHM) of the obtained photo peaks. The study shows that the energy resolution of the detector does not change much with the variation of bias voltages. However, at almost all the bias voltages the energy resolution at 622 keV comes around 3% which is comparable to the best resolution obtained for this detector.

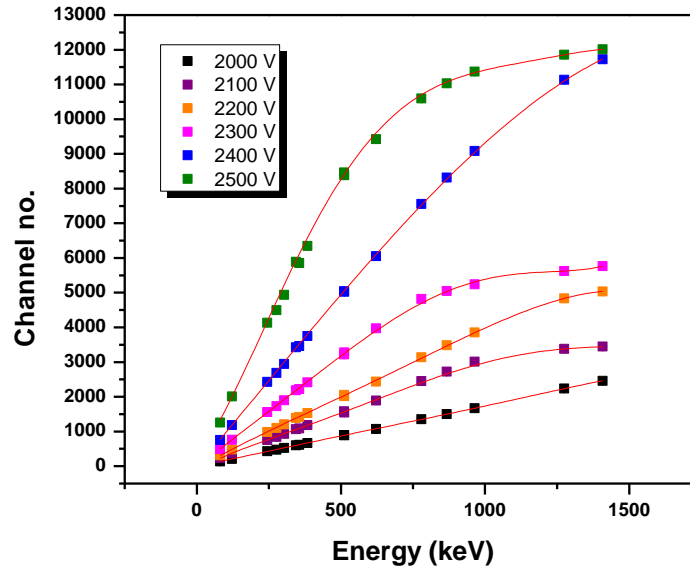


**Figure 2.3:** The energy response curve for LaBr<sub>3</sub> (Ce) detector up to 1.4 MeV.

This information on the energy linearity of LaBr<sub>3</sub> (Ce) detector has an important application in the extraction of data during post-acquisition period by putting gates between different  $\gamma$ -cascades, specially while working with multi-probe systems as mentioned earlier.

### 2.3. Resolving Time:

For a fast-slow coincidence setup, the resolving time of the fast-slow coincidence unit is the measure of the width of the time distribution of the coincidence counts of two simultaneous

events. In principle, the coincidence counts should show a single line for simultaneous events. However due to the variation in the response of the detectors for different events, photomultiplier tubes and the electronic modules, a distribution develops in the time response resulting in the widening of the line spectrum. Amplitude and time walk in the time pick-off lead to a finite resolving time of the coincidence circuit. Prompt time spectrum has been measured for the 511-511 keV cascade for the  $^{22}\text{Na}$  positron annihilation and shown in Fig. 2.4. The time resolution is  $340 \pm 10$  ps with the  $\text{LaBr}_3(\text{Ce})$  detector.

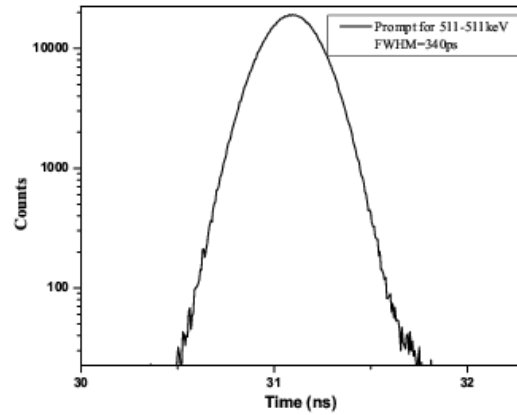


**Figure 2.4:** Prompt for 511-511 cascade of  $^{22}\text{Na}$  source.

The FWHM of the TAC peaks has been estimated at different bias voltages in order to study the time resolution of the  $\text{LaBr}_3(\text{Ce})$  detector coupled to the same XP2020/URQ PMT. The best time resolution is obtained at 2500 Volt bias voltage. The variation of time resolution with bias voltage of the PM Tube has been shown in Fig. 2.5 up to 2400 Volt.

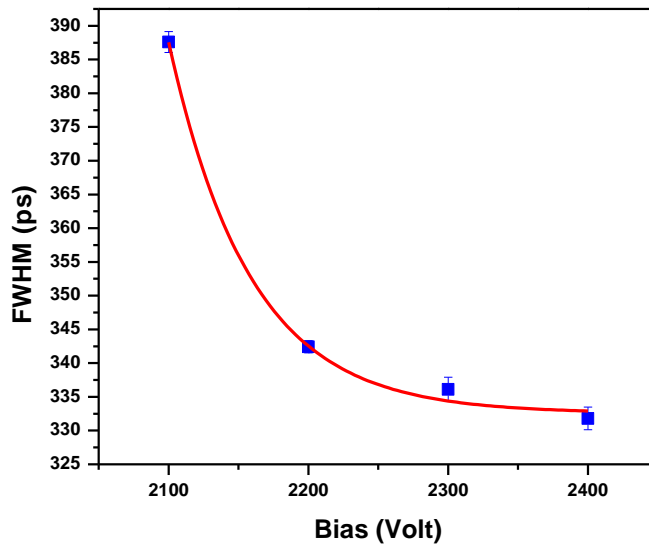


**Figure 2.5:** The variation of time resolution of the detector at different bias voltages.

The variation of time resolution with the high voltage can be explained in terms of the transit time of electrons from photocathode to anode.

#### 2.4. Electronic Modules:

The **amplifier** is one of the most important components in a pulse-processing system for applications in counting, timing or energy spectroscopy. The simplest concept for pulse shaping is the use of a CR high-pass filter followed by an RC low-pass filter. This pulse-shaping technique can be used with scintillation detectors. For that application, the shaping time constant should be chosen to be at least three times the decay time constant of the scintillator to ensure complete integration of the scintillator signal. The disadvantage of using the CR-RC shaping with scintillation detectors is the much longer pulse duration compared with that of single-delay-line shaping. In the present case, the dynode pulse from PM tube is fed into the amplifier and amplifier output is directly fed into the ADC to get the energy spectrum. The shaping time

constant of the amplifier has been set to  $1\mu\text{s}$  and the gain has been adjusted according to the energy of the cascade  $\gamma$ -rays used in different measurements.

**Fast timing discriminators** are designed to achieve the best time resolution and the highest counting rates by operating on the fast-rising detector signal. The negative anode pulse from the PM tube is directly fed into the fast timing discriminator. The “rise time” refers to the time taken to make the transition from 10% to 90% of the pulse amplitude on the leading edge of the pulse. The primary function of a timing discriminator is to mark the arrival time of the detected events with precision and consistency. The timing discriminator has to be chosen in a proper way based on the characteristics of the detector and intended application in order to get the optimum time resolution. Jitter, walk and drift are the three major factors limiting time resolution. Walk can be of two types: time walk and amplitude walk. Time jitter and time walk apply to cases where the amplitudes of the input pulses are constant. The effect due to amplitude walk is realized when the amplitudes of the input pulses are varying. An important source of time jitter is the random fluctuation in the size and shape of the signal pulse. Such fluctuations appear due to the electronic noise added by the components which process the linear pulses prior to the time pick-off. Other sources of jitter are of discrete nature of the electronic signal as generated in the detector. When the number of information carriers that make up the signal is less, statistical fluctuation and time of occurrence of the ion pairs is reflected in the size and shape of the pulse. This effect is large for small pulses and for detectors that generate less number of information carriers. Drift is the long term error introduced by the component aging and by temperature variation during long measurement periods.

In the time pickoff process, two ways of triggering are possible to derive the logic time signal from an analog input, viz., leading edge triggering and constant fraction triggering. A leading-

edge triggering incorporates a simple voltage comparator with its threshold set to a desired voltage. “Walk” is normally the dominant limitation on time resolution with this method. Again, the contribution from time jitter is associated with scintillation detector due to the statistical fluctuations in the arrival time of the pulse at the detector output. The existence of an optimum triggering fraction in leading-edge timing with scintillation detectors stimulated the design of a circuit that would always trigger at the optimum fraction of the pulse height for any pulse height [189-190]. This is known as Constant Fraction Discriminator (CFD). The additional benefit of CFD is the elimination of amplitude walk. Here, the input signal is split into two parts: one fraction is attenuated to a fraction ‘f’ of the original amplitude and the other part is delayed and inverted. These two signals are subsequently added to form the constant-fraction timing signal which is a bipolar signal with a zero-crossing time. Since the time of zero-crossing is independent of pulse-amplitude, the CFD delivers virtually a zero walk at the expense of jitter. Walk and jitter are minimized by the proper adjustment of the zero-crossing reference and by selection of the correct attenuation factor and delay. Again time jitter can be reduced by reducing the number of electronic components. One obvious way of doing this is to take the dc coupled anode output from the PM tube where the additional capacitor circuit between anode and CFD can be avoided. Another important modification is to use high gain PM tube so that the amplification of the anode output from the PM tube is not required. The timing resolution from a CFD is better than that from leading-edge timing. With scintillation type of detectors, a fraction somewhere between 0.2 and 0.4 is a reasonable choice.

When a timing application demands picoseconds precision, a **Time to Amplitude Converter** (TAC) is the right solution. TAC converts the time interval between “start” and “stop” signals into voltage. The output of a TAC is a rectangular pulse with a width of a few microseconds and

amplitude that is proportional to the time interval between “start” and “stop” pulses. Typically, the fast CFD outputs are used as the start and stop signals to TAC. By adding a single-channel pulse-height analyzer (SCA) to the output of a TAC, it can be used to identify the coincidence events between two detectors. The SCA output from the TAC acts as the “master gate” to ADC, i.e., only those TAC pulses which fall within the SCA window will be analyzed by the ADC. The SCA threshold can be adjusted to ensure that only the events in the peak are accepted. Subsequently, the SCA output can be used as the coincidence gate when analyzing the energy spectrum from scintillation detector on the ADC. TAC is used for the measurements on time ranges less than 10  $\mu\text{s}$  when time resolution from 10 ps to 50 ns is required. TAC range is adjusted according to the resolution required for that particular measurement. In a  $\gamma\text{-}\gamma$  coincidence measurement, the lifetime of the intermediate level decides the TAC resolution required for that measurement. Another parameter called as Time Per Channel (TPC) is defined for a particular coincidence measurement. For that, time calibration of TAC is performed by inserting cable delays of known length between the timing discriminator output and TAC input. For higher accuracy in time-calibration, a separate time-calibrator can be a better choice. It uses an accurate digital clock to produce stop pulses at precisely spaced intervals after a start pulse.

An **Analogue to Digital Converter** (ADC) measures the maximum amplitude of an analogue pulse and converts that value to a digital number. This digital output is a proportional representation of the analogue amplitude at the ADC input. For sequential arriving of pulses, a histogram is generated representing the spectrum of the input pulse heights. There are two types of ADC, viz., Wilkinson ADC and successive-approximation ADC. In the present work CAMAC 8K ADC which is of second type has been used.

## 2.5. Energy of Photons:

The width of the instrumental response, apart from being dependent on the aforesaid factors, depends strongly on the energy of the photon. The energy of the photons decides the number of information carriers that make up the signal. As the photon energy reduces, the height of the anode pulse reduces and consequently the slope of the leading edge of the pulse is also reduced. So the time uncertainty due to jitter increases and so does the response function.

## 2.6. Data Reduction:

A least-square fitting of the experimental coincidence data with the theoretical expression for the perturbation function, modified with the effect of asymmetry of EFG, frequency distribution and resolving time of the coincidence circuit, using a software Winfit version 3.0.4 [191]. The fitting program extracts the TDPAC parameters, viz.  $\omega_Q, \eta, \delta$ , with errors. The software also carries out cosine type fast fourier transform to find out all the interaction frequencies with their individual populations. From the measured data, the true coincidences are obtained by subtracting background, accidental coincidences and contributions from other coincident  $\gamma$ -rays present in the source. The true number of coincidences can now be written as:

$$C^t(\vartheta) = Mp_1p_2\Omega_1\varepsilon_1\Omega_2\varepsilon_2\varepsilon_cK(\vartheta) \quad (1.105)$$

M is the number of nuclear disintegration per unit time,  $p_i$  the probability per disintegration that the radiation selected in counter  $i$  is emitted,  $\Omega_i$  the solid angle in unit of  $4\pi$ ,  $\varepsilon_i$  the efficiency of channel  $i$  and  $\varepsilon_c$  the efficiency of the coincidence circuit.  $K(\vartheta)$  denotes the directional correlational function as measured with the instrument.

The  $\chi^2$  value indicates a first clue to the fit performance. This value should be as small as possible and in the ideal case close to one. The program is iteration-based meaning that it changes the initial parameters until  $\chi^2$  becomes minimized. In this fitting process, spectra can be

added, inverted or even the theoretical function can be subtracted from the data to visualize potential modulations in the residual spectra. So, all the fractions, present in the sample, can be seen individually. The cross correlation analysis [192] is helpful in choosing good start values for the fit. It can also serve to get an idea of frequency distributions. Suppose we have a single fraction and the two parameters  $V_{zz}$  and the asymmetry parameter. Instead of plotting these two parameters, it is more convenient to plot  $V_{xx}$  versus  $V_{yy}$  or even better to plot  $Y = -2V_{xx}$  versus a linear combination of  $V_{xx}$  and  $V_{zz}$ , i.e.,  $X = 2(2V_{zz} + V_{xx})/\sqrt{3}$ . This is exactly what the Czjzek-plot does. Alternatively, the abscissa and the ordinate can also be expressed in terms of  $\omega_Q(\sqrt{3} + \eta/\sqrt{3})$  and  $\omega_Q(1 - \eta)$ .

Lastly, it is to be kept in mind that the coincidence rate  $K(\vartheta)$  corresponds to the correlation function only under the assumption of centered point sources and point detectors. In order to compare the experimental results with theoretical calculations, the coefficients  $A_{kk}^{exp}$  must be corrected for the deviations from an ideal arrangement. First, it has to be corrected for the finite solid angle of the counters and secondly, the corrections for the finite source extension while working with large sources (e.g., axial source) are also necessary. After having corrected the coefficients  $A_{kk}$  for finite solid angle and finite source extension, one is left with the problem of correcting them for in the source. There are two effects: (i) some of the  $\gamma$ -rays get deflected before being counted. This effect, caused by Compton scattering, tends to smear out the correlation by decreasing the magnitude of the coefficients. (ii) The  $\gamma$ -ray pairs that give coincidences in the  $90^\circ$  direction are on the average less absorbed than those pairs giving coincidences in the  $180^\circ$  direction. Thus one misses more coincidences at  $\theta = 180^\circ$  than at  $\theta = 90^\circ$ . The absorption is very pronounced for low  $\gamma$ -ray energy and sources with high atomic number  $Z$ . If the radioactive source is very thin but surrounded by scattering material,

then only effect (i) is present and correlation is attenuated. The corrections due to scattering in the source are treated in ref. [193].

## **2.7. Conclusion:**

A new methodology of coincidence counting using CAMAC electronics and LaBr<sub>3</sub>(Ce) detectors has been introduced. The present TDPAC spectrometer with LaBr<sub>3</sub>(Ce) detector system has the best energy resolution and reasonable time resolution. It has been demonstrated that the present fast-slow coincidence setup has got several advantages due to the incorporation of LaBr<sub>3</sub>(Ce) detectors and the CAMAC data-acquisition system. Again, the interplay of all the electronic components is also significant for the setup. The energy linearity of the new detector system coupled to fast PM tubes has been studied and the dependence of time resolution of the coincidence circuit has been presented. The behaviour of the detector with other fast PM tube can also be studied in order to optimize the utility of the LaBr<sub>3</sub>(Ce) detector system. The PAC probes having close  $\gamma$ - $\gamma$  cascade can be studied with this new system. The energy gates can be precisely selected due to an excellent energy resolution of the LaBr<sub>3</sub>(Ce) detectors and the systems containing more than one probe can be studied in a single experiment. The present setup can be applied in the measurement of nuclear level lifetime of  $\sim$ ps order due to its excellent time resolution. Hence, the scope of this new TDPAC spectrometer is highly widened both in the field of material science and nuclear spectroscopy.

## Chapter 3. TDPAC Study of Group-IVB Oxides in Bulk Dimension

### 3.1. Bulk Oxides:

#### 3.1.1. Introduction:

In last two decades,  $\text{TiO}_2$  has emerged as one of the most important materials in basic research and found applications in different technologically important areas.  $\text{TiO}_2$ , either in pure form or in doped form, has uses as photocatalyst, energy converter in solar cells, white pigment in paints, sunscreen material, just to name a few.  $\text{ZrO}_2$  is mostly used for its structural properties. The strengthening afforded by its martensitic phase transformation has made it the material of choice for high-temperature applications. Other common applications include fuel cell electrodes, thermal barrier coatings, cutlery and jewelry etc.  $\text{HfO}_2$  is often thought to be a higher temperature substitute for  $\text{ZrO}_2$ . This is mostly due to the similarities in their chemical properties.  $\text{HfO}_2$  has uses in nuclear applications also due to its high neutron absorption efficiency. More recently it has found application as high-k dielectric materials and has proved to be a promising candidate to replace  $\text{SiO}_2$  as the gate oxide in transistors, to obtain electronics with smaller feature sizes.

$\text{TiO}_2$ , among several natural polymorphs, exists in three main crystalline modifications- rutile, anatase and brookite, each of which occurs naturally. Of these, rutile is the most stable form. Other forms are converted into rutile on heating. Each contains 6 coordinate Ti but rutile is the most common form, both in nature and as produced commercially. The rutile structure is based on slightly distorted hcp of oxygen atoms with half the octahedral interstices being occupied by Ti atoms. Anatase and brookite are both based on cubic rather than hexagonal close packing of oxygen atoms, but again the Ti atoms occupy half the octahedral interstices. At room

temperature,  $ZrO_2$  (baddeleyite) and isomorphous  $HfO_2$  have a monoclinic structure in which the metal is 7-coordinated.

In the present work, two nuclear probes  $^{181}Hf/^{181}Ta$  and  $^{111}In/^{111}Cd$  have been introduced into the bulk matrix of Ti, Zr and Hf-oxides during the chemical preparation of these oxides so that the probe can occupy a definite lattice site in these oxide matrices. It is expected that Hf, being the same group element with similar ionic radii in +4 state, can replace the metal site even in the other two oxides, i.e.,  $TiO_2$  and  $ZrO_2$ . For the structure of rutile an axially asymmetric EFG at the Ti site is expected. Anatase, on the other hand, for its structural symmetry, is expected to have an axially symmetric EFG. However, a small non zero asymmetry has been observed with a  $^{44}Sc$  probe [194]. In the present work, two probes have been used to find out the TDPAC parameters. Furthermore, the chemistry of the probes used in this work with the host matrices is also different. The quadrupole interaction parameters can thus be good tools to understand the probe-host interaction. Another aspect concerning the dependence of the EFG on the mother isotope i.e. the origin of the probe or decay mode through which the probe is formed has been addressed in this present work.

Both  $HfO_2$  and  $ZrO_2$  have monoclinic structure with almost similar unit cell dimensions. So it is expected that they will have identical TDPAC parameters. The TDPAC parameters for the bulk have also been measured with two probes, viz.,  $^{181}Hf/^{181}Ta$  and  $^{111}In/^{111}Cd$ .  $In^{3+}$  ion has an ionic radius of  $0.81\text{\AA}$  which matches closely to that of  $Ti^{4+}$  ( $0.68\text{\AA}$ ),  $Hf^{4+}$  ( $0.81\text{\AA}$ ) and  $Zr^{4+}$  ( $0.80\text{\AA}$ ) ions.

### 3.1.2. Sample Preparation:

In case of the  $^{181}Hf/^{181}Ta$  probe, it was produced by neutron irradiation in a thermal neutron-flux of  $\sim 5 \times 10^{13}$  n/cm<sup>2</sup>/s at Dhruva Reactor, BARC, Mumbai by the reaction  $^{180}Hf (n,\gamma) ^{181}Hf$ . The

second probe was produced by the  $\alpha$ -beam facility at Variable Energy Cyclotron Centre, Kolkata via the reaction  $^{nat}\text{Ag}(\alpha, xn)^{111}\text{In}$  at  $E_\alpha = 30$  MeV and  $I = 500\text{-}600$  nA. The  $^{111}\text{In}$  activity was separated in carrier-free form by a radiochemical separation method. The irradiated Ag-foil was dissolved in conc.  $\text{HNO}_3$ , diluted with water and then precipitated as AgCl by addition of Conc. HCl dropwise till complete precipitation. The precipitate was isolated by centrifugation and the solution contained the  $^{111}\text{In}$  –activity in carrier free form. Ti-isopropoxide, Zr-oxychloride and Hf-oxychloride were used as the precursor for  $\text{TiO}_2$ ,  $\text{ZrO}_2$  and  $\text{HfO}_2$  respectively. The probes were introduced in the matrix during their preparations via the coprecipitation method. The probe was added at a very low concentration ( $<0.01$  atom%) so that the crystal structures of the host matrices remain unaffected. The required amount of the precursors was dissolved in dil. HCl and then the probe solution was added to it. The metal-hydroxides were precipitated along with the probe by the addition of ammonia solution. The precipitates were thoroughly washed with water to remove any ammonia. They were then dried and annealed under different conditions to produce the respective oxides. It was observed that  $\text{TiO}_2$  annealed at 823K/4h remained in the anatase phase and it was converted into rutile phase at 1123K/4h. For  $\text{ZrO}_2$  and  $\text{HfO}_2$ , the respective samples were annealed at 1273K for 20h.

### 3.1.3. Results and Discussion:

TDPAC spectra for the anatase and rutile  $\text{TiO}_2$  with  $^{181}\text{Ta}$  probe are shown in Figure 3.1. On the left of the figure are shown the  $A_2G_2$  spectra and the corresponding cosine transforms are shown on the right. From the  $A_2G_2$  spectra, it is seen that rutile gives a sharper pattern than anatase. However, a well-defined pattern of  $A_2G_2$  indicates that the probe atom could occupy a definite lattice site in the present matrices. So, the present method of sample preparation via coprecipitation method is proved to be a very mild chemical method where the probe atom could

occupy definite lattice position during the preparation of the host matrix. Although the TDPAC results for rutile were previously known [195], the same for anatase was measured for the first time. Again the method for sample preparation is also different from the previous works.

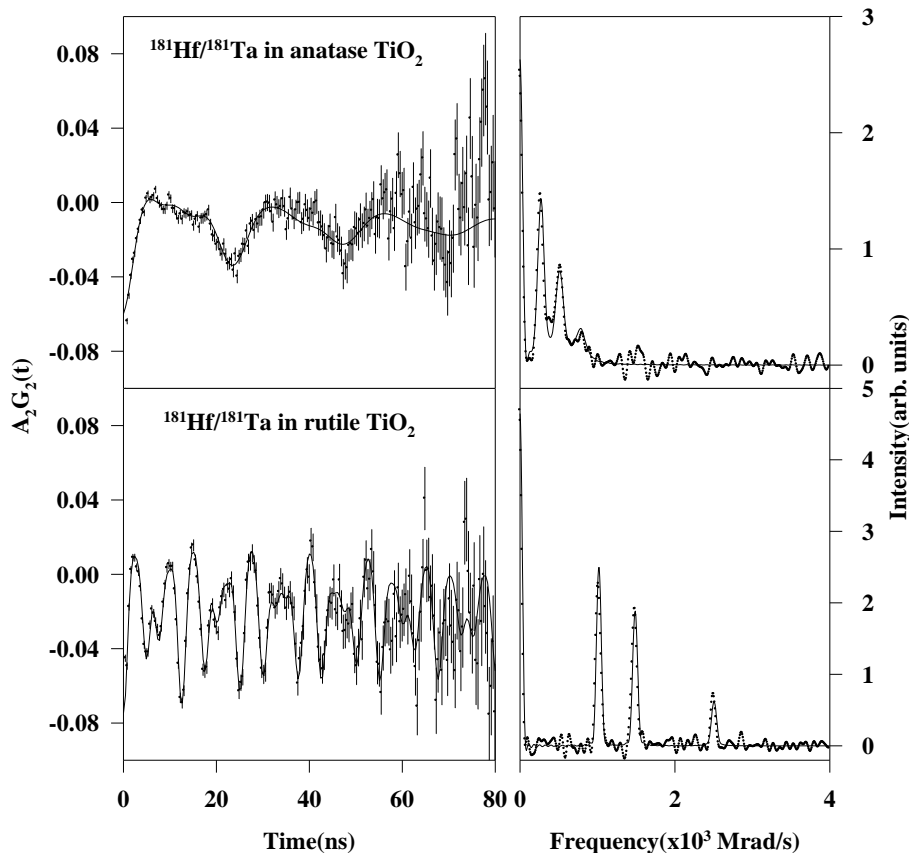


**Figure 3.1:** TDPAC spectra with cosine transform for anatase and rutile with  $^{181}\text{Ta}$  probe.

For both  $\text{HfO}_2$  and  $\text{ZrO}_2$ , the spectra appear to be identical and hence a representative TDPAC spectrum for both  $\text{HfO}_2$  and  $\text{ZrO}_2$  is shown in Figure 3.2. The spectrum represents the monoclinic structure around the probe atom. In case of  $\text{HfO}_2$ , the probe becomes the indigenous probe but in case  $\text{ZrO}_2$ , it is expected that Hf atom could replace the Zr-atom in the  $\text{ZrO}_2$  matrix. The well-defined  $A_2G_2(t)$  pattern confirms that the  $^{181}\text{Hf}$  atom could substitute the Zr-site. Hence

from the TDPAC measurements, it can be concluded that the present probe  $^{181}\text{Hf}/^{181}\text{Ta}$  could occupy the lattice sites in all the three oxides to give well-defined spectra

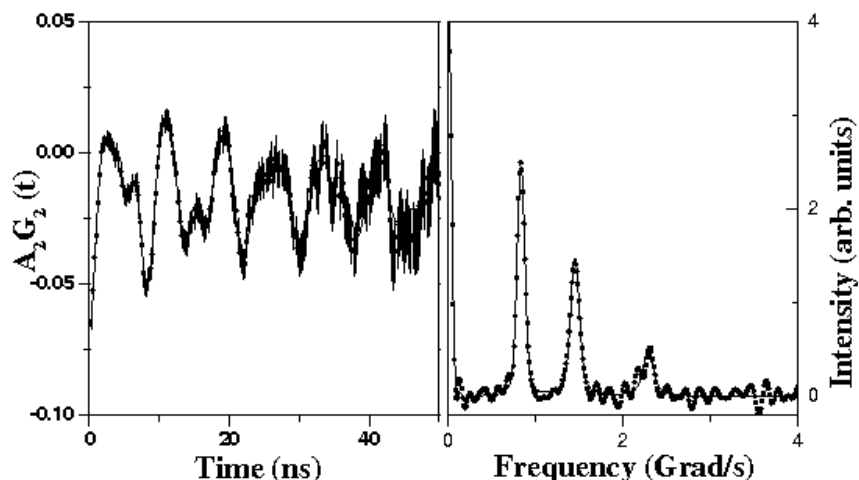


**Figure 3.2:** Representative TDPAC spectra with cosine transform for  $\text{HfO}_2$  and  $\text{ZrO}_2$ .

The TDPAC parameters for these three oxides for  $^{181}\text{Hf}/^{181}\text{Ta}$  probe are furnished in Table 3.1.

**Table 3.1: TDPAC parameters for  $^{181}\text{Hf}/^{181}\text{Ta}$  probe**

Samples	$\omega_Q$ (Mrad/s)	$\eta$	$\delta$ (%)
Anatase $\text{TiO}_2$	44.01(3)	0.22(1)	3.2 (1)
Rutile $\text{TiO}_2$	130.07(9)	0.56(1)	1.1 (1)
Pure $\text{ZrO}_2$	124.1 (5)	0.35 (1)	3.3 (3)
Pure $\text{HfO}_2$	126.1 (1)	0.36 (1)	6.4 (1)

Any probe other than the indigenous atom Ti is an impurity in the  $\text{TiO}_2$  chemical bonding of this impurity with the host matrix is different than in the indigenous matrix leading to the difference in the hyperfine parameters for different probes. The crystal symmetry in anatase is  $4m2$  which implies axial symmetry ( $\eta = 0$ ). However the nonzero  $\eta$  ( $=0.22$ ) for the probe  $^{181}\text{Ta}$  can be

attributed partly due to the relatively large distribution width of  $\omega_Q$ . The poor crystallinity due to the low temperature annealing was probably responsible for this observation. The width of the frequency distribution for the anatase phase in this sample also was relatively large and it could not be improved to the extent of rutile. Another reason for the nonzero  $\eta$  could be the 0.1% impurity due to the probe nucleus in the  $\text{TiO}_2$  matrix. The strength of EFG is more in case of rutile than that in case of anatase. This can be explained in terms of the O-positions in the lattice around the probe nucleus. There are two sets of O- atoms around the probe atom: four O-neighbours (with M-O distance, say,  $d_1$ ) and two O- neighbours (with M-O distance, say,  $d_2$ ) in the  $\text{MO}_6$  octahedra. The calculated values of  $d_1$  and  $d_2$  in anatase and rutile phases vary depending on the probe and the number of electrons to be added over the indigenous Ti ion. It is found [196] that though  $d_1$  increases, there is a decrease in  $d_2$  in rutile compared to those in anatase. Using these M-O parameters,  $V_{zz}$  in rutile has been found to be larger in rutile for the present probe [197].

The second probe  $^{111}\text{In}/^{111}\text{Cd}$ , incarrier free form was introduced into these three oxides via the same coprecipitation method. The TDPAC spectrum for rutile matrix with the  $^{111}\text{In}/^{111}\text{Cd}$  probe is shown in Fig. 3.3.

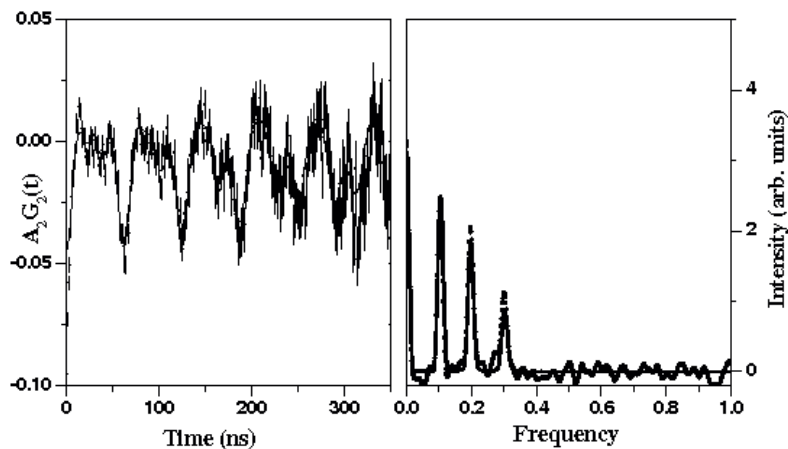


**Figure 3.3:** TDPAC spectra with cosine transform for rutile  $\text{TiO}_2$  with  $^{111}\text{In}$  probe.

In case of rutile structure, the probe could occupy the Ti-sites in the crystal to give the well-defined TDPAC spectrum. A representative TDPAC spectrum for  $\text{ZrO}_2$  and  $\text{HfO}_2$  with the  $^{111}\text{In}/^{111}\text{Cd}$  probe is shown in Fig. 3.4.

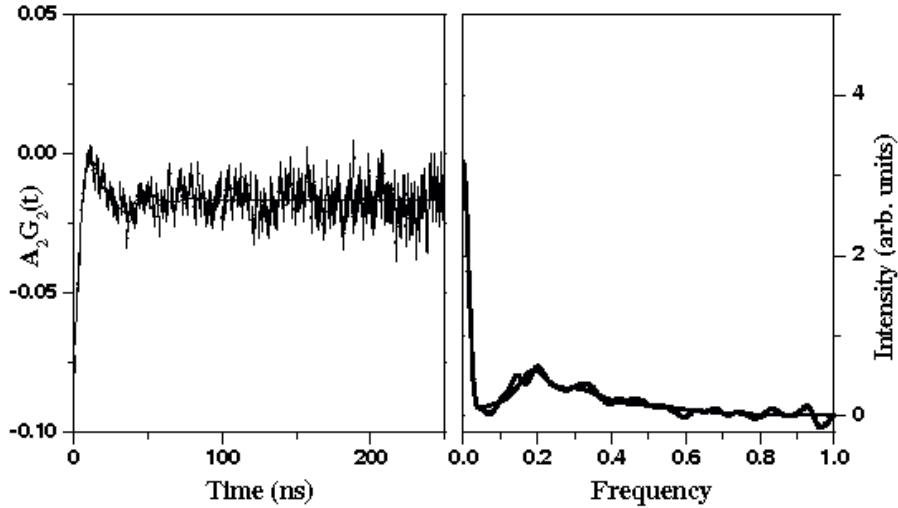


**Figure 3.4:** Representative TDPAC spectrum for  $\text{HfO}_2$  and  $\text{ZrO}_2$  with  $^{111}\text{In}$  probe.

In both  $\text{ZrO}_2$  and  $\text{HfO}_2$ ,  $^{111}\text{In}$  does not seem to occupy a definite site as there is large damping. The TDPAC parameters for the three oxides with  $^{111}\text{In}/^{111}\text{Cd}$  probe are furnished in Table 3.2.

**Table 3.2: TDPAC parameters for  $^{111}\text{In}/^{111}\text{Cd}$  probe**

Samples	$\omega_Q$ (Mrad/s)	$\eta$	$\delta$ (%)
Rutile $\text{TiO}_2$	16.6 (2)	0.2 (1)	1.1 (1)
Pure $\text{ZrO}_2$	25.9 (3)	0.33 (2)	23.3 (3)
Pure $\text{HfO}_2$	27.1 (1)	0.39 (2)	25.4 (1)

$^{111}\text{Cd}$  probe finds definite site in rutile  $\text{TiO}_2$  but not in  $\text{ZrO}_2$  and  $\text{HfO}_2$ . However, in both  $\text{ZrO}_2$  and  $\text{HfO}_2$ , the results are very close which is expected as these two have same crystal structure. To remove the doubt of sample preparation,  $\text{HfO}_2$  was prepared in the same condition with  $^{181}\text{Hf}$  probe. This sample shows clearly definite site occupancy in the TDPAC spectrum. It was thus

confirmed that the monoclinic phase of  $\text{HfO}_2$  and  $\text{ZrO}_2$  is attained under the present annealing condition. So either the  $\text{In}^{3+}$ -ion could not occupy the lattice site in these two oxides while it could occupy the lattice site in rutile or the correlation is attenuated by the preceding decay feeding the cascade.  $\text{In}^{3+}$  ion has a radius ( $0.81\text{\AA}$ ) which is close to those of  $\text{Hf}^{4+}$  ( $0.81\text{\AA}$ ) and  $\text{Zr}^{4+}$  ( $0.80\text{\AA}$ ) ions but different from  $\text{Ti}^{4+}$  ( $0.68\text{\AA}$ ) ion.  $\text{In}^{3+}$  is thus expected to replace more easily the Hf/Zr ions than Ti ion. Another sample was prepared even at a higher annealing condition ( $1673\text{K}/4\text{h}$ ) when the similar spectrum with large damping was obtained. So it might be due to the after effects of EC-decay of  $^{111}\text{In}$  feeding the cascade. The symmetry around the probe atoms is not disturbed while the system could not attain fully crystalline phase. The absence of any time dependant part in the perturbation factor excluded the possibility of oxygen hopping.

### **3.2. Doped Oxides:**

#### **3.2.1. Introduction:**

It is known that either by reducing the dimension of the material or by doping with suitable metal ion, the material property can be tailor-made to adopt it for a particular application. There has been an extensive study on the effect of transitional metal ion doping and rare earth metal ion doping for enhancing the photocatalytic efficiency of titania. The optical properties of  $\text{TiO}_2$  can be tuned properly by suitable dopants for its use in different applications. Again, for another important application of the photocatalytic property of  $\text{TiO}_2$  towards the hydrogen production, it is required to adjust band-gap of  $\text{TiO}_2$ . For this purpose,  $\text{TiO}_2$  is doped with transition metal ions (Fe, Mn, Ni, Cr etc.) and non-metals (N, S, C, B etc.). Noble metals, including Pt, Au, Pd, Rh, Ni, Cu and Ag, have also been found to be very effective for enhancing the photocatalytic efficiency of  $\text{TiO}_2$ . For iron doped  $\text{TiO}_2$  [198] has been found to absorb at higher wavelength than the pure one and it thus suits for a photo catalyst at the visible radiation range. The other

two oxides, namely  $\text{HfO}_2$  and  $\text{ZrO}_2$  have found their applications in different phase including high-temperature phases. There have been a number of studies on the stabilization of high-temperature phases by doping with suitable elements. The doping with a tetravalent cation (same valence as of  $\text{Hf}^{4+}$  and  $\text{Zr}^{4+}$ ) with a larger ionic radius than that of  $\text{Hf}^{4+}$  or  $\text{Zr}^{4+}$  ions leads to an enlargement of the crystal system in order to accommodate the larger ion resulting in the stabilization of the high temperature phases. Again, the doping with a cation having a lower valence than the  $\text{Hf}^{4+}$  or  $\text{Zr}^{4+}$  ions introduces oxygen vacancies which play a key role in the stabilization of the high temperature phases. The Mn-dopant stabilizes the cubic phase of hafnia. The variable valences of Mn leading to the different ionic-sizes of Mn and the oxygen vacancies play an important role to stabilize the cubic phase.

The mechanism of the material modification by doping of certain ion is not clearly understood so far. Several possibilities are: (i) the variable valency of Ti, (ii) the edge sharing of  $\text{TiO}_6$  octahedron, (iii) the unpaired d-electrons of the transition metal ions, (iv) the oxygen vacancies, (v) metal-metal interaction. In the TDPAC experiment one exploits the perturbation of the angular correlation of the cascade photons emitted by the probe nucleus attached to the matrix under study. The perturbation is caused by the interaction between the nuclear quadrupole moment of the probe nucleus and the EFG around it. This EFG and its asymmetry obtained from the TDPAC experiment describe the electron distribution around the probe atom. This is again decided by the arrangement of the atoms in the lattice and the electron sharing between the probe and surrounding atoms or ions. In general, the probe is not the same indigenous atom of the host lattice. The probe thus acts as an impurity in the lattice. However it is added in very insignificant quantity and thus it does not affect the overall lattice structure. But the hyperfine parameters mentioned are not same compared to the situation where the probe and the host atoms are same.

These parameters give the information about the microscopic aspects of the lattice with atomic scale resolution. If the lattice is doped with some foreign impurity in significant concentration, the lattice structure or the electron distribution around the probe atom would change and it would be reflected in the hyperfine parameters. Therefore the TDPAC results would be of great help in describing the possible mechanism of the aforesaid modification of  $\text{TiO}_2$  by doping with different dopants. In the present work, rutile matrix has been doped with one transition element Mn and another same group element Zr. The effect of the doping has been investigated with the TDPAC method. The  $^{181}\text{Hf}/^{181}\text{Ta}$  was used as the PAC probe in the present study.

### 3.2.2. Sample Preparation:

The same coprecipitation method was followed for the preparation of the doped sample. For Mn-doped sample, a required amount of  $\text{MnCl}_2 \cdot 4\text{H}_2\text{O}$  salt was added along with the probe solution to prepare the 5 atom% Mn-doped anatase and rutile samples. For Zr-doped rutile sample, the required amount of Zr was added in the form of  $\text{ZrOCl}_2 \cdot 8\text{H}_2\text{O}$ . The amount of Zr-atom was adjusted to get the  $\text{TiO}_2$  samples of 1, 5 and 10 atom% of Zr.

### 3.2.3. Results and Discussion:

The TDPAC spectrum for 5% Mn-doped anatase  $\text{TiO}_2$  is shown in Fig. 3.5

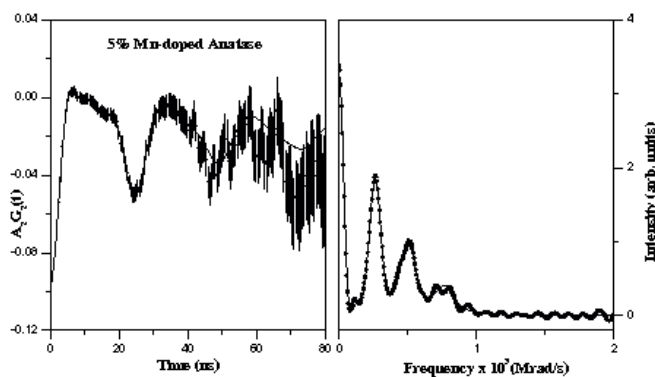


**Figure 3.5:** TDPAC spectrum for 5% Mn-doped anatase  $\text{TiO}_2$ .

and the corresponding spectrum for rutile is shown in Fig. 3.6.

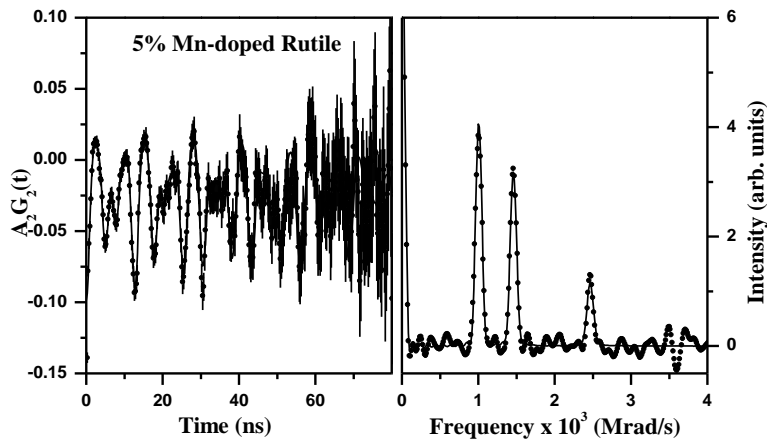


**Figure 3.6:** TDPAC spectrum for 5% Mn-doped rutile  $\text{TiO}_2$ .

The TDPAC parameters for the doped systems match very closely with that for the pure systems. The Mn-ion could occupy definite lattice structure in both anatase and rutile structures. The similar hyperfine parameters indicate that the probe-metal interaction remains same both in pure and doped systems. However, the distribution of frequency in doped systems is higher than that in pure system indicating a higher degree of inhomogeneity in doped matrices.

The TDPAC spectrum for 1% Zr-doped rutile is shown in Fig. 3.7.

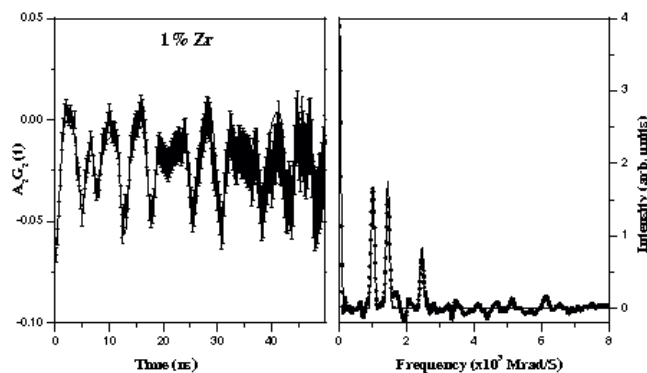


**Figure 3.7:** TDPAC spectrum for 1% Zr-doped rutile  $\text{TiO}_2$ .

The spectrum closely resembles to that for the pure rutile system. The TDPAC spectra for rutile systems doped with 5 and 10 atom% of Zr are shown in Fig. 3.8.

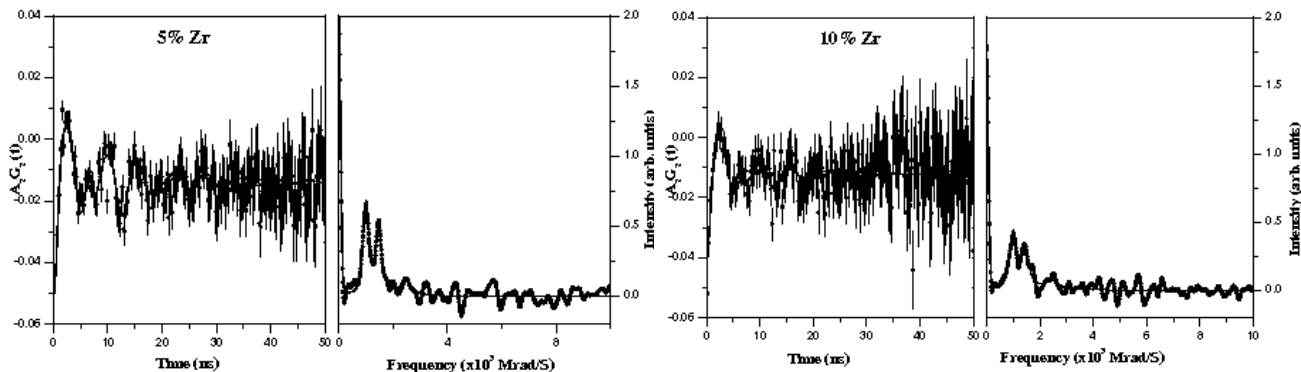


**Figure 3.8:** TDPAC spectra for 5% (left) and 10% (right) Zr -doped rutile  $\text{TiO}_2$ .

The fitted TDPAC parameters are shown in the Table 3.3.

**Table 3.3:** TDPAC parameters for Zr-doped rutile different samples

Samples	$\omega_Q$ (Grad/S)	$\eta$	$\delta$ (%)
Pure rutile	130.07(9)	0.56(1)	1.1(1)
1% Zr/rutile	127.04(4)	0.55(1)	1.3(1)
5% Zr/rutile	126.2(3)	0.58(1)	8.3(9)
10% Zr/rutile	127.44(7)	0.55(3)	12.8(5)

Rutile  $\text{TiO}_2$  has a tetragonal structure with space group  $P4_2/mnm$ . In this, the Ti atom is surrounded by eight O atoms as the nearest neighbors in an octahedral geometry. In the next layer there are eight Ti atoms in the corner of the tetragon. The important feature of the rutile structure is that the O-O contacts in the  $\text{MO}_6$  octahedron are not same and possibly the base of the octahedron is not a square. Similarly the M-O bonds may or may not be of same length. They may be apically elongated or compressed. This tetragonal distortion gives rise to the non zero asymmetry of the EFG [197]. Another important feature of the rutile structure is the role played

by the M-M interaction in the tetragonal distortion. In this present work we looked into this aspect by doping with Zr having same chemical nature of the indigenous Ti atom.  $Zr^{+4}$  has an ionic radius of 0.8 Å which almost resembles to that of  $Ti^{+4}$  (0.7 Å) and hence,  $Zr^{+4}$  is expected to replace the  $Ti^{+4}$  site in the rutile structure. In the present situation, Zr atoms are statistically distributed and there is maximum one Zr atom in each unit cell of the  $TiO_2$  matrix for the 10 atom% sample. In the lower concentration of Zr the chance of one Zr atom in each unit cell is still less. The results in this work indicate that interaction frequency and the asymmetry parameter remain more or less same. But the distribution ( $\delta$ ) of the frequency is increased steadily with Zr concentration. This tells that the M-M interaction between the central atom (here it is the probe  $^{181}Ta$ ) with metal atoms in the next nearest neighbor exists and they are different in case of Zr than when all atoms were Ti. The statistical distribution of the Zr atoms in the unit cell of  $TiO_2$  gives rise to the increase in the width of the frequency distribution. One of the important areas of interest in the rutile structure [199] is the cation-cation interaction which has been looked into in this present work [200] by doping Zr atom being the same chemical counterpart of the indigenous atom Ti. The interaction between the probe and the Zr atom are different than that with the host atoms. This is not reflected in the mean values of the interaction frequency and the asymmetry parameter. The width of the frequency distribution has been found to increase steadily with the Zr concentration. So the hyperfine technique TDPAC can be utilized to investigate the role of dopant in the host matrix and its interaction with the host atoms. The effect of varying concentration of dopant can also be looked into by this microscopic tool.

### 3.3. Radiation Damage Study:

#### 3.3.1. Introduction:

The effect of  $\gamma$ -irradiation on the crystal structure of  $\text{TiO}_2$  has been attempted by following the leaching behavior of  $^{181}\text{Hf}$  from the  $\text{TiO}_2$  matrix as well as by the present hyperfine tool TDPAC. Radioactive wastes remain an imposing problem for safe disposal. Considerable efforts have been extended in this direction. The immobilization processes involve the conversion of the wastes to chemically and physically stable forms in order to minimize the leaching of the radioactivity during storage, transport and disposal. The most frequently applied methods for the immobilization are cementation, bituminization or incorporation into polymers. There has recently been an increased interest in the use of mobile units to condition radioactive waste from nuclear power plants [201]. Immobilisation in a chemically durable matrix has been highlighted for the disposal of long-lived waste.  $\text{TiO}_2$  has great potential as an advanced high-level nuclear waste form as discussed by Adelhelm et al. [202]. Higher actinides have been found to be the major component of high-level nuclear waste. In this work, the leaching behavior of actinides embedded in the  $\text{TiO}_2$  matrix has been simulated using the lower homologue hafnium which can replace the lattice site of Ti in  $\text{TiO}_2$  matrix [197]. After incorporating  $^{181}\text{Hf}$  tracer into  $\text{TiO}_2$  matrix, the leaching property of the resulting matrix was studied in water, sodium chloride and humic acid solutions. The leaching was measured in each of the case by following the radioactivity of  $^{181}\text{Hf}$ .  $\text{TiO}_2$  matrix has also been exposed to  $\gamma$ -radiation field. For this, the leaching of Hf from  $\text{TiO}_2$  matrix has been investigated in different media, like, water, NaCl solution and humic acid solution. The selection of the leaching media stems from the fact that water is the most common medium of contact, NaCl solution simulates the medium of sea-water and humic acid solution represents the soil environment. In all the cases, the leaching has been

monitored by following the radioactivity of  $^{181}\text{Hf}$  tracer. The effect of  $\gamma$ -dose on the crystal structure of  $\text{TiO}_2$  has been investigated with the hyperfine interaction technique, viz., TDPAC and it has been correlated with the leaching behavior of  $\text{TiO}_2$ .

### 3.3.2. Sample Preparation:

A stock solution of  $^{181}\text{Hf}$  tracer with 0.1572mg/ml hafnium was prepared by dissolving neutron-irradiated  $\text{HfCl}_4$  in dilute  $\text{HCl}$ .  $\text{TiO}_2$  was prepared from  $\text{Ti}$ -isopropoxide and  $^{181}\text{Hf}$  was incorporated in situ during the preparation of  $\text{TiO}_2$ .  $\text{TiO}_2$  was prepared from  $\text{Ti}$ -isopropoxide and  $^{181}\text{Hf}$  was incorporated in situ during the preparation of  $\text{TiO}_2$ . 300 $\mu\text{l}$  of stock  $^{181}\text{Hf}$  solution was taken in 10ml of 3(N)  $\text{HCl}$  and 7ml of  $\text{Ti}$ -isopropoxide solution was added to it dropwise resulting in the formation of white lump. It was stirred until the lump was dissolved and a clear solution was obtained. To this solution, ammonia solution was added dropwise to obtain a white precipitate doped with  $^{181}\text{Hf}$ . The white precipitate was filtered off and washed with water several times. Then, the precipitate was dried and crushed to have  $\text{TiO}_2$  matrix doped with  $^{181}\text{Hf}$ . The dry precipitate was powdered and sieved through two meshes of sizes 150 and 200 to obtain the particles of mesh-size 150-200. It was then divided in two equal portions. One half was annealed at 823K for 4h to get anatase  $\text{TiO}_2$  and the other half was annealed at 1123K for 4h to get rutile  $\text{TiO}_2$ , both labeled with  $^{181}\text{Hf}$  tracer. Another set of anatase and rutile samples was prepared following the aforesaid method and then  $\gamma$ -irradiated for 7 days at a dose-rate of 5.3 KGy/h in a  $^{60}\text{Co}$  irradiator at UGC-DAE-CSR, Kolkata. Each sample got an average specific activity of 11,000 Bq/gm with respect to  $^{181}\text{Hf}$  tracer.

### 3.3.3. Leaching Study:

At first, the specific activity of both the anatase and rutile  $\text{TiO}_2$  doped with  $^{181}\text{Hf}$  was measured by taking a weighed amount of  $\text{TiO}_2$  and counting on a well-type  $\text{NaI(Tl)}$  detector. Then, a

measured amount of both anatase and rutile forms of Hf-doped TiO<sub>2</sub> sample before  $\gamma$ -irradiation was taken in two separate 100 mL conical flasks. 20 mL of water was added to each of the mixtures and the mixtures were stirred overnight. Each mixture was filtered through Whatmann-42 filter paper and activity of 2 mL of each of the filtrates was measured. Same procedure was followed for 1% aq. sodium chloride solution and 1% aq. humic acid solution. The TiO<sub>2</sub> samples after  $\gamma$ -irradiation were taken in two separate conical flasks and leaching was followed as mentioned above. The leaching percentage was calculated from the activity of the leached solution and the initial activity of the starting material. Results are shown in Table 3.4.

**Table 3.4:** Result of leaching of <sup>181</sup>Hf from different TiO<sub>2</sub> samples.

Samples	Leaching solutions	% Leaching	
		Anatase	Rutile
Pristine	pH4 Solution	0.43	0.38
	1% aq. NaCl	0.47	0.44
	1% aq. Humic acid	0.54	0.48
After $\gamma$ -irradiation	pH4 Solution	0.35	0.32
	1% aq. NaCl	0.41	0.40
	1% aq. Humic acid	0.52	0.42

#### 3.3.4. Results and Discussion:

The percentage leaching has been obtained from the mean values of the radioactivity. These numbers fall within the statistical uncertainty of the counts. This indicates a negligible leaching

for both the anatase and rutile samples. TDPAC spectrum along with its Fourier transform for a typical rutile sample after  $\gamma$ -irradiation is shown in Fig. 3.9.

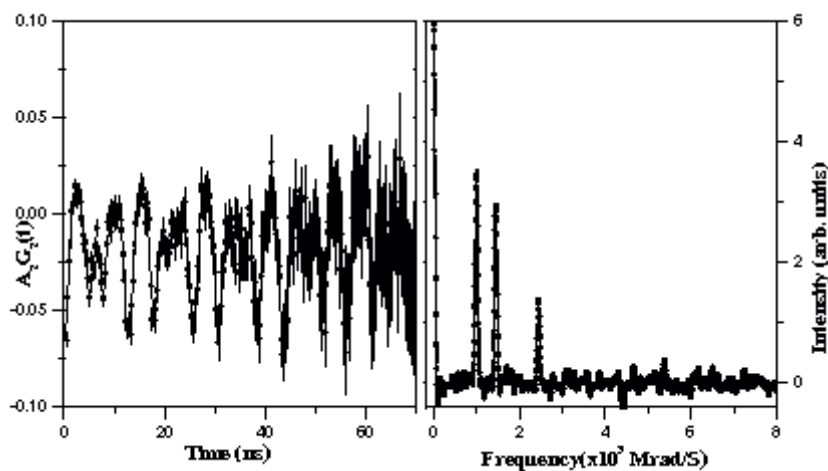


**Figure 3.9:** TDPAC spectrum with cosine transform for  $\gamma$ -irradiated rutile  $\text{TiO}_2$ .

TDPAC parameters for both anatase and rutile  $\text{TiO}_2$  are shown in Table 3.5.

**Table 3.5:** Hyperfine parameters for rutile  $\text{TiO}_2$  before and after  $\gamma$ -irradiation.

Samples	$V_{zz} \times 10^{17} \text{ (V/cm}^2\text{)}$		$\eta$		$\delta$		Comment
	Rutile	Anatase	Rutile	Anatase	Rutile	Anatase	
Pristine	13.65 (10)	4.62 (1)	0.56 (1)	0.22 (1)	0.001 (1)	0.057 (2)	Ref. 197
After $\gamma$ - irradiation	13.41 (02)	4.64 (2)	0.57 (1)	0.23 (1)	0.001 (1)	0.058 (2)	This work

The percentage leaching has been obtained from the mean values of the radioactivity. These numbers fall within the statistical uncertainty of the counts. This indicates a negligible leaching for both the anatase and rutile samples. It is known that rutile form is thermodynamically more stable than anatase form. Rutile is obtained by heating anatase phase at higher temperature ( $\geq 1123\text{K}$ ) and this is an irreversible process. Both the anatase and rutile forms possess tetragonal

structure with rutile form having shorter and hence stronger metal–oxygen bond. Again, as Ti and Hf fall in the same group, Hf is expected to replace Ti from some of the lattice sites in the  $\text{TiO}_2$  crystal. So, Hf–O bond is stronger in rutile form than that in anatase and, hence, Hf is expected to be trapped more efficiently in rutile cage than in anatase cage. However, the present study indicates an almost similar extent of leaching of Hf from the anatase and rutile matrices. This might be due to the fact that the bond energy required for entrapping the Hf-ion in  $\text{TiO}_2$  is sufficient in both anatase and rutile matrices to ensure negligible leaching of Hf-radioactivity. TDPAC parameters shown in Table 3.5 for pure anatase and rutile at  $^{181}\text{Hf}$  site remain unaltered even after  $\gamma$ -irradiation indicating the fact that the Hf–O bond in the matrix is not disturbed by this irradiation. This indicates that the  $\text{TiO}_2$  matrix has so stable crystal structure that it is not disturbed by a long  $\gamma$ -irradiation and Hf is strongly adhered in the  $\text{TiO}_2$  matrix. The present leaching study [203] indicates the strong adherence of Hf-ions in the  $\text{TiO}_2$  matrix in its polymorph, anatase or rutile. Radiation dose has minimal effect on the crystal structure of  $\text{TiO}_2$  and hence on its leaching property. Nuclear probe measurement also corroborates the above observation as the structural change in the  $\text{TiO}_2$  matrix was insignificant after the irradiation with the  $\gamma$ -dose. The defects, if any, produced by the irradiation was so dilute that it could not interact with the probe. The microstructural aspects of the system are also not disturbed.

### **3.4. Study of $\text{HfO}_2$ Fibre:**

#### **3.4.1. Introduction:**

A suitable refractory material which can be heated to elevated temperatures is an essential requirement for an efficient production of the radioactive ion beams (RIB) using the isotope separation on-line (ISOL) technique [204]. At a high temperature, there is a fast release of the product species from the target but at the same time there should not be sufficient vaporization or

sublimation of the target material itself. Among various refractory materials viz.  $\text{HfO}_2$ ,  $\text{Y}_2\text{O}_3$ ,  $\text{CeO}_2$ ,  $\text{Al}_2\text{O}_3$  etc. satisfying the physical, chemical, metallurgical and thermodynamical properties, hafnium oxide ( $\text{HfO}_2$ ) has been considered as a potential RIB target material [204]. The temperature, at which the vapor pressure of the target material reaches  $10^{-4}$  torr, is the highest (2773K) for  $\text{HfO}_2$ . Moreover, Hafnium being the highest Z element among the metal ions of the above mentioned materials, the stopping range of the recoil products is the least in  $\text{HfO}_2$  and thus the reaction products cannot penetrate the surface and would be released faster increasing the efficiency of the RIB intensity. Fibrous targets of  $\text{HfO}_2$  have been used successfully for the production of the  $^{17}\text{F}$  radioactive beam [205]. It has been observed that the  $\text{HfO}_2$  targets can be operated at a higher temperatures (2373-2573K) compared to the others leading to a more efficient release of the required radioactive isotopes [206]. The properties of the targets using  $\text{HfO}_2$  in various forms are studied for the RIB facility which is being developed at Variable Energy Cyclotron Centre (VECC), Kolkata incorporating the traditional ISOL technique [207]. According to the simulation studies, it is found that the temperature at the  $\text{Al}_2\text{O}_3$  target would be 1000-2000K depending on the energy deposited by the proton or alpha beam used for the irradiation. It is expected that the  $\text{HfO}_2$  fibrous targets for the RIB production would be heated to such high temperatures under similar irradiation conditions. In addition,  $\text{HfO}_2$  has several other applications due to its high mechanical hardness, significant thermal stability and high refractive index.  $\text{HfO}_2$  having a high dielectric constant can be considered as a gate dielectric in the form of thin film [208]. A recent study [209] describes the annealing behavior of the  $\text{HfO}_2$  thin film. Since  $\text{HfO}_2$  undergoes a polymorphic structural transition [210] with the temperature from monoclinic (RT-1443K) to tetragonal (1443-2643K) to cubic (>2645K), it is imperative to study the structural transformation of fibrous  $\text{HfO}_2$  in this temperature range. In

this present work, the fibrous  $\text{HfO}_2$  doped with  $^{181}\text{Hf}/^{181}\text{Ta}$  probe was studied using the TDPAC technique where  $^{181}\text{Ta}$  occupying the Hf sites acted as a TDPAC probe.  $\text{HfO}_2$  fibrous samples were annealed at different temperatures in 1000-2000K range and the structural aspects were investigated in the samples annealed at such high temperatures using TDPAC technique.

In order to understand the TDPAC results obtained from the  $^{181}\text{Ta}$  doped  $\text{HfO}_2$  fibrous sample and also the annealing effects on these samples, we performed the first principle electronic structure calculations based on density functional theory (DFT) [211] using WIEN2K code [212]. We first studied the electronic structures of the bulk  $\text{HfO}_2$  as we expect that understanding the electronic distribution around the probe  $^{181}\text{Ta}$  and sources contributing to the electric field gradient (EFG) at the probe site in a bulk sample would lead to a better understanding of the changes that would occur when a fiber or the thin film of  $\text{HfO}_2$  is prepared and annealed thereafter.

### **3.4.2. Experiments and Measurements:**

The  $\text{HfO}_2$  fiber (make: Zicar Zirconia Inc. USA; purity: 99 wt%) of diameter 6-7 $\mu\text{m}$  and density 1.21  $\text{g}/\text{cm}^3$  was used in the present experiment.  $^{181}\text{Hf}$  tracer was produced by  $^{180}\text{Hf} (n, \gamma)^{181}\text{Hf}$  irradiating  $\text{HfO}_2$  fiber in a thermal neutron flux of  $1.0 \times 10^{13}$  neutrons per  $\text{cm}^2$  per second in DHRUVA reactor at Bhabha Atomic Research Centre, Mumbai, India. A part of the irradiated sample was annealed at 1173K for 6h and other part at 1673K for 6h. Then both the samples were counted for TDPAC at room temperature. The inactive counterparts of the sample, annealed under identical conditions, were used for the XRD and SEM measurements. Bulk  $\text{HfO}_2$  was prepared by precipitating hafnium hydroxide  $\text{Hf}(\text{OH})_4$  from  $\text{HfCl}_4$  solution by adding ammonia solution in presence of  $^{181}\text{Hf}$  tracer. This precipitate was centrifuged, dried and heated at 1173K for 6 h. This sample was then counted on the TDPAC setup.

### 3.4.3. Results and Discussion:

XRD spectra showed in Fig. 3.10 indicate the lines to correspond to the typical monoclinic  $\text{HfO}_2$ . However, a small increase in the width of the XRD peaks is observed with annealing temperature. This can be qualitatively explained as a partial loss of crystallinity in the  $\text{HfO}_2$  fiber. A similar trend has also been observed in the TDPAC parameters as mentioned below.

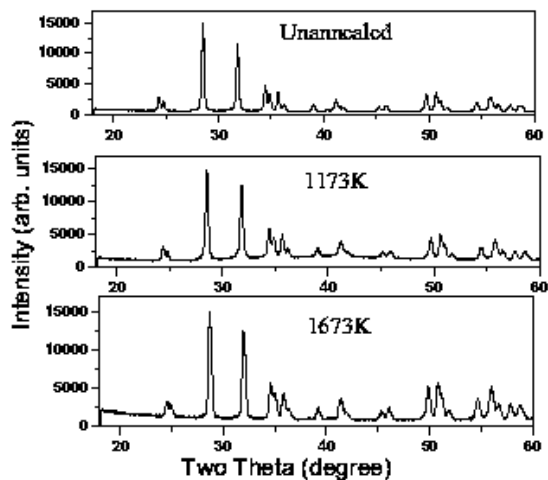


**Figure 3.10:** XRD spectra of the  $\text{HfO}_2$  fiber annealed at different temperatures.

SEM picture shown in Fig. 3.11 indicates that the fiber, annealed up to 1673K, does not undergo any significant change in its dimension of 6-7 $\mu\text{m}$ .

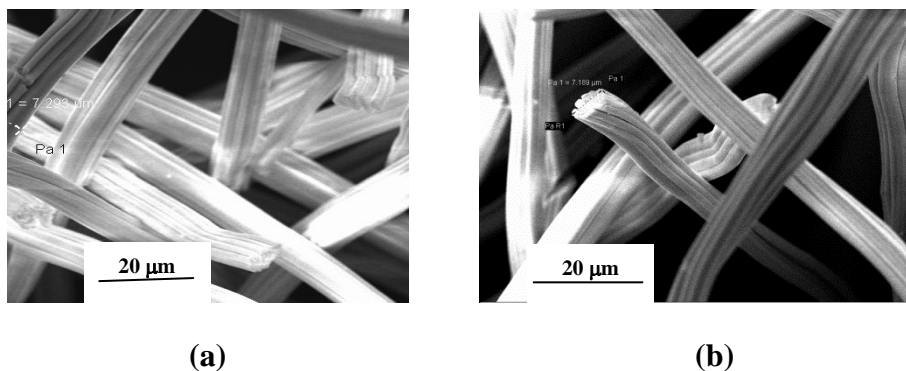


**Figure 3.11:** SEM picture of  $\text{HfO}_2$  fiber annealed at (a) 1173K and (b) 1673K.

TDPAC spectra shown in Fig. 3.12 indicate no change in the electronic structure around the probe atom for all the three samples. However, a small increase in the frequency distribution as shown in Table 3.6 may be attributed to a minor structural change with temperature.

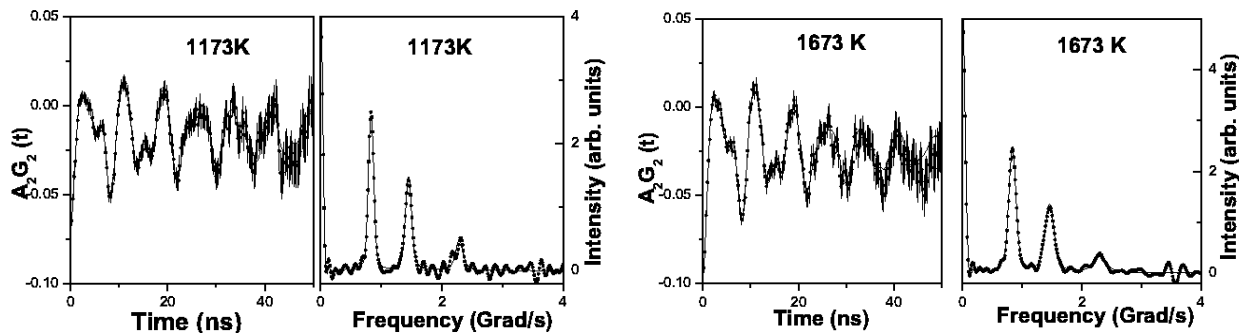


**Figure 3.12:** TDPAC spectra for the HfO<sub>2</sub> fiber annealed at different temperatures.

**Table 3.6:** Results for the TDPAC measurements of HfO<sub>2</sub> fiber

HfO <sub>2</sub> fiber	$V_{ZZ} \times 10^{21}$ (V/m <sup>2</sup> )	$\eta$	$\delta$ (%)
<b>Unannealed</b>	13.08 (1)	0.35(1)	2.6(2)
<b>Annealed at 1173K</b>	13.01 (1)	0.36(1)	3.0(1)
<b>Annealed at 1673K</b>	13.08 (1)	0.35(1)	3.2(2)
<b>Bulk HfO<sub>2</sub></b>	13.04 (2)	0.34 (1)	2.4 (2)

### 3.4.4. Wien2K Calculation:

The Linearized Augmented PlaneWave (LAPW) method has proven to be one of the most accurate methods for the computation of the electronic structure of solids within density functional theory. A full-potential LAPW-code for crystalline solids has been developed over a period of more than twenty years. A first copyrighted version was called **WIEN** and it was published by P. Blaha et al. [213]. A new version WIEN2k is based on an alternative basis set. This allows a significant improvement, especially in terms of speed, universality, user-friendliness and new features.

Ab-initio study of the Ta-doped HfO<sub>2</sub> bulk samples has recently been done [214] where the effect on EFG parameters around the probe atom due to the charge state considerations has been observed but it has not been elucidated. In the present work, the electronic structure calculations were performed based on the density functional theory (DFT) and the augmented plane wave plus local orbital (APW+LO) method as embodied in the WIEN2K code was used in order to understand the effect of charge state on the EFG parameters. The exchange and correlation effects were included in our calculation using Generalized Gradient Approximation (GGA) [215]. The basic input requirement for these electronic structure calculations of a crystal are the cell settings and lattice parameters. These required structure parameters used in our calculations are the same as mentioned earlier. The crystal structure of HfO<sub>2</sub> is monoclinic where there are four HfO<sub>2</sub> molecules in each unit cell and each Hf metal ion is surrounded by the seven oxygen atoms. Since the doping of HfO<sub>2</sub> samples with <sup>181</sup>Ta probes for the TDPAC studies were produced by irradiating the HfO<sub>2</sub> samples with thermal neutrons, the recoil of the probe nucleus is negligible. However, the recoil due to the prompt gamma emission can not be neglected. Though there is an evidence of recoil induced damage [209], it is expected that these will be removed when the sample is annealed at high temperatures in the present experiment. As we know that the electric field gradient which determines the hyperfine parameters being extremely sensitive to the electronic environment around the probe site, the charge state of the probe atom is of a prime consideration. In order to decide whether Ta would remain in 5+ state at the probe site as it would exist in a pure tantalum compound or there would be a change in the charge state of the probe Ta atom, two independent calculations were performed. In one case it was assumed that there is no change in the charge state of the dopant Ta atom as it replaced Hf atom and called it as neutral state calculations. It was found partially filled impurity levels having Ta “d” and

oxygen “*p*” character. In the second case referred to as the charge state calculation, it was assumed that tantalum would act as a donor impurity. So, one valence electron was removed from the unit cell, neutralized the charge by adding one electron to the homogeneous negative background and thereafter performed the self consistent calculations. It is interesting to note that the variation in EFG parameter around the probe atom Ta considering the neutral and charge state configurations is in agreement with the earlier work [213]. There is a speculation that Ta exists in two different charge states in Ta-doped monoclinic HfO<sub>2</sub> and considerable amount of the magnetic moment can be induced depending on impurity charge state [216]. The  $V_{zz}$  component of EFG for different *l*-projected states was determined and the contribution to EFG at Ta site from the electrons having different *l*-values was studied. In the calculation, one of the Hf atoms of the host HfO<sub>2</sub> was replaced by a probe Ta atom in the unit cell i.e. a Ta concentration of 25% (Hf<sub>0.75</sub>Ta<sub>0.25</sub>O<sub>2</sub>) was considered as shown in Fig. 3.13.

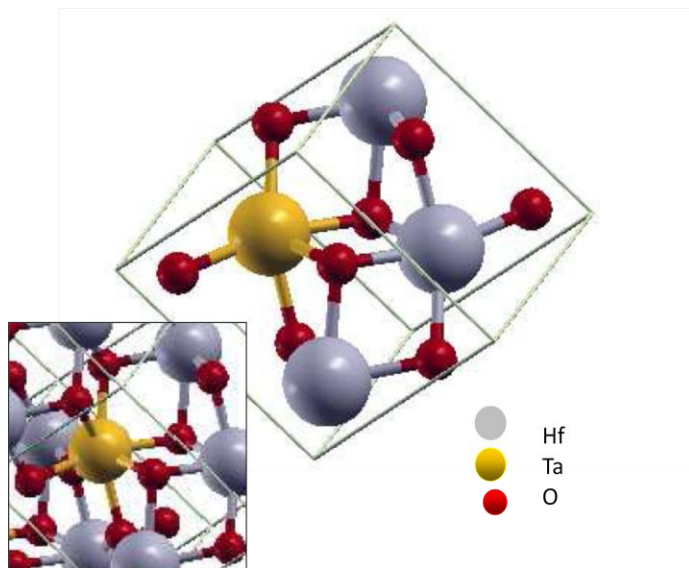


**Figure 3.13:** HfO<sub>2</sub> crystal doped with Ta

The probe atom Ta also exhibits a sevenfold-coordination with the Oxygen atoms as shown in the left panel of figure4. When a group-VB tantalum atom replaces a group-IVB hafnium atom,

charge state consideration is of a fundamental significance. In HfO<sub>2</sub> crystal, hafnium is expected to exist in 4+ charge state whereas Ta, the substituted probe atom normally exists in 5+ charge state. Electronic structure calculations based on DFT for Ta atom replacing an Hf-atom in HfO<sub>2</sub> shows that the EFG at the Ta site considering Ta having a charge  $q=+1$  has a reasonable agreement with that of the experimentally measured value. In Table 3.7, it is seen that the EFG value at the probe Ta site is comparatively very large when the neutral state calculations were performed and *l*-state projections indicate that the EFG at the probe Ta site has unusually large contribution from the outer *d*-electrons. On the other hand, when the charged state of Ta was considered, essentially one outer d-electron was delocalized and as a result the d-electron contribution to total EFG at the probe Ta site reduced drastically and it was found that the maximum contribution to EFG was from inner p-electrons.

**Table 3.7:** Comparison between neutral and charged state calculations for <sup>181</sup>Ta

doped HfO<sub>2</sub> bulk samples

HfO <sub>2</sub> sample	$V_{zz}(\times 10^{21} \text{ V/m}^2)$	$\eta$	Calculated EFG components ( <i>l</i> projections)		
Experimental	13.06	0.34	p	D	s-d
Neutral	18.78	0.18	12.07	7.10	0.21
Charged	14.62	0.44	14.37	1.27	0.23

In order to confirm the charge state of the Ta in HfO<sub>2</sub>, the densities of states (DOS) vs energy for the Ta doped HfO<sub>2</sub> obtained from the electronic structure calculations using WIEN2K code considering the charge state of Ta and the neutral state of Ta has been plotted in Fig. 3.14.

Comparing the total DOS (lowest panel) and the f-state projection of impurity Ta (middle panel), a dramatic change in the density of states for the f-electrons of Ta atom was observed but with no significant difference in the density of states of d-electrons (top panel).

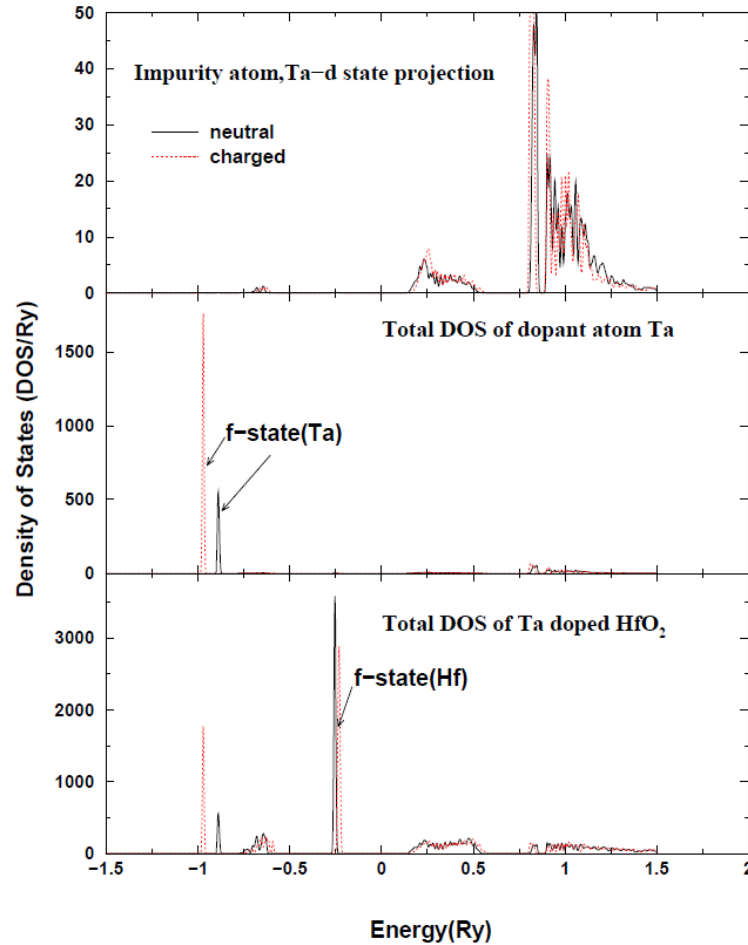


**Figure 3.14:** Lowest panel: Plot of Total Density of states (DOS) vs energy for Ta doped  $\text{HfO}_2$ . Middle panel: Plot of Atom (Ta) projected DOS vs energy, Upper panel: Plot of projected DOS vs energy of probe Ta in  $\text{HfO}_2$ .

The shift in the energy state of the f-electrons indicates that these electrons are more bound when charged state is considered. As the f-electrons screen the outer d-electrons, a reduction in the contribution of the d-electrons was observed and the contribution of the inner p-electrons to EFG is enhanced due to the shift in f-level electrons. Thus we conclude from the experimental

measurement of EFG and electronic structure calculations that the probe Ta in the  $\text{HfO}_2$  matrix would remain in a charged state configuration and the inner p-electrons would contribute the most to the EFG at the probe Ta site.

The density of states calculated for Ta doped  $\text{HfO}_2$  samples were compared with that of pure undoped  $\text{HfO}_2$ . In Fig. 3.15, it was found that the density of states at the neighboring Hf site Hf1, Hf2, Hf3 calculated considering the neutral state of Ta, essentially remain unaffected when the  $\text{HfO}_2$  sample is doped with Ta (upper panel) compared to pure  $\text{HfO}_2$  as shown in the lowest panel.

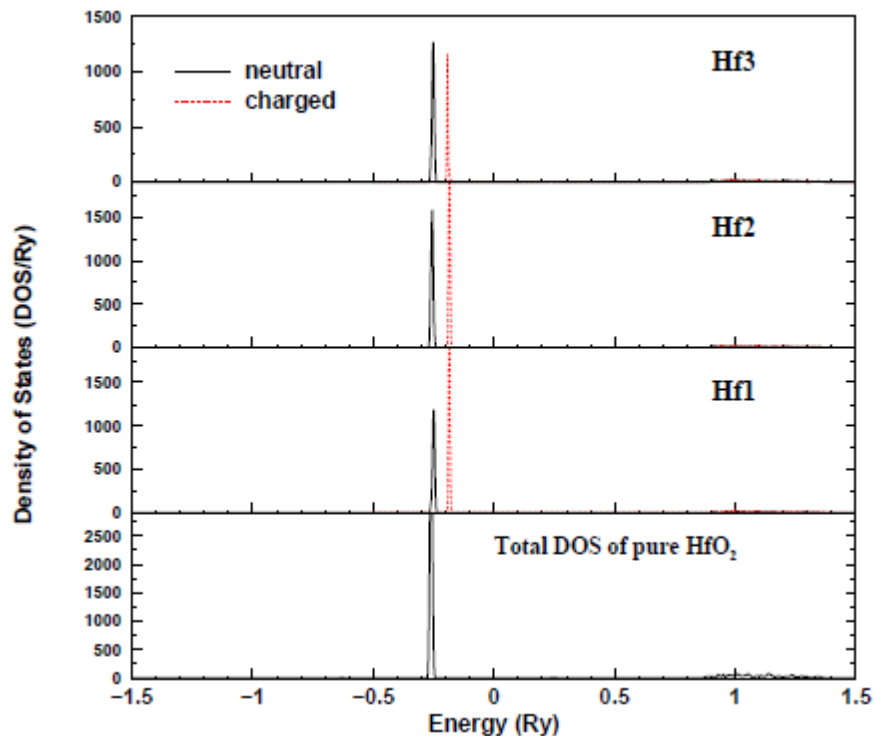


**Figure 3.15:** Lowest panel: Plot of Density of states vs energy for pure  $\text{HfO}_2$ . Upper panel: Plot of atom projected density of states vs energy of nearest neighbor of probe Ta.

This is due to the seven-fold coordination of oxygen atoms surrounding the probe and thus EFG measurements give only localized information around the probe Ta. As a result, 6-7  $\mu\text{m}$  diameter fiber of  $\text{HfO}_2$ , behaves as a bulk sample and no change in EFG parameter is observed during

experimental measurement of doped fibers. As some structural stress developed when Ta replaced Hf in HfO<sub>2</sub>, the system was allowed to undergo structural relaxations and calculations were performed at several stages till the stress was minimized.

**Table 3.8:** Change in EFG parameters after relaxation of atomic position.

Configuration	Total Energy(Ryd)	$V_{zz}$ ( $\times 10^{21}$ V/m <sup>2</sup> )	$\eta$
HfO <sub>2</sub> -1	-123045.70388	14.843	0.44
HfO <sub>2</sub> -2	-123045.71232	14.977	0.42
HfO <sub>2</sub> -3	-123045.71386	14.986	0.41
HfO <sub>2</sub> -4	-123045.71428	14.987	0.42
HfO <sub>2</sub> -5	-123045.71433	14.989	0.42

In Table 3.8, a little variation in total energy of HfO<sub>2</sub> doped with Ta indicates that the sample has stable configuration even though atomic positions of the neighboring atoms of Ta probe are slightly changed. The existence of the several stable configurations with slightly varying EFG explains the broad distribution in delta when the experimental measurements at room temperature were performed for the sample annealed at 1173K and 1673K.

So the results from XRD, SEM and TDPAC study indicate little change in the structure of the HfO<sub>2</sub> fiber annealed upto 1673K. But no phase transition could be observed under the present experimental condition. Thus the HfO<sub>2</sub> fiber can well be used as the target material for RIB production. HfO<sub>2</sub> fiber of dimension 6-7  $\mu$ m has essentially the same TDPAC patterns as those of the bulk HfO<sub>2</sub>. This indicates no difference between the structures of the bulk and the fiber HfO<sub>2</sub>. However, there is a signature of slight loss of crystallinity in HfO<sub>2</sub> annealed at 1173K and 1673K as indicated by the small increase in quadrupole frequency distributions with annealing temperature. DFT calculation of the HfO<sub>2</sub> system indicates that the <sup>181</sup>Ta probe is in the charged

state in the lattice position and the contribution of the EFG is mainly due to the p-electrons. Density of states indicates that the doping with Ta does not affect the neighboring Hf atoms of the host. As a result, EFG parameters of the fiber having 6-7  $\mu\text{m}$  diameter doped with Ta are expected to remain unaltered compared to those of bulk  $\text{HfO}_2$ .

### **3.5. Conclusion:**

The present TDPAC study in bulk dimension delivers the versatility and sensitivity of the present hyperfine technique TDPAC. A general trend of higher  $V_{zz}$  in the rutile phase than in the anatase phase has been observed in this work. This is true for other probes as well and was explained in terms of the O-positions around the probe nucleus. A similar  $V_{zz}$  value for  $\text{HfO}_2$  and  $\text{ZrO}_2$  systems has also been explained in terms of their similar crystal structure. In general, it has been demonstrated that the TDPAC parameters for a crystal system have a direct correlation with the lattice parameters of that crystal system. The TDPAC parameters for the pure group-IVB oxides in bulk dimension measured with the new coincidence setup involving the latest  $\text{LaBr}_3(\text{Ce})$  detectors would be a guideline for the study of these oxides in other dimensions as well as in doped forms. The method has been applied in the doped anatase and rutile systems for the first time. The minute effect on the crystal structure of the system with increasing dopant concentration has been demonstrated with the TDPAC technique. These data would also offer a guideline to study the doped nano  $\text{TiO}_2$  having versatile applications. The stability of the  $\text{TiO}_2$  structure against  $\gamma$ -irradiation as studied by TDPAC in the present work would inspire a further study of this system for the immobilization of long-lived nuclear waste. The present work on the  $\text{HfO}_2$  fiber concludes that this oxide does not undergo either any significant structural change or any phase transition and hence it can be used as the target material for RIB production upto an annealing temperature of 1673K.

## Chapter 4. TDPAC Study of Group-IVB Oxides in Low Dimension

### 4.1. Phase Transition in Nano TiO<sub>2</sub>:

#### 4.1.1. Introduction:

TiO<sub>2</sub> among several natural polymorphs exists in two main crystalline modifications- anatase and rutile. Anatase is kinetically while rutile is thermodynamically stable. The temperature range at which the phase transition from anatase to rutile takes place is 673K -1473K for bulk TiO<sub>2</sub>. The transformation from rutile to anatase for the bulk is forbidden. But at nano dimension (<16nm) phase transformation reverses from rutile to anatase. This is attributed to a higher surface energy of rutile than that of anatase (1.32 J.m<sup>-2</sup> for anatase and 1.91 J.m<sup>-2</sup> for rutile). Therefore, the stability of either polymorph has an important dependence on the size of the crystallite. This aspect of the average size dependence on the anatase to rutile phase transformation has been studied by several authors. In different applications, it is either the anatase or the rutile form which is required. For example, in photocatalysis, anatase shows a higher activity than the rutile form. Since the photocatalysis process occurs on the surface, crystallites with low dimension are more useful. Therefore it is important to understand the nature of the surface and the phase stability with respect to the size of the crystallite. In certain situations, a high temperature sintering of TiO<sub>2</sub> is required for its application in nuclear waste disposal. This process is enhanced by phase transformation which again has a strong dependence on the size of the crystallites. It is thus evident that the anatase to rutile phase transformation is an important aspect of TiO<sub>2</sub> and this is required to be understood in order to use TiO<sub>2</sub> for different applications.

The probable mechanism for the anatase to rutile phase transformation was suggested as the nucleation of rutile on the coarser TiO<sub>2</sub> (anatase) due to the cooperative movement of Ti & O atoms. The observation of the growth of the rutile polymorph during the transformation was

explained as the formation of rutile crystal and its rotation around another particle, either anatase or rutile, to convert the smaller rutile particle into a bigger rutile particle when they attach each other in a favorable crystallographic orientation. In this work, the issues related to the role played by the coarsening of smaller crystallites and also the surface/bulk mass transfer in the temperature mediated transformation process have been addressed. The nuclear technique TDPAC having atomic scale resolution has been used to study these processes. The hyperfine parameters for bulk anatase and rutile TiO<sub>2</sub> [197] have been used to characterize the different phases during the phase transition process. In the present work, the hyperfine parameters obtained after annealing the sample at different temperatures have been used to address the surface-bulk mass transfer and its role in the phase transformation taking place in 70 nm TiO<sub>2</sub>.

#### **4.1.2. Sample Preparation:**

The method of preparing bulk TiO<sub>2</sub> doped with the nuclear probe has already been described for both anatase and rutile phases. The sample was annealed at different temperatures and counted on the coincidence setup mentioned above. The PAC parameters were measured for anatase and rutile TiO<sub>2</sub> and used for the subsequent measurements. Commercially available anatase TiO<sub>2</sub> was ball milled to bring down the average size of TiO<sub>2</sub> to ~70 nm. This size and its distribution were confirmed by AFM and XRD. A stock solution of <sup>181</sup>Hf tracer was made by dissolving the neutron irradiated HfCl<sub>4</sub> salt in water. A few sets of samples were prepared using this tracer. In all the cases, adsorption of <sup>181</sup>Hf activity on the aforesaid nano crystallites of TiO<sub>2</sub> was carried out in pH7 solution from solid solution interface by adding a weighed (300 mg) amount of the nano TiO<sub>2</sub> in 25 ml of solution containing the <sup>181</sup>Hf tracer. This mixture was stirred continuously for two hours at room temperature to reach the equilibrium. The <sup>181</sup>Hf labeled TiO<sub>2</sub> was then washed with water several times and dried at 373K to remove any moisture from TiO<sub>2</sub>. One such

sample was counted on TDPAC spectrometer and the corresponding TDPAC spectrum has been marked as S1. Another set of samples was prepared by annealing the dried TiO<sub>2</sub> mentioned above, at 823K for 4h and 8h followed by counting on TDPAC spectrometer. The corresponding spectra have been named as S2 and S3 respectively. The fourth sample consisted of the rutile TiO<sub>2</sub> prepared by heating the starting anatase TiO<sub>2</sub> at 1123K for 4h. <sup>181</sup>Hf tracer was then adsorbed on this rutile sample by the same method as described above. Then this <sup>181</sup>Hf-adsorbed rutile TiO<sub>2</sub> was annealed at 1123K for 4h followed by counting for the TDPAC measurement. The corresponding spectrum is S4. The next set of samples was prepared by annealing the anatase TiO<sub>2</sub> at 1123K for 4h and 8h. Those samples were then counted on the TDPAC spectrometer and the spectra are S5 and S6 respectively. The last sample was prepared by annealing the anatase TiO<sub>2</sub> at 1223K for 8h and counted for TDPAC. The corresponding spectrum has been marked as S7.

#### 4.1.3. Results and Discussion:

The size distribution as determined by the AFM measurement for ball-milled TiO<sub>2</sub> particles is shown in Fig. 4.1.

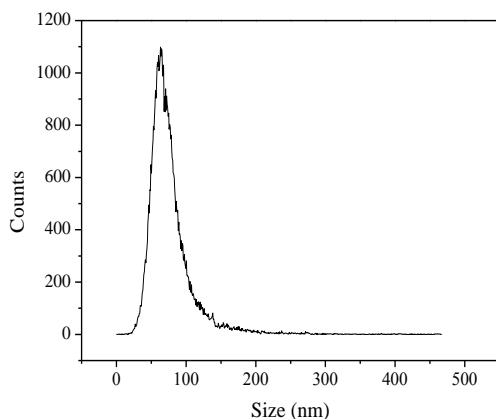


**Figure 4.1:** Size distribution of the TiO<sub>2</sub> nanoparticles.

The figure indicates a mean size of 70 nm. The XRD patterns for TiO<sub>2</sub> samples annealed at different temperatures are shown in Fig. 4.2.

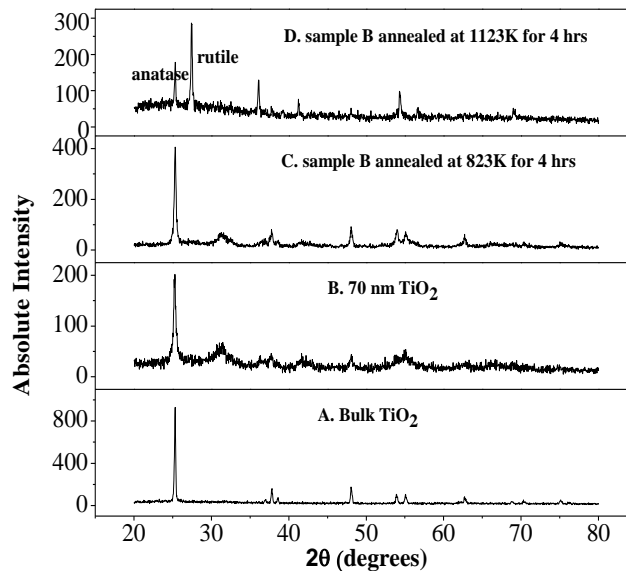


**Figure 4.2:** XRD spectra of TiO<sub>2</sub> annealed at different temperatures.

The widths of the anatase peak at different stages of annealing are shown in Table 4.1.

**Table 4.1:** Width of XRD peak for TiO<sub>2</sub> samples annealed at different temperatures

Sample	Centre(2θ degrees)	Width(2θ degrees)
Bulk TiO <sub>2</sub>	25.287	0.172
70 nm TiO <sub>2</sub> (ball milled)	25.248	0.357
70 nm TiO <sub>2</sub> annealed at 823K for 4 h	25.303	0.262
70 nm TiO <sub>2</sub> annealed at 1123K for 4 h	25.301	0.150

The detailed description of the seven samples along with their annealing condition is given in Table 4.2. The temperature and duration of annealing for each sample along with their existing phases after annealing are enlisted in the table.

**Table 4.2:** Description of the TiO<sub>2</sub> samples with annealing condition

Notation	Description	Annealing Temperature (K)	Duration(h)	Remarks
S1	Anatase	373	2	Probe on the surface; No Phase Transition
S2	Anatase	823	4	Probe on the surface; Particle growth without Phase Transition
S3	Anatase	823	8	Probe in the bulk; Partial Phase Transition
S4	Rutile	1123	4	Diffusion of Probe into bulk
S5	Anatase	1123	4	Probe in the bulk; Partial Phase Transition
S6	Anatase	1123	8	Partial Phase Transition with higher rutile population
S7	Anatase	1223	8	Complete Phase Transition

The hyperfine parameters for different samples after each annealing along with the bulk modifications are furnished in Table 4.3:

**Table 4.3:** TDPAC parameters for different samples

Sample	$\omega_Q$ (Mrad/sec)		$\eta$		$\delta$ (%)		Population (%)	
	Anatase	Rutile	Anatase	Rutile	Anatase	Rutile	Anatase	Rutile
Anatase	44.01(3)	-	0.22(1)	-	5.1(2)	-	100	0
Rutile	130.07(9)	-	-	0.56(1)	-	1.1(2)	-	100
S1*	82.9(4)	-	0.36(11)	-	32.0(2)	-	100	-
S2*	77.5(5)	-	0.62(7)	-	25.2(5)	-	100	-
S3	44.6(2)	132.4(1)	0.30(2)	0.53(2)	0.0(1)	7.9(1)	5	95
S4	-	134.0(7)	-	0.51(1)	-	5.2(5)	0	100
S5	44.0(6)	130.9(3)	0.27(4)	0.54(2)	6.2(3)	1.1(6)	21	79
S6	44.0(7)	130.3(1)	0.30(5)	0.55(1)	0.1(1)	0.3(1)	8	92
S7	-	130.5(1)	-	0.55(1)	-	1.0(1)	0	100

\*TDPAC parameters do not correspond to either anatase or rutile.

TDPAC spectra for  $\text{TiO}_2$  samples annealed at different temperatures and for different duration are shown in Fig. 4.3 with the individual spectrum denoted as S1, S2 and so on.

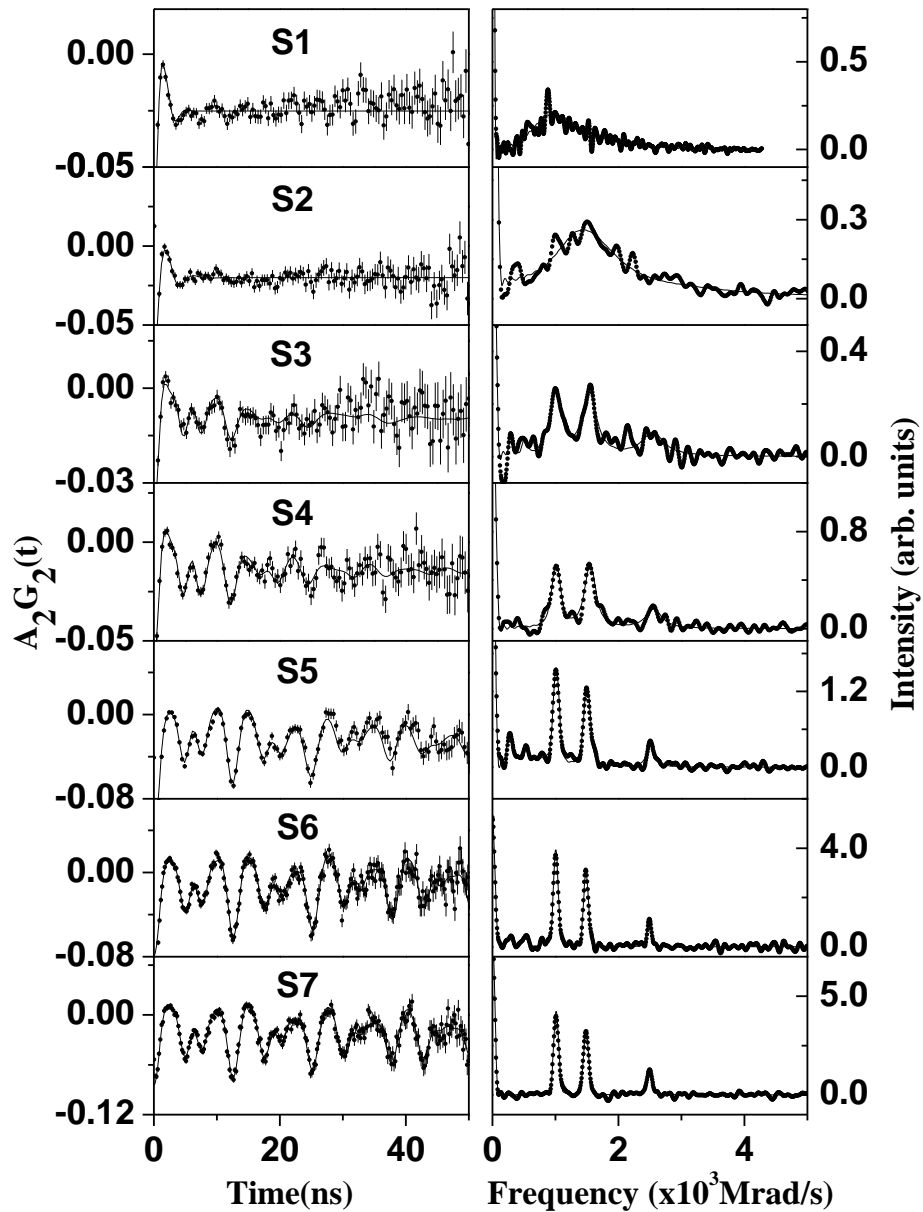


**Figure 4.3:** TDPAC spectra of nano  $\text{TiO}_2$  samples annealed at different temperatures

Sample S1 shows a broad frequency distribution. S2 also shows a frequency distribution which is narrower than that of the S1. In S3 the frequency spectrum indicates the peaks for a mixture of anatase and rutile phases. The spectrum in S4 indicates the presence of only the rutile phase. To get a qualitative idea of the diffusion rate of the  $^{181}\text{Hf}$  tracer in the anatase and the rutile phases, the samples were annealed for different durations. S5 and S6 are the spectra for the annealing time of 4h and 8h respectively. Both these spectra indicate the presence of the mixture of both the anatase and the rutile phases but with the reduction of the anatase component for longer annealing time. S7 shows the unique spectrum of the rutile phase indicating the complete transformation into the rutile phase.

In this paper we address some aspects of  $\text{TiO}_2$  crystallite with a particular reference to the phase transition from anatase to rutile. First, we measured the hyperfine parameters:  $\omega_Q$  and  $\eta$  for the anatase and rutile phases in the bulk form to identify these phases formed in the nano  $\text{TiO}_2$  samples. In our earlier experiment [194] we found that  $\text{TiO}_2$  prepared by the hydrolysis of Ti-isopropoxide and annealed at 823K remains in the anatase phase and the transformation from anatase to rutile takes place only at 1123K. In this present work same conditions were maintained. Here the nuclear probe used is  $^{181}\text{Ta}$ .

XRD and AFM measurements indicate that the starting  $\text{TiO}_2$  is anatase with an average size of 70nm. We found significant adsorption (~90%) of  $^{181}\text{Hf}$  tracer on this nano  $\text{TiO}_2$  surface from the neutral solution of the tracer. Hafnium tracer in neutral medium is expected to exist as positively charged poly ionic form similar to that of zirconium [217] and gets adsorbed on the surface of  $\text{TiO}_2$ . It may thus be expected that the surface of  $\text{TiO}_2$  is negatively charged. TDPAC study of this adsorbed sample, S1 (dried at 373K to remove moisture) showed a broad distribution ( $\delta$ ) of the quadrupole frequency. This is a clear indication of a static inhomogeneity of the  $\text{TiO}_2$

surface. A possible explanation for this inhomogeneity is expected to have an origin in the uneven arrangement of oxygen bridging sites [218] in TiO<sub>2</sub> nano particles. The same sample when annealed at 823K for 4 h does not show much difference in the TDPAC spectrum (S2) except the reduction in the width of the frequency distribution. This indicates a partial removal of the surface inhomogeneity by heating process. Another explanation for this enhanced homogeneity is the increased surface smoothness due to the growth of the particle size at higher temperature. TDPAC results indicate that <sup>181</sup>Hf tracer remains on the surface only till 4 h of heating at 823K was done. XRD and TDPAC results show that there occurs neither any phase-transition nor any diffusion of the tracer in the matrix after annealing the sample at 823K for 4 h. The measurement of the peak-width in the XRD spectra of the anatase and rutile phases, mentioned in Table 4.1, envisages the fact that there occurs a steady decrease in the width clearly indicating the growth of the crystallite. However, no phase transition took place till four hours of annealing at 823K was done.

A different behavior, however, was found when this sample was annealed at 823K for 8 h (S3). The broadening ( $\delta$ ) is removed completely and the TiO<sub>2</sub> crystallite is transformed into rutile with a small contribution of anatase. But a large fraction for the probe could not be accounted for. Only a small fraction (25%) of the total anisotropy was identified as rutile plus anatase out of which 95% is rutile and only 5% is anatase. There is a fast decrease in anisotropy. This decrease is yet to be understood. This observation leads to a few conclusions. To speak of the first, the kinetics of the phase transition or the mass transfer from surface to bulk is a sluggish process in the present situation. The question, however, arises why almost no probe is found in anatase part. In the experiment with bulk TiO<sub>2</sub>, we did not see any phase transformation at 823K. It is not unusual for nano particle to undergo phase transformation at lower temperature. During this

process of phase change, the probe enters into the bulk from the surface and goes preferably to rutile phase. The other possibility is that the rutile phase might have been formed first and then the probe diffuses into the different phases. Nevertheless, both the processes mentioned above might be operating simultaneously. This conclusion is substantiated on the basis of the following results.

Initially anatase  $\text{TiO}_2$  (70 nm) was annealed at 1123K to convert it into rutile. Then the  $^{181}\text{Hf}$  probe was adsorbed on this preformed rutile surface. There was much less adsorption of the probe on the rutile surface than that on the starting anatase surface due to the lowering of surface area on going from anatase to rutile phase. This rutile  $\text{TiO}_2$  adsorbed with the TDPAC probe was annealed at 1123K for 4 h again to check the surface to bulk mass transfer. A significant amount of the probe was found to be in the rutile phase and nothing in the anatase phase (S4). It means that either there is no anatase phase existing in the sample when annealed at 1123K or  $^{181}\text{Hf}$  does not diffuse into anatase phase. However the subsequent experimental results indicate that the first inference on the nonexistence of anatase is not true. When the anatase  $\text{TiO}_2$  adsorbed with  $^{181}\text{Hf}$  was annealed at 1123K for 4 h, although a major fraction of the probe goes into the rutile phase (79%), a significant amount (21%) goes into the anatase phase as well. This indicates the existence of anatase phase when  $\text{TiO}_2$  was annealed at 1123K for 4 h (S5). But the probe was not found in anatase as evident in S4. Thus the existence of the probe in anatase phase in S5 is not due to the diffusion process. Had this been so, a significant amount of the probe could have been observed in the anatase phase in S4 as has been found in S5. We have already commented on the sluggishness of the process of phase transition from anatase to rutile  $\text{TiO}_2$ . To establish it further, anatase  $\text{TiO}_2$  adsorbed with the probe was annealed at 1123K for 8 h. Having doubled the duration of annealing at the same temperature (1123K), the population of rutile phase was found

to get enhanced further as indicated by the spectrum (S6). Annealing for the same duration (8h) but at a higher temperature (1223K) converts the anatase completely to rutile phase (S7). Hence, the phase transition in 70nm TiO<sub>2</sub> can be modeled in the following way. The surfaces of the nano particles roll over each other during the annealing process causing the growth in the crystallite and the <sup>181</sup>Hf/<sup>181</sup>Ta probe from the surface gets transferred into the bulk which transforms into the rutile phase and partly remains as anatase. The probe gets into the rutile phase either during the process of phase transition or due to diffusion after the rutile is formed or both. Hence the present work [219] involves a hyperfine interaction study of the process of phase transition in nano TiO<sub>2</sub> from anatase to rutile phase and concludes that the phase transition incorporates a temperature-mediated mass transfer from surface to its bulk.

## **4.2. Study of Core-shell Nanoparticles:**

### **4.2.1. Introduction:**

TiO<sub>2</sub> is a large band gap semiconductor with 3.2 eV for anatase and 3.06 eV for rutile and these have absorption in the UV region. This is why it is used as sunscreen material in cosmetic and skin care products. In the nano form this material can be synthesized in such a dimension that it is transparent to visible light but absorbs UV radiation thus causing no whitening effect. One very important use of TiO<sub>2</sub> is as a photocatalyst in the UV region. However absorption region can be shifted to visible by doping TiO<sub>2</sub> with other metal ions to make it sensitive in the visible region as well. Photocatalytic activity of TiO<sub>2</sub> mentioned above is inhibited due to the recombination of holes with the electrons produced during absorption of radiation. The efficiency of photocatalysis can however be enhanced if the electrons are removed from the semiconductor. This can precisely be done in a core-shell nanoparticle with a metal core acting as an electron sink.

Kamat and Hirakawa have reported that for Ag@TiO<sub>2</sub> core-shell nanoparticles, the photo-induced electron in TiO<sub>2</sub> shell can inject into the silver core under the illumination of ultraviolet light [220]. Recently it has been reported [221] that metal core such as silver with favorable Fermi energy ( $E_F = 0.4\text{V}$ ) are good electron acceptors where a facile electron transfer and proportionate rise in the hole concentration can take place from the excited TiO<sub>2</sub> shell to the metal core. Hence, the photocatalytic efficiency due to extra holes of nano TiO<sub>2</sub> is enhanced by the metal core. The phase transformation from anatase to rutile in the core-shell environment is also of much importance for its specific application. For example, DEGUSSA-P25 [222], a mixture of anatase and rutile in the proportion of 3:1 is an efficient photocatalyst.

In the present work, Ag@TiO<sub>2</sub> core-shell nanoparticles have been synthesized by preparing TiO<sub>2</sub> by controlled hydrolysis process on the preformed Ag nanoparticles in a sequential route. The thermal behavior as well as the anatase to rutile phase transitions in this system as a function of annealing temperature has been investigated. The behavior of the core-shell system has been compared with the pure TiO<sub>2</sub> nanoparticles. The study has been carried out with the nuclear probe technique TDPAC with an atomic scale resolution in combination with another standard analytical technique XRD which has been used to estimate the crystallite size utilizing the Debye-Scherrer equation. PAC spectroscopy relies on the nuclear quadrupole interaction (QI) between the quadrupole moment of the probe nucleus (here, <sup>181</sup>Ta) and the Electric Field Gradient (EFG) at the probe site. The EFG eventually implies the charge distribution around the probe atom and because of its  $r^{-3}$  dependence, the major contribution to QI from the nearest neighbor charges. PAC therefore provides the information on the short-range order and has been applied [219] to explain the anatase to rutile phase transition in case of ~70 nm anatase TiO<sub>2</sub> particles in our previous work. In the present work, the same technique has been used to elucidate

the thermal behavior of Ag@TiO<sub>2</sub> nanoparticles. However, this technique was previously utilized [223] to investigate the structure and grain growth of other core-shell nanoparticles, such study in case of Ag@TiO<sub>2</sub> is for the first time.

#### **4.2.2. Experimental Procedure and Measurements:**

The core-shell Ag@TiO<sub>2</sub> nanoparticles have been synthesized through the sequential route by the controlled hydrolysis [224] of titanium (IV) tetra-isopropoxide at pH1.5 in the medium containing the previously formed Ag nanoparticles prepared by gamma radiolysis method [225]. The dimensions of the Ag nanoparticles are in the range 15-18 nm. It is assumed that the acacia acting as the capping agent for Ag nano particles is removed by the TiO<sub>2</sub> formed in situ during hydrolysis. The resulting solution was concentrated at 313 K with a rotary evaporator and then dried under nitrogen stream to yield the nano-powder of Ag@TiO<sub>2</sub>. The active sample containing the PAC probe <sup>181</sup>Hf/<sup>181</sup>Ta was obtained by adding the probe at 0.01% level in the Ag nanoparticle solution at the beginning of the synthesis. The core-shell structure was confirmed by the TEM measurement. To study the thermal behavior to look into the phase transition from anatase to rutile, the sample was annealed at 473, 673, 873 and 1073K respectively for 6h. The active samples were used for the TDPAC study and the inactive counterparts were used for the XRD measurements. A parallel study was carried out with the pure TiO<sub>2</sub> nanoparticles in order to compare its annealing effect with that of Ag@TiO<sub>2</sub> nanoparticles.

Transmission electron microscopy (TEM) measurements were performed on Tecnai G<sup>2</sup> 30 Super Twin high resolution TEM with an acceleration voltage of 300 kV. The XRD patterns were obtained with Bruker AXS (D8) X-ray diffractometer with CuK $\alpha$  radiation. To study the grain growth and evolution of the rutile structure from anatase, both the samples were annealed at different temperatures as mentioned earlier and XRD pattern was recorded at room temperature

after each annealing. The particle size after each annealing was determined from the Scherrer formula using the line width of the XRD peak.

#### 4.2.3. Results and Discussion:

The UV–vis absorption spectra were analyzed by a Hitachi U-3900H spectrophotometer. The UV–vis absorption spectra of Ag and Ag@TiO<sub>2</sub> nanoparticles were shown in Fig. 4.4.

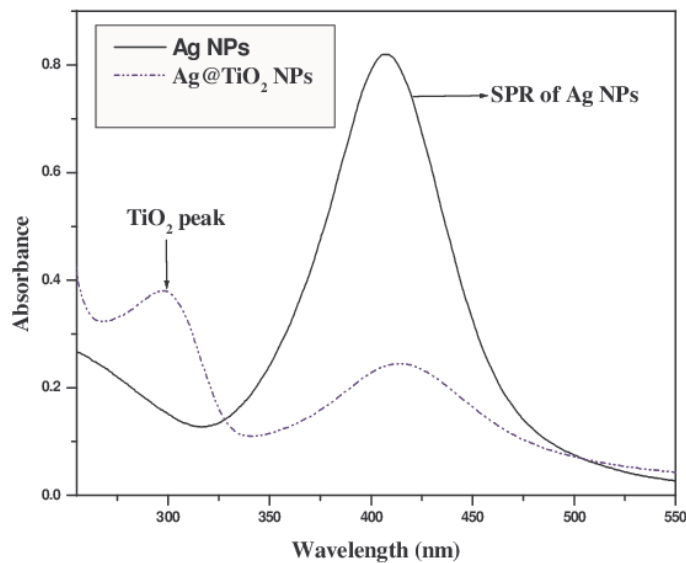


**Figure 4.4:** UV-vis absorption spectra for Ag and Ag@TiO<sub>2</sub> nanoparticles.

Typical TEM image of Ag@TiO<sub>2</sub> core-shell nanoparticles shown in Fig. 4.5 reflects that the as-synthesized nanoparticles are monodisperse and spherical.

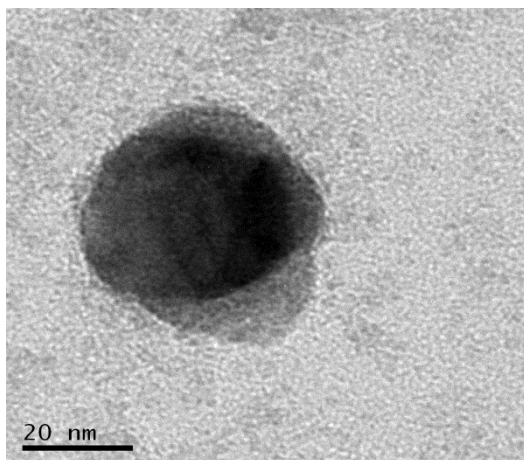


**Figure 4.5:** TEM picture of Ag@TiO<sub>2</sub> core-shell nanoparticles.

The darker part is the Ag core and the TiO<sub>2</sub> shell looks like a shadow. The XRD patterns of the Ag@TiO<sub>2</sub> core-shell nanoparticles annealed at 473K, 673K, 873K and 1073K respectively for 6h are shown in Fig. 4.6.

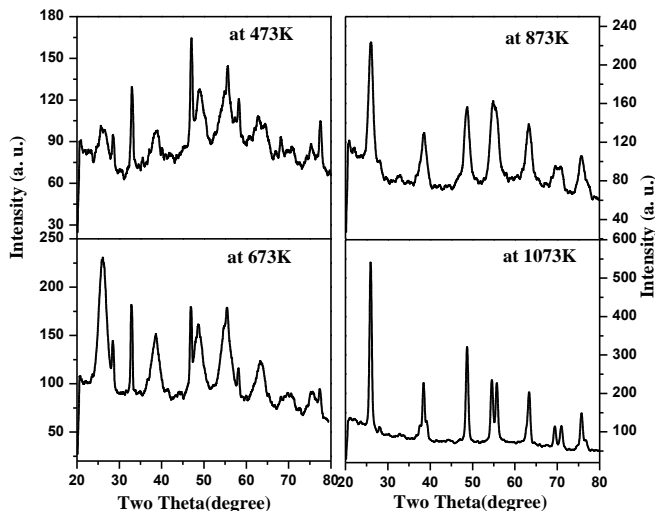


**Figure 4.6:** XRD patterns at different annealing temperature for Ag@TiO<sub>2</sub> nanoparticles.

The XRD patterns of as-synthesized nanoparticles are same as that annealed at 473K and hence the XRD pattern of the as-synthesized nanoparticles has been omitted. The corresponding XRD patterns for pure TiO<sub>2</sub> nanoparticles under the similar annealing conditions are shown in Fig. 4.7.

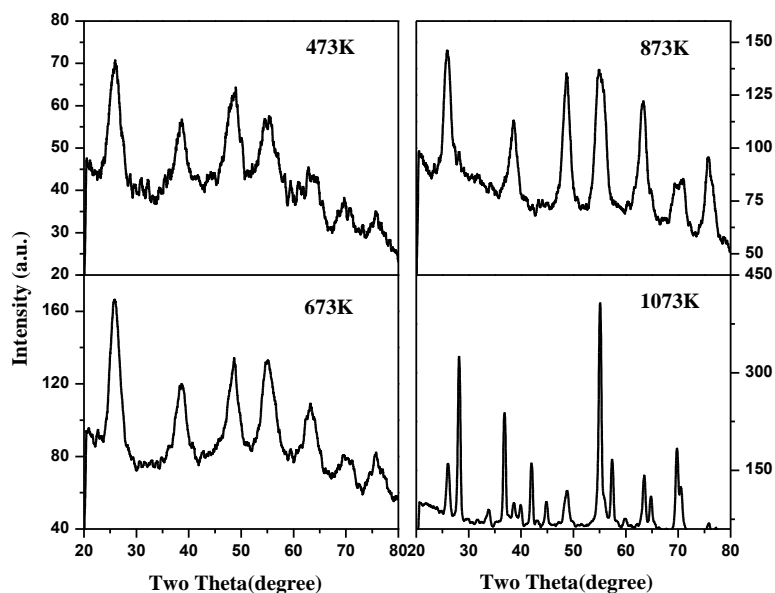


**Figure 4.7:** XRD patterns at different annealing temperature for pure TiO<sub>2</sub> nanoparticles.

The existing phase(s) and the corresponding particle size at different annealing temperatures obtained from the Scherrer formula have been furnished in Table 4.4. However, up to 673K, the peaks are broad indicating amorphous phase in both the cases. After annealing at 873K, the anatase phase starts to appear indicated by the presence of peak at  $2\theta=25^\circ$  for 101 planes. At 1073K, the rutile phase ( $2\theta=27^\circ$  for 110 planes) coexists with anatase phase in case of pure TiO<sub>2</sub> nanoparticles. The existence of this dual phase can be clearly seen from its XRD patterns. In contrast, this dual phase does not exist in the core-shell structure at an annealing temperature of 1073K. The change of grain size with annealing temperature in case of both the nanoparticles has been plotted in Fig. 4.8.

**Table 4.4:** Grain sizes and phases present at different annealing temperatures.

Annealing Temp (K)	Pure TiO <sub>2</sub> nanoparticle		Ag@TiO <sub>2</sub> nanoparticle	
	Size (nm)	Phase	Size (nm)	Phase
473	3.8	amorphous	2.1	amorphous
673	4.5	amorphous	4.8	amorphous
873	6.4	anatase+ amorphous	8.1	anatase+ amorphous
1073	16.1	anatase + rutile	16.4	anatase

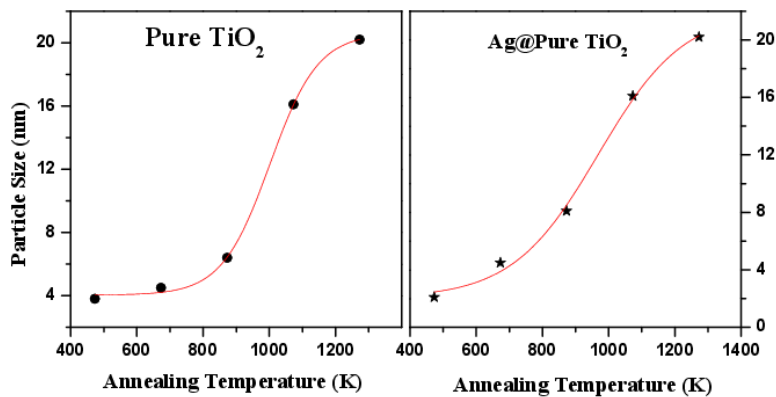


**Figure 4.8:** Nature of grain growth with annealing temperature.

The TDPAC spectra of Ag@TiO<sub>2</sub> nanoparticles are shown in Fig. 4.9. The time spectrum is on the left and the corresponding cosine transform is on the right.

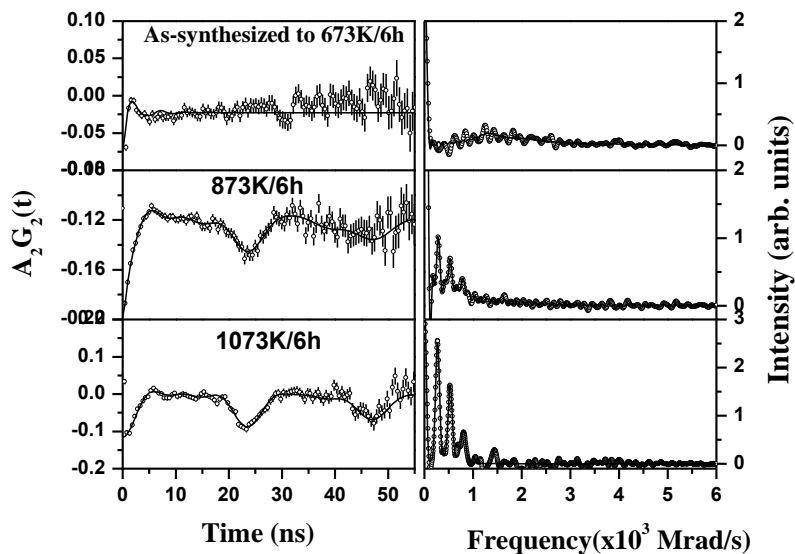


**Figure 4.9:** TDPAC spectra of Ag@TiO<sub>2</sub> at different annealing temperatures.

The topmost spectrum represents the as-synthesized nanoparticles and it remains same up to the annealing temperature of 673K upto which the cosine transform implies the amorphous nature of the sample. The following spectrum represents the nanoparticles annealed at 873K, typical for anatase TiO<sub>2</sub> along with a broad component. The PAC spectrum is fitted with two components: one with the anatase phase parameters  $\omega_Q=45.5$  (2) Mrad/S and  $\eta= 0.16$  (2) and other with a

broad component with equal proportions. The third spectrum from the top represents the nanoparticles annealed at 1073K at which a complete conversion of the amorphous phase into the anatase phase is observed.

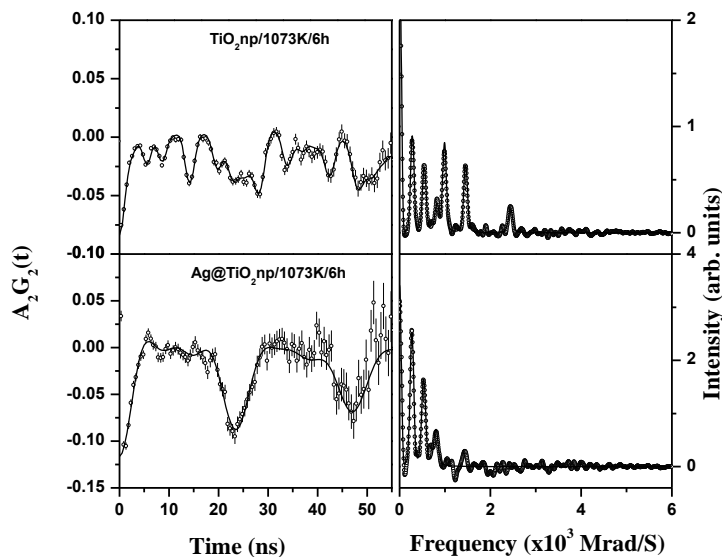


**Figure 4.10:** TDPAC spectra of pure  $\text{TiO}_2$  and  $\text{Ag@TiO}_2$  nanoparticles at 1073K.

When compared with the pure  $\text{TiO}_2$  nanoparticles, the behaviour almost follows the similar trend except at 1073K where the anatase phase appears with rutile phase with equal population without any amorphous phase. The difference between the pure and core-shell nanoparticles at 1073K in the TDPAC structure has been presented in Fig. 4.10. The rutile phase could not evolve at 1073K for  $\text{Ag@TiO}_2$  nanoparticles. The difference in behaviour has been explained schematically as shown in Fig. 4.11.

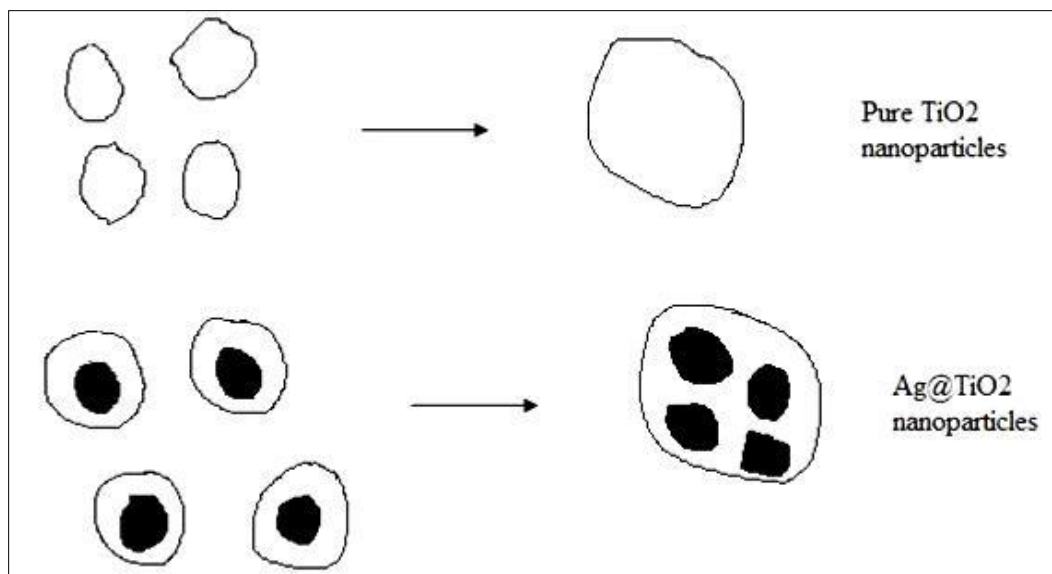


**Figure 4.11:** Schematic of particle growth in pure  $\text{TiO}_2$  and  $\text{Ag@TiO}_2$  nanoparticles.

The hyperfine interaction technique TDPAC in combination with XRD and TEM delivers a detailed process of structural evolution of the  $\text{TiO}_2$  shell and its relation with the grain growth in  $\text{Ag@TiO}_2$  core-shell nanoparticles. The absorption peak of Ag nanoparticles in Fig. 4.4 appeared at  $\sim 408$  nm. After capping with  $\text{TiO}_2$  shells, the absorption band was nm red-shifted to  $\sim 415$  nm. This significant shift might be due to the high refractive index of  $\text{TiO}_2$  shells and revealed the coverage of Ag cores with  $\text{TiO}_2$  shells. In addition,  $\text{Ag@TiO}_2$  nanoparticles showed very strong absorption at  $\sim 300$  nm. This could be attributed to the absorption of  $\text{TiO}_2$  in UV light region. The core-shell structure can be seen from the TEM image as shown in Fig. 4.5. This shows that the gross diameter of the  $\text{Ag@TiO}_2$  particle is around 40 nm. The shell thickness of this as synthesised particle is 4 nm as obtained from XRD measurement. Therefore the Ag core has a dimension of  $\sim 30$  nm. The difference in the dimension of the starting Ag nanoparticle and the final Ag core may be explained by the fact that during the formation of  $\text{TiO}_2$  from hydrolysis the capping agents get removed and Ag particles aggregates and grow in size. The difference in the behaviour under the similar annealing condition for pure  $\text{TiO}_2$  nanoparticles has also been

depicted in this work. Both the XRD and the TDPAC patterns of the as-synthesized core-shell nanoparticles imply that the  $\text{TiO}_2$  shell is amorphous in nature and remains amorphous until an annealing temperature of 673K. The nano shell then starts crystallizing in anatase structure at 873K with an equal fraction of the amorphous counter-phase. If the above thermal behaviour is compared with that of the pure  $\text{TiO}_2$  nanoparticles, it yields the similar trend upto 873K. After annealing at 1073K, the nano  $\text{TiO}_2$  shell is completely converted to anatase phase but still it cannot assume the rutile structure to any extent. In contrast, however, the rutile phase starts to appear when annealed for 6 hours at 1073K for pure  $\text{TiO}_2$  nanoparticles and the anatase and the rutile phases coexist with equal proportion. Both the XRD and the TDPAC patterns indicate the above difference. Although the rate of grain growth is similar in both the cases, the rate of phase transition does not follow the similar trend. The broad frequency distribution in the PAC spectra stems from the fact that the oxygen atoms in the  $\text{TiO}_2$  nano shell are in a highly disordered state. The hyperfine interaction between the electric quadrupole moment of the probe nucleus and the EFG eventually represents the charge distribution at the nearest-neighbor environment around the probe atom due to the  $r^{-3}$  dependence of the EFG tensor. The Hf probe atom replaces the Ti atom in the  $\text{TiO}_2$  shell and the nearest neighbor of Ti (or Hf) in the  $\text{TiO}_2$  shell are oxygen atoms. Hence the broad distribution of quadrupole frequency eventually implies the less ordered distribution of oxygen atoms around the probe atoms. As the broad frequency distribution persists up to an annealing temperature 673K, this broadness cannot be attributed only to the surface oxygen atoms. The bulk oxygen atoms are also in a disordered state giving rise to that broad distribution of the quadrupole frequency. From the particle size determination, it is inferred that the anatase phase persists up to a shell thickness (for core-shell NPs) or particle size (pure NPs) of 16nm in both the cases.

The nanoparticles under study had a white to brownish yellow colour for as-synthesized and annealed samples. As the color of  $\text{TiO}_2$  is highly sensitive to the Ti:O ratio [226], this ratio does not remain constant in the nanostructure of the  $\text{TiO}_2$  shell. Hence, this lattice defect could also contribute to the broad frequency distribution. The bulk as well as the surface oxygen atoms in the disordered state gradually gets ordered with increase in annealing temperature. After annealing at 873K,  $\text{TiO}_2$  shell-lattice could only assume the anatase phase at that grain size. But at the above annealing temperature, the broad component still persists at equal contribution with the anatase phase. This broad distribution might be attributed to the surface oxygen atoms when the bulk oxygen atoms have already assumed the anatase phase. With increasing the annealing temperature further at 1073K, almost all the particles in the  $\text{TiO}_2$  shell assume the anatase structure with inherent broadness, but rutile phase does not appear even at this annealing temperature. In contrast, the surface particles assume the anatase phase and the already assumed anatase particles in the bulk get transformed to the rutile phase resulting in a dual phase of anatase and rutile with equal population at 1073K in case of pure  $\text{TiO}_2$  nanoparticles.

The above contrast in the thermal behavior might be attributed to the fact that the anionic oxygen atoms in the  $\text{TiO}_2$  shell-lattice get chemically attached to the cationic surface of the Ag core. Due to this attachment, the surface to bulk mass transfer becomes difficult in case of core-shell nanostructure even after attaining the anatase phase. This core-shell structure modifies the nature of phase transition as well as its rate due to the chemical interaction between metal core and semiconductor shell. Another explanation for the above observation can be provided with the fact that the effective grain growth (bulk to surface ratio) required for the rutile-conversion does not take place in case of  $\text{Ag@TiO}_2$  nanoparticles as depicted in Fig. 4.11. The schematic shows that the correlation of the attainment of the rutile phase with the grain growth holds good for the

pure TiO<sub>2</sub> nanoparticles. But, due to the presence of Ag-core inside the TiO<sub>2</sub> shell, although the Ag@TiO<sub>2</sub> nanoparticles undergo the grain-growth under the similar annealing environment, the effective grain-size or the bulk to surface ratio for TiO<sub>2</sub> nano-shell could not suffice to evolve the rutile phase.

Thus, the present work [227] describes that the anatase to rutile phase transformation does not follow the same trend in the two systems. In case of core-shell nanoparticles, even after attaining the critical size for rutile phase transformation at 1073K, rutile structure could not be attained. But, for pure TiO<sub>2</sub> nanoparticles, the rutile phase starts to appear at 1073K and at a grain size of 16nm. This core-shell structure thus modifies the nature of phase transition as well as its rate either due to a chemical interaction between metal core and semiconductor shell or due to an insufficient effective grain growth of TiO<sub>2</sub> shell in case of Ag@TiO<sub>2</sub>nanoparticles.

### **4.3. Study of Thin Film:**

#### **4.3.1. Introduction:**

In the last few decades, mainly SiO<sub>2</sub> was used as the gate-dielectric material in the silicon-based Complementary Metal Oxide Semiconductor (CMOS) technology. The rate and scale of miniaturization of integrated circuit elements followed Moor's law [228]. Since integrated circuits are getting continuously smaller, the use of SiO<sub>2</sub> is facing its own limitations. Therefore, there has been a considerable effort to find a substitute for the SiO<sub>2</sub> dielectric [229]. The basic idea evolves from the fact that the material replacing SiO<sub>2</sub> should have a higher dielectric constant ( $k$ ) than that of SiO<sub>2</sub> but be compatible with the present Si technology. In the last ten years, hafnium dioxide (HfO<sub>2</sub>) has received a great deal of attention because of its high chemical stability, desirable dielectric properties ( $k \approx 23$ ) and mechanical hardness [230]. It has also a wide band gap of 5.7-5.8 eV. Again for many promising *high-k* material, it is also known that they are

thermally unstable and a silicidation process evolves out of the oxide/Si interface resulting in the formation of a low-k interfacial layer [231]. Hence, today the major concern is the thermal stability of the system  $\text{HfO}_2/\text{Si}$ . During the last few years, it was shown that the annealing of the system above 973K leads to the formation of three-dimensional Hf-silicide structures [232-233]. It was also reported long ago [234] that Hf and Si react at temperatures as low as 873K to form HfSi and at 1038K to form  $\text{HfSi}_2$ . Again in some other literature [232], it was found that hafnium silicide starts to appear even at a lower annealing temperature of 573K. For annealing temperature around 773K, almost all the metallic Hf is converted to at least one silicide component and forms an amorphous or polycrystalline phase. They found no evidence of any structural phase transition from an ordered HfSi to an ordered  $\text{HfSi}_2$  with annealing except the formation of 3D islands in the high temperature annealing regime. It has been observed that  $\text{SiO}_2$  layer on the Si substrate appears to form a barrier that slows down the interdiffusion process necessary for the reaction to proceed [235]. However, Hf on Si substrate can react at 1273K despite the presence of a  $\text{SiO}_2$  layer at the interface with a thickness of up to 50 nm. Hence the reaction between Hf and Si, the inter-diffusion process resulting in the silicidation reaction and the fate of  $\text{HfO}_2$  in this nano-phase domain of Hf-silicide are really to be understood for the long-term application of  $\text{HfO}_2$  based devices.

A minute insight of the process in the atomic scale resolution can be achieved by the study of NQI at the nuclear probe site by the TDPAC technique as it delivers the direct measurements of the local structure and electronic environment around the probe atom. There have been a number of efforts [236-240] to investigate the above phenomena with the aid of this hyperfine technique. In all these works, the thin film deposited on the Si-substrate was the oxide itself and then the oxide thin film was studied by the hyperfine PAC tool under different experimental conditions.

But to investigate the microstructural aspects of the silicidation process in the Hf/Si interface and their interdiffusion process, it is highly required to start with the metallic Hf thin film on the Si-substrate. In this paper, we report the formation of monoclinic phase of HfO<sub>2</sub> from the metallic Hf deposited on Si (111) surface under 10mbar O<sub>2</sub> pressure. Si (111) was chosen as the literature indicates that the quality of the gate oxide is slightly better on (111) substrate in the direct tunneling regime [241]. The change in the morphology of the surface of the ~50 nm thin film with the annealing process has also been followed by AFM measurements and correlated with the PAC results. The annealing condition of 10 mbar O<sub>2</sub> pressure was chosen in order to ensure the fact that the oxidation process of Hf-metal to HfO<sub>2</sub> maintains thermodynamic reversible condition resulting in a better adherence to the Si-surface. The interfacial behavior of Hf/Si layer with the annealing condition and any possible silicide formation at the Hf/Si interface during annealing have been monitored by the hyperfine technique TDPAC in this present study.

#### **4.3.2. Experimental Study:**

The Si(111) single crystals were cleaned by ultrasonication with ethanol to get a clean surface for thin film deposition. Initially Hf metal film was deposited onto this Si(111) substrate by Ion beam sputtering method. Ion beam sputtered thin film deposition method is one of the best known methods for synthesis of high quality thin films. All the processes take place at room temperature and hence there are no stresses of any form in the synthesized films that would occur due to elevated temperatures. Fig. 4.12 shows the schematic of ion beam sputtering process. Here inductively couple plasma based RF ion source operating at 13.56 MHz was utilized to produce high current heavy ions such as Ar<sup>+1</sup> ions. RF power was maintained at 100W and 1 mA of 5 KeV. Ar<sup>+</sup> ions were used to sputter the Hf plate placed at 60 degree inclination to the beam. The substrates were mounted on the movable sample holder in-front of the inclined Hf plate.

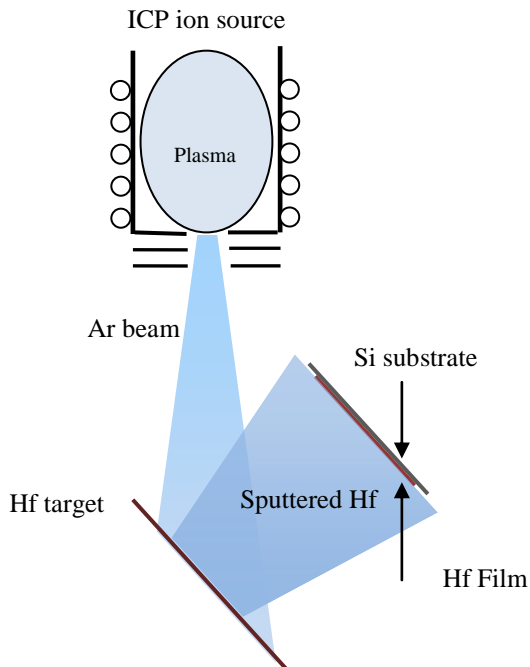


**Figure 4.12:** Schematic of Thin film preparation by ion beam sputter deposition.

The sample was moved horizontally as well as vertically so as to obtain thin film with uniform thickness. Total duration to prepare thin film with a thickness of  $\sim 50$  nm was 30 minutes. The pressure in the vacuum chamber was maintained at a value of  $\sim 8 \times 10^{-6}$  mbar. The film quality and thickness synthesized in this experiment is very much reproducible. The thickness of the thin films was measured both directly and indirectly. Indirect method involves  $\alpha$ -spectroscopy of the Hf-film deposited on a cellophane paper under identical deposition condition. Again the thickness of as-prepared thin films on the Si-surface was directly measured by Rutherford Back-Scattering (RBS) method. Both the measurements yield a thickness of  $\sim 50$  nm.

This thin film of Hf was neutron irradiated in a thermal neutron-flux of  $\sim 5 \times 10^{13}$  n/cm<sup>2</sup>/s at Dhruva Reactor, BARC, Mumbai to produce the  $^{181}\text{Hf}/^{181}\text{Ta}$  probe by the reaction  $^{180}\text{Hf}(n,\gamma)^{181}\text{Hf}$  for TDPAC study. The film was annealed at 673K, 873K and 1073K for 4h under 10mbar O<sub>2</sub> pressure. The same film then was annealed at 1273K for 4h, 8h and 12h. The thin film was also directly annealed at 1273K for 4h, 8h and 12h. After each annealing, the film was counted

for TDPAC at room temperature. Surface topographical analyses were carried out using an M/S NT-MDT make Solver Pro AFM by using semi-contact mode of operation. The mechanical stability of the HfO<sub>2</sub> layer on the Si-substrate is also of major importance for its long-term application. The radioactive property of the <sup>181</sup>Hf nuclei present in the HfO<sub>2</sub> layer on Si has been utilized for the adherence study. After the complete attainment of the monoclinic phase of HfO<sub>2</sub> on Si-substrate, the thin film was ultrasonicated in ethanol for 30min. But no <sup>181</sup>Hf-activity leached out of the thin film. It implies a strong adherence of HfO<sub>2</sub> film on the Si-surface.

#### 4.3.3. Results and Discussion:

In  $\alpha$ -spectroscopic method of thickness measurement, the attenuation in the  $\alpha$ -energy due to the deposited thin film was correlated with the amount of Hf present in the film. The RBS experiment was carried out at Nuclear Fuel Complex, Hyderabad. The characterization of the thin film before annealing was carried out using 5.2 MeV <sup>12</sup>C-ions in RBS chamber. The detector was kept at 170° angle. The RBS spectrum, analysed by SIMNRA 6.0, is shown in Fig. 4.13.

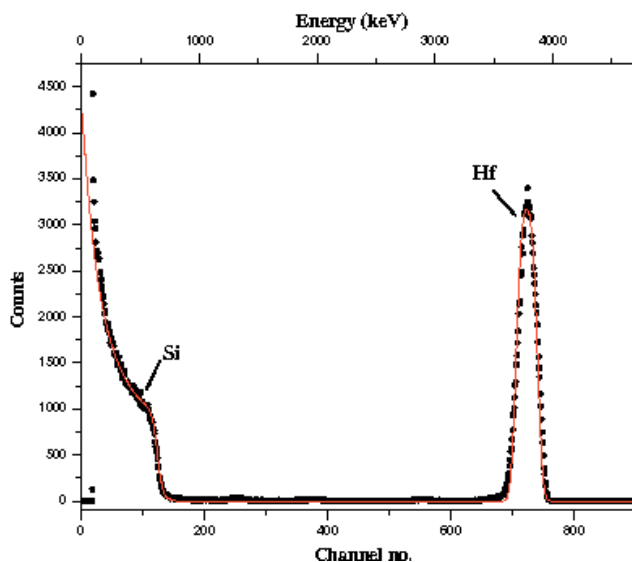


**Figure 4.13:** RBS spectrum for unannealed Hf thin film on Si (111) substrate.

After determining the thickness of the films by  $\alpha$ -spectroscopy and RBS to be ~50nm, TDPAC measurements were carried out under different annealing conditions.

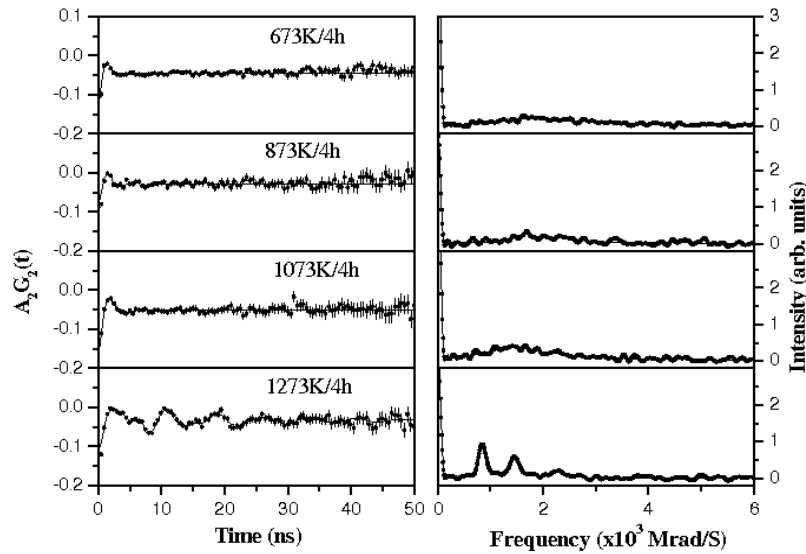


**Figure 4.14:** TDPAC spectra of thin film annealed under 10mbar O<sub>2</sub> pressure.

Three different stages of TDPAC measurements have been performed. At first, the Hf metal thin film was annealed at 673K, 873K, 1073K and 1273K under 10mbar oxygen pressure. The sample was annealed for 4h at each annealing temperature. After each annealing, the sample was counted for TDPAC measurement at room temperature. The corresponding TDPAC spectrum is shown in Fig. 4.14. The left part of the figure shows the  $A_2G_2(t)$  spectra and on the right shown is the corresponding cosine transform. In the second stage, the same sample, already annealed upto 1273K for 4h in the first stage, was annealed twice, each for another 4h at the same 1273K temperature. This annealing sequence where it starts at 673K and reaches 1273K at an interval of 200K was termed as stepwise (SW) annealing. After reaching 1273K in SW manner, the sample was annealed at this 1273K temperature for 4h, 8h and 12h and the corresponding spectrum is shown in Fig. 4.15.

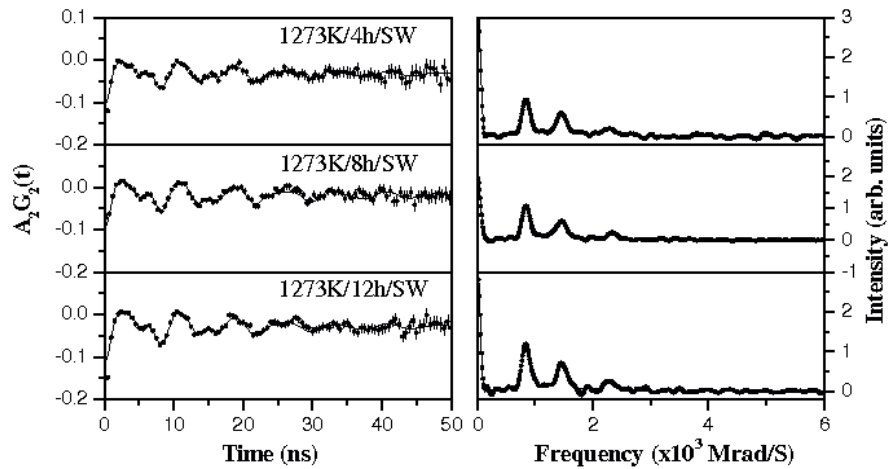


**Figure 4.15:** TDPAC spectra of the thin film annealed at 1273K under 10mbar  $O_2$  pressure for different durations.

In the last stage of experiment, the sample was directly annealed at 1273K for three different durations, viz., 4h, 8h and 12h. The corresponding PAC spectrum is shown in Figure 4.16.

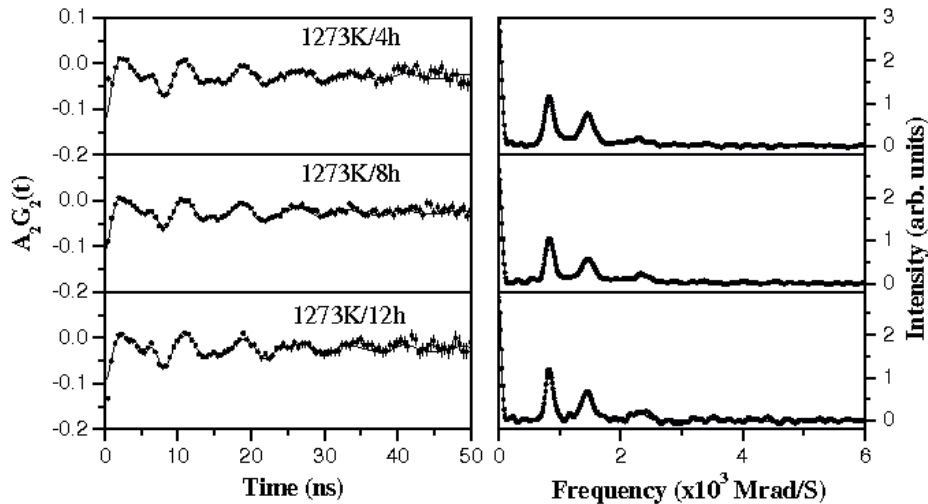


**Figure 4.16:** TDPAC spectrum of the thin film annealed directly at 1273K under 10mbar  $O_2$  pressure for different durations.

The evolution of the monoclinic phase of  $HfO_2$  from the metallic Hf thin film in partial  $O_2$  environment has been compared and presented in Figure 4.17.

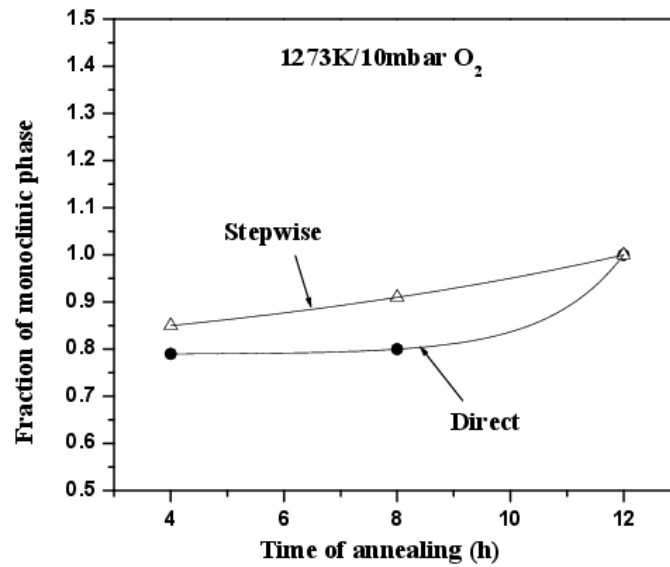


**Figure 4.17:** Evolution of monoclinic phase under different annealing conditions.

The morphology of the surface of the thin film has also been followed at each step of the annealing process. In the paper, only two AFM pictures of as prepared thin film and thin film annealed at 1273K have been represented in Fig. 4.18.

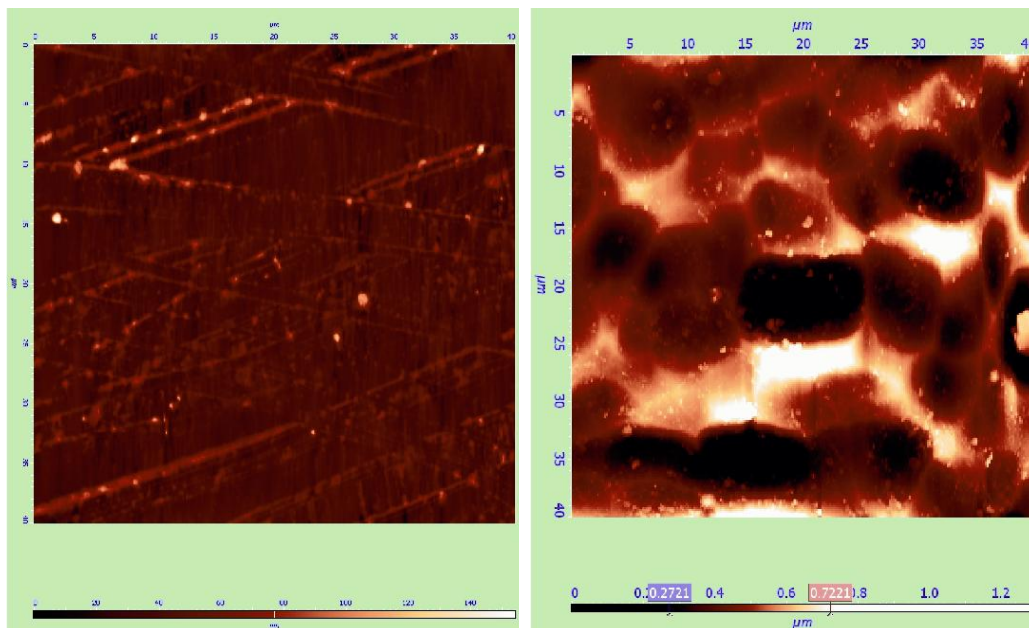


**Figure 4.18:** AFM pictures of thin film as prepared (left) and annealed at 1273K (right)

**Table 4.5:** TDPAC parameters for different annealing conditions under 10 mbar O<sub>2</sub> pressure:

Annealing Condition	$\omega_Q$ (Mrad/S)	$\eta$	$\delta$ (%)	Site Fraction(%)
673K/4h	234.8 (19.4)	0.49 (9)	32.9 (9.2)	100
873K/4h	210.3 (10.1)	0.59 (6)	16.5 (5.2)	100
1073K/4h	166.1 (23.4)	0.59 (18)	37.8 (18.4)	100
1273K/4h (SW)	124.1 (1.2)	0.37 (2)	5.5 (8)	85
	197.5 (15.4)	0.57 (12)	7.5 (9.5)	15
1273K/8h (SW)	125.1 (7)	0.36 (1)	4.5 (4)	91
	120.2 (44.7)	0.97 (13)	8.2 (8)	09
1273K/12h (SW)	124.6 (6)	0.36 (1)	5.8 (4)	<b>100</b>
1273K/4h (direct)	124.9 (8)	0.34 (1)	5.1 (5)	79
	134.7 (13.6)	0.75 (16)	13.7 (12.0)	21
1273K/8h (direct)	126.1 (6)	0.33 (1)	5.5 (5)	80
	176.9 (14.5)	0.48 (10)	16.1 (9.8)	20
1273K/12h (direct)	124.4 (5)	0.35 (1)	4.6 (4)	<b>100</b>

The TDPAC parameters at different annealing condition have been furnished in Table 4.5. From Fig. 4.14, it is obvious that after annealing at 673K for 4h in 10 mbar O<sub>2</sub> partial pressure the spectrum could be fitted with a broad frequency component having high  $\delta$ -value. This implies that the probe could not occupy a definite lattice site. The inhomogeneity in the electronic environment around the probe atom is reflected by the large distribution of the quadrupole frequency. However, high magnitude and asymmetry of the EFG tensor are perceived by the high frequency value and the high  $\eta$ -value respectively. The large inhomogeneity in the electronic environment around the probe atom also indicates the presence of large number of defects around the probe atom. When the same thin film is annealed at 873K for 4h under

similar oxygen environment, the spectrum could still not be fitted with a narrow frequency distribution. The spectrum (Fig. 4.14) showed a large frequency distribution with a large  $\delta$ -value. The nature of the spectrum did not change even after annealing at 1073K for 4h as shown in Fig. 4.14. The frequency value was not identical in all these three annealing conditions but it was in the range of ~165-235 Mrad/s with  $\delta$ -value ranging from 16-38 %. The asymmetry in the EFG value ranges from 0.49-0.59. As there was no significant change in the asymmetry value of EFG, it can be inferred that the variation in the frequency parameter might be attributed to the large number of defects present surrounding the probe atom. Generally, the reorientation in the electronic structure around the probe atom leads to a significant change in the asymmetry of the EFG value. Again considering the errors associated with the frequency as well as the  $\delta$ -values, the values lie almost within their individual error limits. At this stage of annealing upto 1073K under controlled oxygen environment, the possibility of HfO<sub>2</sub> formation could not be fully ignored. The as prepared Hf thin film is amorphous in nature as evidenced from the TDPAC measurement. It is also expected as it was prepared at room temperature. Among the layers of metallic Hf on the Si-surface, first few top-most layers are first converted to HfO<sub>2</sub> and it remains in amorphous phase over the amorphous metallic Hf layers. This partial conversion of metallic Hf into HfO<sub>2</sub> and co-existence of Hf and HfO<sub>2</sub> might have occurred at the beginning of the annealing process. Now as the annealing temperature increases, the diffusion of oxygen in the inner layers of metallic Hf might take place and Hf layers gradually get converted into the amorphous HfO<sub>2</sub> phase till 1073K. During this conversion process, the amorphous Hf and HfO<sub>2</sub> phases exhibit a range of values for their TDPAC parameters (Table 4.5). At 1273K, the amorphous HfO<sub>2</sub> phases start to attain the monoclinic phase when it also starts the 3D-island formation. So it is inferred that the 3D-island formation by HfO<sub>2</sub> plays a key role in attaining

the monoclinic phase. When it was annealed at the same temperature but for a higher duration (8h), the percentage of monoclinic phase increased as shown in Fig. 4.15. The attainment of the monoclinic phase of  $\text{HfO}_2$  is completed after annealing at 1273K for 12h. So the kinetics for the attainment of the monoclinic phase is slow. To see any possible effect of the sequence of annealing on the attainment of the monoclinic phase, another thin film sample of same thickness was directly annealed at 1273K for 4h when the monoclinic phase evolved to almost similar extent as in case of previous step-wise annealing sequence. When the duration of annealing was increased upto 12h, the attainment of monoclinic phase was completed. The evolution of the monoclinic phase has been shown in Fig. 4.16. However, it is to be noted that the inherent broadness of the frequency for the monoclinic  $\text{HfO}_2$  formed over the nano-phase is higher than that for bulk monoclinic  $\text{HfO}_2$ . In Fig. 4.17, the evolution of the monoclinic phase of  $\text{HfO}_2$  from the metallic Hf thin film under two different annealing sequences has been compared. It is seen that there is no significant difference in the evolution process. The 3D-island formation by  $\text{HfO}_2$  under the present annealing condition initiated at 1273K as obvious from AFM measurements shown in Fig. 4.18. From the present study it is seen that the  $\text{HfO}_2$  phase gradually evolves from the metallic Hf-film and remains amorphous upto an annealing temperature of 1073K and also till the formation of 3D-island. As soon as the 3D-island formation started at 1273K, the monoclinic phase could be attained. So it can be inferred that the 3D-island formation by the  $\text{HfO}_2$  nano-phase plays an important role in the attainment of the monoclinic  $\text{HfO}_2$  phase. Again in the present study, the formation of Hf-silicide in the Hf/Si interface could not be observed during the evolution process of monoclinic  $\text{HfO}_2$  phase from the metallic Hf-thin film. Hence, the study reveals that the amorphous  $\text{HfO}_2$  phase associated with large amount of defects is formed from the metallic Hf and remains amorphous upto 1073K. However, when it is annealed

at 1273K the monoclinic phase starts to appear along with 3D-island formation and the percentage of monoclinic phase increases with the duration of annealing at the same temperature. Hence the kinetics of this evolution process is slow. It is only the monoclinic HfO<sub>2</sub> phase which exists after annealing at 1273K for 12h. Non-existence of any other component in the TDPAC spectrum rules out the formation of any Hf-silicide phase in the present work.

#### **4.4. Conclusion:**

The present chapter contains the synthesis of pure and core-shell nanoparticles by controlled hydrolysis method. After synthesis, the particles have been characterized by UV-visible and TEM measurements. The nanoparticles containing the <sup>181</sup>Hf/<sup>181</sup>Ta probe have been used for TDPAC measurements. The XRD measurements have been used for long-range information. The surface to bulk mass transfer during the phase transition of nano TiO<sub>2</sub> has been demonstrated by the TDPAC technique. Again the stability of anatase phase in presence of Ag-core has also been identified by TDPAC method and explained in terms of ineffective grain-growth with annealing in core-shell system. This study will guide to the synthesis of nano-TiO<sub>2</sub> with enhanced stability of anatase phase. The thin film of Hf has been prepared on Si(111) surface and annealed under controlled oxygen environment. The role of 3D-island formation on the evolution of monoclinic HfO<sub>2</sub> phase has been demonstrated in the present work. The TDPAC study also confirms the absence of any Hf-silicide in the present reaction sequence.

## Chapter 5. Summary and Outlook

This thesis describes the potential of the  $\gamma$ - $\gamma$  Perturbed Angular Correlation Technique applied to both the bulk and lower dimension of materials. The application of this technique in the nanomaterials including core-shell nanoparticles and thin films is very limited. The method of labeling the samples with the nuclear probe has been carried out under mild condition and with  $\sim 0.1$  atom% concentration of the probe so that the material property of the host matrix does not get affected. The TDPAC spectrometer is based on CAMAC electronics where the data are collected in LIST mode. The setup has got LaBr<sub>3</sub>(Ce) detectors coupled with fast PM Tubes. The optimum operational condition has also been determined by the characteristics study of these detectors under different working conditions. The time resolution of the system has been determined with the new setup.

The characteristics of the new LaBr<sub>3</sub>(Ce) detectors have been studied at different bias voltages of the PM Tube. The linearity of the energy response for these detectors has been followed with varying bias voltages. The dependence of the time resolution of the coincidence setup with the PM Tube bias has been looked into in order to determine the optimum working condition of this coincidence setup based on the LaBr<sub>3</sub>(Ce) detectors. The TDPAC parameters for the bulk TiO<sub>2</sub>, ZrO<sub>2</sub> and HfO<sub>2</sub> have been determined following the present method of sample preparation based on coprecipitation technique. In this case two probes, viz., <sup>181</sup>Hf/<sup>181</sup>Ta and <sup>111</sup>In/<sup>111</sup>Cd, have been used. First probe was produced by neutron irradiation method while the second probe was obtained by charged particle reaction at VECC, Kolkata. The high cross-section of <sup>180</sup>Hf (natural abundance  $\sim 35\%$ ) for thermal neutron absorption ( $\sim 13$  barn) produces sufficient amount of the probe <sup>181</sup>Hf/<sup>181</sup>Ta which is subsequently used along with the other Hf-isotopes. On the other hand, the <sup>111</sup>In-probe, after its production, is separated in carrier-free form and then used for

subsequent study. The strength of EFG is comparable in case of rutile  $\text{TiO}_2$ ,  $\text{HfO}_2$  and  $\text{ZrO}_2$  for both the probes. However, the strength of EFG is lower in case of anatase  $\text{TiO}_2$ . This observation is expected from the corresponding crystal structures of the oxides. The rutile matrix has been doped with one transition element Mn and another same group element Zr. The effect of the doping has been investigated with the TDPAC method. The  $^{181}\text{Hf}/^{181}\text{Ta}$  was used as the PAC probe in the present study. The interaction of the probe atom with the dopant atom is different from that with the host atoms. This is not reflected in the mean values of the interaction frequency and the asymmetry parameter. The width of the frequency distribution has been found to increase steadily with the dopant concentration. So the hyperfine technique TDPAC can be utilized to investigate the role of dopant in the host matrix and its interaction with the host atoms. The effect of varying concentration of dopant can also be looked into by this microscopic tool. The radiation-damage study of the rutile matrix has been carried out with TDPAC technique. For this, the leaching of Hf from  $\text{TiO}_2$  matrix has been investigated in different media, like, water, NaCl solution and humic acid solution. The selection of the leaching media stems from the fact that water is the most common medium of contact, NaCl solution simulates the medium of seawater and humic acid solution represents the soil environment. In all the cases, the leaching has been monitored by following the radioactivity of  $^{181}\text{Hf}$  tracer. The effect of  $\gamma$ -dose on the crystal structure of  $\text{TiO}_2$  has been investigated with the hyperfine interaction technique, viz., TDPAC and it has been correlated with the leaching behavior of  $\text{TiO}_2$ . The  $\text{TiO}_2$  matrix has so stable crystal structure that it is not disturbed by a long  $\gamma$ -irradiation and Hf, simulant for actinide in high-level waste, is strongly adhered in the  $\text{TiO}_2$  matrix which might thus be used as an immobilizing medium for nuclear waste.

A hyperfine interaction study of the process of phase transition in nano TiO<sub>2</sub> from anatase to rutile phase has been carried out. The phase transition in 70nm TiO<sub>2</sub> could be described in the following way. The surfaces of the nano particles roll over each other during the annealing process causing the growth in the crystallite and the <sup>181</sup>Hf/<sup>181</sup>Ta probe from the surface gets transferred into the bulk which transforms into the rutile phase and partly remains as anatase. The probe gets into the rutile phase either during the process of phase transition or due to diffusion after the rutile is formed or both. The phase transition incorporates a temperature-mediated mass transfer from surface to its bulk.

The same technique has been used to elucidate the thermal behavior of Ag@TiO<sub>2</sub> core-shell nanoparticles and compare the similar behavior for pure TiO<sub>2</sub> nanoparticles. The anatase to rutile phase transformation does not follow the same trend in the two systems. In case of core-shell nanoparticles, even after attaining the critical size for rutile phase transformation at 1073K, rutile structure could not be attained. But, for pure TiO<sub>2</sub> nanoparticles, the rutile phase starts to appear at 1073K and at a grain size of 16nm. This core-shell structure thus modifies the nature of phase transition as well as its rate either due to a chemical interaction between metal core and semiconductor shell or due to an insufficient effective grain growth of TiO<sub>2</sub> shell in case of Ag@TiO<sub>2</sub>nanoparticles.

The formation of monoclinic phase of HfO<sub>2</sub> from the metallic Hf deposited on Si (111) surface under 10mbar O<sub>2</sub> pressure has been studied using TDPAC. The change in the morphology of the surface of the ~50 nm thin film with the annealing process has also been followed by AFM measurements and correlated with the PAC results. The amorphous HfO<sub>2</sub> phase associated with large amount of defects is formed from the metallic Hf and remains amorphous upto 1073K. However, when it is annealed at 1273K the monoclinic phase starts to appear along with 3D-

island formation and the percentage of monoclinic phase increases with the duration of annealing at the same temperature. Hence the kinetics of this evolution process is slow. It is only the monoclinic  $\text{HfO}_2$  phase which exists after annealing at 1273K for 12h. Non-existence of any other component in the TDPAC spectrum rules out the formation of any Hf-silicide phase in the present work.

The fibrous  $\text{HfO}_2$ , used as the RIB target material, doped with  $^{181}\text{Hf}/^{181}\text{Ta}$  probe was studied using the TDPAC technique where  $^{181}\text{Ta}$  occupying the Hf sites acted as a TDPAC probe.  $\text{HfO}_2$  fibrous samples were annealed at different temperatures in 1000-2000K range and the structural aspects were investigated in the samples annealed at such high temperatures using TDPAC technique.

In order to understand the TDPAC results obtained from the  $^{181}\text{Ta}$  doped  $\text{HfO}_2$  fibrous sample and also the annealing effects on these samples, the first principle electronic structure calculations were performed based on density functional theory (DFT) using WIEN2K code. DFT calculation of the  $\text{HfO}_2$  system indicates that the  $^{181}\text{Ta}$  probe is in the charged state in the lattice position and the contribution of the EFG is mainly due to the p-electrons. Density of states indicates that the doping with Ta does not affect the neighboring Hf atoms of the host. As a result, EFG parameters of the fiber having 6-7  $\mu\text{m}$  diameter doped with Ta are expected to remain unaltered compared to those of bulk  $\text{HfO}_2$ .

**References:**

1. M. Elvira, *Journal of Chemical Education* (1932) 1231–1243.
2. D. Coster and G. Hevesy (1923-01-20), *Nature* **111** (2777) 79–79.
3. J. Adam and M. D. Rogers, *Acta Crystallographica*, **12**[11] (1959).
4. R. Ruh and P. W. R. Corfield. *J. Am. Ceram. Soc.* **53**[3] (1970) 126–129.
5. J. D. McCullough and K. N. Trueblood. *Acta Cryst.* **12** (1959) 507–511.
6. H. Zhang and J. F. Banfield. *J. Mater. Chem.* **8** (1998) 2073.
7. H. Zhang and J. F. Banfield. *J. Phys. Chem. B* **104** (2000) 3481–3487.
8. P.I. Gauma and M. J. Mills, *J. Am. Ceram. Soc.* **84**(3) (2001) 619.
9. A. Navrotsky and O.J. Kleppa, *J. Am. Ceram. Soc.* **50** (1967) 626.
10. J. F. Banfield, B.L. Bischoff and M.A. Anderson, *Chemical Geology* **110** (1993) 211.
11. A. Suzuki and R. Tukuda, *Bull. Chem. Soc. Japan* **42** (1969) 1853.
12. K.P. Kumar, *Scripta Metallurgica et Materialia* **32** (1995) 873.
13. Dorian A. H. Hanaor and Charles C. Sorrell. *J. Mater. Sci.* **46** (2011) 855–874.
14. K. N. P. Kumar, K. Keizer, A. J. Burggraaf. *J. Mater. Sci. Lett.* **13** (1994) 59.
15. R. L. Penn and J. F. Banfield. *Am. Miner.* 84 (1999) 871.
16. A. Rothschild et al. *Surf. Sci.* **532** (2003) 456.
17. P. A. Cox (1992). “Transition metal oxides: an introduction to their electronic structure and properties”. Clarendon Press, Oxford.
18. K. H. Harold (1989) Transition metal oxides: surface chemistry and catalysis. Elsevier, Oxford.

19. M. Batzill, E. H. Morales, U. Diebold. *Phys. Rev. Lett.* **96** (2006) 26103.
20. R. D. Shannon, J. A. Pask. *J Am Ceram Soc* **48** (1965) 391.
21. R. D. Shannon. *AEC Rep. No.* UCRL-I1001 (1964) 97 pp. (Chem. Abstr.63,2468b).
22. J. A. Pask. *Amer. Mineral.* **49** (1964) 1707-1717.
23. A.W. Czanderna, C. N. R. Rao , J. M. Honig. *Trans. Faraday Soc.* **54** (1957) 1069-1073.
24. A. N. R. Rao. *Can. J. Chem.* **39** (1961) 498-500.
25. F. Cardarelli (2000). *Materials Handbook*, Springer, London.
26. G. Teufer. *Acta Crystallographica*, **15**[11] (1962) 1187-1187.
27. J.Wang, H. P. Li, R. Stevens. *Journal of Materials Science*, **27**[20] (1992) 5397-5430.
28. A.G. Khachaturyan (1983). "Theory of Structural Transformations in Solids", John Wiley & Sons, New York.
29. G. M. Wolten. *J. Amer. Ceram. Soc.* **46** (1963) 418.
30. J. Fisher and T. A. Egerton (2001) Titanium compounds, inorganic, Kirk-Othmer encyclopaedia of chemical technology. Wiley, New York.
31. J. Sun, L. Gao, Q. Zhang. *J. Am. Ceram. Soc.* **86** (2003) 1677.
32. K. Fujihara, T. Ohno, M. Matsumura. *J. Chem. Soc. FaradayTrans.* **94**(1998) 3705.
33. A. Fujishima, K. Honda. *Nature* **238**(1972) 37.
34. A. O'Regan, M. Gratzel. *Nature* **335** (1991) 737.
35. M. Gratzel. *Inorg. Chem.* **44** (2005) 6841.
36. D. S. Muggli, L. Ding. *Appl. Catal.* **B32** (2001) 184.
37. A. Fujishima, X. Zhang, D. A. Tryk. *Surf. Sci. Rep.* **63** (2008) 515.
38. K. Okamoto et al. *Bull. Chem. Soc. Jpn.* **58** (1985) 2015.
39. R. W. Matthews. *J. Phys. Chem.* **91** (1987) 3328.

40. R. L. Pozzo, M. A. Baltanas, A. E. Cassano. *Catal. Today* **39** (1997) 219.
41. N. Daude, C. Gout, C. Jouanin. *Phys. Rev. B* **15** (1977) 3229.
42. A. Linsebigler, G. Lu, J. T. Yates. *Chem. Rev.* **95** (1995) 735.
43. Y. Paz, A. Heller. *J. Mater. Res.* **12** (1997) 2759.
44. J. M. Herrmann. *Catal. Today* **53** (1999) 115.
45. A. Mills and S. Le Hunte, *J. Photochem. Photobiol. A*, **108** (1997) 1-35.
46. T. Tachikawa, M. Fujitsuka, T. Majima, *J. Phys. Chem. C* **111** (2007) 5259-5275.
47. P. D. Cozzoli et al., *Mat. Sci. Eng. C* **23** (2003) 707-713.
48. C. A. Emilio et al., *Langmuir* **22** (2006) 3606-3613.
49. W. Choi, A. Termin, M. R. Hoffmann, *J. Phys. Chem. B*, **98** (1994) 13669-13679.
50. A. Sclafani, *J. Phys. Chem.*, 100 (1996) 13655-13661.
51. N. F. Mott, R. S. Allgaier, *Phys. Status Solidi (b)* **21** (1967) 343.
52. J. C. Yu et al., *Chem. Mater.* **14** (2002) 3808.
53. A. Sclafani, J. M. Herrmann, *J. Phys. Chem.* **100** (1996) 13655.
54. M. A. Fox, M. T. Dulay, *Chem. Rev.* 93 (1992) 341.
55. T. Ohno et al., *Appl. Catal. A* **244** (2003) 383.
56. T. Ohno et al., *J Phys Chem B* **101** (1997) 6415.
57. J. Yu et al., *J. Mol. Catal. A*, **253** (2006).
58. A. Weyl and D. Janke, *J. Am. Ceram. Soc.* **79**[8] (1996) 2145-2155.
59. H. Ibegazene, S. Alperine, and C. Diot, *J. Mater. Sci.*, **30**[4] (1995) 938- 951.
60. P. Kofstad, D.J. Ruzicka, *J. Electrochem. Soc.* **110** (1963) 181
61. L.A. McClaine, C.P. Coppel, *J. Electrochem. Soc.* **113** (1966) 80.
62. K.J. Hubbard, D.G. Schlom, *J. Mater. Res.* **11** (1996) 2757.

63. J.H. Choi, Y. Mao, J.P. Chang, *Materials Science and Engineering R* **72** (2011) 97-136.
64. S.A. Campbell et al., *IEEE Trans. Electron Devices* **44** (1997) 104.
65. R.C. Smith et al., *Adv. Mater. Opt. Electron.* **10** (2000) 105.
66. C.C. Ting, S.Y. Chen, D.M. Liu, *J. Appl. Phys.* **88** (2000) 4628.
67. G.D. Wilk, R.M. Wallace, and J.M. Anthony, *Appl. Phys. Lett.* **74** (1999) 2854.
68. G.D. Wilk, R.M. Wallace, and J.M. Anthony, *J. Appl. Phys.* **87** (2000) 484.
69. B.H. Lee et al., *Appl. Phys. Lett.* **76** (2000) 1926.
70. H. Yanagida, K. Koumoto, M. Miyayama (1996), "The Chemistry of Ceramics", John Wiley & Sons.
71. Adriana Zaleska, *Recent Patents on Engineering* **2** (2008) 157-164.
72. X. Nie et al., *International Journal of Photoenergy* (2009); doi:10.1155/2009/294042.
73. S. Sato. *Chem. Phys. Lett.* **123** (1986) 126-128.
74. R. Asahi et al., *Science* **293** [5528] (2001) 269–271.
75. H. Irie, Y. Watanabe, K. Hashimoto. *J. Phys. Chem. B* (2003) 5483-5486.
76. T. Umebayashi et al., *Appl. Phys. Lett.* **81**(3) (2002) 454–456.
77. T. Ohno et al., *Appl. Catal. A: Gen* **265** (2004) 115–121.
78. S.U.M. Khan, M. Al-Shahry Jr., W. BI, *Science* **297** (2002) 2243–2245.
79. M. Okada et al., *Thin Solid Films* **442** (2003) 217–221.
80. A. Hattori et al., *Chem. Lett.* (1998) 707–708.
81. W. Y. Choi, A. Termin, M. R. Hoffmann, *J. Phys. Chem.* **84** (1994) 13669–13679.
82. X. S. Wu et al., *Wuli Huaxue Xuebao [in Chinese]* **20**(2) (2004) 138–143.
83. A.W. Xu, Y. Gao, H. Q. Liu, *J. Catal.* **207** (2002) 151–157.
84. M. Ni et al., *Renewable and Sustainable Energy Reviews* **11** (2007) 401–425.

85. X. Zhao and D. Vanderbilt, *Phys. Rev. B* **65** (2002) 233106.
86. J. D. Schieltz, J. W. Patterson, D. R. Wilder, *Electronchemical Science* **11** (1971) 1257.
87. M. F. Trubeljia and V. S. Stubican, *J. Am. Ceram. Soc.* **74** (1991) 2489.
88. L. Gao et al., *Ceramics International* **38** (2012) 2305-2311.
89. Nettleship and R. Stevens, *Int. J. High Technology Ceramics* **3** (1987) 1-32.
90. W.D. Kingery, H.K. Bowen and D.R. Uhlmann (1976): *Introduction to Ceramics*, Wiley, New York, USA.
91. S. Ran et al., *J. Eur. Ceram. Soc.* **27** (2007) 683.
92. J.J. Swab, *J. Mater. Sci.* **26** (1991) 6706.
93. E. S. Elshazly, S.M. El-Hout, M. El-Sayed Ali, *J. Mater. Sci. Technol.* **27(4)** (2011) 332.
94. D. R. Hamilton, *Phys. Rev.* **58** (1940) 122.
95. G. Goertzel, *Phys. Rev.* **70** (1946) 897.
96. E. L. Brady and M. Deutsch, *Phys. Rev.* **72** (1947) 870.
97. H. Aeppli et al., *Helv. Phys. Acta* **25** (1952) 339.
98. H. Albers-Schonberg et al., *Phys. Rev.* **90** (1953) 322.
99. F. Pleiter, *Hyp. Int.* **5** (1977) 109.
100. A. Lerf and T. Butz, *Angew. Chem. Int. Ed. Engl.* **26** (1987) 110.
101. M. Zacate and H. Jaeger, *Defect and Diffusion Forum* **311** (2011) 3.
102. E. N. Kaufmann and R. J. Vianden, *Rev. Mod. Phys.* **51(1)** (1979) 161-214.
103. C. A. Sholl, *Proc. Phys. Soc. Lond.* **91** (1967) 130.
104. T. Butz, *Z. Naturforsch.* **51a** (1996) 396-410.
105. J. P. Adloff, *Radiochimica Acta* **25** (1978) 57-74.
106. L. C. Biedenhern and M. E. Rose, *Rev. Mod. Phys.* **25** (1953) 729.

107. H. Fraunfelder, *Phys. Rev.* **82** (1951) 549.
108. H. Aeppli et al., *Phys. Rev.* **82** (1951) 550.
109. K. Alder, *Helv. Phys. Acta* **25** (1952) 235.
110. A. Abragam and R. V. Pound, *Phys. Rev.* **92** (1953) 943.
111. H. Fraunfelder and R.M.Steffen, Alpha Beta and Gamma Ray Spectroscopy, K.Sieghbahn, Ed. Vol II, Chap. XIX , North Holland, Amsterdam(1965).
112. R. M. Steffen and H. Fraunfelder: Perturbed Angular Correlation, E. Karlson, E. Matthius, K. Sieghbahn Eds., Chap. I, North Amsterdam(1964).
113. H. Haas and D. A. Shirley, *J. Chem. Phys.* **58** (1973) 3339.
114. H. H. Rinneberg, *At. Energy Rev.* **17** (1979) 477.
115. M. E. Rose (1957), Elementary Theory of Angular Momentum, John Wiley and Sons, New York.
116. C. Eckart, *Rev. Mod. Phys.* **2** (1930) 305.
117. G. Racah, *Phys. Rev.* **62** (1942) 438.
118. L. C. Biedenhern, J. M. Blatt and M. E. Rose, *Rev. Mod. Phys.* **24** (1952) 249.
119. G. Schatz and A. Weidinger : Nuclear Condensed Matter Physics: Nuclear Methods and Applications (John Wiley, New York, 1996).
120. R. M. Steffen and K. Alder, in: *The Electromagnetic Interaction in Nuclear Spectroscopy*, edited by W. D. Hamilton, North-Holland Publishing Company, Amsterdam (1965).
121. S. P. Lloyd, *Phys. Rev.* **85** (1952) 904.
122. S. P. Lloyd, *Phys. Rev.* **88** (1952) 906.
123. G. Racah, *Phys. Rev.* **84** (1951) 910.

124. M. Rotenberg, R. Bivins, N. Metropolis and J. K. Wooten, Jr., *The 3j and 6j-symbols*, Technology Press MIT, Cambridge, MA 1959.
125. E. Matthias, W. Schneider and R. M. Steffen, *Phys. Lett.* **4** (1963) 41.
126. R. P. Feynman, *Phys. Rev.* **84** (1951) 108.
127. E. Matthias, W. Schneider and R. Steffen, *Phys. Rev.* **125** (1962) 261.
128. K. Alder et al., *Helv. Phys. Acta* **26** (1953) 761.
129. R. Beraud et al., *Nucl. Instr. Methods* **69** (1969) 41.
130. M. H. Cohen, *Phys. Rev.* **96** (1954) 1278.
131. E. Matthias, B. Olsen and W. Schneider, *Arkiv for Fys.* **24** (1963) 245.
132. B. R. T. Frost, *Progress in Meta Physics* **5** (1954) 96.
133. M. Blume, *Phys. Rev.* **174** (1968) 351.
134. M. Blume, *Nucl. Phys.* **A167** (1971) 81.
135. C. Scherrer, *Nucl. Phys.* **A157** (1970) 81.
136. A. G. Marshall and C. F. Meares, *J. Chem.Phys.* **56** (1972) 1226.
137. R. M. Lynden-Bell, *Molecul. Phys.* **21** (1971) 891.
138. A. G. Marshall, L. G. Werbelow and C. F. Meares, *J. Chem.Phys.* **56** (1972) 1226.
139. D. A. Shirley, *J. Chem.Phys.* **55** (1971) 1512.
140. G. Graf, J. C. Glass and L. L. Richer, *Adv. Exp. Med. Biol.* **48** (1974) 639.
141. D. Dillenburg and Th. A. J. Maris, *Nucl. Phys.* **33** (1962) 208.
142. E. P. Kooper, *Phys. Rev.* **61** (1942) 1.
143. Th. A. Carlson, *Phys. Rev.* **130** (1963) 2361.
144. H.E. Mahnke, *Hyp. Int.* **49** (1989) 77.
145. M. Iwatschenko-Borho and R. Schmitzer, *Hyp. Int.* **35** (1987) 1011.

146. G. Czjzek, *Hyp. Int.* **14** (1983) 189.
147. W. Körner et al., *Hyp. Int.* **15/16** (1983) 993.
148. C. Vogdt et al., *Proc. VIIIth Int. Congr. Catal.* (Berlin 1984) Vol. III, p. 117.
149. C. Vogdt et al., *Polyhedron* **5** (1986) 95.
150. H. de Waard, *Phys. Scr.* **11** (1975) 157.
151. H. Bernas, *Phys. Scr.* **11** (1975) 167.
152. E. Recknagel and T. Wichert, *Nucl. Instr. Methods* **182/183** (1981) 439.
153. F. Pleiter and C. Hohenemser, *Phys. Rev. B Condens. Matter* **25** (1982) 106.
154. M. Deicher et al., *Hyp. Int.* **10** (1981) 675.
155. M. Deicher et al., *Hyp. Int.* **10** (1981) 667.
156. I. J. R. Baumvol et al., *Phys. Rev. B Condens. Matter* **22** (1980) 5115.
157. K. Krolas et al., *Phys. Rev. B Condens. Matter* **28** (1983) 1864.
158. G. Scahafes, P. Herzog, B. Wolbeck, *Z. Phys.* **257** (1972) 336.
159. A. Weidinger, *J. Less-Common Met.* **103** (1984) 285.
160. U.H. Kopvillem and L.W. Shakhmuratova, *Phys. Lett.* **42A(1)** (1972) 63.
161. M.R. Gaertther and B.W. Maxfield, *Phys. Rev. Lett.*, **26** (1971) 119.
162. K. H. Speidel, *Hyp. Int.*, **34** (1987) 167.
163. M. C. Caracoche et al., *Hyp. Int.* **23** (1985) 221.
164. A. M. Rodriguez et al., *J. Chem. Phys.* **82** (1985) 1271.
165. W. Keppner et al., *Phys. Rev. Lett.* **54** (1985) 2371.
166. T. Butz et al., *Hyp. Int.* **15/16** (1983) 925.
167. P. Boyer et al., *Chem. Phys. Lett.* **14** (1972) 601.
168. R. Bauer, *Q. Rev. Biophys.* **18** (1985) 1.

169. P. W. Martin, S. El-Kateb and U. Kuhnlein, *J. Chem. Phys.* **78** (1982) 3819 and references therein.
170. R. D. Vis et al., *Nucl. Instr. Methods* **163** (1979) 265.
171. D. J. Lurie, F. A. Smith and A. Shukri, *Int. J. App. Rad. Isot.* **36(1)** (1985) 57.
172. C. A. Kalfas, E. G. Sideris and P.W. Martin, *Int. J. App. Rad. Isot.* **35(9)** (1984) 889.
173. G. Then et al., *Hyp. Int.* **15/16** (1983) 893.
174. H. Appel et al., *Hyp. Int.* **35** (1987) 953.
175. H. Appel et al., *Hyp. Int.* **35** (1987) 957.
176. M. De. Bruin, R. W. Hollander and J. vander Plicht, *J. Inorg. Nucl. Chem.* **38** (1976) 2149.
177. G. R. Demille et al., *Chem. Phys. Lett.* **44** (1976) 164.
178. A. Baudry, P. Boyer and P. Vulliet, *Hyp. Int.* **29** (1976) 279.
179. J. A. Martinez et al., *Chem. Phys. Lett.* **67(1)** (1979) 618.
180. H. Jaeger et al., *Hyp. Int.* **80** (1990) 615.
181. Hyperfine Interaction VI, R.S. Raghavan, D.E. Murnik (Eds.), North Holland, Amsterdam (1978).
182. H. Haas, *Phys. Scripta*, **11** (1975) 221.
183. P. Scherrer, *Göttinger Nachrichten Gesell.*, **2** (1918) 98.
184. A. Patterson, *Phys. Rev.* **56 (10)** (1939) 978.
185. [www.tifr.res.in/lamps](http://www.tifr.res.in/lamps).
186. S. Koichi, M. Manasijevic and B. Cevic, *Hyp. Int.* **14** (1983) 105.
187. E. V. D. van Loef et al., *Applied Physics Letters* **79** (2001) 1573-1575.
188. E.V.D. van Loef et al., *Nucl. Instr. & Meth in Phys. Res.* **A486** (2002) 254.

189. D. A. Gedcke and W. J. McDonald, *Nucl. Intr. & Meth.* **55(2)** (1967) 377.
190. D. A. Gedcke and W. J. McDonald, *Nucl. Intr. & Meth.* **58(2)** (1968) 253.
191. <http://uni.leipzig/~nfp>.
192. T. Butz et al., *Physica Scripta* **54** (1996) 234.
193. E. Breitenberger, *Proc. Phys. Soc. (London)* **A67** (1954) 1108.
194. S. B. Ryu et al., *Phys. Rev.* **B77** (2008) 094124.
195. J. A. Adams and G. L. Catchen, *Phys. Rev.* **B50(2)** (1994) 1264.
196. L.A. Errico, G. Fabricius and M. Renteria, *Phys. Rev.* **B67** (2003) 144104.
197. S. K. Das, S. V. Thakare, T. Butz, *J. Phys. Chem. Solids* **70** (2009) 778.
198. R.S. Sonawane, B.B. Kale and M.K. Dongre, *Mat. Chem. and Phys.* **85** (2004) 52.
199. A. A. Bolzan et al., *Acta Cryst.* **B53** (1997) 373.
200. D. Banerjee et al., *Hyp. Int.* **198(1-3)** (2011) 193.
201. V. M. Efremkov, *IAEA Bulletin* **4** (1989) 37–42.
202. C. Adelhelm et al., (1988) TiO<sub>2</sub>-A ceramic matrix. In W.Lutze and R.C.Ewing, Eds., from *Radioactive Waste Forms for the Future*, p.393-426. Elsevier, New York.
203. D. Banerjee et al. *J. Radioanal. Nucl. Chem.* **290** (2011) 119.
204. G. D. Alton, *Nucl. Intr. & Meth.* **A382** (1996) 207.
205. K. A. Chipps et al., *Phys. Rev. C* **62** (2000) 055804.
206. Y. Liu and G. D. Alton, *Nucl. Intr. & Meth.* **A438** (1999) 210.
207. D. Bhowmick et al., *Nucl. Intr. & Meth.* **539** (2005) 54.
208. P. S. Priambodo, J. A. Maldonado and R. Magnusson, *Appl. Phys. Lett.* **83** (2003) 3248.
209. C.C. Dey et al., *J. Appl. Phys.* **109** (2011) 113918.
210. F. Cardarelli (2000) *Material Handbook*, Springer, London.

211. P. Hohenberg and W. Kohn, *Phys. Rev* **136** (1964) B864; W. Kohn and L. J. Sham, *ibid* **140** (1965) A1133.
212. P. Blaha et al., WIEN2k\_12.1 (Release 30.08.2012): An Augmented Plane Wave Plus Local Orbitals Program for Calculating Crystal Properties.
213. P. Blaha et al., *Comput. Phys. Commun.* **59** (1990) 399.
214. R. E. Alonso et al., *Phys. Rev. B* **78** (2008) 165206.
215. J. P. Perdew, K. Burke and M. Ernzerhof, *Phys. Rev. Lett.* **77** (1996) 3865.
216. M. A. Taylor et al., *Phys. Rev. B* **82** (2010) 165203.
217. D.C. Bradley and P. Thornton (1973), Chapter 33 in *Comprehensive Inorganic Chemistry*, Ed. J.C. Bailar, H.J. Emeleus, Sir Ronald Nyholm, A.F. Trotman-Dickenson, Pergamon Press, p. 451.
218. L. Sirghi et al., *Langmuir* **17(26)** (2001) 8199.
219. D. Banerjee et al., *J. Phys. Chem. Solids* **71** (2010) 983.
220. T. Hirakawa and P.V. Kamat, *Langmuir* **20** (2004) 5645.
221. T. Hirakawa and P.V. Kamat, *J. Am. Chem. Soc.* **127** (2005) 3928.
222. T. Ohno et al., *Journal of Catalysis* **203** (2001) 82.
223. S. Schlabach et al., *J. App. Phys.* **100** (2006) 024305.
224. D. Bahnemann et al., *J. Phys. Chem.* **88** (1984) 709.
225. Y. N. Rao et al., *Rad. Phys. Chem.* **79** (2010) 1240.
226. J. C. Parker and R. W. Siegel, *Appl. Phys. Lett.* **57** (1990) 943.
227. D. Banerjee and S.K. Das, *J. Radioanal. Nucl. Chem.* (accepted).
228. G. E. Moore, *Electronics* **38** (1965) 8.
229. C. J. Först et al., *Nature (London)* **427** (2004) 53 and references therein.

230. R. Govindaraj, C. S. Sundar and R. Kesavamoorthy, *J. Appl. Phys.* **100** (2006) 084318.
231. T. J. Hubbard and D. G. Schlom, *J. Mater. Res.* **11** (1996) 2757.
232. H. Johnson-Steigelman et al., *Phys. Rev.* **B69** (2004) 235322.
233. N. Miyata et al., *Phys. Rev.* **B71** (2005) 233302.
234. C. J. Kircher et al., *Appl. Phys. Lett.* **22**(1973), 81; J. F. Ziegler et al., *J. Appl. Phys.* **44** (1973) 3851.
235. A. de Siervo et al., *Phys. Rev.* **B74** (2006) 075319.
236. R.A. Quille and A.F. Pasquevich, *Journal of Alloys and Compounds* **495** (2010) 634.
237. F. H. M. Cavalcante et al., *Hyp. Int.* **198** (2010) 41.
238. A.F. Pasquevich, F. H. M. Cavalcante and J. C. Soares, *Hyp. Int.* **179** (2007) 67.
239. F. H. M. Cavalcante, A. W. Carbonari and J. C. Soares, *Journal of Physics: Conference Series* **249** (2010) 012051.
240. C. C. Dey et al., *Journal of Applied Physics* **109** (2011) 113918.
241. H. S. Momose et al., *IEEE Trans. Electron Devices* **49** (2002) 1597.

## Index

### A

Abragam And Pound Model, 80  
 Adiabatic Approximation, 82  
 Ag@TiO<sub>2</sub> Nanoparticles, 165  
 Anatase, 21  
 Anisotropy, 56  
 Applications  
   HfO<sub>2</sub>& ZrO<sub>2</sub>, 33  
   TiO<sub>2</sub>, 29  
 Asymmetry Parameter, 53  
 Atomic Force Microscope, 104

### C

Computer Automated Measurement And Control, 110  
 Coprecipitation Method, 128  
 Core-Shell nanoparticles, 165  
 Correlation Time, 80, 81  
 Crystal Structure  
   HfO<sub>2</sub> & ZrO<sub>2</sub>, 22  
   TiO<sub>2</sub>, 21

### D

Density Functional Theory, 148  
 Dillenburg and Maris Theory, 83  
 Directional Correlation Function, 53  
 Doped Oxide  
   HfO<sub>2</sub> and ZrO<sub>2</sub>, 40  
   TiO<sub>2</sub>, 36  
 Doped Oxides  
   HfO<sub>2</sub> and ZrO<sub>2</sub>, 40

### E

Electric Field Gradient, 51  
 Electronic Modules  
   Amplifier, 119  
   Analogue to Digital Converter, 122  
   Constant Fraction Discriminator, 121  
   Time to Amplitude Converter, 121  
 Energy Linearity of LaBr<sub>3</sub> (Ce) Detector, 117

### F

Fast Slow Coincidence Circuit, 110  
 Fast timing discriminators, 120

### G

Group-IVB Metal Oxides, 20

### I

In-Beam PAC, 88  
 Ion Beam Sputter Deposition, 178

### L

LaBr<sub>3</sub> (Ce) Detector, 113  
 Leaching Study, 140

### M

Martensitic Transformations. *See* Phase Transformation  
 Master Gate, 122

### N

Nano TiO<sub>2</sub>, 155

### P

Perturbation Function, 66  
 Perturbation of Angular Correlation  
   Electrical Perturbation, 72  
   Magnetic Perturbation, 71  
 Perturbed Angular Correlation Function, 62  
 Perturbed Angular Correlation Spectroscopy, 43  
 Perturbed Angular Distribution, 87  
 phase Stabilized Zirconia, 34  
 Phase Transformation  
   Diffusionless Transformation, 27  
   Displacive Transformation, 27  
   HfO<sub>2</sub> and ZrO<sub>2</sub>, 25  
   Hysteresis, 28  
   Kinetics, 25  
   Martensitic, 27  
   TiO<sub>2</sub>, 23  
 Photo Multiplier Tube, 114  
 Photocatalysis by TiO<sub>2</sub>. *See* Applications  
 PSZ, 42

### Q

Quadrupole Frequency, 73  
 Quadrupole Moment, 47

**R**

Random Phase Approximation. *See* Time Dependant Perturbation  
 RIB target material, 144  
 Rise Time, 120  
 Rutherford Backscattering Spectrometry, 107  
 Rutile, 21

**S**

Scanning Electron Microscope, 103  
 Static Magnetic and Electric Field  
   Magnetic, 71  
 Stochastic Theory, 80

**T**

TDPAC Probes, 92  
 TDPAC Results  
   Ag@TiO<sub>2</sub> and Pure TiO<sub>2</sub> nanoparticles, 167  
   HfO<sub>2</sub> Fibre, 146  
   Mn-doped TiO<sub>2</sub>, 135  
   Nano TiO<sub>2</sub>, 157  
   Pure Oxides, 128  
   Thin Film of Hf, 179  
   Zr-doped Rutile, 136  
 Thermal Neutron Irradiation, 178  
 Thin Film of HfO<sub>2</sub>, 175  
 Thin Film Preparation, 177

Time and Amplitude Walk, 120  
 Time Dependant Perturbation  
   Diffusion Model, 79  
   Strong Collision Model, 79  
 Time Dependent Perturbations, 79  
 Time Differential PAC (TDPAC), 55  
 Time Jitter, 120  
 Time Per Channel (TPC), 122  
 Time Pick-off Process, 120  
 Time Resolution, 117  
 Transformation Toughening, 42  
 Transmission Electron Microscopy, 103  
 TZP, 35

**U**

UV-Vis Spectrophotometry, 106

**W**

WIEN2K Code, 148

**X**

XP2020/URQ, 115  
 X-ray Diffraction, 101

**Y**

YSZ, 35